Alma Mater Studiorum - Università di Bologna

DOTTORATO DI RICERCA IN

CHIMICA

Ciclo 33

SILICON NANOCRYSTALS TAILORED FOR BIOIMAGING AND ENERGY CONVERSION

Presentata da: Sara Angeloni

Coordinatore Dottorato

Domenica Tonelli

Supervisore

Paola Ceroni

Co-supervisore

Giacomo Bergamini

Esame finale anno 2021

II

What is that feeling

When you're driving away

From people and they recede on the plain

Till you see their specks dispersing?

It's the too-huge world vaulting us,

And it's good-bye.

But we lean forward

To the next crazy adventure

Beneath the skies

Jack Kerouac

Silicon Nanocrystals Tailored for Bioimaging and Energy Conversion

Abstract

This thesis focus is the development of hybrid organic-inorganic systems based on Silicon Nanocrystals (SiNCs) with possible applications in the field of bioimaging and solar energy conversion. SiNCs were engineered thanks to the realization of a strong covalent Si-C bond on their surface, which allowed us to disperse them in different solvents with different final purpose. **Chapter 1** introduces the basic properties of nanomaterials, focusing our attention on quantum dots, SiNCs in particular. **Chapter 2** describes all the synthetic procedures to obtain the organic molecules-functionalized SiNCs, showing both the literature techniques and the ones adopted in our laboratory. **Chapter 3** illustrates an organic-inorganic antenna system based on SiNCs conjugated with diphenylanthracene (DPA) photoactive molecules, which was also embedded into Luminescent Solar Concentrators (LSC) made of a polymeric matrix. The optical and photovoltaic performances of this device were compared with the ones of a LSC embedded with a physical mixture made of SiNCs plus DPA at the same concentrations of the two components in the covalent system. **Chapter 4** shows many different techniques to functionalize SiNCs with polyethylene glycol (PEG) chains in order to make them dispersible in water, for biomedical imaging applications. All the in vivo and ex vivo measurements reported in this chapter were acquired by Jennifer R. Shell, Xu Cao and Brian Pogue, in the Center for Imaging Medicine, Thayer School of Engineering, Dartmouth College, Hanover, NH 03755. **Chapter 5** presents the synthesis of dyes and/or SiNCs loaded Polymer Nanoparticles (PNPs) capable of excitation energy transfer (EET)

mechanism. This work has been started at the University of Strasbourg in the laboratory of Biophotonics and Pharmacology led by the professor Andrey Klymchenko. **Chapter 6** is focused on the realization of photo-switchable systems based on azobenzene derivatives-functionalized SiNCs. These organic-inorganic hybrid materials were studied to possibly obtain a new light-driven response of SiNCs. In the end, **chapter 7** reports the activity I followed in America, at The University of Texas at Austin, in the laboratory led by the professor Brian Korgel. Here I studied and compared the properties of high temperature hydrosilylated SiNCs and room temperature, radical promoted, hydrosilylated SiNCs.

Contents

x

Acknowledgments

This thesis has been written during the strangest period in my life since I was born. There was a global pandemic and we were all locked in our houses. Many people around us, close or not, were passing away and we could not even say a last good-by. In such strange time, we discovered a new way of living; we learned to love people sharing them our affection 1.5 meters apart or behind a screen. During this bad time, many of us finally understood what is important in life: not money, not a nice and big house (even if in a bigger house I could have passed a better lockdown), not an expensive car or what else, but to love and to be loved. Relationships and being around the people we love, these are the most important things in life. In addition, being healthy, of course. In this strange time, I found myself writing this PhD thesis. Well, I have always imagined this moment differently from what it revealed to be. Therefore, I want to say thanks to the people -all around the world- that I love, to the people who gave me moral support during this bad moment, to the people who made my work at the University of Bologna and this thesis possible.

I wish I will always have you around me, always starting new amazing adventures, always falling in love with all the life little things.

Whoever stops does not fall in love anymore.

Preface

"Modern civilization is the daughter of coal (…), modern man uses it with increasing eagerness and thoughtless (…). The earth still holds enormous quantities of it, but coal is not inexhaustible. The problem of the future begins to interest us (…). The supply is enormous but, with increasing consumption, the mining of coal becomes more expensive on account of the greater depth to which it is necessary to go. (…) Is fossil solar energy the only one that may be used in modern life and civilization? That is the question."[1] This brief extract from the famous Giacomo Ciamician's speech, hold during the VIII International Congress of Applied Chemistry in New York, 1912, allows us to understand the general ideas, intuitions and concepts born from his studies. More than 100 years ago, Ciamician was already asking the scientific community to start looking beyond fossil fuels, aware that this gift given us from the earth was not limitless. Going on reading his prophetic speech, which was published in many different languages, is surprising to learn how much his scientific research, on fields such as artificial photosynthesis, molecular electronics, molecular photonics and luminescent sensors, is considered as a workhorse of nowadays-scientific research. Modern research on these fields is closely correlated to Ciamician's intuitions reported on his papers and conferences at the beginning of the XX century, even if sophisticated tools such as lasers, or the current knowledge about the nature of the light, were not available at that time. This is the reason why we can consider Ciamician as the inventor of the photochemistry. *"The photochemical processes have not had so far any extensive practical application outside of the field of photography. (…) But notwithstanding the many applications photography represents only a small part of photochemistry. (…) The photochemical reactions follow the fundamental laws of affinity, but have a special character. They are especially notable for the small temperature coefficient and are, however, comparable to the reactions which take place at very high temperatures.*

XIII

According to a brilliant idea of Plotnilrow, luminous radiations produce a different ionization from that due to electrolytic dissociation; the separation of an ion requires a quantity of light, which is determined by the theory of Planck and Einstein. For our purposes, the fundamental problem from the technical point of view is how to fix the solar energy through suitable photochemical reactions. To do this it would be sufficient to be able to imitate the assimilating processes of plants. (…) The polymerizations, the isomeric changes, the reductions and oxidations with organic and inorganic substances, and the autoxidations which light causes so easily should already find profitable applications in some industries if researches were carried out carefully with this in mind."[1] Another impressive fact is that Ciamician was not just underlining, in a prophetic way, a problem of the oncoming society but he was also trying to suggest different inputs to solve it. He was the first one telling the scientific community that the best way to solve these problems would have been copying the sophisticated world of the nature. He was also suggesting the industries to give more consideration to this new branch of chemistry, because of the chance to drive many reactions in milder conditions than the usual. He was definitely the first one laying the background of the Green Chemistry and everyone who works in this field or in the field of Photochemistry should be considered as one of his students. *"And if in a distant future the supply of coal becomes completely exhausted, civilization will not be checked by that, for life and civilization will continue as long as the sun shines! If our black and nervous civilization, based on coal, shall be followed by a quieter civilization based on the utilization of solar energy that will not be harmful to progress and to human happiness. The photochemistry of the future should not however be postponed to such distant times; I believe that industry will do well in using from this very day all the energies that nature puts at its disposal. So far, human civilization has made use almost exclusively of fossil solar energy. Would it not be advantageous to make better use of radiant energy?"*[1] These final sentences in his speech represent a message full of hope and positivity, which is definitely still valid in our century, where energy is the most important issue.[2]

Photochemistry and photophysics are currently playing an important role in the development of science and technologies as the branches of chemistry who deal with the light-matter interaction. Photochemical and photophysical processes can be exploited for novel applications in different scientific fields such as energy conversion, nanotechnology and medicine.

The nature of light is nowadays well known. Since the wave model acceptance, in 1860 thanks to Maxwell's studies,[3] light has been seen like an electromagnetic radiation who does not need a medium to spread and the visible light has been accepted as just as tiny part of the whole electromagnetic spectrum (**figure 2**). In this spectrum, the electromagnetic waves are grouped considering the wavelength. This radiation is composed by an electric and a magnetic oscillating field, who are not only perpendicular one each other, but also perpendicular to the light's spreading direction (**figure 1**).
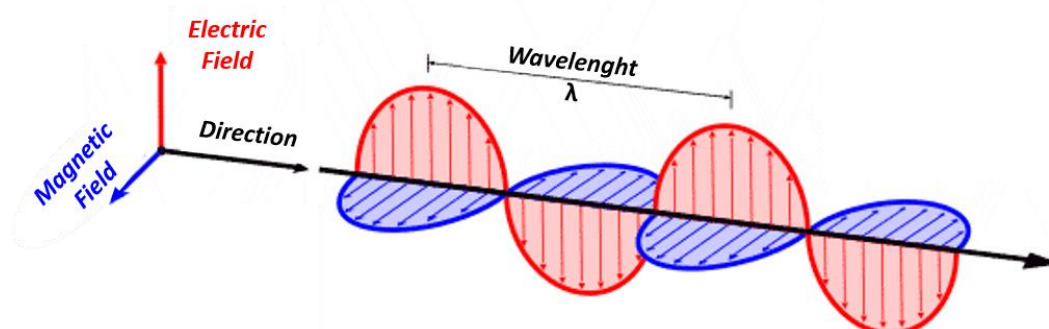
Figure 1- representation of the electromagnetic radiation.

In 1900, Max Planck gave birth to the "Quantum Theory". In Planck's assumption, the electromagnetic waves are emitted in discrete packets of energy, the so-called "*quanta*". Few years later Albert Einstein came out with his studies on the photoelectric effect,[4] giving rights to the existence of the "*quanta*" as real objects and realizing that the light was composed by the photons. Only in 1926, Gilbert Lewis coined the name "*photon*",[5] used to call and to describe those packets of energy. In the same years the double nature of the light, the so-called wave-particle duality,

has been accepted thanks to Louis De Broglie.[6] He revealed that every quantum entity might be described as either a particle or a wave.

In this model, the electromagnetic radiation is characterized by a wavelength, λ, a frequency, ν, and a velocity, c, correlated by the following equation:

$$\lambda\nu = c \quad (1)$$

Where the value of c is constant and equal to $2.998*10^8$ m s^{-1} in vacuum, whereas λ, and ν as a consequence, may have different values considering the **figure 2** and in the International System of Units (SI) these two quantities are measured in meter (m) and hertz (Hz) units respectively. We can also easily find the wavenumber $\bar{\nu}$ (number of waves per centimeter) as a way to characterize the electromagnetic radiation. The electromagnetic spectrum's range (**figure 2**) we usually consider in photochemistry goes from 200 nm to 1200 nm, including the Ultra Violet (UV) light, the visible (Vis) light and the Near InfraRed light (NIR). In particular, the visible light portion of the electromagnetic spectrum only goes from 380 nm to 780 nm, more or less. Considering that, in the quantum model a beam of radiation is seen as a stream of photons and we can measure the energy of each photon with the following equation:

$$E = h\nu \quad (2)$$

Where h is the Planck's constant equal to $6.63*10^{-34}$ J s.

Regarding the light-matter interaction, we usually consider the interaction between one molecule with one photon, described with the following reaction scheme:

$$A + h\nu \rightarrow {}^*A \quad (3)$$
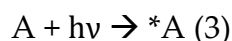
Where A is the ground-state molecule (which could only undergoes thermal reaction), hν the absorbed photon of suitable energy and *A the molecule in an electronically excited state (which undergoes different kinds of deactivation processes such as a photochemical reaction, a radiative energy loss or a non-

radiative energy loss in order to go back to the starting ground-state) . *A needs to be considered as a new chemical species, with different chemical and physical properties from A, because of the new electronic structure, since light absorption causes bond breaking. All these processes are well shown using the Jablonski's diagram, which came out for the first time around 1933, still irreplaceable to illustrates the electronic states of a molecule and the electronic transitions between the different electronic states of that molecule. For more details, see the book Photochemistry and Photophysics: concepts, research, applications, by Vincenzo Balzani, Paola Ceroni and Alberto Juris.[7]
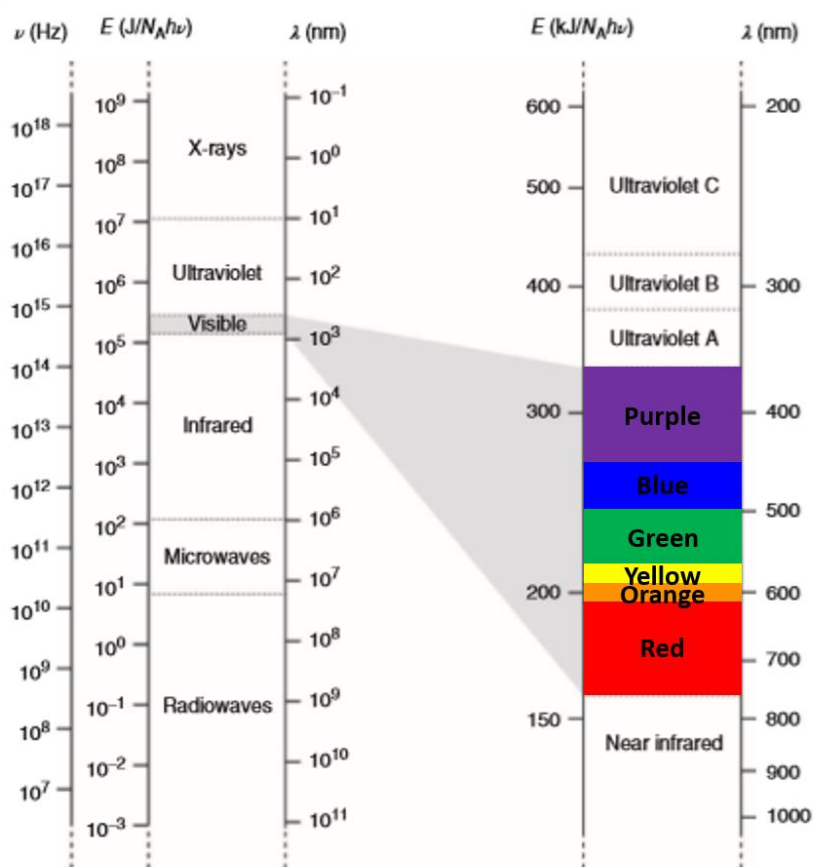
Figure 2- The electromagnetic spectrum, adapted from the ref.[7]

1 Introduction

1.1 Nano Overview

"*Nano*" is a numerical word derived from the Greek vocabulary and stands for the English "dwarf"; more precisely, it refers to a billionth. Consequently, a nanometer is one billionth of a meter (10^{-9} m). Starting from the mid-1990s, the scientific community started to use it referring to different forms of matter existing, at least in one of the three dimensions, in this submicron-length scale. These very small materials gained the nickname of "nanomaterials", which were not just smaller materials, but they were also characterized by unique physicochemical properties arising from phenomena emerging at this nanoscale.[8] The scientific field, which studies the phenomena, the properties and the responses of materials at atomic, molecular and macromolecular scales, is called nanoscience, while the design, manipulation, building, production, and application of structures, devices, and systems with sizes below 100 nm, are referred to the nanotechnology field of knowledge. Nanotechnology is emerging as a dynamic, powerful field with many potential application areas, coupled with great potential benefits, due to the possibility to take advantage of these new physicochemical properties. Nowadays, many research groups are working on and improving nanotechnology systems in order to find new applications for different fields which could improve the human lifestyle such as pharmaceutics, cosmetics, processed food, chemical engineering, high-performance materials, electronics, precision mechanics, optics, energy production, environmental sciences, information and communication, biology, medicine, and metrology. In particular, nanotechnologies applied to medicine are attracting lot of attention, especially if we consider all the potential applications in the diagnostic (disease diagnosis and imaging) and in the discovery of new drug-delivery systems. A new industrial revolution has started.[9,10]

Noteworthy is thinking that the studies about colloids or interfaces started before the mid-'90s or their use at least. They have been dated back to that period when none was talking about nanotechnology or nanoscience yet and a vivid example of that is the famous Lycurgus Cup from the 4th century, which is ruby red in transmitted light and green in reflected light, due to the presence of gold colloids. Advancing on the timeline, Richard Zsigmondy won the Nobel Prize in Chemistry in 1925 for his demonstration of the heterogeneous nature of colloid solutions and for the methods he used to prepare such solutions.[11] Zsigmondy has also been the first one to use the term "nanometer" explicitly. Few years later, in 1932, Irving Langmuir, won the Nobel Prize in Chemistry introducing the concept of a monolayer, a layer of material which was one molecule thick.[12] Anyway, the birth of the nanotechnology concept can be addressed to the famous speech gave by the Nobel laureate and quantum theorist Richard Feynman, during the annual meeting of the American Physical Society at the California Institute of Technology, 1959, first published in 1960: ``*There is Plenty of Room at the Bottom''*.[13] The lecture has always been considered as a manifesto for physicists to take control of both the physical and biological sciences, moreover as a nanotechnologies manifesto since for the first time someone was talking about manipulating the matter on a very small scale, the atom scale.[14] In 1959 Feynman was already aware of two important facts: the physical properties of the matter change going from the bulk to the atomic level and to study and manipulate the matter at this level a new kind of electronic microscope would have been necessary, characterized by a higher resolution.[13]

Taniguchi first introduced the term nanotechnology, to describe ultrafine machining of matter, in 1974 during a speech hold in Tokyo during the International Conference on Production Engineering and transcribed on in his paper "On the Basic Concept of Nanotechnology"[1]. Nevertheless, the idea of building on a small scale is usually attributed to Richard Feynman who inspired many people with his lecture, which is considered one of the two important events that have marked the

nanotechnology story. The second important event is the near-field microscopes (the scanning tunneling microscopes, STM, and the atomic force microscopes, AFM) invention at the beginning of 1980s, providing both the "eyes" and "fingers" required for nanostructures measurement and manipulation.[15] Gerd Binnig and Heinrich Rohrer were awarded the Nobel Prize in Physics for the STM invention in 1986[16] and the same Gerd Binnig, Calvin Quate, and Christoph Gerber invented the AFM in 1985.[17] Furthermore, at IBM (International Business Machines Corporation) in the United States, a technique called electron beam lithography was used to create nanostructures and devices as small as 40 to 70 nm in the early 1970s.[18] Researchers working with these so-called nanomaterials are asked to overcome unique challenges, which can be grouped in three principle categories such as their *visualization*, their *measurement* and their *manipulation*. Regarding the first one, as already introduced, once materials approach the nano-scale dimension they can no longer be seen with a conventional light microscope, since the "Abbe's diffraction limit" arises. In particular, scientists only notice this effect when objects become smaller than the wavelengths of light associated with the visual spectrum (wavelengths under 200 nm). When this happens, in order to be able to see the nanoparticles, a different range of the electromagnetic spectrum is required, electron microscopes are required which use a beam of accelerated electrons as a source of illumination. Regarding the second challenge, since nanostructures are affected by many different events occurring at the nanoscale (aggregation in solution for instance), an ensemble of different techniques is needed in order to measure their properties and all the acquired data need to be interpreted considering the particular context in which we are every single time. In the end, considering the third challenge, researchers have repurposed nanoparticle measurement tools like AFM, optical tweezers, and ion beams to achieve rudimentary positioning or assembly capabilities. Furthermore, researchers are using clever techniques to functionalize nanoparticle surfaces with chemical or

biological moieties that allow to enable their selective attachment to other structures.[9]

The essence of nanotechnology is the ability to work at the molecular level, atom by atom, creating larger structures with new interesting properties and manufacturing them by self-organization and self-assembly processes to create entities from the "*bottom up*" rather than the "*top down*" method.

Nanotechnology is based on the following statements:

- Going towards the nanoscale new physicochemical properties arise, as we have already seen, but these new features are usually not predictable just by looking at the macroscale;

- The most important changes are due to intrinsic phenomena becoming predominant at the nanoscale, such as quantum confinement and predominance of interfacial phenomena;

- Once it is possible to control important features as size, shape, chemical composition, crystalline structure of these nanomaterials, it is also possible to enhance the material properties;

- Nanotechnologies need to be a multidisciplinary field by nature (**figure 1.1**).[15]
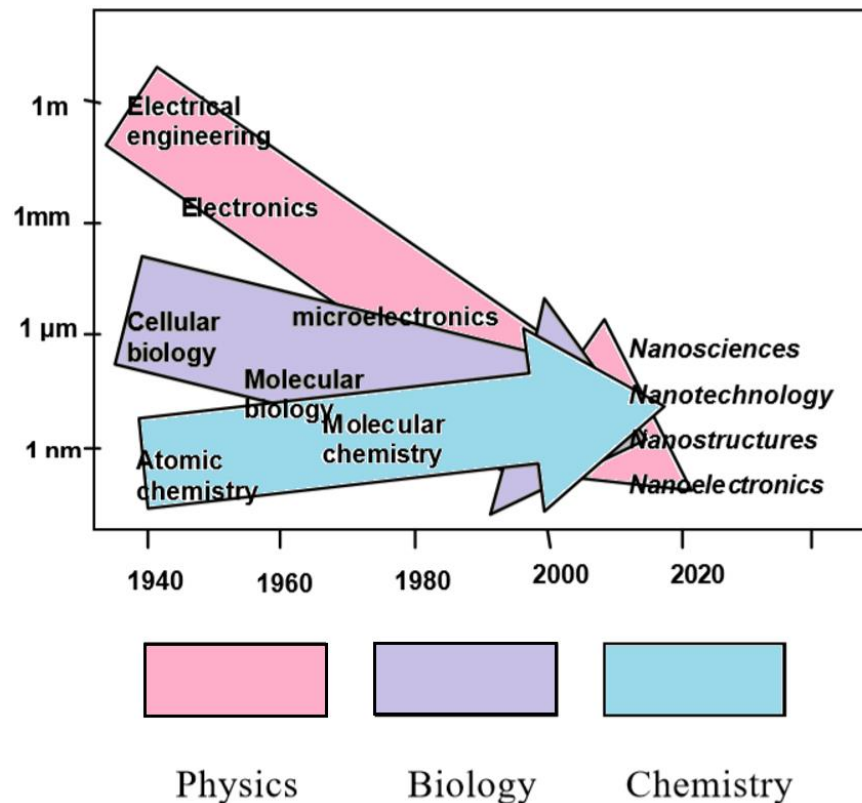
Figure 1.1- experimental sciences converging toward the nano-world from the mid-1990' to nowadays. Adapted from the ref.[15]

Nanostructured materials include different kinds of morphologies, such as atomic clusters, layered or lamellar films, filamentary structures, and bulk nanostructures. All of them are characterized by a common property; they must have at least one dimension under 100 nm. Consequently, depending on how many dimensions they show in the nanoscale, we can identify four different classes: 0D (zero dimensional) if the three spatial dimensions exhibits a nanometric size, 1D (one dimensional) if only two dimensions have a nanometric size or 2D (two dimensional) if just one spatial dimension is nanometric. Bulk nanostructures are classified as 3D (three dimensional) systems. The first three classes are usually named respectively as follow: *quantum dots*, *quantum wires*, and *quantum wells* (**figure 1.2**).[10]
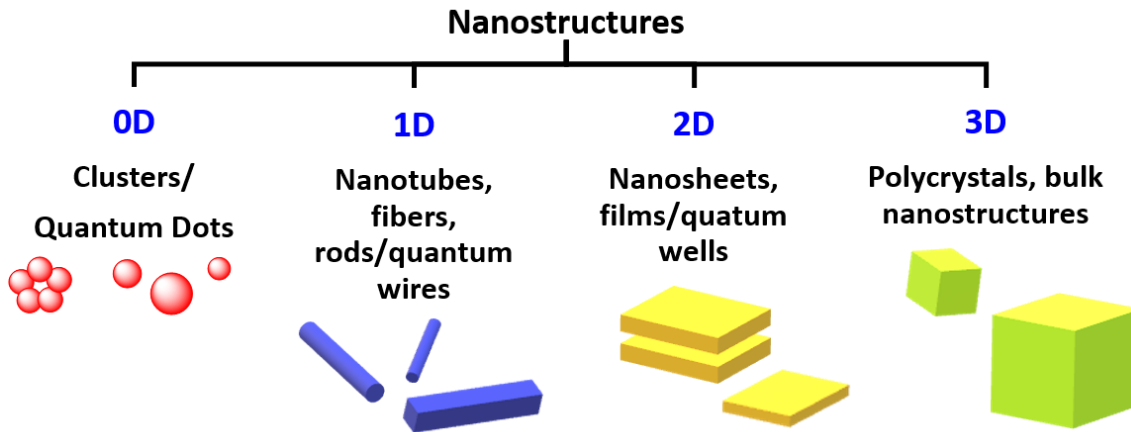
Figure 1.2- nanomaterial classification according to dimensionality. Adapted from the ref.[10]

The main difference between them and the bulk structures is the percentage of atoms at the surface, which is bigger if they present at least one nano-dimension because of the increased surface/volume ratio, and the quantum confinement phenomena. In nanocrystals the electronic energy levels are not continuous as in the bulk but are discrete (finite density of states), because of the confinement of the electronic wavefunction to the physical dimensions of the particles. This phenomenon is called quantum confinement and therefore nanocrystals are also referred to as quantum dots (QDs). Systems with different dimensionalities show different peculiar density of states and so different optical properties. A bulk material exhibits a square root energy ($E^{1/2}$) dependence of the density of states, while in a 2D system it is described by a step function, the 1D systems show an $E^{-1/2}$ dependence for each quantized state, and in 0D, all available states exist only at discrete energy values since the electron is confined in all three spatial dimensions (**figure 1.3**).[10,19]
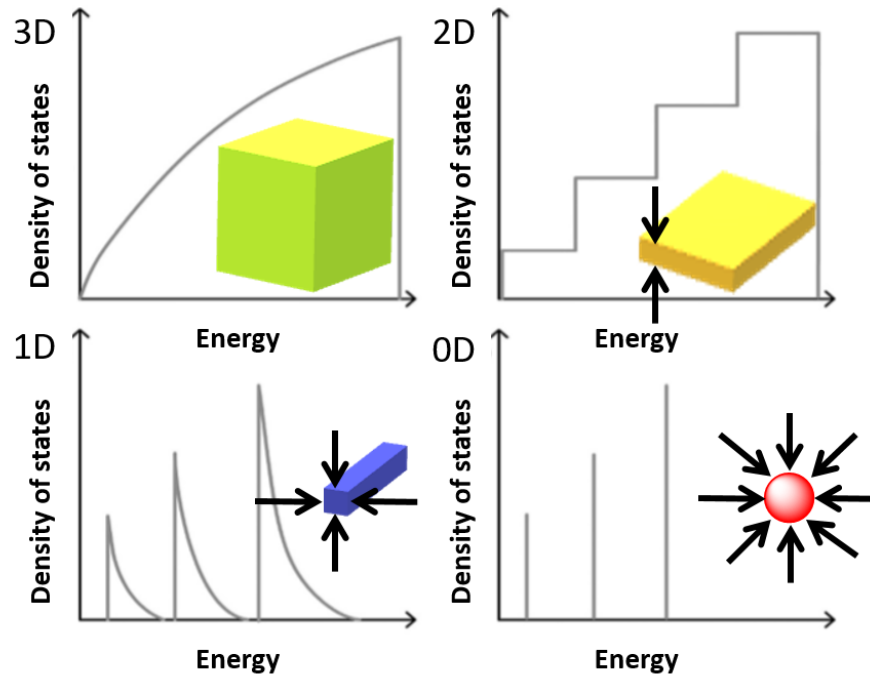
Figure 1.3- Electronic density of states for bulk 3D, 2D, 1D nanostructures, and 0D quantum dots. The arrows represent the spatial confinement occurring in each system. Adapted from the ref.[19]

The two different approaches used in nanofabrication are the *Top-Down* and the *Bottom-Up* methods. The first one is recognised as the Taniguchi approach and it works from the larger to the smaller. It uses controlled physical or chemical means to break down a larger bulk material into increasingly smaller particles that possess the desired nanoscale-size dimensions and associated material properties. This method can be seen as an approach where the building blocks are removed from the substrate to create the nanostructures. Dexler introduced the second one in 1986 as a method of building larger objects starting from their atomic and molecular components precursors. A bottom up synthesis method implies that molecular precursor materials (e.g., a variety of metal salts) are reacted chemically to nucleate and grow particles of varying chemical composition, size, and shape. A bottom-up approach can thus be viewed as a synthesis approach where the building blocks are

added onto the substrate to form the nanostructures. The bottom-up approach is considered to be more advantageous than the top-down approach because the former has a better chance of producing nanostructures with less defects, more homogenous chemical composition, and better short- and long-range ordering, since atoms or molecules will be specifically placed and connected following our ideal.

Although the control of individual atoms is the ultimate `manufacturing technology', other approaches based on *self-assembly* are also promising. In self-assembly, the atoms or molecules required to construct the desired product are brought together in a suitable environment in order to arrange themselves and form a product. Examples of self-assembly of large molecules, which can then assemble themselves into ordered arrays, are found widely in chemistry and biology and the field of supramolecular chemistry.[20]

1.2 Quantum Dots

Inorganic solids have been historically divided into three well-known classes: metals, semiconductors, and insulators. They mostly differ on the nature of their electronic bands and this affect all the properties they are characterized by, such as the electrical conduction, the thermal conduction, and all the optical properties.
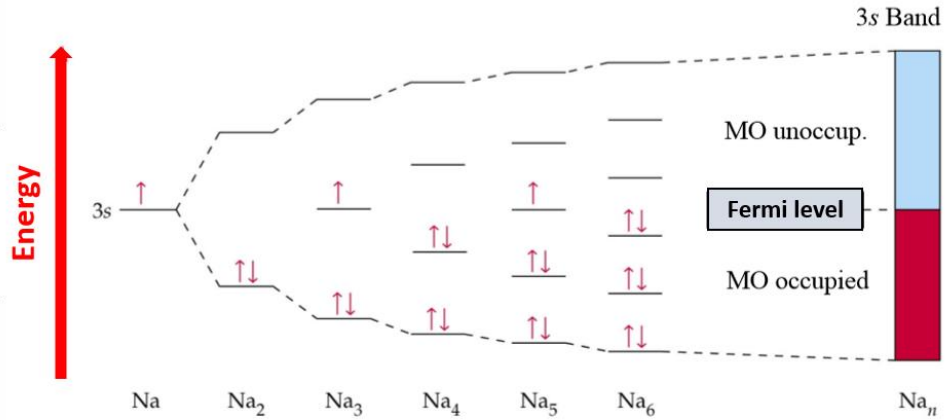
Figure 1.4- theoretical model describing the states of electrons for sodium, starting from a single atom and consequently adding more atoms until a bulk solid has been reached.

The band of permitted energies in a solid is related to the discrete allowed energies (the so-called energy levels) of single, isolated atoms. When the atoms are brought together to form a solid, these discrete energy levels become perturbed through quantum mechanical effects, and the many electrons in the collection of individual atoms occupy a band of levels in the solid called the valence band (VB). Empty states in each single atom also broaden into a band of levels that is normally empty, called the conduction band (CB). These two parts are divided by the so-called *Fermi level*, which is a hypothetical energy level for electrons with a 50% probability of being occupied at the thermodynamic equilibrium (**figure 1.4**). The location of the Fermi level in the band structure of a material is important to determine its electrical behaviour. Different energy bands characterize the three existing inorganic solids and their properties. Considering a conductor material, a metal, the VB and the CB are adjacent and the electrons motion from the first one to the second one is always allowed, even at very low temperature, without a perturbation of the system. Otherwise, an insulator material is characterized by an energy band gap between the two bands and electrons in the VB can never be promoted to the CB because it would require an enormous amount of energy. Semiconductor materials lay on the

middle between metals and insulators and their properties too. Semiconductors show a smaller energy band gap between the VB and the CB. In some of these cases, we can still have promoted electrons from the VB to the CB, even without an external perturbation, but just a little of them. The real motion of electrons is seen by giving energy to the system (**figure 1.5**).
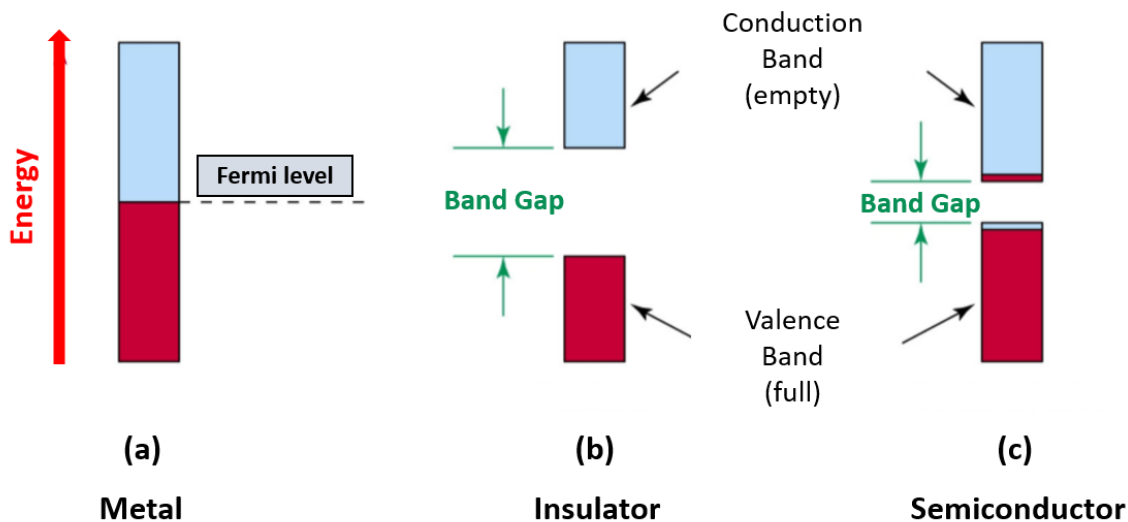
Figure 1.5- Electronic band theory for metal, semiconductor and insulator materials.

Considering nanoparticles instead of bulk materials, the density of states becomes discrete at the band edges, this is the area where the quantum confinement begins (**figure 1.6**). The Fermi level is in the centre of the metal continuous band both in the bulk and in the nanocrystals; therefore the discretization of the energy levels, which occur in the nanocrystal system, does not interest the area around the Fermi level. Only metal nanoparticles of a very small size can exhibit the quantum confinement's consequences by a spectroscopic point of view. Otherwise, in semiconductors the Fermi level lies between the two bands, in the middle of the energy band gap (E_g). Considering semiconductor nanoparticles, this is the area where the density of states becomes discrete because it is affected by the quantum confinement effect and this is also the area where the electronic transitions occur

when we perturbate the system. Consequently, by a spectroscopic point of view, we can immediately notice this fact, even for big nanoparticles sizes (**figure 1.6**). Because of this phenomenon, the Eg increases in smaller semiconductor nanocrystals and decreases in bigger semiconductor nanocrystals. Semiconductor nanocrystals exhibit strongly size-dependent optical and electronic properties.[21,22]
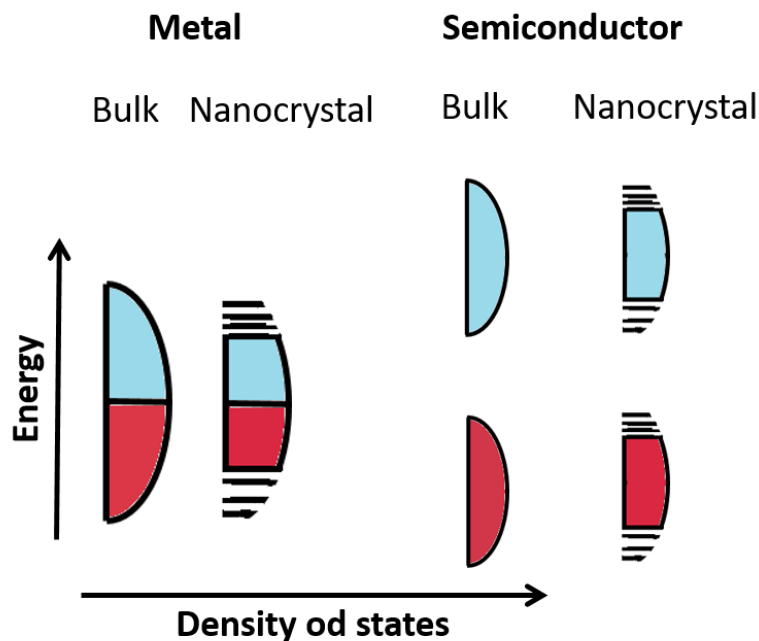
Figure 1.6- Schematic illustration of the density of states in metal and semiconductor bulks and nanocrystals. Adapted from the ref.[21]

Since the semiconductor nanocrystals, even called Quantum Dots (QDs), discovery in the early 1980s [23,24], these particles have promised to be a valid alternative to molecular species for luminescence applications.[25,26] QDs are spherical particles with diameters typically ranging between 1 and 15 nm. As we have already seen, because of their nano-metric size, quantum effects, resulting for example in size-dependent absorption and emission spectra, affect the optical and electronic properties of QDs. Their Eg can be changed upon varying the particle size. To a first

approximation, the quantum confined band gap energy of the QD, $E_{g,QD}$, can be described as follows (**equation 1.1**):

$$E_{g,QD} = E_{g,b} + \left(\frac{h^2}{8R^2}\right)\left(\frac{1}{m_e} + \frac{1}{m_h}\right) - \left(\frac{1.8e^2}{4\pi\varepsilon_0\varepsilon R}\right) \qquad \textbf{(equation 1.1)}$$

Where $E_{g,b}$ is the band gap energy of the bulk semiconductor, R is the QD radius, m_e is the effective mass of the electron in the solid, *e* is the elementary charge of the electron, *h* is the Planck's constant, m_h is the effective mass of the hole in the solid and ε is the dielectric constant of the solid. In particular, the middle term on the right-hand side of the **equation 1.1** is a 'particle-in-a-box-like' term for the excitation, while the third term on the right-hand side represents the electron-hole pair Coulombic attraction, mediated by the solid. We can extrapolate that the Eg is correlated with the QD size and, as already seen, as the dimension of the QD decreases, the Eg increases (**figure 1.7**).
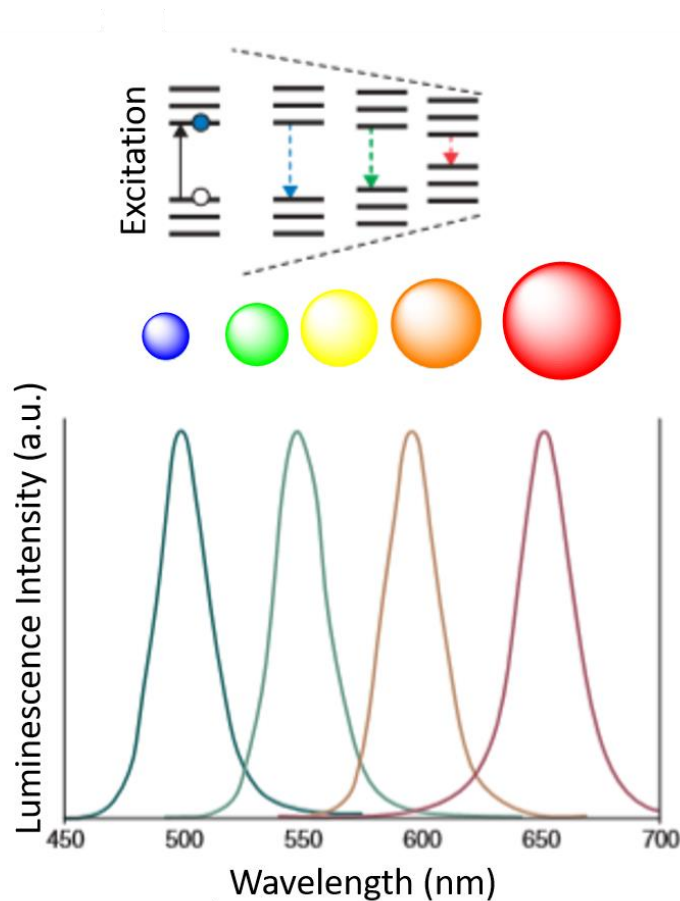
Figure 1.7- Quantum confinement effect on changing the QD size. Top: electronic structure of QDs by varying the QD diameter. Bottom: emission band red shift by increasing the QD size. Adapted from the ref.[22]

However, the actual QD band structure is more complicated and the model shown before is just its simplified approximation. QDs show a very high surface to volume ratio, resulting in imperfections onto their surface. These imperfections are called "*trap-sites*" and they have their own electronic energy states, which are usually localized within the QDs Eg. Therefore, they must be taken into consideration during the optical processes in which QDs are involved because they could be the reason of the non-radiative relaxation after the excitation of an electron from the VB to the CB (**figure 1.8**). Trap-sites can really negatively affect the QDs luminescence quantum yield and, in order to reduce -or to totally eliminate- this eventuality, two

or more semiconductors forming heterojunctions can be used to obtain the so-called "*core-shell QDs*". In this case, the shell is made of a wider band-gap semiconductor material, which passivates the surface trap-sites. Another possible procedure, to avoid the surface trap-sites to reduce the QD luminescence quantum yield, is the QD surface functionalization with organic ligands via the formation of covalent bonds. This may noticeably alter the chemical and physical states of the quantum surface.[22]

When a QD is irradiated with light of photon energy (hv) equal to or higher than the Eg, an electron is promoted, excited, from the VB to the CB, living a hole (equal to an electron absence) in the VB. The generated electron–hole pair is bound by the electrostatic attraction between the opposite charges and is called "*exciton*". The *exciton Bohr radius* measures the average distance between the photogenerated electron and hole. The optical excitation can be followed by different processes like the thermal relaxation of the excited electron and hole, the radiative exciton recombination (luminescence); the non-radiative exciton recombination mediated by an oxidizing surface state (electron trap), the non-radiative exciton recombination mediated by a reducing surface state (hole trap) (**figure 1.8**).[27]
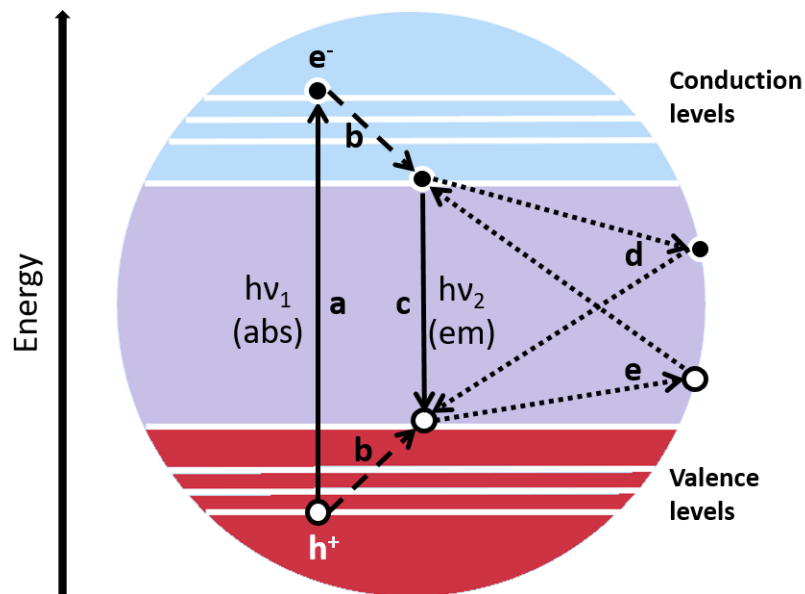
Figure 1.8- Schematic representation of optical and electronic processes in a semiconductor nanocrystal. Solid and dashed lines represent radiative and non-radiative processes, respectively. Legend of processes: a, optical excitation; b, thermal relaxation of the excited electron and hole; c, radiative exciton recombination (luminescence); d, non-radiative exciton recombination mediated by an oxidizing surface state (electron trap); e, non-radiative exciton recombination mediated by a reducing surface state (hole trap). Adapted from the ref.[27]

When photons have energies equal to -or greater than- the QD Eg they can be absorbed. An important feature of the obtained absorption spectrum is the band sharpness on the low energy side of the electromagnetic spectrum, corresponding to the population of the first exciton state exhibiting strong oscillator strength. The actual band position and intensity depend on the particle diameter, while its width and the shape are affected by the QDs size distribution. Considering classic QDs, the ones who show a direct band gap, the absorption band is continuous, with very large molar absorption coefficients (ε), in the UV-visible region especially. These QDs can be efficiently excited in a wide spectral region and with low intensity light. In direct band gap QDs the lowest energy conduction level and the highest energy

valence level have the same momentum. Classic example of these QDs are the ones made of CdS, CdO, CdSe, CdTe, ZnS, ZnSe, GaAs and InP. Their luminescence is usually very intense, narrow and with a symmetric profile, their energy distance between the absorption and luminescence band maxima (the so-called Stokes shift) is usually remarkably small and the emission wavelength can be modified in the UV-IR spectral region by varying the used chemicals and the size of the QDs. The luminescence lifetimes of direct band gap QDs at room temperature are usually comprised between 10 and 40 ns. These lifetime values are long enough to enable the time-gated detection technique, which is used in bioimaging for example. However, researchers are looking for different materials with higher lifetime values (in the microseconds scale) in order to simplify the working set-up used for the signal detection and to improve the signal to noise ratio avoiding the collection of the background auto-fluorescence. QDs are also well known for their resistance to photobleaching, which is much higher than that of molecular fluorophores.[27]

1.3 Bulk Silicon and Silicon Nanocrystals

The most popular direct band gap QDs are made of elements from the groups II–VI (e.g. CdSe, CdS, CdTe), III–V (e.g. InP, InAs, GaAs), and IV–VI (e.g. PbSe and PbS), therefore one problem associated with them is the use of heavy, toxic, expensive and rare metals.[27,28] With increased awareness of the harmful effect of these materials on the human health and on the environment, their use has been limited or even banned in some cases. Consequently, many efforts have been done to establish a new class of QDs made of nontoxic and hearth-abundant materials, such as Silicon. Silicon nanocrystals (SiNCs) are viewed as an attractive alternative to classic quantum dots.[29]

Silicon (Si) is the 14th element on the periodic table with an electronic configuration equal to ($1s^2 2s^2 2p^6 3s^2 3p^2$); therefore, it can donates or shares four valence electrons

to form bonds, with a hybridization of sp^3. Si belongs to the IVA group of the periodic table, together with carbon, germanium, tin and lead and it is famous to be one of the most abundant elements on the earth's crust (only oxygen comes first). Si is also relatively easy to isolate from SiO_2 and it is inherently nontoxic. Si has become one of the workhorse materials of the modern society for its properties as a semiconductor material; we actually live in a technological world made possible by Si, indeed, which is at the basis of many modern applications from microelectronics, to solar cells and optoelectronics.

Despite bulk Si has dominated the technological world for over half a century, it does not show any luminescence at room temperature (RT), thus it has limited optical applications.[29] Silicon is a classic example of indirect semiconductor with an Eg of 1.12 eV at RT. Its band structure shows an *indirect bang gap*: two different crystal momenta characterize the VB maximum-energy state and the CB minimum-energy state. In general, a radiative transition (both absorption and emission) requires the conservation of both the energy and the crystal momentum. In an indirect band gap material, these transitions cannot occur directly but only under the involvement of a phonon, where the phonon momentum equals the difference between the electron and hole momentum. Since these processes are difficult to happen, radiative transitions are less efficient in indirect band gap semiconductors compared to direct band gap ones (**figure 1.9**). For all these reasons, bulk silicon does not show any emission at room temperature.
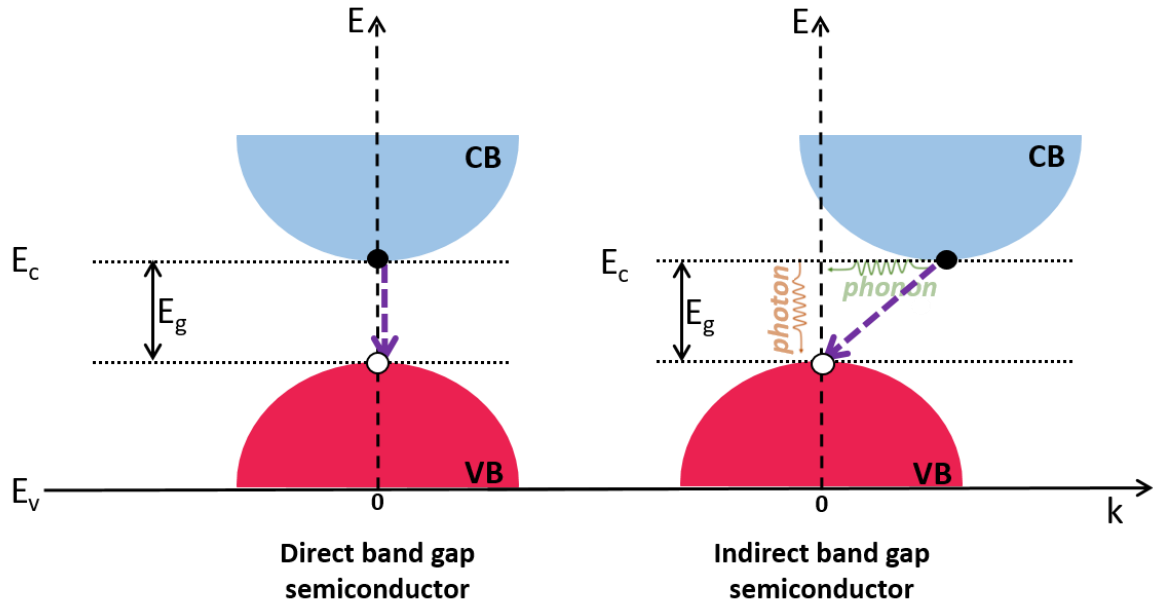
Figure 1.9- energy diagrams, for both the direct and the indirect band gap semiconductors, plotted as a function of the crystal momentum (k). The purple dashed arrows represent the radiative transitions (the electron-hole recombination called emission, in this case). On the right, the typical phonon-assisted transition from the conduction to the valence band is shown.

It was only thanks to the discovery of visible light emission from porous silicon (p-Si) in the early 1990s by Cahham[30] that nanostructured Si began being explored and applied for its interesting optical properties.[29,31–37]

Silicon nanocrystals (SiNCs) in the size range below 12 nm have a weak absorption, due to the indirect band gap; nevertheless, they emit photoluminescence (PL) in the visible and in the NIR range of the spectrum, when excited with UV light. This behaviour is explained by the quantum confinement effect that occurs in the SiNCs when their size approach the exciton Bohr radius of Si (see chapter 1.2 for more details). In this case, a direct radiative transition, without the involvement of a phonon, is favoured. When the materials approach the nanometer scale, the relaxation of the momentum conservation rule[38] is observed. This effect is related to

the Heisenberg uncertainty principle: $\Delta r * \Delta k > 1/2$, where r is the radius of the nanocrystal and k is the wave vector of the electron or hole in the nanocrystal. The decrease of nanocrystal dimension brings about a spread in momentum that induces the overlap of electron and hole wavefunctions in k-space and thus increases the probability of the lowest energy electronic radiative transitions (**figure 1.10**), which is negligible in bulk silicon.[33,36,41] Consequently, the ε of SiNCs per Si atom, both in oxide-embedded nanocrystals[42] and alkylpassivated ones[43], is higher than the absorption coefficient of bulk silicon. However, the ε of SiNCs is much lower than one reported for the lowest energy absorption band of conventional QDs, such as CdSe. In line with the absorption properties, a comparison of emission properties of bulk silicon and SiNCs evidences an increase of the radiative rate constant (k_r). The radiative constant (or better its inverse, called the radiative lifetime, τ) has been simulated to be dependent on the size of the nanocrystal with both ab initio and linear combination of bulk bands for silicon nanocrystals.[40,44] Photoluminescence is also affected by superficial effects such as oxidation or functionalization with various surface groups.[45] Because of the indirect band gap, the "apparent" Stokes Shift is higher and the lifetime is longer (in the μs scale) than classic QDs.[46]
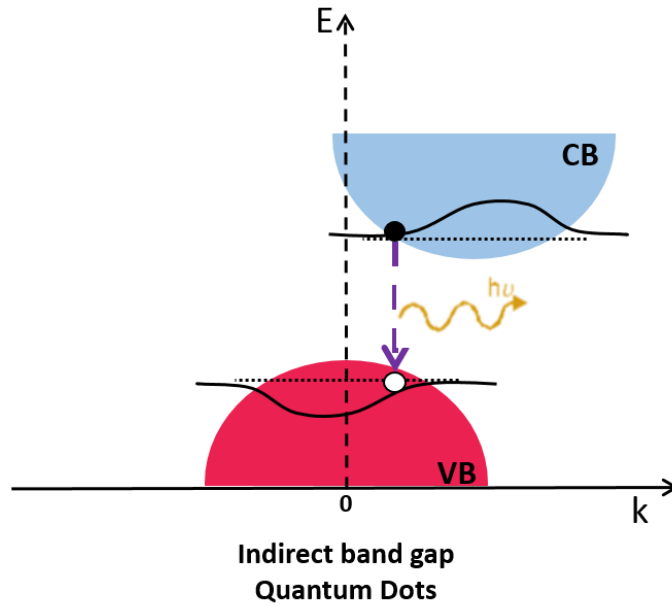
Figure 1.10- energy diagram for indirect band gap Quantum Dots, plotted as a function of the crystal momentum (k). The electron-hole recombination process is shown with the purple dashed arrow (radiative recombination) and it is followed by light emission (hν).

Furthermore, SiNCs surface can be passivated with more functionalization methods than classic QDs, such as the formation of a covalent bond between Si and C atoms where the C atom comes from the chosen organic ligand and Si atom is onto the SiNCs surface. Surface passivation is an important process to avoid a further possible oxidation caused by atmospheric O_2, to reduce the surface trap-sites formation, to disperse SiNCs in solvents with different polarity and to avoid their colloidal aggregation. Therefore, surface passivation allows us to protect SiNCs with an outer shell. The SiNCs covalent bond shows advantages over the classic QDs non covalent bond, which causes instability of the molecular coating, degradation of the optical properties, QDs aggregation and so QDs poor versatility.

As we mentioned before, SiNCs optical properties depend strongly on their size, due to the quantum confinement effect (see chapter 1.2). Absorbance and emission

spectra, measured for dodecene-capped SiNCs of different sizes (diameter of 3 and 5 nm) dispersed in toluene at known concentrations, show how the ε and the maximum emission wavelength ($\lambda_{em,max}$) respectively change with increasing SiNCs dimensions (**figure 1.11**). As we can see in **figure 1.11**, the ε is low and the absorption spectra are essentially featureless because of the indirect band gap of Si. Absorption spectra shape does not change by varying SiNCs size; on the contrary, we can observe a significant change in ε value, which increase with increasing SiNCs size due to the quantum confinement effect. We can also observe that the lower the wavelength, the higher the absorbance. The ε value, measured at 400 nm, can vary from 3×10^4 $M^{-1}cm^{-1}$ for the 3 nm diameter SiNCs to 1×10^6 $M^{-1}cm^{-1}$ for the 12 nm diameter SiNCs. At near infrared (NIR) wavelengths, the region where biological tissues are relatively transparent, the absorption is a few orders of magnitude lower but is still significant: at 650 nm, $\varepsilon = 4 \times 10^2$ $M^{-1}cm^{-1}$ for the smallest SiNCs and increases up to values of $\varepsilon = 2 \times 10^5$ $M^{-1}cm^{-1}$ for the largest SiNCs.[46]
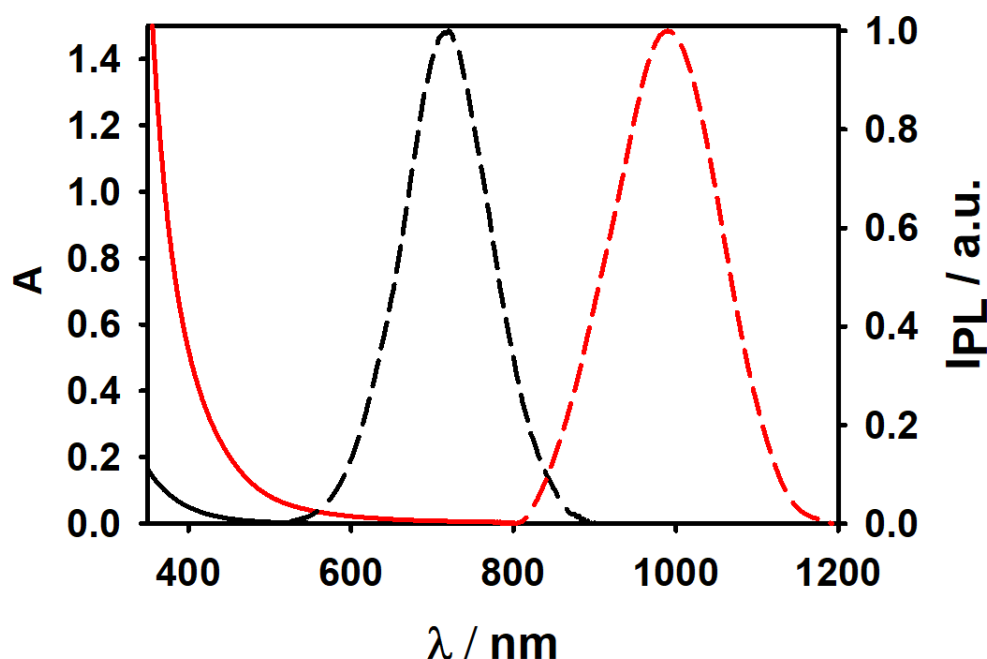
Figure 1.11- SiNCs band gap dependence on the size of the nanocrystals (3 nm diameter SiNCs are represented in black, 5 nm in red) measured by absorption (continuous lines) and emission (dashed lines) spectra.

Figure 1.11 also shows room-temperature photoluminescence (PL) spectra of dodecyl-capped SiNCs. The $\lambda_{em,max}$ changes from VIS to NIR because of the SiNCs size and the synthetic method used; in particular, the bigger the SiNCs size, the higher the $\lambda_{em,max}$ and the lower the Eg. The quantum yield (QY) measurements (defined as the ratio of emitted to absorbed photons) show values up to 70%[47,48]; nanocrystals larger than about 12 nm did not have measurable PL due to the quantum confinement disappearance. SiNCs are able to emit in the NIR range with relatively high QY values, this is remarkable for in vivo applications.[46] A rising trend in the QY values has been observed by increasing the SiNCs diameter, if we are under the quantum confinement theory, obviously. Alkyl passivated SiNCs show a QY variation from 5% to more than 45% by increasing their diameter from 1 nm to more than 5 nm. In order to explain this behaviour, we need to take into

consideration that the QY value and the internal quantum efficiency are assumed to be directly correlated and so the radiative rate constant (k_r) and the non-radiative rate constant (k_{nr}) value can be extracted from the QY value with no further treatment. Therefore, the QY value variation is explained with the strong influence of the k_{nr} for the smaller nanocrystals (where the core is closer to the surface and so to the trap sites are more involved in the deactivation process of the exciton), prevailing on the radiative component and reducing both the τ and the QY. The τ value goes from few microsecond to some millisecond and it is correlated to the SiNCs diameter, as already demonstrated, and to the synthetic method used.[49] We also need to take into account that a colloidal solution of SiNCs is always an ensemble of different sizes and different optical properties nanocrystals and, consequently, the QY is averaging all the SiNCs assembly behaviours. SiNCs non-radiative channels, which compete with the radiative channel during the QDs post absorption deactivation, can be classified as follow:[50]

- Fast non-radiative transitions, with a few nanoseconds decay time, due to dangling bonds, surface defects (…), which make SiNCs dark;[51]
- Non-radiative channels with a decay rate similar to the radiative one which consequently affects the internal quantum efficiency;
- Slow non-radiative transitions (in the time scale of about seconds or even minutes).

All of these behaviours, together with the possible presence of heteroatoms on the SiNCs surface, can modify both the QY and the τ values of a SiNCs colloidal solution. Nitrogen impurities[52] or diols[53] can turn the red/NIR luminescence of SiNCs with µs-scale lifetime into a blue luminescence characterized by a very fast decay in the ns-scale.

How the quantum confinement effect allows the size dependent spectral tunability of the SiNCs PL between the VIS and the NIR region of the electromagnetic spectrum has been already demonstrated in this dissertation, in particular inside

the range from 590 to 1130 nm. Differently, the SiNCs PL properties in the range from 530 to 580 nm are still a source of doubts.[29,46,49,54] Wen et al. published in a paper that $\lambda_{em,max}$ equal to 590 nm is the short-wavelength limit of the size-dependent PL spectrum for SiNCs.[55] Otherwise, other research groups have reported possible SiNCs emissions even at shorter wavelengths, Korgel et al.[56], for example, used a single-dot spectroscopic technique to capture a narrow PL spectrum with a $\lambda_{em,max}$ equal to 566 nm. Veinot et al.[57] also reported that a prolonged hydrofluoric etching of the SiO$_2$/Si matrix (see chapter 2 for more details regarding the synthetic procedures) results in green and yellow-emitting colloidal solutions. A short-living visible and weak PL band, the so-called "fast band" (F-band) is also reported to exhibit a red spectral shift in the blue-red (λ_{em} = 430–650 nm) range with a decreasing SiNCs diameter.[58] Recently, Ozin et al.[59] reported for the very first time a size region of SiNCs where a fast relaxation (on time scales of hundreds of picoseconds) is responsible for efficient radiative recombination between photo-excited electrons and holes, leading to high PLQY, in the wavelength range from 530 to 580 nm. They demonstrated that the effective mass approximation (EMA), **equation 1.1** (see chapter 1.2), usually used to investigate the relationship between the QD size and its Eg value, cannot be used to describe the properties of SiNCs with a diameter under 1.7 nm. These SiNCs respond to different behaviours and this implies that an alternative model of the electronic structure is necessary to explain the unique trend of Eg observed for these QDs (1.1<d< 1.7 nm). A very fast PL decay process on the hundreds of ps time domain is observed for these SiNCs, with no measurable long-lived PL signal on the μs-ms time scale. Ozin et al. demonstrated that the five-orders-of-magnitude variation in decay time suggests that 1.7 nm is a "critical diameter" of change in a radiative carrier relaxation for recombination that emits PL. A possible explanation of this different behaviour could be the massive presence of non-radiative relaxation channels on the surface of these small SiNCs. These channels include the oxide defects, which, as previously demonstrated, influence the PLQY, which could be enhanced through optimal surface passivation, as well

as it is possible for red-NIR emitting Si QDs (1.7<d<5 nm).[40,60,61] Ozin et al. explain this phenomenon with the emergence of molecule-like energy states, which arise in the smallest size range of the SiNCs. These ultra-fast decay dynamics imply that the 1.1-1.7 nm is a too small diameter range in order to retain the bulk-inherited electronic structure. In their opinion, it may be more reasonable to consider a molecule like configuration to discuss the carrier transition and recombination mechanism for the short-lived, visible PL bands, rather than considering the bulk-inherited electronic structure responsible for μs PL emissions in the orange-NIR region.[59]

2 Synthetic Methods

2.1 Different Techniques for SiNCs Synthesis

Most of the fundamental knowledge on the properties of Silicon Nanocrystals (SiNCs) has been gained after the discovery of the first luminescent nanoporous Silicon (pSi), by Canham in 1990s,[30,62] prepared by electrochemical etching[63] of a Si wafer. This material was already characterized by a size-tuneable luminescence and an efficient electroluminescence, but the downsides were the poor photochemical stability and a very broad size and shape distribution. Improved synthetic methods were needed, in order to allow a better control over the sizes and properties, fundamental to better understand the link between them and the visible photophysical variations.

Nowadays, SiNCs can be synthesized with a wide variety of techniques. The different approaches can be classified taking into account:[39]

- the nature of the resulting material, which could be either SiNCs in solid-state matrices or colloidal solutions of SiNCs;
- how the nanoscopic dimension is reached, otherwise if the considered method belongs to the "*top down*" or to the "*bottom up*" methods. This step determines the nanocrystals nucleation.

SiNCs in solid-state matrices are the first methods that have been developed. They can be mainly obtained by ion implantation of silica,[64,65] plasma enhanced chemical vapour deposition,[66–69] sputtering[70–72] and molecular beam deposition[73] and they show good control over the size and density. The most used technique involves the thermal annealing of substoichiometric Silicon oxide (SiO$_x$, x<2) producing high quality SiNCs, but in a very small amount. Unfortunately, all these techniques suffer from the presence of the silica matrix, which limits the already weak size tunability

of emission and the charge extraction, fundamental to electronics and photovoltaic applications.

Colloidal solutions of SiNCs can be obtained with both "top down" and "bottom up" methods. As already mentioned in chapter 1.1 of this dissertation, in "top down" methods, larger pieces of silicon are broken up until nanoparticles are formed, while "bottom-up" methods start from molecular precursors, which assemble in chemical reactions to form SiNCs. The most relevant ways to produce SiNCs, the methods that have shown a better size-/shape-/surface-control than the original pSi, are grouped together in **figure 2.1**.

Among the "top down" techniques, the most commonly used methods are ball milling, electro-chemical etching of bulk silicon and laser ablation. The first one consists in crushing silicon pieces until nanoparticles are obtained and it was demonstrated by Muller et al. using ball milling.[74] The second one uses an electrochemical etching of bulk silicon in HF electrolytes and results in the formation of pSi. Sailor et al. showed that by ultra-sonication of pSi, a luminescent dispersion of SiNCs is obtained.[62,75,76] In the third one SiNCs are prepared by laser ablation of a crystalline silicon wafer in water, employing a fundamental harmonic beam (1064 nm) of a Q-switched Nd:YAG laser operating at 1 Hz with 18 ns pulse width.[77] These methods suffer from a poor control of size and properties of the material produced, but they can be a valid alternative to produce high amounts of low cost (and low quality) SINCs.

 A much higher control can be reached with the "bottom-up" approaches, which are numerous. We can list:

- Laser Pyrolysis: SiNCs are formed by silane gas (SiH_4) decomposition under high temperature (> 1000°C) using a laser beam;[78–80]

- Plasma Synthesis: a non-thermal plasma dissociates a molecular precursor such as SiH_4.[60,81,82] This method yields SiNCs with superior emission quantum efficiencies of ~60% in the infrared spectral region[83] and is up-scalable;[84]

- Synthesis in Supercritical Fluids: SiNCs are prepared by the decomposition of precursor molecules in supercritical solvents;[56]

- Precursor Reduction in Solution: reduction of $SiCl_4$ in solution to form SiNCs;[85]

- Zintl Salt Based Synthesis: silicon Zintl salts like NaSi, KSi and Mg_2Si form silicon nanocrystals either by metathesis-type reaction with silicon halides or oxidation with bromine;[86]

- Disproportionation of Silicon Rich Oxides: silicon-rich oxides (SiO_x, $x < 2$) can be used as precursor material for SiNCs. When heated to temperatures above 1000 °C (1000-1400 °C), under a slightly hydrogenated inert gas atmosphere, a disproportionation reaction takes place and silicon nanoparticles are formed incorporated into a SiO_2 matrix. To obtain freestanding, hydride-terminated SiNCs, the SiO_2 is removed by etching with hydrofluoric acid.[57,87–89] The silicon precursor can be either commercially available, as in the case of the hydrogen-silsesquioxane[57] (HSQ), or prepared by the sol-gel polymerisation of an alkoxy or halide Silicon precursor.[90]

Most of the solution-based syntheses lead to SiNCs with versatile surface terminations and SiNCs with bright emission in the blue-green region of the visible spectrum with short fluorescence lifetime (ns range). Nevertheless, all these properties achieved through these methods are still not sufficient compared to the ones obtained for the direct band-gap semiconductors QDs prepared with the same techniques. The disproportion of Si rich oxide is the method that also allows reaching a higher size control given by the thermal process with the flexibility of the freestanding nanocrystals. SiNCs with a VIS-NIR tunable emission and a longer luminescence lifetime (µs scale) can be obtained by following this approach.
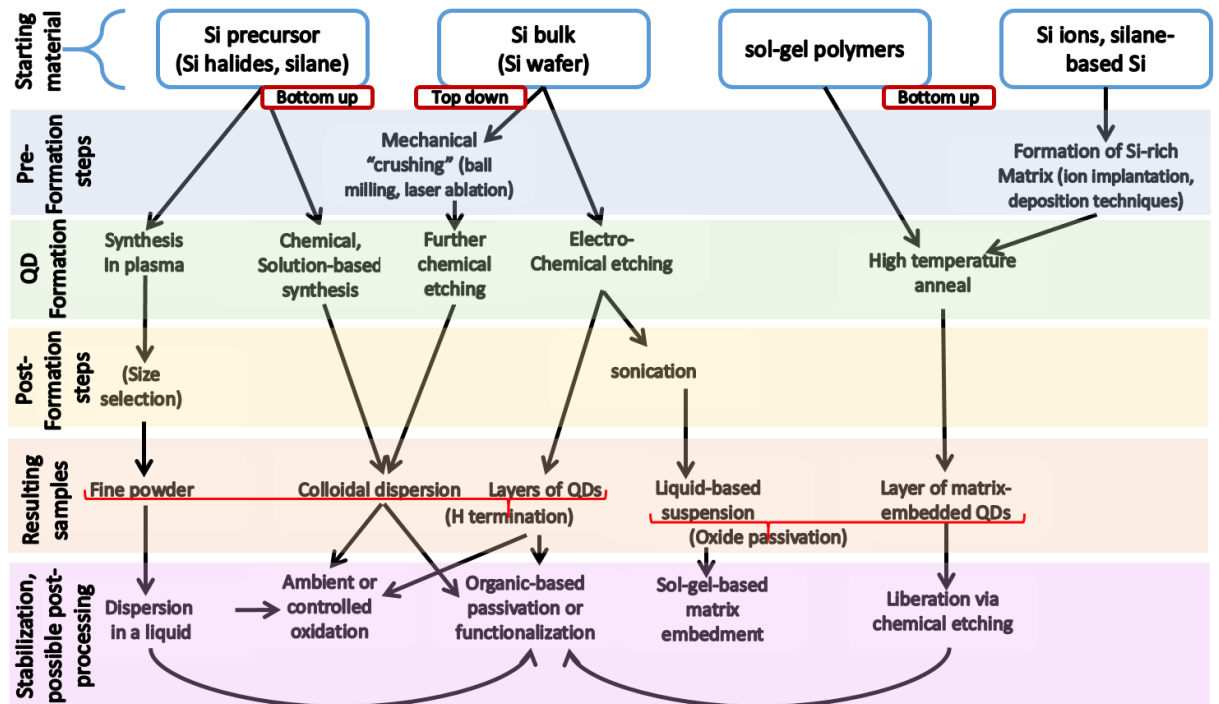
Figure 2.1- A general overview of the most common sequences of steps in the preparation of matrix-embedded and free-standing SiQDs. Adapted from the ref.[39]

2.2 Different Techniques for SiNCs Surface Passivation

Quantum Dots are characterized by an increased surface to volume ratio with respect to the bulk structure; consequently, they show a very high percentage of atoms at the surface (see chapter 1.1 and 1.2 for more details), which contribute to the QD electronic structure. This statement explains why QD are extremely sensitive to the surrounding environment and to the surface passivation.[91] "Dangling bonds" are very common onto the SiNCs surface (considering Silicon Quantum Dots), which are un-passivated bonds that can badly affect the SiNCs photophysical properties, for instance they can considerably reduce their PLQY and PL lifetime, by incrementing the so-called non-radiative losses. Reducing the presence of the dangling bonds is possible by selecting the best synthetic path to obtain SiNCs.

SiNCs can be synthesized by following many different methods (reported in the previous section, 2.1) and the majority of them deliver hydride-terminated SiNCs (H:SiNCs) dispersions. The HF etching of the silica matrix, after the disproportionation reaction of silicon rich oxides carried at high temperature and under inert gas and partial reductive atmosphere, yields to hydride-terminated SiNCs colloidal solutions, for example. Indeed, despite H-termination is the highest surface coverage percentage that can be obtained, the big downsides are the very low stability of the Si-H bond against photo-oxidation, in the presence of oxygen, and the poor colloidal stability of this system.[92–94] Otherwise, oxide-based capping (O:SiNCs) is more stable than hydride-capping by a photochemical point of view, and the Si-O bond can also undergo further reaction steps in order to modify the shell surrounding the SiNC. This is particularly relevant to achieve SiNCs with different physical and photophysical properties, such as the solubility in different solvents or a different PL emission color. Oxygen reacts with Si atoms onto the SiNCs surface in many different ways, creating a variety of types of bonds, such as an oxygen bride (Si-O-Si), a single bond (Si-OH, a silanol), an alkoxy bond (Si-O-C-) and a double bond (Si=O), which is the less stable one because usually it reacts in the presence of water.[95] A stable bond against photo-oxidation is the Si-C bond obtained by linking organic molecules onto the SiNCs surface (C:SiNCs), it is also less reactive than Si-O or Si-F bonds. However, the nature of the organic ligand needs to be considered; short organic molecules might not provide the SiNCs surface with a compact protecting shell, so molecular oxygen can still penetrate the capping layer and oxidize the SiNCs surface.[96] Otherwise, longer organic ligands prevent SiNCs aggregation improving their stability in colloidal solutions and modifying their solvent affinity.[97–101] Consequently, the PL efficiency is also increased.[40] The Si-C covalent bond is obtained thanks to the hydrosilylation reaction, which takes place exposing the hydride-terminated SiNCs to a terminal unsatured organic compound (such as terminal alkenes or alkynes). In this radical reaction, the Si-H bond can be activated by the temperature, by the UV-light or, at

room temperature, thanks to a radical initiator; every procedure is conventionally carried out in oxygen-/water- free conditions. The H group is homolitically cleaved away and a very reactive surface silyl radical is provided, which can efficiently react with terminal alkenes or alkynes.

The *thermal activation* of the Si-H bond (**figure 2.2**) is usually carried out in a pure ligand solution at a temperature above 100°C.[102] A surface coverage percentage equal to 58% can be reached, where the theoretical predicted maximum is 60%.[103] The biggest disadvantage of this procedure is the limit in the use of high-temperature stable ligands and high boiling point solvents; for this second reason, the ligand solution is usually used also as the reaction solvent, if this is possible, introducing a big excess of it. Therefore, exotic ligands cannot be involved in such reactions. A study carried out by Veinot at el.[102] investigate the nature of the capping ligands on the SiNCs surface obtained from the thermally induced hydrosilylation both in the presence of air and under inert gas. The presence of oxygen in the reaction mixture enables hydrogen abstraction, accelerating the hydrosilylation process and generating sufficient silyl radicals as initiator to interact with unsaturated bonds, promoting chain propagation and generating ligand oligomers (**figure 2.3**). The oxygen presence allows the reaction to proceed faster and at lower temperature, but, therefore, the rate of the oligomerization process increases. Based on this study, it is clear that, in order to inhibit ligand oligomerization and obtain monolayer coverage on SiNC surfaces, low temperature, inert gas atmosphere and dilute ligand concentration are crucial and all of these conditions should be applied during the thermal hydrosilylation.
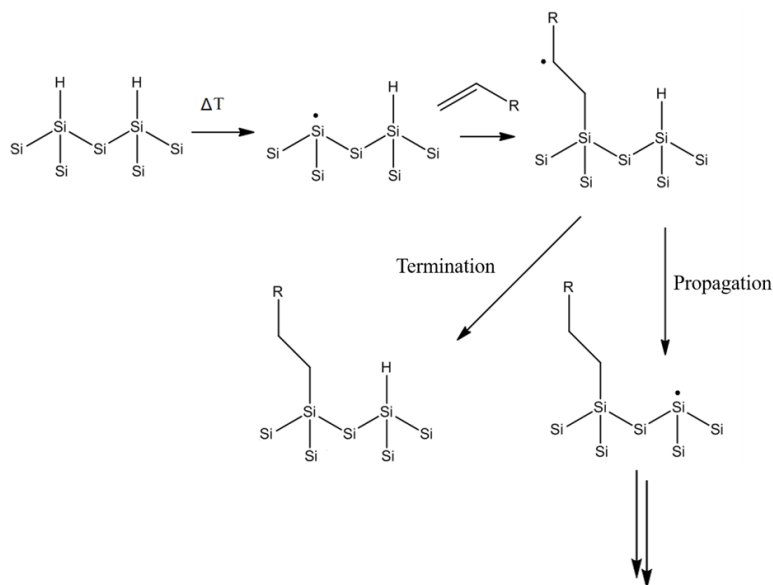
Figure 2.2- Proposed mechanism of thermal hydrosilylation, involving the homolytic cleavage of Si-H bond (activated by the high Temperature) on the SiNCs surface, the silyl radical interaction with the terminal alkene, the propagation step and the termination step, when an hydrogen is abstracted from some other species in solution.

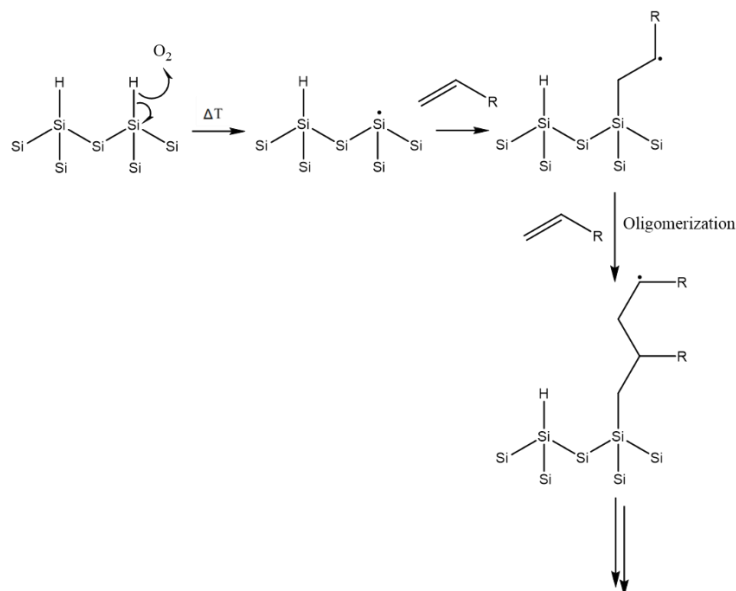**Figure 2.3-** Proposed mechanism of thermal hydrosilylation, involving hydrogen abstraction by oxygen on the SiNCs surface, the silyl radical interaction with the terminal alkene and the oligomerization step. Termination and Propagation steps are still happening as in **figure 2.2**. Adapted from the ref.[102]

The *photochemically induced hydrosilylation* is an interesting alternative to the thermal procedure,[104,105] which enables the Si-H bond activation at room temperature upon irradiation with near-UV[106], far UV-light[107] or even white light[108]. This path is promising because it is clean, direct, it requires no additional reagents such as catalysts or input of thermal energy and thus may have reduced surface contamination and numbers of defects. The study of the photochemically promoted hydrosilylation started by making connections between the molecular silane literature, and the first reports of UV-mediated hydrosilylation of an alkene on a silicon surface, a reaction that was assumed to operate via a radical mechanism. Differently from the molecular silane reactions, new mechanisms caused by the solid-state electronics of the silicon itself were discovered. From exciton involvement, to the influence of plasmonics, to the role of photoemission, the area of silicon surface hydrosilylation has become incredibly rich.[108] However, the limit of this method is the kind of ligand and solvent used, which should not absorb the light used to activate the radical reaction. Near-UV photochemically induced hydrosilylation is usually carried out with an excitation $\lambda \leq 365$ nm to sufficiently and homolytically cleave the Si-H bond to initiate the functionalization procedure.[109] There are several advantages on choosing these wavelengths. First, commercially available UV-LEDs can be used, which offer relatively high power and low heat output, and may present a "gentler" method for surface modification in comparison to other light sources. Secondly, many alkene or alkyne of interest for SiNCs functionalization strongly absorb deep-UV light ($\lambda \cong 200$ nm) and this process may degrade them and may be responsible for many by-products formation.[110] Moreover, a near-UV source light might be able to initiate the SiNCs functionalization through both the free-radical (UV excitation is able to cleave Si-H bonds to produce surface radicals) and the exciton mediated mechanism (the light produces electron-hole pairs, with the holes inducing nucleophilic attack by the alkenes),[111,112] which are the two main proposed mechanism for photochemically activated hydrosilylation.[106]

Hydrosilylation reaction can also be achieved at *room temperature*, in relatively mild conditions, via borane-catalysed (BH_3 acts as Lewis acid catalyst) passivation (**figure 2.4**) of the SiNCs with different length alkylic chains,[113] or by using a coupling catalyst such as a Platinum complex,[114,115] or a radical initiator (**figure 2.5**)[116]. The proposed mechanism for the borane-catalysed reaction involves the formation of a hydroboration product (**figure 2.4**, bottom, pathway A) or direct activation of the alkene/alkyne (**figure 2.4**, bottom, pathway B). For Pathway A, an intermediate A-II is formed from the reaction of $BH_3 \bullet THF$ with alkene/alkyne, followed by insertion of the intermediate A-II to Si-H bond. For Pathway B, an activated complex B-I is formed from direct activation of the alkene/alkyne by $BH_3 \bullet THF$, followed by formation of the complex B-II from the reaction of activated complex B-I and H-SiNCs.[113]
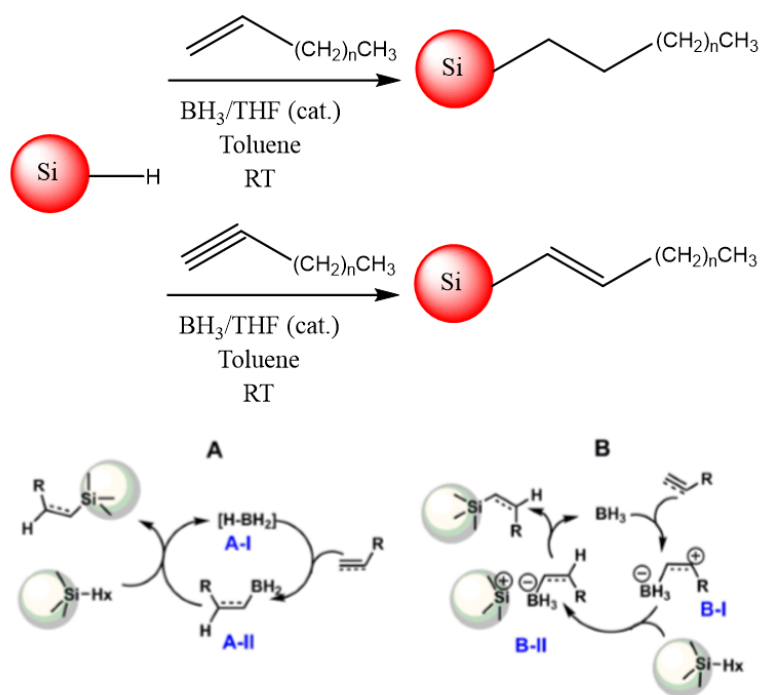
Figure 2.4- Reaction scheme for borane-catalyzed functionalization of H:SiNCs to yield alkyl/alkenyl-passivated SiNCs, on the Top; two different proposed mechanisms of borane-catalyzed functionalization of H:SiNCs using alkenes/alkynes, on the bottom. Reprinted with ACS permission from the ref.[113]

The use of radical initiators, which are usually organic molecules, is convenient since they can be easily removed from the reaction mixture, while the transition metal complexes are more difficult to be removed from the batch and, therefore, they can badly influence the SiNCs photophysical properties. Diazonium salts are the most common organic radical initiators used and Hölein et al. made the first attempt in 2014 using them to initiate the SiNCs hydrosilylation reaction.[116] This reaction shows many advantages, one of them is the possibility to functionalize SiNCs surface using many different ligans.[117]
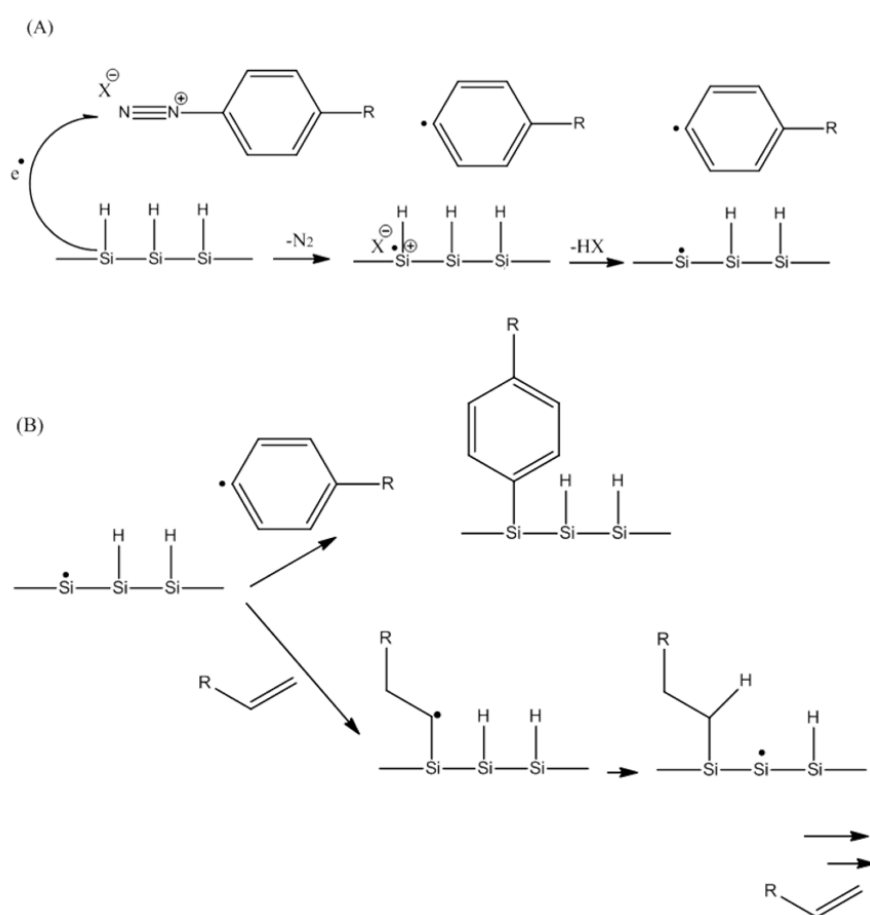
Figure 2.5- Reaction mechanism of silicon surfaces with diazonium salts. A) Reduction of the diazonium salt and formation of an aryl radical with release of nitrogen and formation of Si-surface radical after deprotonation. B) Possible reactions of the Si-centered radical to form Si-C bonds with radicals or terminal olefins. Adapted from the ref.[116]

The *diazonium salt-promoted hydrosilylation* reaction mechanism is shown in **figure 2.5**. In general, it proceeds by a one-electron reduction of the diazonium salt, release of nitrogen, generation of an aryl radical from the diazonium compound, and formation of a surface-silyl radical cation. After deprotonation, coupling of the two radicals gives a robust silicon–carbon bond. The formation of silicon-surface radicals during the diazonium reaction offers also another path to SiNC surface modification through the attachment of a variety of terminal olefins. In particular, this is considered to be the most favourite path. Many different toluene-soluble diazonium salts were synthesized. Those with electron-withdrawing groups, such as 2,6-bromo-4-decyl-diazobenzene tetrafluoroborate, have shown to be the most reactive. The diazonium salt-promoted hydrosilylation demonstrated to give photoluminescent stable colloidal SiNCs dispersions, in a new, mild and fast reaction procedure. [116]

Hydrosilylation is with no doubts the best approach toward SiNCs surface functionalization, nevertheless other approaches have been studied. While hydrosilylation leads to optical properties depending mainly on the SiNCs energy band gap, the other functionalization pathways yield materials whose emission is dominated by defect/surface states. Furthermore, in many cases, the functionalization is incomplete and a significant surface oxidation occurs. H-SiNCs react directly with amines,[52,118] with CO_2[119] at high pressures and temperatures, with phosphine oxides;[45] and all of these reactions lead to particle size-independent and surface-species-based blue-green photoluminescence.[120] Hohlein et al. also demonstrated that H:SiNCs react directly and at room temperature with organolithium reagents via cleavage of surface Si-Si bonds to form Si-Li and Si-H surface species. The Si-H bonds can be further functionalized.[121]

Hydride-terminated SiNCs also spontaneously undergo several halogenation reactions in order to achieve chloride-, bromide- or iodide- terminated SiNCs, which can further react with Grignard or organolithium reagents.[122,123] Chloride terminated

SiNCs can be obtained through the room temperature reaction between H:SiNCs and PCl$_5$, without the use of a radical initiator.[124] What we must consider about this approach is that PCl$_5$ also etches the Si-NC surface at elevated temperatures and can completely dissolve the particles.[125] Alkyl-functionalized SiNCs obtained from chloride, bromide, and iodide surfaces exhibit blue, red, and yellow-orange photoluminescence, respectively (**figure 2.6**) and in particular, the blue and yellow-orange photoluminescence appear to be originated from surface defects and they are characterized by nanosecond lifetimes.[29]
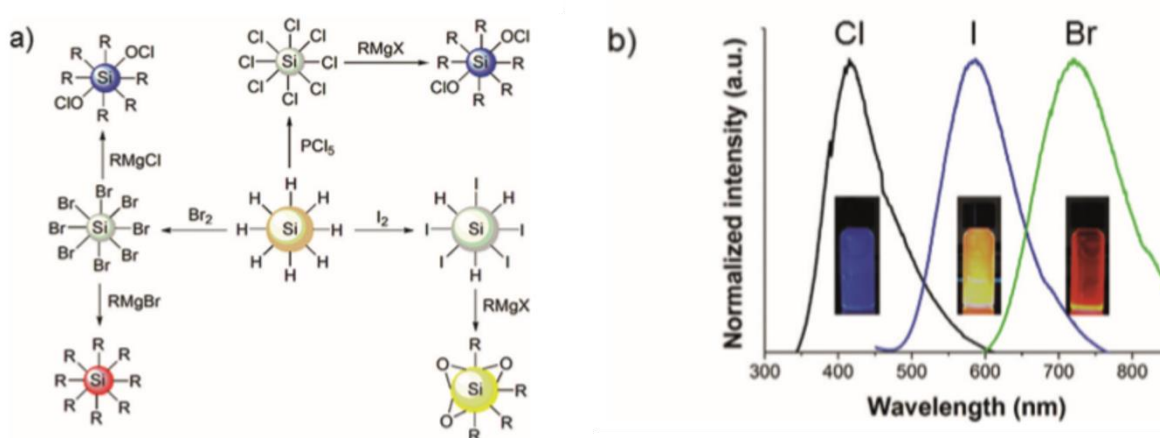
Figure 2.6- a) Schematic representation of halogenation and alkylation of hydride terminated Si-NCs and b) PL spectra of alkylated Si-NCs derived from halogenated surfaces. Reproduced with permission from the ref.[29]

The direct hydrosilylation reaction remains the best route to tune the surface of the SiNCs, modifying all the surface properties such as solubility, aggregation and chemical interactions, by preserving the peculiar optical properties of the Silicon core.

2.3 Experimental Techniques for SiNCs Synthesis and Passivation

This chapter reports the experimental procedures developed and adapted in our laboratory, starting from the techniques reported in the previous section of this dissertation (see chapter 2.2). The synthesis of different sized hydride-terminated SiNCs and their surface passivation will be detailed described, starting from the synthesis of the hydrogen silsesquioxane (HSQ) precursor (a non-stoichiometric silicon-rich oxide precursor) followed by its thermal annealing and decomposition, grinding and etching procedure with a mixture of EtOH:H$_2$O:HF (1:1:1). As discussed before, the surface functionalization step is fundamental to obtain a stable colloidal dispersion of SiNCs, to prevent their surface oxidation, to modify their solubility and to enhance their photophysical properties such as the absorbance and the photoluminescence quantum yield.

2.3.1 Synthesis of Hydrogen Silsesquioxane (HSQ)

Polymeric hydrogen silsesquioxane (HSQ) was prepared from HSiCl$_3$ following an adaptation of a literature procedure.[57,101,116] The procedure consists in the partial oxidation of HSiCl$_3$ in order to obtain a polysilane with the desired Si/O ratio.

22.5 mL of toluene was added dropwise to a mixture composed by 6.16 mL of concentrated sulfuric acid (98%) and 3.11 mL of fuming sulfuric acid (20% SO$_3$) in a nitrogen purged and dry environment; the two phases were left stirring for 30 minutes under nitrogen atmosphere. Then HSiCl$_3$ (8 mL) in toluene (55 mL) was slowly added dropwise and the reaction was left stirring for an additional hour before the two phases were separated. The organic layer was washed with a saturated CaCO$_3$ solution. The solution was dried over MgSO$_4$, filtered and finally concentrated under vacuum. The product, polymer [HSiO$_{1.5}$]$_n$, was collected as a white solid (2.2 g, yield 52%) (**figure 2.7**).
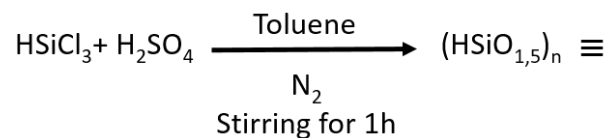
Figure 2.7- Reaction scheme for the HSQ synthesis. In photo: HSQ after concentration under vacuum.

2.3.2 Synthesis of Hydride-Terminated SiNCs

The produced HSQ powder was placed in a quartz reaction boat and it was treated via thermally induced disproportionation reaction under reducing atmosphere (93% N_2, 7% H_2) in a tube furnace at a heating rate of 16 °C/min with a final temperature of 1100°C (for SiNCs of diameter ca. 3-4 nm), or 1200°C (for SiNCs of diameter ca. 5 nm) and kept at the peak processing temperature for one hour. Upon cooling to room temperature, the oxide-embedded silicon nanocrystals (SiNCs) were extracted from the furnace. The resulting amber solid (**figure 2.8**) was ground into a fine brown powder using a mortar in order to remove large particles. Further grinding was achieved via shaking the powder for a night with 20/30 glass beads using a mixer. The resulting SiNCs/SiO_2 (oxide-embedded SiNCs) composite powder was stored in a standard glass vial.
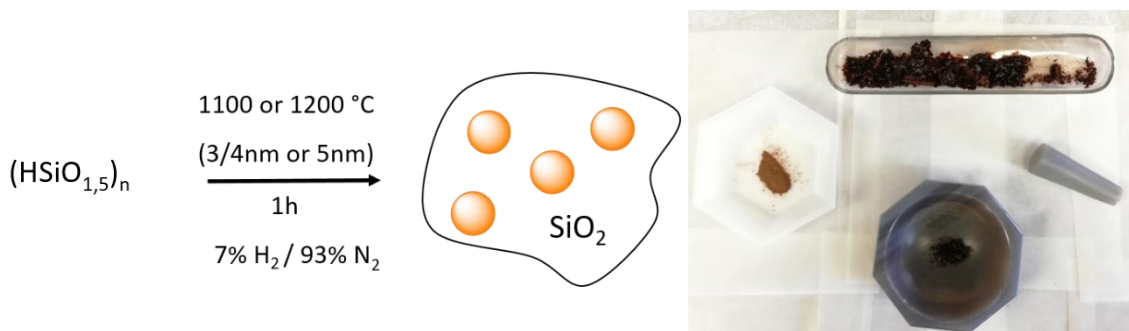
Figure 2.8- High Temperature Processing of HSQ to form oxide-embedded SiNCs. Adapted from the ref.[89] In photo: oxide-embedded SiNCs before (amber solid in the quartz boat) and after (brown powder in the weighing boat) manual grinding.

To remove the oxide matrix, 100 mg of oxide-embedded SiNCs were chemically etched with a 1:1:1=EtOH:H_2O:HF (48%) solution for 1.5 h, in the environmental light, at room temperature and under air atmosphere. The so-formed hydride-terminated SiNCs were extracted into three 5 mL portions of toluene and centrifuged (**figure 2.9**). The sample was than rinsed with toluene and centrifuged twice (8000 rpm for 5 min, each cycle). The solid product, the precipitate, was immediately transferred in a nitrogen purged glove-box and re-dispersed in 1 mL of oxygen-free anhydrous toluene to obtain a turbid brownish dispersion of hydride-terminated silicon nanocrystals.
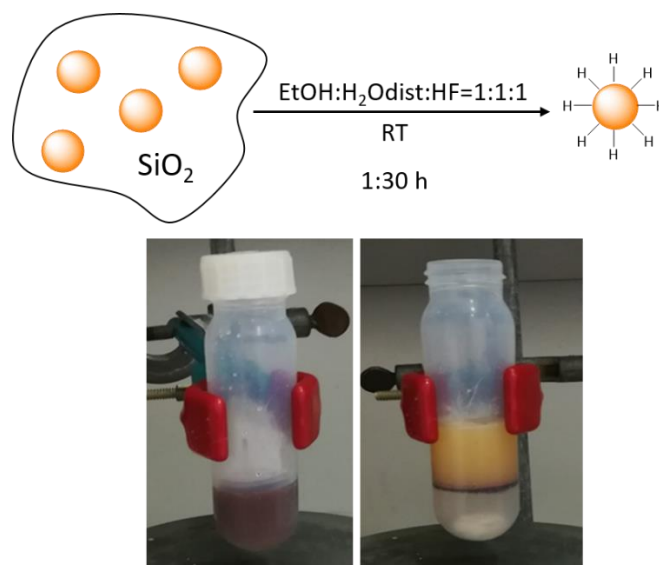
Figure 2.9- Production of hydride-terminated SiNCs by HF etching of oxide-embedded SiNCs. Adapted from the ref.[89] In photo: oxide-embedded SiNCs in 1:1:1=EtOH:H₂O:HF on the left and hydride-terminated SiNCs extracted in toluene on the right.

The hydride-terminated SiNCs need to be immediately functionalized with an outer protective shell in order to improve their solubility, to avoid surface oxidation and SiNCs agglomeration and to preserve all the SiNCs photophysical properties.

2.3.3 SiNCs Surface Passivation

Different surface passivation methods, hydrosilylation especially, have already been discussed in the chapter 2.2 of this dissertation. In this section, the experimental techniques adopted in our laboratory will be presented.

The Si-H bond onto the SiNCs surface is a kinetically metastable bond and it can be homolitically cleaved by providing external energy. The nature of this external input can be either thermal, photochemical or chemical by using a radical initiator. In these ways, a highly reactive silyl radical is obtained, which can then react with terminal olefins with a small activation barrier, producing both a Si-C covalent bond

and a new β-silyl radical. The reaction can either propagate or terminate, when a hydrogen is abstracted from some other species in solution. This is the most accredited path, but not the only one as previously shown (especially referring to the photochemical activated hydrosilylation).

Experimentally, the *thermal-activated hydrosilylation* is carried out by dissolving the brownish precipitate of hydride-terminated SiNCs, obtained after the etching procedure of 100 mg oxide-embedded SiNCs powder, in 3-4 mL of 1-dodecene (DDE), or of a different high-boiling temperature ligand, if needed. The turbid brownish dispersion is then immediately transferred in a nitrogen-purged three-neck flask and three freeze-pump cycles are done in order to totally remove the oxygen from the solution. The solution is then heated to 190 °C under N_2 flow for ca. 15 hours, by controlling the solution temperature with a thermocouple. After about half an hour it is already possible to notice the reaction activation since the turbid dispersion is slowly becoming optically clearer and more transparent, which means that SiNCs are being passivated. After the whole reaction time, the turbid dispersion is converted in a clear, transparent colloidal solution of surface-functionalized SiNCs. Passivated SiNCs need now to be purified from the excess ligand molecules. The purification procedure is carried out by transferring the reaction mixture to a glass vial and filling it with an anti-solvent, usually acetone or EtOH, until the clear solution becomes turbid again, in order to precipitate the SiNCs, which are strongly un-polar when functionalized with DDE or similar ligands. The nanocrystals can be therefore separated from the excess ligands by a centrifugation step (8000 rpm, 5 min). This purification procedure is usually repeated thrice, each time dissolving the precipitated SiNCs in a little amount of toluene and using acetone, or EtOH, to precipitate them again. The obtained SiNCs colloidal dispersion can be further filtered over a 0.20 or 0.45 μm PTFE syringe filter in order to remove the un-passivated SiNCs (if any) from the solution, making it even clearer. Un-soluble SiNCs can also be removed with a centrifugation step of

the sample in toluene, in this case, the supernatant is saved and the precipitate is thrown away. In the end, passivated SiNCs may be concentrated under vacuum and re-dispersed in optically pure solvents (spectroscopic toluene for example) in order to study their photophysical properties.

The *photochemical-activated hydrosilylation* is a valid alternative to the thermal functionalization, wherever the ligands are not stable at high temperature. For this purpose, the ligands should not absorb the light used to activate the reaction since the most accredited path takes into account the use of the light to homolytically cleave the Si-H bond onto the SiNCs surface (even if there are four different studied paths, as reported in the chapter 2.2). We have already described how much this photochemical method is promising since it is clean, direct, it requires no additional reagents (catalysts) or the input coming from the thermal energy, it leads to a less contaminated SiNCs surface, characterized by less defects. Nevertheless, the photochemical-activated hydrosilylation could be accelerated and facilitated by the use of a photoinitiator. The photoinitiator is considered the most important element of a free-radical photo-initiated reaction because it starts the initiation process, which is the first step of this kind of reactions. It is responsible for the conversion of the light energy into a chemical potential, by means of the production of initiating species, the radicals, which are reactive with the monomers present in the reaction mixture. There are two different types of free-radicals photoinitiators, the so-called "type-I" and "type-II". Type-I photoinitiators rely on the bonds dissociation of a photoinitiator molecule to yield one or two radicals, while type-II systems associate a photoinitiator with a co-initiator to ensure the production of the active species. The chosen reaction excitation wavelength must fit the photoinitiator absorption spectrum to induce this first reaction step. High-performance systems require the light to be absorbed with a high efficiency to produce strongly reactive species in a short time scale and with a maximum yield. When a photon is absorbed by the photoinitiator an electron is promoted from an occupied molecular orbital to an

unoccupied one of higher energy. This process lead to the molecule excited states formation. The first excited state of a type-I photoinitiator has a singlet nature, with a lifetime in the ns time-scale. Thanks to the intersystem crossing process (ISC), the triplet state is obtained, which is characterized by a longer lifetime, in the µs time-scale. In type-I photoinitiators, the initiating radicals are formed through a photo-cleavage process from the triplet state. However, both the singlet and the triplet states can always deactivate to the ground state without giving rise to any initiating radicals through a series of deactivation processes that can occur (internal conversion, luminescence, reaction with oxygen or with a monomer…). All of these deactivation paths should be reduced if possible. Type-I photoinitiators are composed by a single molecule, generally built around the benzoyl chromophoric group, which is promoted to its triplet state shortly after the absorption of the excitation light thanks to a fast ISC. In this case, the triplet energy is higher, or very close, to the bond dissociation energy and thus a cleavage reaction occurs and the initiating radicals are generated. The photodissociation yield depends on the molecule chemical structure, which easily affects the triplet state energy and the bond dissociation energy. The rate constant of the photodissociation is generally quite high and governs the lifetime of the triplet state, which can spans from hundreds of picoseconds to the microsecond time-scale.[126,127]

In this work, a type-I photoinitiator has been used to photoinitiate the hydrosilylation reaction on the SiNCs surface, the diphenyl(2,4,6-trimethylbenzoyl)phosphine oxide (TPO) (**figure 2.10**). TPO maximum absorption wavelength is at 395 nm, with a high molar absorption coefficient, which is extremely important by an experimental point of view because allows us employing lower concentrations of the photoinitiator itself. TPO is also quite colorless, photostable when irradiated with visible light and easy to be removed from the hydrosilylation reaction mixture by a centrifugation step.
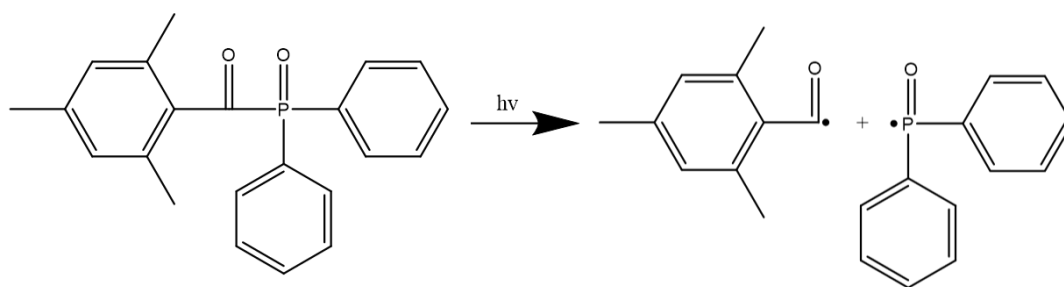
Figure 2.10- Photodissociation of TPO photoinitiator caused by light absorption and initiating radicals formation.

Experimentally, a large excess of ligand (3-4 mL of DDE for instance or a different ligand if needed) is added to the precipitate of hydride terminated SiNCs, obtained after the etching procedure of 100 mg of oxide-embedded SiNCs powder, and a brownish turbid suspension is obtained. 5-10 mg of TPO is added to the reaction mixture. The dispersion is sonicated and then transferred into a nitrogen-purged two-neck flask. Three freeze-pump cycles are done in order to remove the oxygen from the solution. The solution is then irradiated using a 365 nm emitting LED as the source of the light and kept under continuous stirring and under N_2 flow, at room temperature, for ca. 2 hours. The 365 nm emitting LED is chosen since TPO has a high molar absorption coefficient at this wavelength. Once the reaction is terminated, the turbid dispersion is converted in a very clear, transparent, colloidal solution of surface-functionalized SiNCs. Passivated SiNCs need now to be purified from the excess ligand molecules and from the unreacted photoinitiator and its by-products. The purification procedure is carried out firstly by filtering the product over a 0.20 or 0.45 μm PTFE syringe filter in order to remove un-passivated SiNCs (if any) from the solution, making it even clearer. Un-soluble SiNCs can also be removed with a centrifugation step of the sample in toluene, in this case, the supernatant is saved and the precipitate is thrown away. Furthermore, the red-emitting colloidal solution is transferred to a glass vial, filling it with an anti-solvent, usually acetone or EtOH, until the clear solution becomes turbid again, in order to

precipitate the SiNCs, which are strongly un-polar when functionalized with DDE or similar ligands. The nanocrystals can be now separated from the excess ligands and from un-reacted TPO by a centrifugation step (8000 rpm, 5 min). This purification procedure is usually repeated thrice, each time dissolving the precipitated SiNCs in a little amount of toluene and using acetone, or EtOH, to precipitate them again. Another way to separate the SiNCs from the excess ligands and the un-reacted TPO is by a size exclusion chromatography (SEC) using Biobeads™ S-X1 Support (200-400 mesh) as the solid phase and the solvent of choice (depending on the SiNCs dispersibility) as the liquid phase. In the end, passivated SiNCs may be concentrated under vacuum and re-dispersed in optically pure solvents (spectroscopic toluene for example) in order to study their photophysical properties.

The *radical-promoted hydrosilylation* is the third and the most used method in our laboratory. The use of radical initiators, usually organic molecules such as diazonium salts, is convenient since they offer mild reaction conditions (room temperature for instance), they can be easily removed from the reaction mixture, thus they do not influence the SiNCs photophysical properties and they allow a fast SiNCs surface passivation through many different ligands. Among all the terminal olefins, we can use a diazonium salt-promoted hydrosilylation to functionalize the SiNCs surface with the chlorodimethyl(vinyl)silane for instance, which is an extremely useful functional group since it can undergo further reaction steps.[101,128,129]

Experimentally, we have chosen the 4-decylbenzene diazonium tetrafluoroborate (4-DDB) as the diazonium salt to initiate the hydrosilylation reaction. 4-DDB has been synthesized in our laboratory by following an adaptation of a literature procedure[130] (**figure 2.11**).
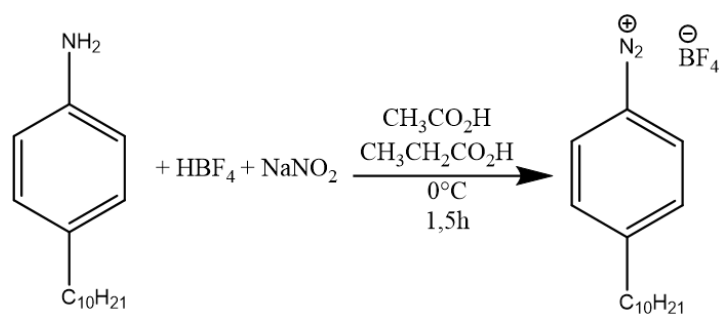
Figure 2.11- 4-decylbenzene diazonium tetrafluoroborate (4-DDB) synthesis reaction scheme

140 mg of 4-decylaniline (0.6 mmol, 1 eq) were solubilized in 1 mL of propionic acid, 1 mL of acetic acid and 0.75 mL of tetrafluoroboric acid solution 50% in water (5.5 mmol, 9 eq). The reaction mixture was then transferred in a 10 mL one-neck round bottom flask together with a magnetic stirrer. The temperature was then cooled down to 0 °C and 60 mg of NaNO$_2$ (0.87 mmol, 1-4 eq ca.) were slowly added. The reaction mixture was left under stirring at room temperature for 1 hour and 30 minutes and then the yellowish suspension was transferred in a 25 mL backer filled with 10 mL of iced distilled water. Finally, the yellowish suspension was filtered with a buchner filter set up. The reaction product was then transferred inside a glass vial and kept under vacuum for few hours. When it is totally dried the color changes from yellowish to pink-orange and it is stored in a freezer.

The brownish precipitate of hydride-terminated SiNCs, obtained after the etching procedure of 100 mg oxide-embedded SiNCs powder, is rapidly brought into a nitrogen-filled Glovebox where it is dispersed in 1-2 mL of anhydrous toluene. 0.2 mL of DDE (0.9 mmol), or a different ligand if needed, are added to the turbid solution together with 2 mg of 4-DDB. The reaction mixture is then left stirring for ca. 12 hours, but few minutes later, it is already possible to notice the reaction activation since the cloudy suspension is becoming optically clear, which means that SiNCs are starting to be passivated. After the whole reaction time, the turbid dispersion is converted in a transparent colloidal solution of surface-functionalized

SiNCs. Passivated SiNCs need now to be purified from the excess ligand molecules and from the un-reacted 4-DDB. The purification procedure is carried out by transferring the reaction mixture to a glass vial and filling it with an anti-solvent, usually acetone or EtOH, until the clear solution becomes turbid again, in order to precipitate the SiNCs, which are strongly un-polar when functionalized with DDE or similar ligands. The nanocrystals can be therefore separated from the excess ligands by a centrifugation step (8000 rpm, 5 min). This purification procedure is usually repeated thrice, each time dissolving the precipitated SiNCs in a little amount of toluene and using acetone, or EtOH, to precipitate them again. The obtained SiNCs colloidal dispersion can be further filtered over a 0.20 or 0.45 μm PTFE syringe filter in order to remove un-passivated SiNCs (if any) from the solution, making it even clearer. Un-soluble SiNCs can also be removed with a centrifugation step of the sample in toluene, in this case, the supernatant is saved and the precipitate is throw away. In the end, passivated SiNCs may be concentrated under vacuum and re-dispersed in optically pure solvents (spectroscopic toluene for example) in order to study their photophysical properties.

3 Hybrid Silicon Nanocrystals for Color-Neutral and Transparent Luminescent Solar Concentrators

The contents of this chapter have been reprinted and adapted with permission from the following publication: Mazzaro, R., Gradone, A., Angeloni, S., Morselli, G., Cozzi, P.G., Romano, F., Vomiero, A., and Ceroni, P. (2019). Hybrid Silicon Nanocrystals for Color-Neutral and Transparent Luminescent Solar Concentrators. ACS Photonics *6*.

3.1 Introduction

Luminescent Solar Concentrators (LSCs) (**figure 3.1**) were proposed for the first time in 1973 by Lerner[131] as a viable alternative to traditional Silicon based photovoltaics cells (PV cells). The LSCs principle aim was to reduce the electricity costs and offering a solution suitable for Building Integrated Photovoltaics (BIPV). Indeed, Si-based PV cells present some disadvantages. They are very expensive, difficult to integrate in buildings architecture due to limitations in color and shape, they show a good response only to incident sunlight (while in the built environment much of the sunlight is diffuse due to scattering and reflections by other objects such as trees, other buildings and clouds) and shade is also common, which reduces the performance of these systems.[132] On the contrary, LSCs promise large area polymer plates with relatively simple procedures and low costs of production,[133] they can be easily integrated in the architecture since they can be made in different shapes and colours (even transparent), they can be flexible and should weigh less than silicon PVs cells.[134–136] In addition, the LSCs work even with the diffuse light.[137,138]
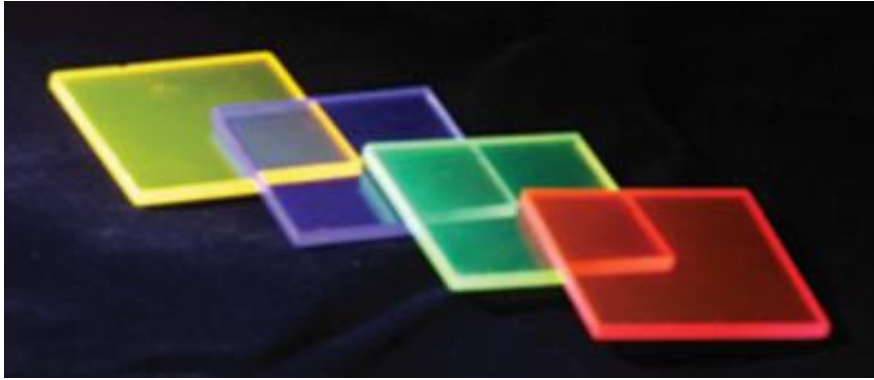
Figure 3.1- LSCs illuminated by UV light. Reprinted with permission from the ref.[132]

After a period of silence, mainly driven by the low cost of oil in the eighties, the research rediscovered this architecture in the latest years, thanks to the development of engineered luminophores, guaranteeing improved optical properties compared to standard organic dyes. LSC architecture consists of a flexible plastic or glass plate embedded with luminescent species (organic dyes, inorganic phosphors or quantum dots) that extensively absorb sunlight and emit in a spectral window where conventional Si cells or GaAs cells have high power conversion efficiency. Thanks to the waveguide mechanism, which takes place inside the LSC matrix, a substantial portion of the higher wavelengths re-emitted light by the embedded luminescent species can be concentrated to the edge of the plate (up to ~75% according to Snell's law for a polyacrylate waveguide) by total internal reflection. Small area band-gap matched and highly efficient conventional PV cells can be attached to the edges of the plate to collect the light and convert it to electricity (**figure 3.2**).[132]
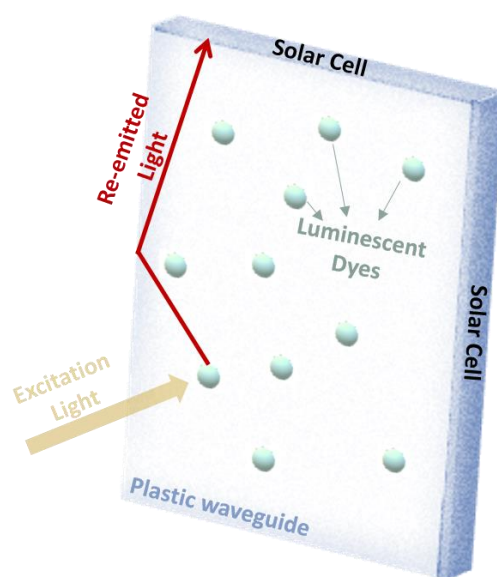
Figure 3.2- LSC simplified scheme. Incoming excitation light (yellow arrow) enters the plastic waveguide and is absorbed by the embedded-luminophores. The light is re-emitted at a longer wavelength (red arrow) and a fraction of it is total internal reflected and collected to the edges attached PV cells for conversion of the light into electricity.

Advanced solutions include also sandwich structures, in which front and bottom glass panels can improve light transport by decreasing light reflection at the plastic surface and reabsorption losses inside the active medium.[139] The record power conversion efficiency for an LSC-coupled PV cell is about 7.1% and it is reported for a luminescent organic dye based LSC.[140] However, this value is not informative since it is highly dependent on the dimension of the LSC and on the amount of light absorbed by the LSC: colorless LSC absorbing only the UV component of the solar spectrum has a lower efficiency,[141] but are best suited as smart windows. Several other classes of luminophores have been employed in LSC devices, such as metal nanoclusters,[142] lanthanides hybrids,[143] conjugated polymers,[144] and molecular aggregates,[145] but these approaches have been followed by limited development due to either limited performance or poor stability. In the past few years, the interest has

moved toward LSC based on nanorods and quantum dots.[146] These luminophores appear as fascinating materials thanks to their optical properties, namely, higher photostability and simpler tunability of the luminescence color. Several examples are reported embedding Cd,[147–150] Pb,[151,152] and perovskite-based[153–155] quantum dots, obtaining relatively good efficiencies. Recently, some concerns about the use of toxic heavy metals in these applications are emerging. As a consequence, research is now focused on heavy metal free QDs such as $CuInS_xSe_{2-x}$ and Mn^{2+}-doped ZnSe QDs,[156,157] carbon dots,[158,159] and SiNCs.[129]

SiNCs represent an interesting alternative for multiple reasons,[47] already shown in the previous chapters of this dissertation. To sum up, SiNCs are attractive not just due to their viability and earth-abundance of Si, but also because of their lack of toxicity, the possibility to functionalize their surface with robust Si-C covalent bond, which ensures stability and dispersibility in different polymer matrices, their tunable and size-dependent photoluminescence properties,[160] and the presence of an apparent large Stokes-shift related to their indirect band gap nature. The last feature results in negligible reabsorption in bulk polymer LSCs based on SiNCs, producing competitive optical efficiency with a non-toxic, widely available luminescent material, as described in a seminal paper by Meinardi et al.[161] SiNCs belong to the indirect band gap QDs family (see chapter 1.3 for more details) and this is the principle reason of their optical downsides such as the poor absorption properties. The molar absorption coefficient is low in the visible region and gradually increases in the UV region, in contrast to the abrupt transition usually observed in direct band gap QDs. Thus, in order to efficiently harvest the solar spectrum, a large concentration of SiNCs must be employed. An accurate control on the shape of the absorption features is of the utmost importance for the preparation of LSCs absorbing mainly in the UV-A region of the solar spectrum (λ = 350–400 nm), to be employed in BIPV. For conventional QDs, this is usually achieved by inorganic core–shell structures or doping the material with transition

metals,[162] where a high band gap semiconductor is responsible for the light absorption in the UV region and luminescence derives from the lower band gap semiconducting material. This approach has not been applied to SiNCs yet, since the luminescence is strongly sensitive to surface chemistry, typically producing partial or complete quenching of the nanocrystal, instead of luminescence tuning.

An appealing alternative approach employs an organic–inorganic hybrid material: organic chromophores covalently attached to the surface of SiNCs absorb light and funnel the excitation energy to the silicon core, the working principle of a *light-harvesting antenna.*[163] As was already proved by our group, this approach is feasible with an efficient sensitization of the luminescence of colloidal SiNC upon excitation in the UV,[164,165] visible,[166] and also NIR[167] spectral region. By this approach, it is possible to tune the absorption properties of the material and to preserve the luminescence properties of the silicon core.

The synthesis and characterization of colloidal SiNCs functionalized with 9,10-diphenylanthracene (DPA) derivatives, and the preparation of polymer LSCs based either on this new hybrid luminophore or on a physical mixture of DPA and SiNCs, are reported on the following chapters. The DPA chromophore was selected because it absorbs in the UV-A spectral region and it does not affect the optical appearance in the visible region. Energy transfer from DPA to SiNCs is expected to occur for both LSCs via the non-radiative or radiative mechanism. Thorough optical and photovoltaic characterization is performed to investigate the properties of the prepared LSC devices and to elucidate the role of the energy transfer process on them.

3.2 Light Harvesting Antennae

SiNCs are weak light absorbers due to the indirect nature of the Si band gap. To enhance the optical absorption of SiNCs while retaining their emissive properties,

it is possible to add chromophores to the system, which have high ε values and can transfer the energy to the SiNCs in an efficient way.[164] This is the working principle of a Light Harvesting Antenna. A molecular antenna is made of multiple chromophoric units, which absorb the incident light and funnel the excitation energy to a common acceptor component, which could be or not covalently linked to them. This system should be an excellent light absorber, stable from the chemical and the photochemical point of view, organized in the dimensions of time, energy and space. The donors must absorb the incident light and immediately transfer it to the acceptor, before the radiative or non-radiative deactivation take place. The energy of the acceptor excited state (or exciton in the case of a QD acceptor) has to be lower or, at least, equal to the energy of the excited state of the donor. The occurrence of the energy transfer requires electronic interactions and therefore the higher the distance between the donor units and the acceptor unit, the lower the rate of the energy transfer. The *sensitized emission QY* of the acceptor ($\Phi_{sensitized}$) is a product of the *emission QY* of the acceptor by its direct excitation ($\Phi_{acceptor}$) and the *efficiency of energy transfer* (η_{et}) from the electronic excited state of the donor to the acceptor:

$$\Phi_{sensitized} = \eta_{et} * \Phi_{acceptor}$$

A more representative measure of the performance of a light harvesting antenna is the *brightness* (B):

$$B = \varepsilon(\lambda_e x) * \Phi_{sensitized}$$

Where $\varepsilon(\lambda_e x)$ is the molar absorption coefficient of the antenna at the excitation wavelength. With higher brightness, lower concentrations of the antenna are required to observe a detectable emission.[163]

Two different methods to obtain light harvesting molecular antennae have been used and both of them will be presented on this dissertation, the covalent (**figure 3.3**) and the non-covalent (**figure 3.4**) one. In the following sections of this chapter

3, only the first technique will be discussed. The covalent method shows many advantages such as the higher stability of the system, the lower distance between the donor and the acceptor, but also some disadvantages: for example, the more complex synthesis. On the contrary, the non-covalent method (see chapter 5 for more details) allows us to have a higher number of chromophores constrained in a small space together with the acceptors, an on/off switchable system by an external stimulus and an easier synthesis; nevertheless, the distance between donor and acceptor is more changeable.[168]
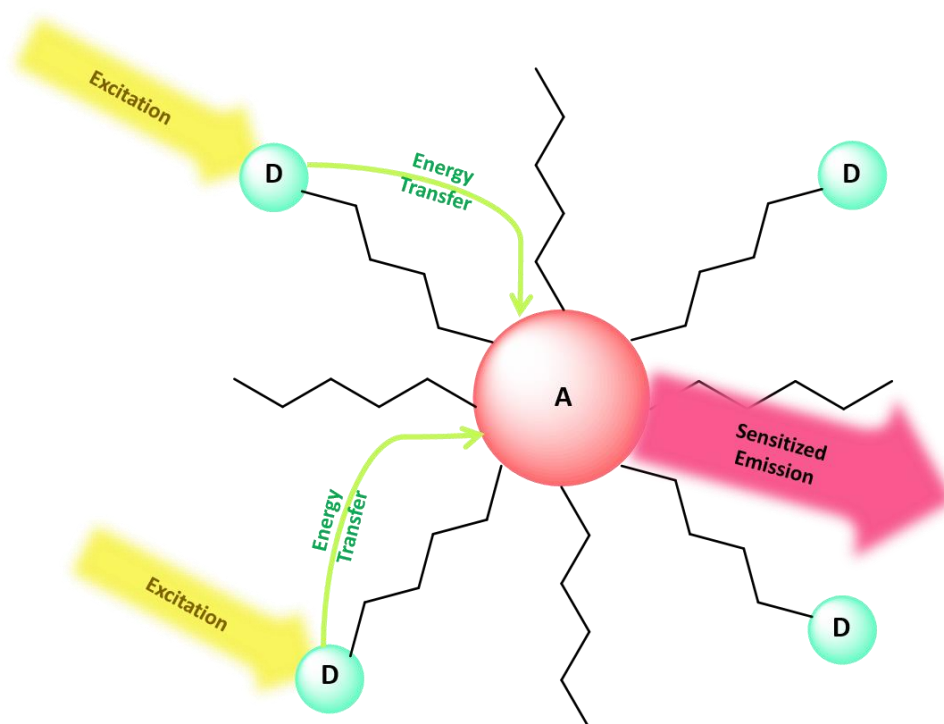
Figure 3.3- General scheme representing the energy transfer process, taking place in an antenna system composed by many donors (D) covalently linked to the acceptor (A) surface. Adapted from the ref.[163]
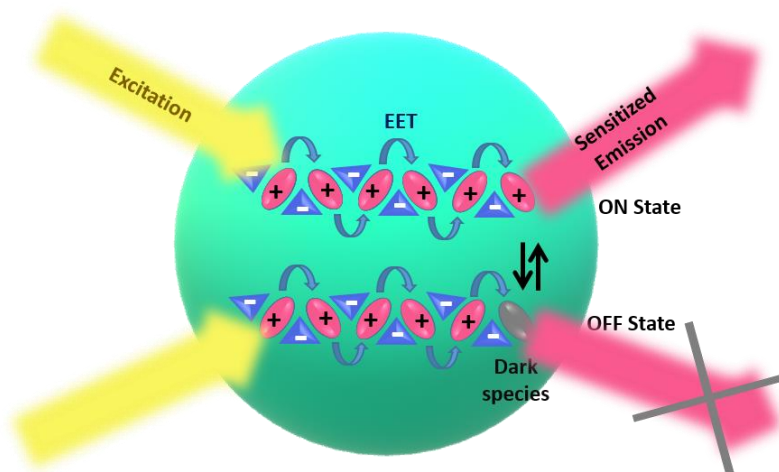
Figure 3.4- General scheme representing a non-covalent light harvesting antenna. The excitation energy transfer (EET) process take place in a confined space, between many species non-covalently linked. An "on state" can be turned to an "off state" by an external stimulus. Adapted from the ref.[168]

3.3 Synthesis of DPA-functionalized SiNCs

SiNCs were produced by thermal disproportionation of hydrogen silsequioxane (HSQ, see chapter 2 for more details) to obtain SiNCs embedded in SiO_2. Etching the oxide matrix with HF yields freestanding H-terminated Si nanocrystals. The surface functionalization of H:SiNCs consisted of a two-step procedure:

- hydrosilylation with chlorodimethylvinylsilane promoted by 4-DDB (4-decylbenzene diazonium tetrafluoroborate), yielding chlorosilane-passivated SiNCs (**figure 3.5 a**);

- post-functionalization by nucleophilic reagents; in the present case, the acetylide derivative of diphenylanthracene (**DPA**) formed in situ with nBuLi, yielding the **Si-DPA** sample.

As the control sample, alkyl-capped SiNCs (**Si**) were prepared by hydrosilylation of H:SiNCs in the presence of 1-dodecene (**DDE**) and initiated with 4-DDB (**figure 3.5 b**).
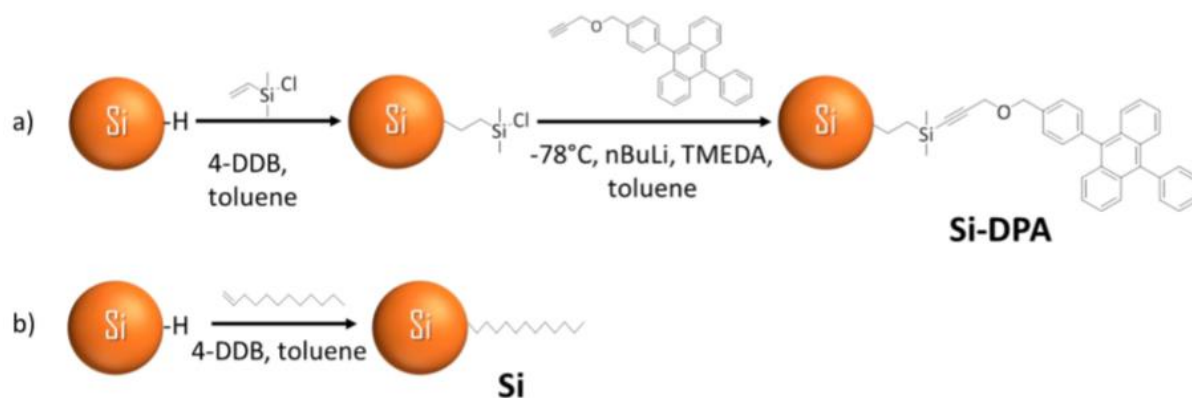
Figure 3.5- Schematic representation of the synthesis of (a) SiNCs covalently functionalized with 9,10-diphenylanthracene chromophores (**Si-DPA**) and (b) alkyl-passivated SiNCs sample (**Si**).

3.3.1 SiNCs Passivated with Chlorodimethylvinylsilane or 1-dodecene (**Si** sample)

Hydride-terminated SiNCs, obtained after the etching procedure of 300 mg oxide-embedded SiNCs powder (see chapter 2 for more details), were dispersed in 4 mL of dry toluene and separated in two 8 mL vials, working inside a nitrogen-filled glovebox. Two milligrams of 4-DDB (about 6 µmol) were added in each one. Afterwards, in a vial, 200 µL of chlorodimethylvinylsilane (1.5 mmol) were introduced to obtain chlorosilane passivated silicon nanocrystals. In the other vial, 330 µL of 1-dodecene (1.5 mmol) were dropped, to passivate the nanocrystals with an alkyl chain. Both mixtures were stirred overnight at RT. The mixture of chlorosilane-passivated SiNCs was then filtered, concentrated at rotary evaporator, transferred again in the dry-box and diluted in 2 mL of fresh dry toluene. The

suspension of dodecyl-passivated nanocrystals was precipitated in an anti-solvent (methanol) and centrifuged three times (8000 rpm, RT, five minutes), each time washing with methanol. The precipitate was readily dissolved in 2 mL of toluene (**figure 3.5**).

3.3.2 Synthesis of (4-(10-phenylanthracen-9-yl)phenyl) methanol

Synthesis of (4-(10-phenylanthracen-9-yl)phenyl)methanol was performed via Suzuki-Miyaura reaction conditions between 9-bromo-10-phenylanthracene and 4-(Hydroxymethyl)phenylboronic acid (**figure 3.6**). To a suspension of degassed toluene (50.0 mL) and K_2CO_3 (12 mL of a 1.6 M solution), under nitrogen atmosphere, 9-bromo-10-phenylanthracene (1.7 g, 5.1 mmol), boronic acid (6.12 mmol, 1.2 equiv.) and a catalytic amount (1.5% m/m) of $Pd(PPh_3)_4$ were added. The resulting mixture was heated at 90°C overnight, then cooled to room temperature, and solvents were removed under reduced pressure at 40°C. The crude was purified via flash chromatography using toluene as the eluent and applying a gradient with ethyl acetate to reach a final ratio of 70:30 (toluene:ethyl acetate). The product was recovered as pale yellow solid after evaporation of solvents, with a yield of 50%. GC-MS m/z: 360.40. ^{1}H-NMR (400 MHz, CDCl3), δ: 7.4-7.6 ppm (17 H, m); 4.90 ppm (1 H, s); 4.71 ppm (2 H, s).
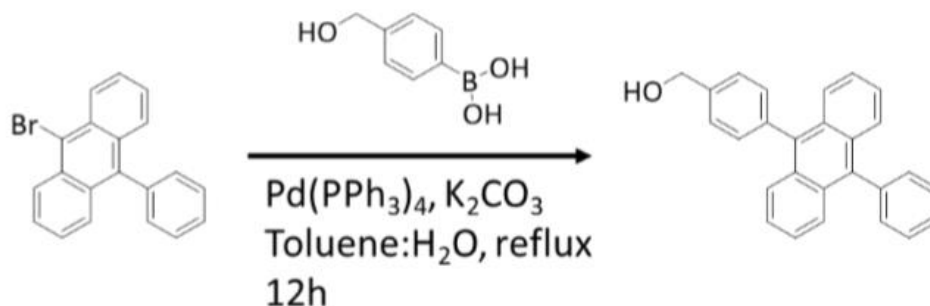
Figure 3.6- Reaction scheme for the synthesis of (4-(10-phenylanthracen-9-yl)phenyl)methanol

3.3.3 Synthesis of 9-phenyl-10-(4-((prop-2-yn-1-yloxy)methyl)phenyl)anthracene

In a 100 mL two-neck round-bottom flask filled with nitrogen atmosphere, 75 mL of acetonitrile were introduced to dissolve 1.4 g of (4-(10-phenylanthracen-9-yl)phenyl)methanol (4 mmol). Later, 290 mg of NaH 95% (12 mmol) were introduced, and the mixture was heated to 78°C. A solution of propargyl bromide (80% in toluene, 1.1 mL, 12 mmol) was added dropwise, and the mixture was stirred at reflux overnight. The reaction was quenched with water (100 mL) and then extracted with dichloromethane (DCM, 3x100 mL). The organic fraction was collected and dried over $MgSO_4$. A flash chromatography (toluene as eluent phase) was performed to isolate 0.96 g of product, a bright yellow solid (60% yield) (**figure 3.7**). GC-MS (EI): m/z 398.51; ^{1}H-NMR (400 MHz, CDCl3), δ: 7-8 ppm (17 H, m); 4.80 ppm (2 H, s); 4.36 ppm (2 H, d, J=4 Hz); 2.55 (1 H, t, J=4 Hz).
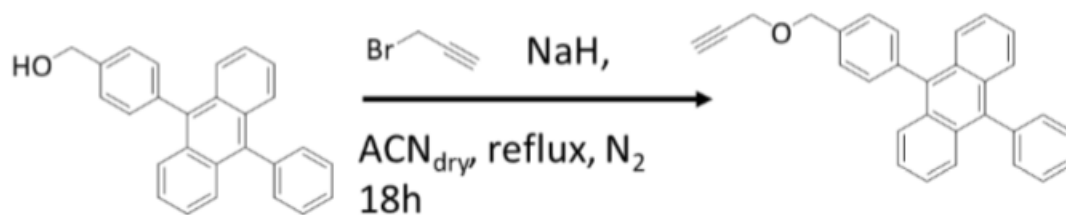
Figure 3.7- Reaction scheme for the synthesis of 9-phenyl-10-(4-((prop-2-yn-1-yloxy)methyl)phenyl)anthracene.

3.3.4 Passivation of SiNCs with 9-phenyl-10-(4-((prop-2-yn-1-yloxy)methyl)phenyl)anthracene to obtain the SiDPA sample

In a two-neck 25 mL round-bottom flask, dried and filled with nitrogen, 120 mg of 9-phenyl-10-(4((prop-2-yn-1-yloxy)methyl)phenyl)anthracene (0.3 mmol) were introduced. The flask was transferred to a nitrogen filled glove box and 70 μL of N,N,N′,N′-tetramethylethylenediamine (TMEDA, 0.45 mmol) and 3 mL of dry toluene were added. The flask was then removed from the dry-box and plugged to a shlenk line filled with N_2. After having cooled the reaction to -78°C with a liquid nitrogen/acetone bath, 120 μL of n-butyllithium (nBuLi, 2.5 M in hexanes, 0.3 mmol) were added dropwise, while stirring. The acetone bath was removed after 45 minutes, and the mixture was stirred for 15 minutes at room temperature. Again at -78°C, a suspension of silicon nanocrystals in 2 mL of toluene was slowly added to the reaction mixture. One hour later, the acetone bath was removed, and the reaction mixture was stirred for an hour at room temperature. Later, it was heated to 40°C, and stirred for another hour. The reaction was cooled again to -78°C and a second amount of nBuLi (60 μL, 0.15 mmol) was added to complete the capping of the surface. The reaction was stirred overnight at RT. The introduction of 7 mL of a 1 M solution of HCl in MeOH made the nanocrystals precipitate. The precipitate

was washed 3 times with methanol and separated from the supernatant by centrifuge (8000 rpm, 5 minutes). The nanocrystals were then dispersed in chloroform, and a size exclusion chromatography over BioBeadsTM S-X1 Support (200-400 mesh) in chloroform was performed to isolate a brownish limpid suspension (**Figure 3.5 a**). ^{1}H-NMR spectra of the anthracene ligand and the functionalized silicon nanocrystals are reported in **figure 3.8**. The aromatic protons and the ones in α-position with respect to oxygen of DPA are present in both spectra, but when the molecule is bonded to the SiNC a broadening of the peaks is induced since the movement of the molecules is hindered on the nanocrystal surface. The terminal proton from the alkyne moiety (around 2.5 ppm) reacts in the functionalization and is no longer present in the spectrum of functionalized silicon nanocrystals.

^{1}H-NMR of dodecyl-capped nanocrystals: (400 MHz, CDCl3), δ: 1.22 ppm (18 H, m); 0.84 ppm (3 H, s).
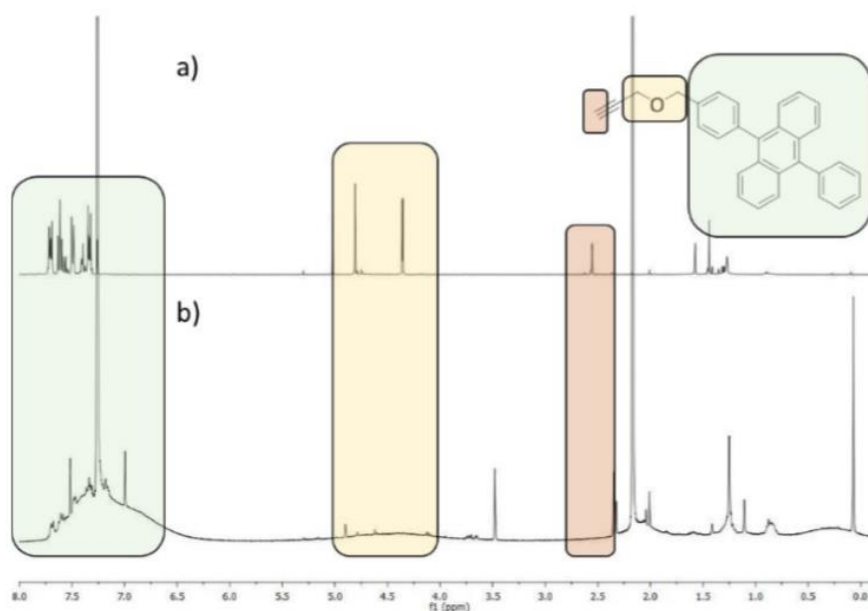
Figure 3.8- ^{1}H-NMR spectra (400 MHz, CDCl₃, RT) **a)** of 9-phenyl-10-(4-((prop-2-yn-1yloxy)methyl)phenyl)anthracene, and **b)** silicon nanocrystals functionalized with 9-phenyl-10-(4((prop-2-yn-1-yloxy)methyl)phenyl)anthracene.

61

3.3.5 Fabrication of Luminescent Solar Concentrators

The PLMA/PMMA plate was fabricated by bulk co-polymerization, using a "home-made" cell casting process characterized by two steps. First, the so-called 'syrup' was prepared: LMA monomer was heated in a beaker to 80°C. When the LMA temperature was stable, lauroyl peroxide (0.5% wt/wt with respect to LMA) was added, the pre-polymerization took place and the monomer temperature increased by a few degrees (exothermic process). After 30 minutes, the syrup was quenched in cold water. In the second step, the MMA monomer, lauroyl peroxide, the cross-linker (EGDM) and/or the DPA and/or SiNCs were added taking into account this ratio between the components: LMA 35% w/w (prepolimerized); MMA 35 % w/w (monomer); EDGM, 30 % w/w; lauroyl peroxide 0.2% w/w respect to LMA (after the pre-polymerization step). In order to obtain a homogeneous solution, the reaction mixture was ultra-sonicated for 10 min. The reaction mixture was then degassed by 3/4 freeze–pump-thaw cycles in order to remove oxygen and nitrogen was purged after each cycle. Finally, the more-viscous liquid was introduced into the casting mould under nitrogen flow, where the polymerization reaction proceeded bringing the mould inside an oven heated at 50°C for an hour and at 80°C for 23h. The casting mould was made by two glass plates sealed with a silicone gasket (to preserve the inert atmosphere) and clamped together. The main advantage of this approach compared to a photoactivated polymerization is to avoid photo-degradation of chromophores like DPA that absorb in the same spectral region of the most commonly used photoinitiators. In addition, a method like this requires a very limited amount of radical initiator, which is mostly responsible for photoluminescence quenching while the pre-polymerization step reduces the formation of heterogeneities in the co-polymer.

3.4 Results and Discussions

Photophysical Characterization in Solution.

The absorption and photoluminescence (PL) spectra of **Si-DPA** samples in toluene solution are reported in **figure 3.9** (green line). The absorption spectrum exhibits the typical featureless absorption of the silicon core gradually increasing in the UV region, as observed for the **Si** sample, plus the structured and sharp band of the **DPA** chromophore limited to the UV-A region. The overall spectrum perfectly matches the one of the control sample constituted by a physical mixture of **Si** and **DPA** (**Si+DPA**, red line) with the same concentration, suggesting that no ground state interaction is affecting their optical properties.
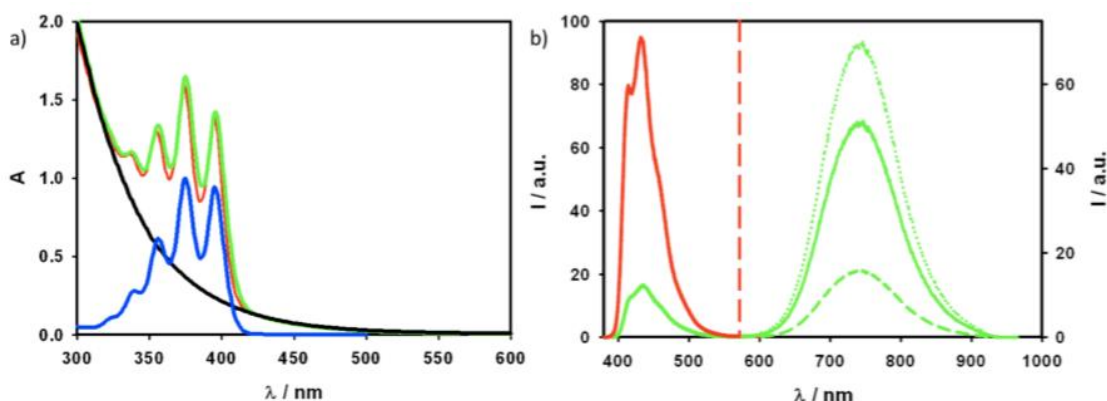
Figure 3.9- a) Absorption spectra of **Si** (black line), **Si-DPA** (green line), **DPA** (blue line), and a physical mixture of Si and DPA (**Si+DPA**, red line) with the same concentration as that of the covalent sample. **b)** PL spectra of **Si-DPA** (green solid line, λ_{ex}=375 nm) and **Si+DPA** (red line, only **DPA** contribution, λ_{em} =390−580 nm) of two isoabsorbing solutions at the excitation wavelength of 375 nm. For the sake of comparison, the PL spectra of **Si-DPA** corresponding to 100% energy transfer (dotted green line) and 0% energy transfer (dashed green line) are reported (for more details, see appendix A). All spectra are registered at room temperature in air-equilibrated toluene.

On the basis of the molar absorption coefficients of **DPA** ($\varepsilon_{375nm} = 1.4 \times 10^4$ M^{-1} cm^{-1}) and **SiNCs** ($\varepsilon_{430nm} = 1 \times 10^5$ M^{-1} cm^{-1} for 3.5 nm diameter) we can estimate an average number of about 80 **DPA** fluorophores per **SiNC**, resulting in a strong enhancement of the absorption properties of the **Si-DPA** upon excitation in the λ = 350–400 nm region. Upon excitation at 375 nm, where most of the light (80%) is absorbed by **DPA** chromophores in the **Si-DPA** sample, two emission bands are observed (green line in **figure 3.9**): one structured-band centered at 440 nm and the other at about 750 nm. The high-energy band is assigned to the **DPA** fluorescence and the low-energy band is due to the **Si** core emission, by comparison with the PL spectra of **DPA** and **Si**. Indeed, the band centered at 440 nm is observed also in the control sample **Si+DPA**, the lower intensity of **DPA** band in the covalent sample being due to a quenching process. The quenching efficiency (η_q) is estimated to be 82% (see appendix A for more details) and it is due to a photoinduced energy transfer from **DPA** to the **Si** core, as demonstrated by the sensitization of the **Si** core emission at 750 nm. Indeed, a close match of the excitation spectrum performed at the SiNC emission (λ_{em}=750 nm) and the absorption spectrum of **Si-DPA** is observed (**figure 3.10**), revealing the presence of a very efficient energy transfer process.
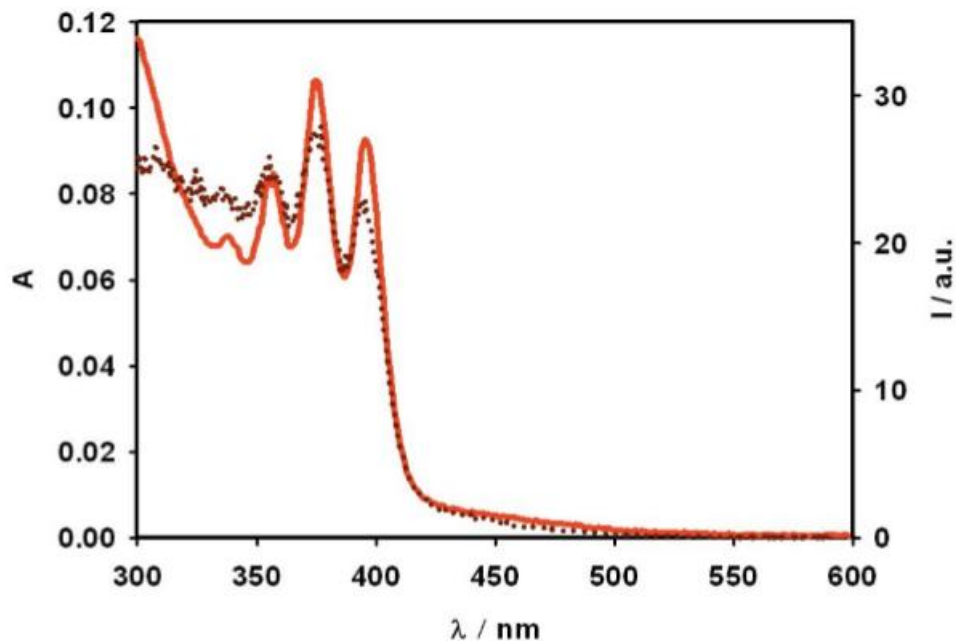
Figure 3.10- Absorption (red continuous line) and excitation (λ_{em}=750 nm, dark red dotted line) spectra of **Si-DPA** in air-equilibrated toluene

The sensitization efficiency (η_s) is estimated to be 70% (see appendix A for additional details), pointing to a very efficient energy transfer. The PL quantum yield (PLQY) of the SiNCs in the **Si-DPA** sample is measured upon selective excitation of the Si core at 460 nm: the resulting value is 26%, lower than that observed for the **Si** sample (45%) under the same experimental conditions. Accordingly, the PL decay time is shorter (50 μs) in **Si-DPA** compared to **Si** (90 μs). The same effect has been previously reported by some of us in the case of SiNCs functionalized by different organic chromophores;[164,166,169] it is likely due to the presence of more defects at the surface of the **Si-DPA** sample compared to the **Si** sample. In this case, it is worth noting that the control sample (**Si**) has been obtained by a different synthetic procedure (**figure 3.5**, see chapter 3.3.1 for more details), and this may have an impact on the resulting PLQY.

LSC Preparation and Optical Properties.
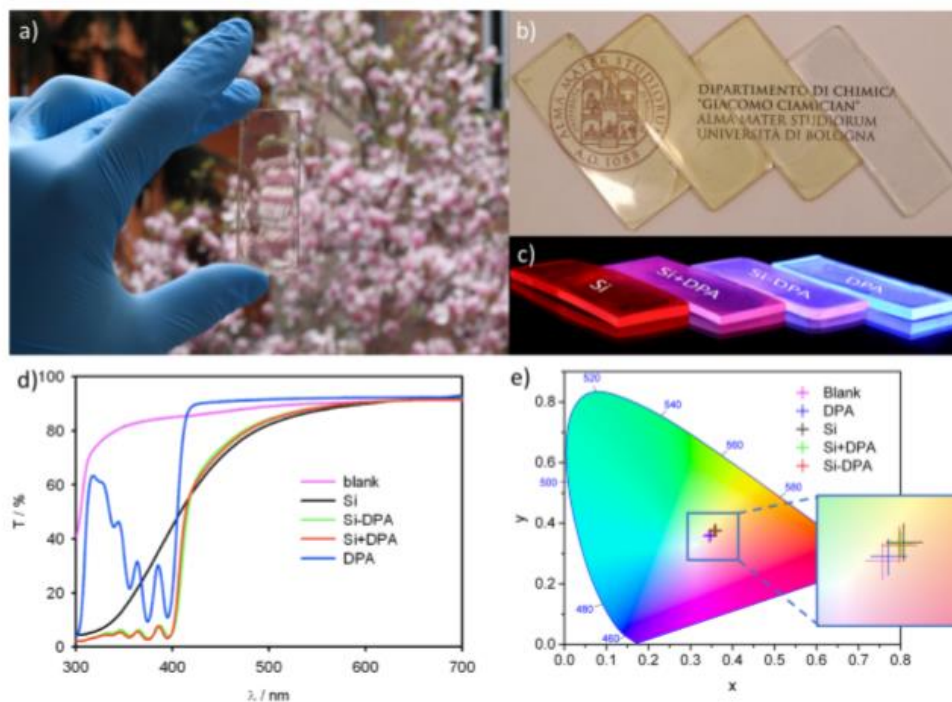
Figure 3.11- Digital picture of the SiNC-based LSCs under visible (**a,b**) and UV illumination (**c**). UV−vis transmittance spectra of the same LSCs (**d**) and CIE 1931 color space chromaticity diagram reporting the color coordinates of the SiNC-based LSCs (**e**). Panel (**b**) was reprinted with permission from the University of Bologna, Department of Chemistry "Giacomo Ciamician".

LSCs were obtained by thermal polymerization of an MMA/LMA monomer blend, in the presence of luminophores and EGDM as cross-linking agent (see chapter 3.3.5 for more details). LSCs based on different combinations of chromophores were prepared: (i) alkyl-capped SiNCs (**Si**), (ii) pure DPA chromophores (**DPA**), (iii) SiNCs covalently functionalized with DPA units (**Si-DPA**), and (iv) a physical mixture of SiNCs and DPA (**Si+DPA**) with the same absorptance as the covalent sample, in order to investigate the role of the covalent bond with respect to the LSC optical performance. The prepared LSCs are transparent and almost colorless (**figure 3.11 a** and **b**), but they display distinctive PL colors upon UV illumination

(**figure 3.11 c**). By comparing the absorption spectra in the low energy region (λ_{abs} = 600−700 nm), no evidence of aggregation is observed and the average transmittance is higher than 85% (**figure 3.11 d**), proving the excellent degree of transparency of the prepared polymer slabs and the lack of scattering centers. As previously observed in the solution phase, both the featureless absorption band of SiNCs and the structured DPA band are visible. The fraction of photons absorbed in the visible region of the solar spectrum $\eta_{abs\text{-}vis}$ (λ_{abs} = 400−700 nm, integrated from transmittance spectra on AM 1.5G spectrum, **table 1**) ranges from 13% of the blank sample, due to surface roughness and incident light trapping in the waveguide, to 27% of the Si sample. Since the absorptance is providing only limited information about the visual appearance of the semitransparent slab, we calculated the color coordinates and the Color Rendering Index (CRI) using the CIE 1931 chromaticity diagram (details are reported on the appendix A). The color coordinates of the LSCs (**table 1**) are located in the central region of the chromaticity diagram reported in **figure 3.11 e**), indicating good achromatic or neutral color sensations with only a small shift toward the yellow-orange region. The CRI values range from 99.0% for the blank sample to 96.8% for Si+DPA sample. No shift is observed upon addition of DPA, proving that the organic chromophore is only contributing to the absorption of the UV portion of the solar spectrum. These values lie in the color-rendering group 1, fulfilling the highest CIE requirements for indoor and outdoor illumination.

	$\eta_{abs\text{-}vis}$ (%)	x	y	CRI
blank	13	0.344	0.356	99.0
DPA	14	0.348	0.361	98.4
Si	27	0.360	0.376	97.0
Si+DPA	24	0.358	0.375	96.8
Si-DPA	24	0.357	0.374	97.0

Table 1- Absorption Properties (Fraction of Absorbed Photons in the Visible Range, λ_{abs} =400−700 nm) and Color Coordinates of the Prepared LSCs.

We then compared the PL properties of LSCs (**figure 3.12**): in all samples, the DPA band at 430 nm is significantly red-shifted with respect to the PL spectrum registered in solution (**figure 3.9 b**) and PLQY drops from 95% for DPA in solution[170] to 57% for DPA sample in the polymer matrix. Reabsorption of emitted light is responsible for both the red-shift and the decrease of PLQY: reabsorption processes are amplified in the LSC architecture by the long optical path in the polymeric waveguide compared to solution phase. A further drop of DPA fluorescence is observed in **Si-DPA** and **Si+DPA** samples. The strong drop in PL intensity in the **Si-DPA** sample was previously observed in solution and results from the non-radiative energy transfer process. On the contrary, the quenching of DPA PL in **Si+DPA** sample is related to a trivial energy transfer process. Indeed, due to the amplified reabsorption processes in the long optical path LSCs, there is a much larger probability for the light emitted by DPA to be reabsorbed by SiNCs. The mechanisms of the quenching processes are further confirmed by the analysis of the decay of DPA fluorescence intensity (**figure 3.13**): a shorter decay, corresponding to a lifetime of 2.5 ns, is observed for **SiDPA**, compatible with the presence of a new non-radiative process for the deactivation of the fluorescent excited state of DPA, while the **Si+DPA** sample exhibits a similar lifetime with respect to pristine **DPA**, about 8.5 and 7.2 ns, respectively. The SiNCs PL band at 750 nm is not significantly affected by embedding in the polymer matrix in terms of both shape and intensity: upon selective excitation of the Si core at 450 nm, PLQY is 43%, 45%, and 27% for **Si**, **Si+DPA**, and **Si-DPA**, respectively, values comparable to those measured in solution phase (45% for **Si** and **Si+DPA**, 26% for **Si-DPA**). Upon excitation at 375 nm, no difference in the emission intensity at 750 nm is observed for **Si**, **Si+DPA**, and **Si-DPA** (after normalization for the intrinsic PLQY drop for SiNCs, **figure 3.12**).
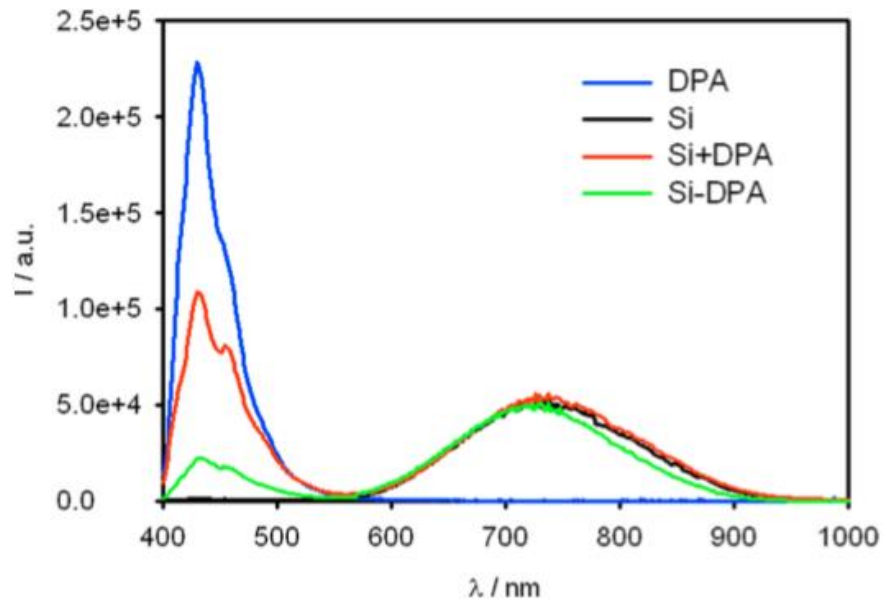
Figure 3.12- PL spectra of **Si** (black line), **DPA** (blue line), **Si+DPA** (red line), and **Si-DPA** (green line) measured inside an integrating sphere by excitation of the larger surface of LSCs at 375 nm. For the sake of comparison, the low energy band at 750 nm of **Si-DPA** was normalized on the PLQY of sample **Si**.
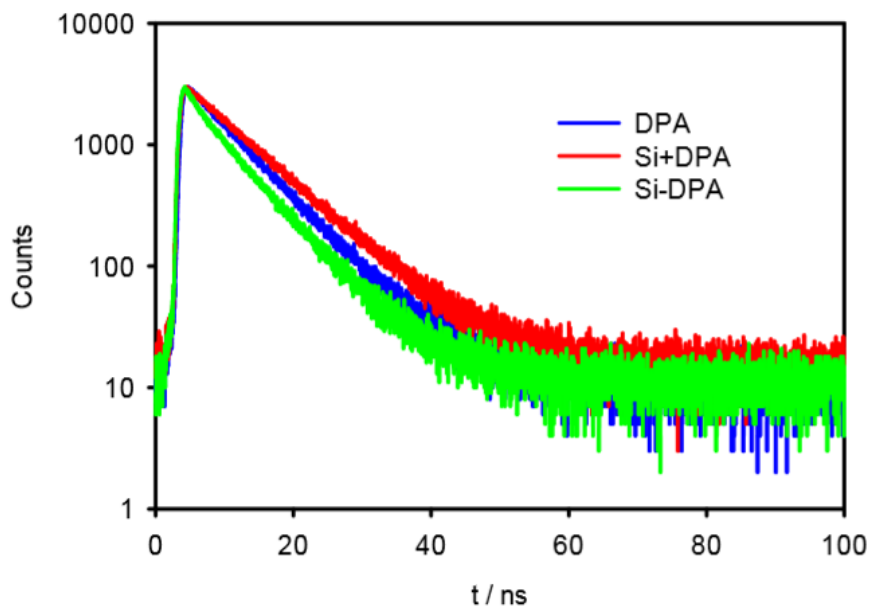
Figure 3.13- Time-resolved PL intensity of **DPA** in the prepared LSCs (λ_{exc}=375 nm, λ_{em}=410 nm) obtained in 45^0 configuration.

SiNCs PL intensity (upon excitation at 375 nm) is expected to be affected by two opposite effects: (i) the *inner filter effect* decreases the SiNCs luminescence intensity, that is, SiNCs absorbs a reduced amount of light in **Si+DPA** and **Si-DPA** samples with respect to Si sample because of the co-absorption of DPA chromophores; and (ii) the *energy transfer process* occurring for **Si+DPA** and **Si-DPA** samples increases the SiNCs luminescence intensity. The lack of observable PL intensity changes in **Si+DPA** and **Si-DPA** samples compared to the pristine **Si** sample proves that the two effects are counterbalanced. Consistently, by applying a mathematical correction for the inner filter effect (see appendix A for more details) to the registered spectra (**figure 3.14**), both **Si+DPA** and **Si-DPA** samples exhibit higher PL intensity with respect to the **Si** sample. This proves the sensitization of SiNCs PL by **DPA** in both samples with similar efficiency, despite the different energy transfer mechanism described in the previous section.
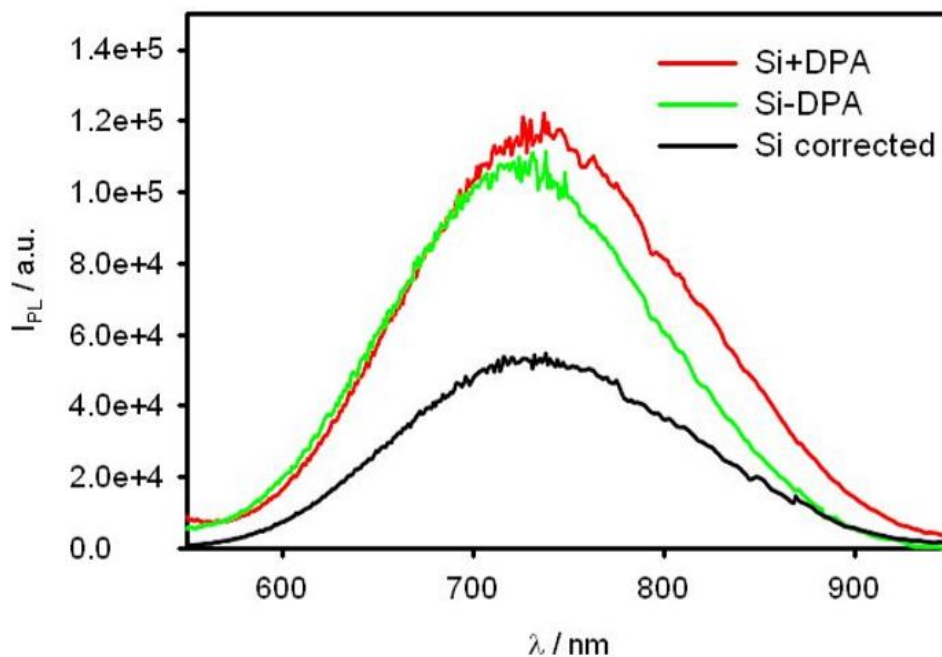
Figure 3.14- PL spectra of **Si+DPA** (red line) and **Si-DPA** (green line) measured inside an integrating sphere by excitation of the larger surface of LSCs at λ_{exc}=375 nm. **Si** sample PL (black line) is also reported for comparison, after applying the inner filter correction, as described in the text.

In order to get information about the optical efficiency of the LSC, we estimated the ratio of photons emitted from the edges of the LSC with respect to the ones emitted by the whole LSC device $\left(\frac{I_{edges}}{I_{tot}}\right)$, as previously reported by Coropceanu et al.[171] Upon excitation at 450 nm, where only the silicon core absorbs light, the ratio is about 74% for all samples containing SiNCs, a value close to the maximum theoretical efficiency of 75% predicted by Snell's law for a polyacrylate waveguide ($\eta_{TR} = \sqrt{\left(1 - \frac{1}{n^2}\right)} = 75\%$)[132]: this is a demonstration of (i) the scattering-free propagation of the emitted light in the polymer matrix, due to the optimal dispersion of the hybrid luminescent structure and the polymeric host, and (ii) lack of reabsorption, allowing an extremely high light trapping efficiency. Upon excitation at 375 nm, where the absorption contribution of **DPA** is at its maximum, **Si** has similar values to the one reported by exciting at 450 nm, while $\left(\frac{I_{edges}}{I_{tot}}\right)$ values decrease to 56% and 54% for **Si+DPA** and **Si-DPA** samples, respectively. This drop is related to reabsorption losses of DPA PL, much stronger than that of the Si core PL. Indeed, the DPA sample shows a much lower value of this ratio $\left(\frac{I_{edges}}{I_{tot}} = 31\%\right)$. Indeed, being the emission by randomly oriented DPA chromophores isotropic, the occurrence of multiple reabsorption and PL processes induces a randomization of the optical path followed by the emitted photons, and a consequent increased probability of photon losses from the top of the waveguide through the escape cone.[172] Further indication of this phenomenon can be assessed by comparing the PL spectra obtained from the edge of the LSC at increasing excitation distance (**figure 3.15**).
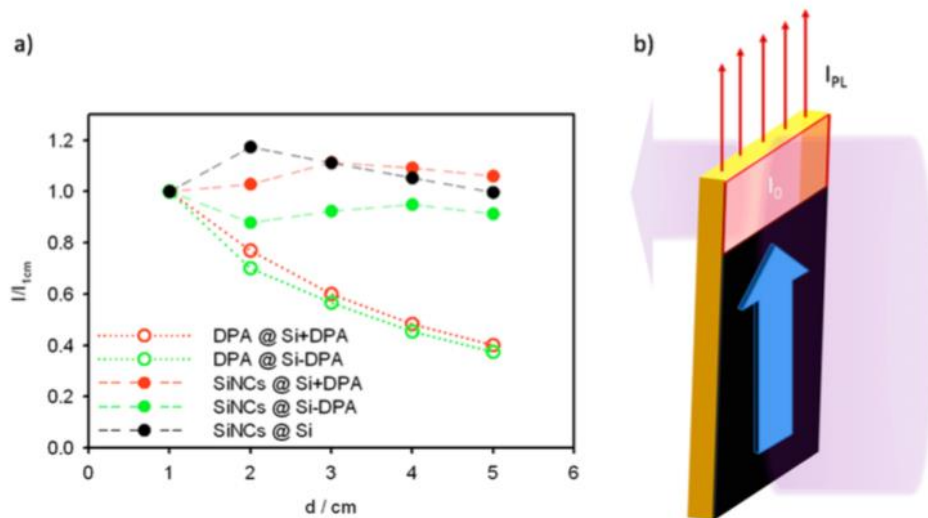
Figure 3.15- (a) Normalized emission intensities of **DPA** (λ_{em} = 400−550 nm, open symbols) and SiNC (λem = 550−900 nm, solid symbols) of **Si+DPA** (red), **Si-DPA** (green), and **Si** (black) as a function of the distance between the excitation area on the top of the polymer slab and the emission registered on one of the edges of the slab, as depicted in the schematic representation reported in **(b)**. The intensity was normalized to the illuminated area and to the emission intensity obtained at 1 cm from the excitation.

The shape of the SiNC emission band at 750 nm is not affected by the distance between the excitation spot on the top of the polymer slab and the emission registered on one edge of the slab in **Si-DPA** (**figure 3.16 a**), **Si+DPA** (**figure 3.16 b**), and **Si** (**figure 3.16 c**), whereas the **DPA** fluorescence band at 430 nm is strongly red-shifted upon increasing the distance between excitation and emission because of the above-discussed reabsorption phenomena.
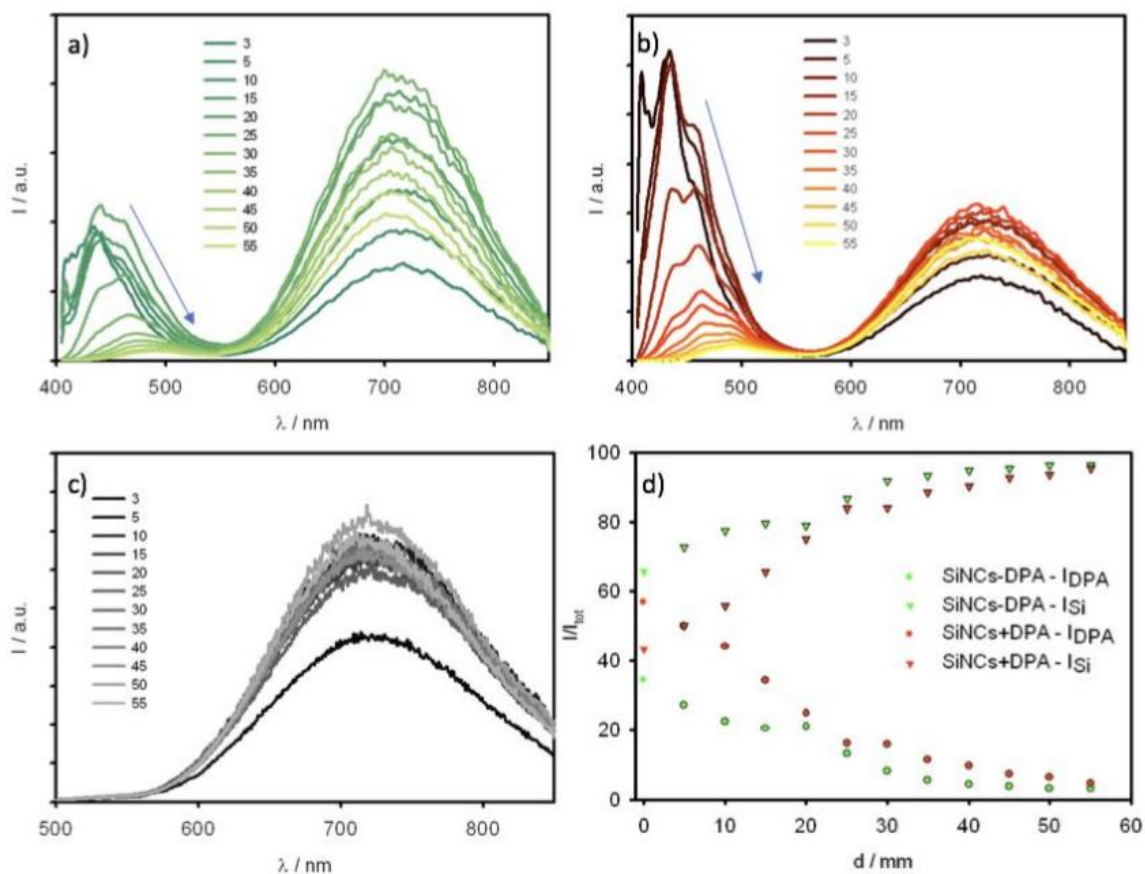
Figure 3.16- PL spectra of **a) Si-DPA**, **b) Si+DPA** and **c) Si** samples as a function of the distance between the excitation spot on the top of the polymer slab, and the emission area, located on one of the edges of the slab. The distance value is reported in the inset (mm). **d)** Integrated PL intensity values for SiNCs emission contribution (triangles, λ_{em} = 550-900 nm) and DPA´s emission contribution (circles, λ_{em} = 400-550 nm) obtained from spectra reported in **figure 3.17a** (green, **Si-DPA**) and **3.17b** (red, **Si+DPA**). X-axis reports distance between the excitation spot on the top of the polymer slab, and the emission area, located on one of the edges of the slab.

As far as intensity is concerned, the SiNCs PL band intensity is almost stable upon increasing the distance between excitation and detection (**figure 3.15**, solid symbols), while DPA PL intensity is dropping as a function of distance (**figure 3.15**, open symbols). By fitting this decreasing trend with an exponential curve, the

expected intensity value of DPA fluorescence after 20 cm of optical path is about 14% of the starting PL value extrapolated at 0 cm. The ratio between DPA and SiNCs PL intensity as a function of the distance between excitation and emission shows the sole contribution of SiNCs at large distances for both **Si+DPA** and **Si-DPA** samples (**figure 3.16 d**). A larger contribution of **DPA** PL in the low distance regime is visible for **Si+DPA**, while the **Si-DPA** sample is characterized by less variability across the distance range, since most of DPAs quenching process is non-radiative and does not depend on the optical path. The photostability of the LSCs was evaluated by irradiating the samples for 48 h with AM 1.5G simulated light: a relatively slow degradation both for DPA and SiNC PL contributions is observed for all the samples (**figure 3.17**). While the overall intensity drop is higher for SiNCs due to a faster initial degradation, SiNCs are more stable in the long term.
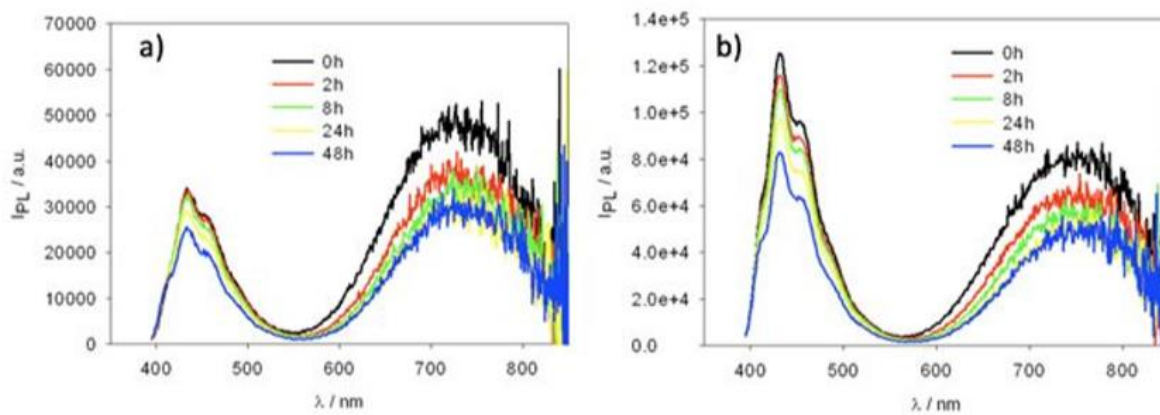
Figure 3.17- PL spectra of **a) Si-DPA**, **b) Si+DPA** under continuous AM 1.5G irradiation, to assess photostability.

Photovoltaic Performance

The photovoltaic performance of our LSCs was evaluated by placing a custom-sized Si−PV cell on one edge of the slab and letting the residual edges uncovered.

Irradiation was perpendicular to the slab surface with a conventional AM 1.5G solar simulator. We carried out a scan of the JV characteristic, from which we calculated the main PV parameters for the different samples, reported in **table 2**.

	G	J_{SC} (mA/cm^2)	V_{OC} (mV)	FF (%)	PCE (%)	η_{opt} (%)	$\eta_{opt,abs\text{-}vis}$ (%)
blank	2.86	1.31	382	54	0.27	1.04	
DPA	2.70	4.05	463	62	1.16	3.59	[b]
Si	2.64	4.14	452	60	1.12	3.54	25.7
Si+DPA	2.56	4.79	455	61	1.33	4.25	38.8
Si-DPA	2.98	4.05	440	59	1.05	3.08	28.1

[a]G factor and η_{opt} are also reported, as described in the main text. [b]DPA $\eta_{opt, abs\text{-}vis}$ was not calculated due to negligible absorption contribution in the visible region of the solar spectrum.

Table 2- Main PV Parameters extracted from JV characteristics of a Si−PV cell attached to one side of the prepared LSCs.

The shape factor, called G factor and defined as the ratio between the surface of the top of the slab and the edges surface, was calculated considering the surface of all edges as active (see appendix A for more details). The area of the concentrator, physically in contact with the cell surface, was considered for the estimation of the short circuit current density (J_{SC}). A comparison of the blank sample with the other samples evidence a slight increase in the open circuit voltage (V_{OC}) and the Fill Factor (FF) and a strong increase in J_{SC}, directly proportional to the increased emitted photon flux incident on the PV cell, resulting in a large enhancement of PCE values. The J_{SC} for the blank sample is not negligible due to the trapping of the incident light in the polymer waveguide, whose contribution, whereas minimal, cannot be fully avoided. Therefore, this value can be considered as a baseline for the evaluation of the optical efficiency of the other LSCs. **DPA** and **Si** samples display very similar results in terms of PCE, since the higher PLQY of **DPA** is counterbalanced by the lack of reabsorption of **Si**, achieving similar results on this

size scale. We expect much larger values for **Si** compared to **DPA** upon scaling up the devices to larger size. The **Si+DPA** sample is characterized by a PCE enhancement of about 15–20 % with respect to the pristine **DPA** and **Si** samples. On the opposite, the PCE of **Si-DPA** is slightly decreased because of the lower PLQY of the silicon nanocrystals, as discussed in the solution phase characterization. More information about the concentration efficiency of the LSC can be extracted from the optical efficiency (η_{opt}), defined as follows:[151]

$$\eta_{opt} = \frac{J_{LSC}}{J_{SC} \; x \; G}$$

where J_{LSC} is the current density of the PV cell coupled to the LSC (i.e., J_{SC} values reported in **table 2**), J_{SC} is the current density of the same cell under direct illumination, that is, 44 mA/cm^2 in our setup, and G is the previously described size factor. The trend is the same of that observed for PCE values with a minimum 3-fold enhancement factor with respect to blank sample. For comparison purposes, a previous paper on SiNC-based LSC reports[161] an η_{opt} = 2.85%, slightly lower than the one reported hereby for the reference **Si** sample, but in the same efficiency range. Again, **Si+DPA** sample exhibits a robust increase with respect to pristine **Si**, proving that the physical mixture of SiNCs and DPA allows for an enhancement of the LSC performance. This suggests that the **Si+DPA** non covalent approach is an effective strategy to enhance SiNCs performance in LSCs. The same trend is observed also applying the reshaping factor, as previously suggested,[148] in order to take into account the mismatch between PV cell EQE and PL spectra of the luminophores (see appendix A for more details). The largest increase in $\eta_{opt,q}$ is displayed by the DPA sample due to the poor match between c-Si EQE spectrum and PL band in the high-energy region of the visible spectrum, while smaller enhancement is observed for all samples containing SiNCs. This proves the superior spectral superposition between SiNC-based LSCs and the most employed conventional c-Si PV cells. On the other hand, while the covalent approach employed in **Si-DPA** does not positively influence optical efficiency and PCE, the

absolute value has to be evaluated as a function of the absorption properties and the PLQY of the luminophore. **Table 1** reports the fraction of photons absorbed in the visible region ($\eta_{abs\text{-}vis}$) by the different LSCs. We estimated the corrected optical efficiency $\eta_{opt,abs}$ by dividing η_{opt} by $\eta_{abs\text{-}vis}$. This value is different from the internal optical efficiency reported elsewhere, since it does only take into account the absorption contribution in the visible region. Therefore, its purpose is to compare performances of LSCs with different absorptances in the visible region, where the aesthetical and functional properties of the LSC are defined. Both **Si-DPA** and **Si+DPA** samples exhibit higher optical efficiency than **Si**, proving the enhancement related to SiNCs sensitization from the organic **DPA** chromophores. Interestingly, an enhancement was observed also for the **Si-DPA** sample, despite the lower PLQY resulting from the functionalization process, pointing out that the sensitization resulting from **DPA** absorbing in the UV region is able to compensate the detrimental drop of PLQY resulting from the synthetic procedure, in case of perfectly iso-absorbing SiNCs in the visible region. Finally, a comparison between the photovoltaic response of the prepared LSCs as a function of the distance between the PV cell and the excitation position was performed, by analogy with the optical characterization previously discussed (**figure 3.18**). The short circuit current density values measured for the samples containing SiNCs are basically constant across the LSC main axis, consistent with the behaviour discussed within the optical characterization and typical for LSCs based on reabsorption free luminophores. The absolute values are close, but a slight enhancement can be observed for the **Si+DPA** sample. On the other hand, in the case of the **DPA** sample, the maximum J_{SC} is achieved close to the PV cell, with even higher values with respect to SiNC-based LSCs, but these values are fading upon increasing the optical path. For comparison purposes, the J_{SC} value for the **DPA** sample at 3.5 cm is about 6.5× and 9× lower than **Si-DPA** and **Si+DPA** samples, respectively. Once again, this behaviour is the typical fingerprint of the reabsorption process for a low Stokes shift, highly luminescent organic luminophore, and demonstrated the superior properties of the hybrid

organic–inorganic material in real-size devices, where the typical panel size will largely exceed the one employed for this proof-of-concept study.
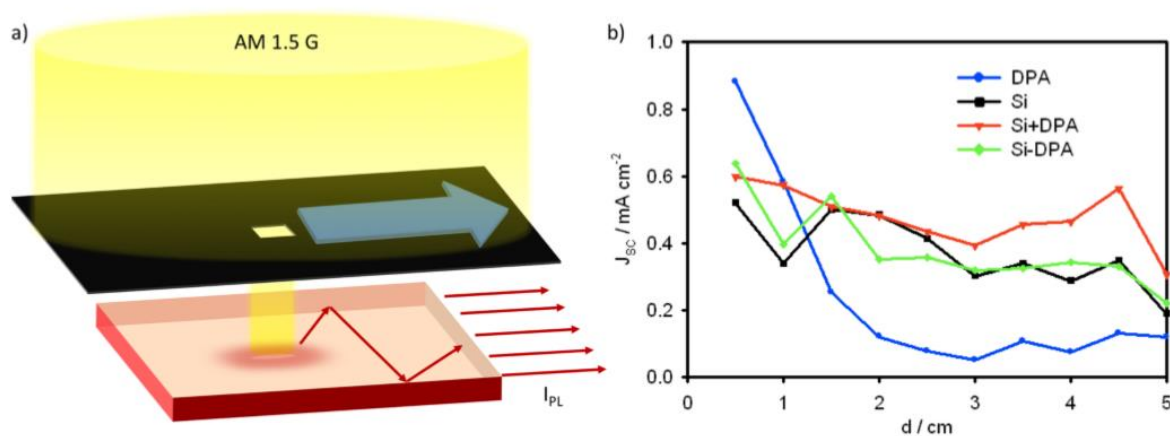
Figure 3.18- (a) Schematic representation of PV response of the prepared LSCs as a function of the distance between the excitation spot on the top of the polymer slab, and the PV cell, located on one edge of the slab. **(b)** Short circuit current densities, upon excitation of a $0.5{\times}0.5$ cm^2 area, as a function of the distance between the center of the excitation area and the PV cell. The contribution of direct excitation was removed by subtracting the reference values obtained with a blank polymer slab.[129]

3.5 Conclusions

We have realized the first example of LSC based on hybrid organic–inorganic silicon nanocrystals able to couple the absorption properties of an organic dye, namely, 9,10-diphenylanthracene, with reabsorption free luminescent SiNCs. The PL and photovoltaic properties were compared for LSCs based on (i) only the organic chromophore (**DPA**), (ii) only SiNCs (**Si**), (iii) a physical mixture of the two components (**Si +DPA**) and (iv) a covalent system (**Si-DPA**). The resulting LSCs are transparent and practical achromatic since DPA absorbs only in the UV region and the SiNC concentration was kept quite low. In the cases of **Si**, **Si+DPA**, and **Si-DPA**, a much larger fraction of emitted light is guided to the edges compared to **DPA**:

74% for **Si** and about 55% for **SiDPA** and **Si+DPA** compared to 31% for **DPA**. SiNC luminescence is not affected by reabsorption phenomena: the shape and intensity of their luminescence bands collected at the edges of LSC devices is practically the same as a function of the distance between excitation and emission compared to a strong red-shift and a decrease in intensity in the case of **DPA** luminescence. These parameters are very significant in view of the construction of much larger LSC devices where reabsorption losses strongly decrease LSC performances. The best performances are obtained for **Si+DPA** sample, demonstrating that coupling organic dyes and inorganic silicon nanocrystals is a promising route to enhance LSC performance. Furthermore, its optical and photovoltaic performances are superior also with respect to the covalent system **Si-DPA** because of the decreased PLQY of the Si core upon covalent functionalization. In the **Si+DPA** LSC, a trivial energy transfer mechanism, enhanced by the long optical path typically encountered in LSC devices, minimizes the loss due to self reabsorption of DPA luminescence. Optical efficiency as high as 4.25% is achieved with this device architecture without affecting the optimal aesthetic properties of the device, whose high CRI values allow for the utilization of this class of LSCs as solar windows for indoor illumination. This proof of concept opens the way to a new class of hybrid luminophores for LSCs delivering tailored optical properties and high efficiency.

4 Water-Soluble Silicon Nanocrystals as NIR Luminescent Probes for Time-Gated Biomedical Imaging

The contents of this chapter have been reprinted and adapted from Ref. Romano, F., Angeloni, S., Morselli, G., Morandi, V., Shell, J.R., Cao, X., Pogue, W., and Ceroni, P. (2020). Water-soluble silicon nanocrystals as NIR luminescent probes for time-gated biomedical imaging, Nanoscale, with permission from The Royal Society of Chemistry.

4.1 Introduction

Luminescence (usually fluorescence) imaging is an emerging technique in biomedicine.[173–176] It is a niche compared to tomographic techniques (CT, MRI, PET), which rely on deep penetrating radiation and are widely employed in clinical practice today. However, fluorescence imaging offers advantages in terms of high temporal (real-time) acquisition and use of non-hazardous optical excitation. The main drawback is the limits of penetration depth: it is impossible to image through more than a few centimetres of tissue, so that optical imaging will never replace diagnostic radiology techniques in the human body, but it can be used for guiding surgery:[177–180] For example, it is widely used in assessment of vascular flow in grafted tissues, tumour localisation (usually in skin, head, neck or breast cancer), sentinel-lymph node removal. Currently, a lot of work is devoted towards NIR luminescence imaging because of reduced scattering of excitation light, minimal absorption and negligible auto-fluorescence by tissues, affording a higher signal to noise ratio and contrast. In particular, NIR-II chromophores[174,181,182] and lanthanide nanoparticles[183,184] with absorption and emission in the so-called NIR-II spectral

region (usually defined as 1000-1700 nm) are gaining wider use to increase image resolution and contrast. Time-gated detection coupled to NIR emission represents a further improvement in terms of signal-to-noise ratio and image contrast. The utilization of time-gated luminescence, in which luminescence is recorded with a certain delay after excitation, suppresses scattered excitation light and short-lived auto-fluorescence of the sample. Until now, lanthanide metal complexes, up-converting nanoparticles[185–187] and heavy-metal complexes, such as Pt or Pd have mostly been employed for this application with μs-gating window, a time scale that allows easy implementation and low cost of the equipment.[188–190] SiNCs were already employed in luminescence imaging, for example in sentinel lymph node mapping,[191] but time-gated detection has not been explored. Time-gated luminescence was reported for a different silicon-based material, namely porous silicon nanoparticles, to image cells, organs or zebrafish.[192–194] However, the dimension of the silicon core was much larger (>100 nm), the emission quantum yield was significantly lower (ca. 5%), sensitive to dioxygen quenching and limited to the visible region (red emission). In the following chapters, we demonstrate that SiNCs are viable alternatives for in vivo time-gated luminescence imaging in the NIR spectral window.

The main challenge to be addressed for biological applications of SiNCs is the coupling of bright long-lived luminescence with colloidal stability in water: aqueous environment facilitates (photo)oxidation of SiNC surface that brings about emission quenching. Until the current study, the main approaches reported to make water dispersible SiNCs are: (i) encapsulation within a water-soluble carrier, such as amphiphilic polymers,[195] solid lipid nanoparticles[196] and micelles or liposomes,[191,197–200] (ii) direct grafting of water solubilising polymers at SiNC surface, such as polyethylene glycol,[99,201,202] poly(acrylic acid),[98,203] (iii) surface functionalisation with highly polar moieties, such as carboxylic acids[109,204,205] and ammonium groups,[206] or biomolecules.[100,207,208] Most of these approaches suffer from

formation of nano-aggregates containing multiple SiNCs and poor luminescence properties compared to SiNCs dispersed in organic solvents. Herein we describe three different synthetic paths: (i) a three-step synthetic protocol involving a thiol-ene click-reaction,[101,209,210] yielding SiNCs covalently functionalised only with PEG chains, (ii) a direct hydrosilylation reaction with a double bond terminated PEG chain and (iii) a two-step synthetic path involving an amide bond formation. These pegylated protective shells provide colloidal stability in water and protect SiNCs from interactions with serum proteins, like albumin, while keeping bright luminescence. The novelty and advantages of the presented synthetic approaches are the following: (i) they can be applied to SiNCs of different size, e.g., average core diameter of 4 or 5 nm; (ii) the reaction procedures occur at low temperature (T ≤ 70°C); (iii) a low amount of PEG derivative is required in the last functionalisation step, considering the two approaches which require more than just one step; (iv) the resulting SiNCs are colloidally stable in water, not affected by surface photo-oxidation and display bright long-lived luminescence, insensitive to dioxygen and solvent quenching. The obtained SiNCs exhibit unique optical properties compared to molecular fluorophores: (i) emission energy tuneable to the red and NIR spectral region, compatible with the biological window; (ii) high photoluminescence quantum yield; (iii) no sensitivity to molecular oxygen; (iv) long-lived luminescence decay in the hundreds of μs, enabling time-gated detection. Therefore, they are ideal candidates as luminescent probes for biomedical imaging.

4.2 Achieving Water-Dispersibility via Covalent Functionalization of SiQDs with PEG Chains

4.2.1 PEG-Passivated SiNCs by Thiol-Ene Click Reaction[101]

Synthesis of allyl functionalized SiNCs
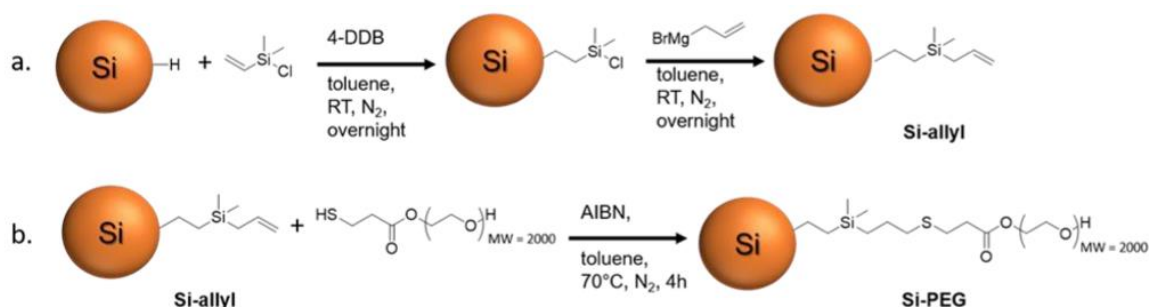
Figure 4.1- Synthetic procedure for the functionalization of hydride-terminated SiNCs by allyl groups (a, **Si-allyl**) and post-functionalization via thiol-ene click reaction by **PEG** groups (b, **Si-PEG**)

Chlorosilane terminated SiNCs were prepared by adding 0.2 mL (1.5 mmol) of dimethylvinylchlorosilane (DMVSiCl) to the hydride-terminated SiNCs dispersion, obtained after the etching procedure of 100 mg of oxide-embedded SiNCs powder, in the presence of ca. 1.5 mg of 4-decylbenzene diazonium tetrafluoroborate (4-DDB).[57] The solution became transparent after few minutes and the reaction was stirred overnight, at room temperature in a nitrogen-filled glove box, in order to completely passivate the surface of SiNCs. The solution was finally dried under vacuum to remove DMVSiCl in excess, then refilled with anhydrous toluene and kept under inert atmosphere. Allyl terminated nanocrystals (**figure 4.1a**) were prepared through the Grignard nucleophilic addition to the chlorosilane passivated SiNCs.[211] In particular, 0.2 mL of allyl magnesium bromide (1 M solution in diethyl ether) was added to the chlorosilane passivated SiNCs solution and left stirring overnight inside the glove box at room temperature. While the addition of the Grignard reagent results in a turbid solution for 5 nm SiNCs, no significant effect

was observed on the 4 nm nanocrystals other than the quenching of the typical red emission under UV light excitation. The samples were then extracted from the glove box and acidified MeOH (0.5mL HCl in 20 mL of MeOH) was added to quench the residual Grignard and precipitate the nanocrystals. The dispersion was then precipitated and washed three times with MeOH, then dissolved again in toluene and stored in vials for further use. The 4 nm diameter SiNCs characteristic red emission was restored. Proton NMR measurements of **Si-allyl** were conducted and proton signals from the double bonds appeared around 6 ppm confirming the functionalization (**figure 4.2 a**).[128]

Synthesis of thiolated-PEG through esterification

Thiolated poly(ethylene glycol) (**PEG-SH**) was prepared as follows:[212] 4.4 g of poly(ethylene glycol), MW=2000 (**PEG**) was introduced in a three-necked flask equipped with a stirrer and a condenser. 50 mL of dry toluene were added to dissolve the **PEG**, then 261 µL (3 eq.) of 3-mercaptopropionic acid and few drops of fuming sulfuric acid were added. The flask was heated to reflux with an oil bath overnight, under nitrogen atmosphere. The reaction was checked with a TLC and cooled to room temperature. The reaction solution was concentrated under vacuum and then diethyl ether was added to precipitate the product. The product was then transferred on a Gooch filter and washed three times with diethyl ether, dried under vacuum and collected as a white waxy solid of 1.4 g (yield 32%). ^{1}H-NMR (400 MHz, CDCl$_3$) δ 4.26 – 4.23 CH$_2$O (m, 2H), 3.62 CH$_2$CH$_2$O (s, 200H), 2.75 CH$_2$SH (m, 2H), 2.66 CH$_2$CO (t, J = 7.3 Hz, 2H), 1.66 SH (t, J = 8.3 Hz, 1H) (**figure 4.2 c**).

Synthesis of PEG-Functionalised SiNCs by thiol-ene click reaction[202]

A batch of **Si-allyl** was dissolved in 10 mL of toluene, then 1 g of **PEG-SH** was added (**Figure 4.1b**). When the **PEG-SH** is completely dissolved, 15 mg of AIBN

(azobisisobutyronitrile) was added to start the thiol-ene click reaction. The solution was purged with nitrogen for 20 min under ultrasonication to remove oxygen traces and then heated for 4h to 70°C. After cooling to room temperature, the suspension became slightly turbid. The sample was dried under vacuum, suspended in ethanol, then dried again and dissolved in distilled water (DW). The ethanol addition is essential to maintain the colloidal stability of the resulting sample. A drastic change in solvent polarity from toluene to DW might induce aggregation of functionalized SiNCs. The excess **PEG-SH** and the residual AIBN were removed by both dialysis (RC dialysis tube, Millipore, MW cut off=14000) and high-pressure filtration (RC filter, Amicon® Stirred Cells, MW cut-off=14000). Finally, the sample was filtered over 0.22 µm RC syringe filter and stored at room temperature. Slight aggregation occurs over the course of several weeks in concentrated solution, but not in diluted solutions (10^{-4} – 10^{-5} M). ^{1}H-NMR spectrum of **Si-PEG** shows new signals of methylene protons in proximity to the thiol-ether group, which is formed upon click reaction between **Si-allyl** and **PEG-SH**. ^{1}H-NMR (400 MHz, CDCl$_3$) δ 4.17 (m, 2H), 3.59 (m, 186H), 2.83 (m, 2H), 2.66 (m, 2H), 2.56 (t, 2H), 1.63 (m, 2H) (**figure 4.2 b**).
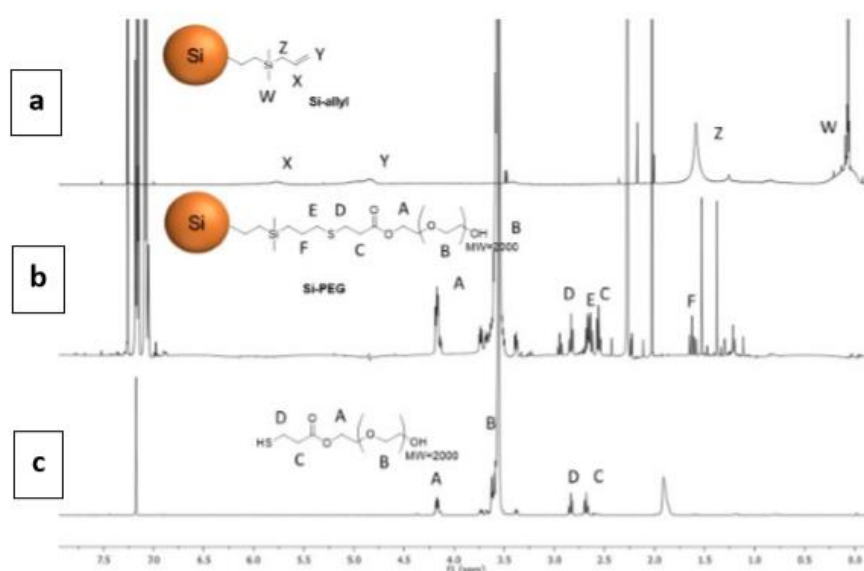
Figure 4.2- NMR spectra (400 MHz, CDCl$_3$) of (a) **Si-allyl**, (b) **Si-PEG** and (c) **PEG-SH**

Figure 4.2 shows the NMR spectra of **Si-allyl** (a), **Si-PEG** (b) and **PEG-SH** (c). It is possible to observe that the signals related to the vinyl protons (indicated as **X** and **Y**) are present only in double bond functionalized SiNC, fading after the click reaction. Moreover, in **Si-PEG** spectrum, the signals of the ligand are preserved but broadened due to the molecules low mobility at the nanoparicles surface resulting in a longer relaxation time.[128,129]

4.2.2 PEG-Passivated SiNCs by Direct Hydrosilylation

Synthesis of 11-(poly(ethylene glycol)) methyl ether undec-1-ene[213]

Figure 4.3- reaction scheme for the synthesis of alkene-terminated PEG with average M_n= 550

Alkene-terminated poly(ethylene glycol) with average M_n= 550 (**PEG$_{550}$DB**) was prepared as follows: 10 g of poly(ethylene glycol) methyl ether MW=550 (18 mmol, 1.4 eq; **PEG$_{550}$**) was introduced in a two-necked round-bottom flask equipped with a stirrer and a condenser. Oxygen was removed with three nitrogen-vacuum cycles and then an inert atmosphere was left inside the flask. **PEG$_{550}$** was dissolved by adding 25 mL of dry tetrahydrofuran (THF); when it was completely solubilized 1 g of NaH (45 mmol, 3.5 eq) was added to the reaction mixture and H$_2$ gas liberation was immediately observed via bubbles formation in a grey reaction mixture. The flask was then heated up to THF reflux temperature with an oil bath and left under stirring and under nitrogen atmosphere for 30 minutes. 2.8 mL of 11-Bromo-1-

undecene 95% (13 mmol, 1 eq) were then inserted and the solution become yellowish with NaBr precipitation. The reaction mixture was left under reflux, under nitrogen atmosphere and under stirring for 24 hours. Thus, it was checked with a TLC and cooled to room temperature. The reaction was concentrated under vacuum, quenched with distilled water (10 mL) and then extracted with Ethyl Acetate (3x150 mL). The organic fractions were collected, dried over $MgSO_4$, filtered and dried under vacuum. Therefore, a flash chromatography (eluent with a polarity gradient using toluene, ethyl acetate and methanol) was performed to isolate 3 g of product, (30% yield) (**figure 4.3**). ^{1}H-NMR (400 MHz, $CDCl_3$) δ 5.66 (m, 1H), 4.85 (d, 1H), 4.79 (d, 1H), 3.51 (m, 44H), 3.23 (s, 3H), 2.64 (t, 2H), 1.9 (m, 2H), 1.10-1.26 (m, 14H).

Synthesis of 11-(poly(ethylene glycol)) undec-1-ene[213]
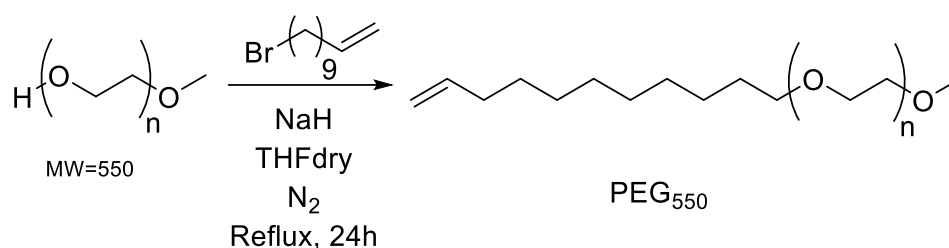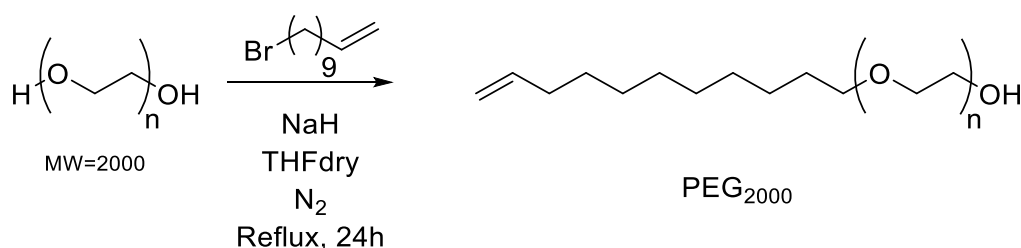

Figure 4.4- reaction scheme for the synthesis of alkene-terminated PEG with average M_n= 2000

Alkene-terminated poly(ethylene glycol) with average M_n= 2000 (**PEG₂₀₀₀DB**) was prepared as follows: 15 g of poly(ethylene glycol) MW=2000 (7.5 mmol, 1.4 eq; **PEG₂₀₀₀**) was introduced in a two-necked round-bottom flask equipped with a stirrer and a condenser. Oxygen was removed with three nitrogen-vacuum cycles and then an inert atmosphere was left inside the flask. **PEG₂₀₀₀** was dissolved by adding 55 mL of dry THF; when it was completely solubilized 0.4 g of NaH (19 mmol, 3.5 eq) was added to the reaction mixture and H_2 gas liberation was immediately observed via bubbles formation in a grey reaction mixture. The flask

was then heated up to THF reflux temperature with an oil bath and left under stirring and under nitrogen atmosphere for 30 minutes. 1.2 mL of 11-Bromo-1-undecene 95% (5.4 mmol, 1 eq) were then inserted and the solution become yellowish with NaBr precipitation. The reaction mixture was left under reflux, under nitrogen atmosphere and under stirring for 24 hours. Thus, it was checked with a TLC and cooled to room temperature. The reaction was concentrated under vacuum, quenched with distilled water (10 mL) and then extracted with Ethyl Acetate (3x120 mL). The organic fraction was collected, dried over $MgSO_4$, filtered and dried under vacuum. Therefore, a flash chromatography (eluent with a polarity gradient using toluene, ethyl acetate and methanol) was performed to isolate 3.5 g of product (23% yield) (**figure 4.4**). ^{1}H-NMR (400 MHz, $CDCl_3$) δ 5.78 (m, 1H), 4.98 (d, 1H), 4.90 (d, 1H), 3.55 (m, 180H), 3.06 (t, 2H), 2.00 (m, 2H), 1.24-1.35 (m, 14H).

Synthesis of tert-butyl 10-undecenoate

Tert-butyl 10-undecenoate was prepared as follows: 10-undecenoic acid (3.3 g, 18 mmol), tert-butanol (3 mL, 30 mmol), DMAP (670 mg, 5.5 mmol) and DCC (5 mg in 40 mL of $CHCl_3$, 24 mmol) were added to a one-neck round-bottom flask. The reaction mixture was stirred two days in air and at room temperature. Therefore, the reaction was checked with a TLC and then it was filtered with a Buchner funnel, washed with distilled water and purified by a flash chromatography, using toluene as the eluent, to isolate 2.64 g of product (80% yield). ^{1}H-NMR (400 MHz, $CDCl_3$) δ 5.78 (m, 1H), 4.99 (d, 1H), 4.90 (d, 1H), 2.20 (t, 2H), 2.05 (m, 2H), 1.58 (dd, 2H), 1.43 (s, 9H), 1.36-1.27 (m, 12H).

Synthesis of SiNCs functionalized with 11-(poly(ethylene glycol)) methyl ether undec-1-ene[214] and dodecene

Figure 4.5- Photo-initiated hydrosilylation procedure for the functionalization of hydride-terminated SiNCs by alkene-terminated PEG and DDE

A batch of 4 nm diameter hydride-terminated SiNCs, obtained after the etching procedure of 100 mg of oxide-embedded SiNCs powder, was dissolved in 2 mL of dodecene (**DDE**; 9 mmol, ca. 70%) and then 4.7 mmol of 11-(poly(ethylene glycol)) methyl ether undec-1-ene (average M_n,=550; **PEG$_{550}$DB**; ca. 30%) were added, together with 5-10 mg of the photo-initiator diphenyl(2,4,6-trimethylbenzoyl)phosphine oxide (TPO) (**figure 4.5**). The reaction mixture was transferred in a 10 mL two-necked round bottom flask and oxygen was removed trough 3 freeze-pump cycles. The reaction was stirred for 2 hours at room temperature, under inert atmosphere, irradiating with a 365 nm emitting LED, where TPO has a high molar absorption coefficient (see chapter 2.3.3 for more details). At the end of the reaction, the turbid sample was filtered over 0.45 μm PTFE syringe filter, in order to remove the un-reacted and precipitated SiNCs from the dispersion, and then it was purified from the un-reacted ligands by a size exclusion chromatography (SEC), using Biobeads™ S-X1 Support (200-400 mesh) as the solid phase and chloroform as the liquid phase. Thus, the sample was dried under vacuum, suspended in ethanol, then dried again and dissolved in distilled water (DW). The ethanol addition is essential to maintain the colloidal stability of the resulting sample, indeed, as we have already seen, a drastic change in solvent polarity from chloroform to DW might induce aggregation of functionalized SiNCs.

Furthermore, the excess **PEG₅₅₀DB** and the residual TPO were also removed by dialysis (RC dialysis tube, Millipore, MW cut off=14000). Finally, the quasi-transparent, red-emitting, colloidal solution of **Si-PEG₅₅₀** was stored at room temperature.

Synthesis of SiNCs functionalized with 11-(poly(ethylene glycol)) undec-1-ene and 10-undecenoic acid

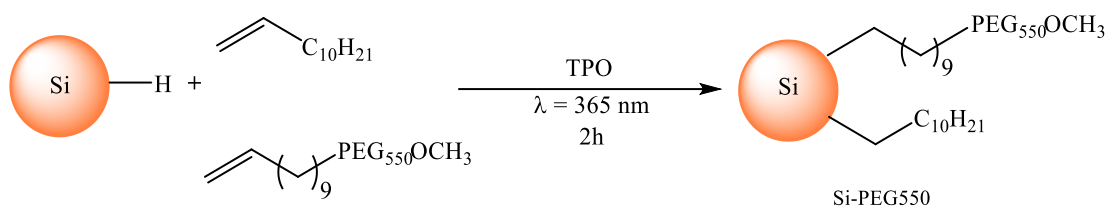**Figure 4.6**- diazonium salt initiated hydrosilylation procedure for the functionalization of hydride-terminated SiNCs by alkene-terminated PEG (M_n= 2000) and tert-butyl 10-undecenoate.

A batch of 4 nm diameter hydride-terminated SiNCs, obtained after the etching procedure of 400 mg of oxide-embedded SiNCs powder, was dissolved in 10 mL of dry toluene inside a nitrogen-filled glove box. The sample was divided in three different vials and different percentages of tert-butyl 10-undecenoate and 11-(poly(ethylene glycol)) undec-1-ene (**PEG₂₀₀₀DB**) were added to each vial. Respectively, 257 mg of tert-butyl 10-undecenoate (1.07 mmol, 90%) and 266 mg of **PEG₂₀₀₀DB** (0.12 mmoli, 10%) were added to the first vial (**Si-(10%)PEG₂₀₀₀**) , 242 mg of tert-butyl 10-undecenoate (1 mmol, 85%) and 400 mg of **PEG₂₀₀₀DB** (0.18 mmoli, 15%) were added to the second vial (**Si-(15%)PEG₂₀₀₀**) and 228 mg of tert-butyl 10-undecenoate (0.95 mmol, 80%) and 532 mg of **PEG₂₀₀₀DB** (0.25 mmoli, 20%) were added to the third vial (**Si-(20%)PEG₂₀₀₀**). 2 mg of the radical initiator 4-DDB was

added to each one, together with a magnetic stirrer. The three reaction mixtures were stirred under inert atmosphere and at room temperature overnight (**figure 4.6**). The turbid solutions started to appear transparent 15-20 minutes after having added the radical initiator, clear evidence of the started hydrosilylation reaction. Therefore, the products were filtered over 0.45 μm PTFE syringe filter to remove the un-reacted and precipitated SiNCs from the solution (if any), concentrated under vacuum and isolated from the un-reacted ligands and 4-DDB by a size exclusion chromatography (SEC), using Biobeads™ S-X1 Support (200-400 mesh) as the solid phase and distilled chloroform as the liquid phase. The first collected fraction from the SEC is the product. Trifluoroacetic acid was added to each product in chloroform (1/3 of the final volume solution) and the reactions were stirred at room temperature, under air, for 4 hours. Trifluoroacetic acid is commonly used to remove the tert-butyl protecting group. Therefore, the solutions were concentrated under vacuum, suspended in ethanol, then dried again and dissolved in distilled water (DW). The ethanol addition is essential to maintain the colloidal stability of the resulting sample, indeed, as we have already seen, a drastic change in solvent polarity from chloroform to DW might induce aggregation of functionalized SiNCs. Furthermore, the excess **PEG₂₀₀₀DB** and the eventually residual reagents were also removed by dialysis (RC dialysis tube, Millipore, MW cut off=14000). Finally, the transparent, red-emitting, colloidal solutions of **Si-(10%)PEG₂₀₀₀**, **Si-(15%)PEG₂₀₀₀** and **Si-(20%)PEG₂₀₀₀** were stored in a fridge in order to avoid mold formation.

4.2.3 PEG-Passivated SiNCs by Amide Bond Formation

Synthesis of SiNCs functionalized with dodecene and 10-undecenoic acid

SiNCs passivated with dodecyl chains and 10-undecenoic acid were synthesized by following an adaptation of a literature procedure[109,215]:

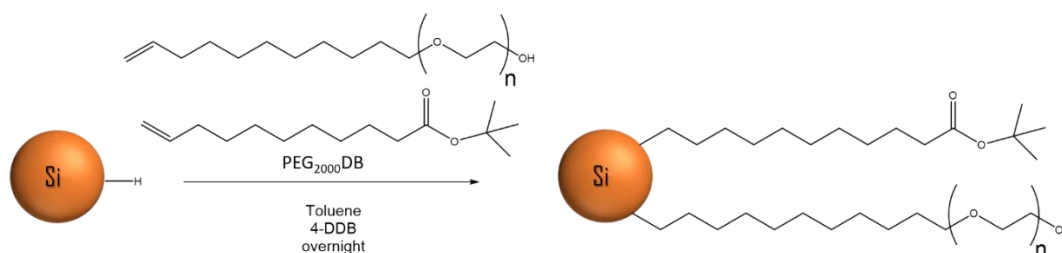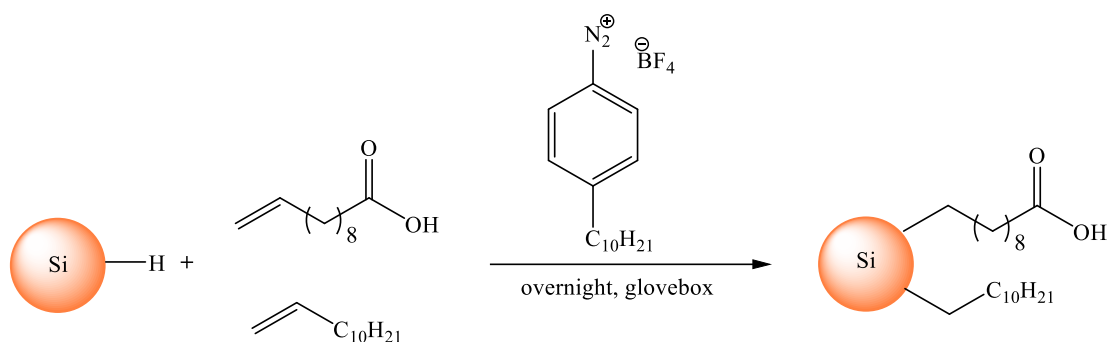**Figure 4.7-** diazonium salt initiated hydrosilylation procedure for the functionalization of hydride-terminated SiNCs by dodecene and 10-undecenoic acid

A batch of 4 nm diameter hydride-terminated SiNCs, obtained after the etching procedure of 400 mg of oxide-embedded SiNCs powder, was divided in three different vials and different percentage of dodecene and 10-undecenoic acid were added to each one inside a nitrogen-filled glove box. The two molecules have been used both as the ligands and as the solvent. Respectively, 2.7 mL of DDE (12 mmol, 90%) and 0.3 mL of 10-undecenoic acid (1.5 mmoli, 10%) were added to the first vial, 2.1 mL of DDE (9.5 mmol, 70%) and 0.9 mL of 10-undecenoic acid (4.5 mmoli, 30%) were added to the second vial and 1.8 mL of DDE (8.1 mmol, 60%) and 1.2 mL of 10-undecenoic acid (5.9 mmoli, 40%) were added to the third vial. 2 mg of the radical initiator 4-DDB were added to each vial, together with a magnetic stirrer. The three reaction mixtures were stirred under inert atmosphere and at room temperature overnight (**figure 4.7**). The turbid solutions started to appear transparent 15-20 minutes after having added the radical initiator, clear evidence of the started hydrosilylation reaction. Therefore, the products were filtered over 0.45 µm PTFE syringe filter to remove the un-reacted and precipitated SiNCs from the solution (if any), concentrated under vacuum and isolated from the un-reacted ligands and 4-DDB by a size exclusion chromatography (SEC), using Biobeads™ S-X1 Support (200-400 mesh) as the solid phase and distilled chloroform as the liquid phase. The

first collected fraction from the SEC is the product, **Si-COOH**. Therefore, the solutions were dried under vacuum and suspended in ethanol. Only the products with 30 and 40% of 10-undecenoic acid were found to be dispersible in a solvent as polar as ethanol, even though, these ligands are not polar enough to make a stable and durable SiNCs suspension in water. ^{1}H-NMR for the DDE 60% 10-undecenoic acid 40% sample (400 MHz, CD$_3$OD): δ=0.86 ppm (bs, 3H); δ=1.2-1.4 ppm (bs, 22H); δ=2.28 (bs, 1.22H). The chemical shifts confirm a ratio of the two ligands on the SiNCs surface equal to the ratio used during the hydrosilylation reaction, DDE 60% and 10-undecenoic acid 40%.

Synthesis of SiNCs functionalized with poly(ethylene glycol) methyl ether amine

Starting from SiNCs functionalized with DDE 70% and 10-undecenoic acid 30%, poly(ethylene glycol) methyl ether amine (average Mn=750) was introduced in a second reaction step in order to obtain a new amide bond.
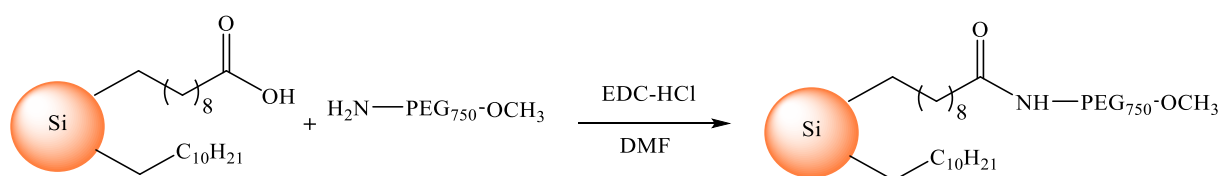
Figure 4.8- reaction scheme for the functionalization of the SiNCs surface with poly(ethylene glycol) methyl ether amine chains

DDE 70% and 10-undecenoic acid 30% functionalized SiNCs were dried under vacuum, dispersed in 2 mL of DMF and introduced inside a one-neck round-bottom flask together with a magnetic stirrer. 0.15 mmol of poly(ethylene glycol) methyl ether amine (average Mn=750) where then added to the reaction mixture. The solution was cooled down to 0°C and, under continuous stirring, 0.16 mmol of the coupling reagent N-(3-Dimethyaminopropyl)-N′-ethylcarbodiimide hydrochloride

(EDC-HCl) were added. Thus, the reaction mixture was stirred at 0°C for 30 minutes, then it was heated to room temperature and left stirring overnight (**figure 4.8**). Therefore, the product was filtered over 0.45 μm PTFE syringe filter to remove the un-reacted and precipitated SiNCs from the solution, concentrated under vacuum and isolated from the un-reacted ligands by a size exclusion chromatography (SEC), using Biobeads™ S-X1 Support (200-400 mesh) as the solid phase and distilled chloroform as the liquid phase. The first collected fraction from the SEC is the product. Therefore, the solution was concentrated under vacuum, suspended in ethanol, then dried again and dissolved in distilled water (DW). The ethanol addition is essential to maintain the colloidal stability of the resulting sample, indeed, as we have already seen, a drastic change in solvent polarity from chloroform to DW might induce aggregation of functionalized SiNCs. The transparent red-emitting colloidal solution, **Si-NH-PEG$_{750}$** was then stored at room temperature.

4.3 Results and Discussions

4.3.1 PEG-Passivated SiNCs by Thiol-Ene Click Reaction

TEM measurements

The size distribution of the so-called 5 nm diameter **Si-PEG** was evaluated by TEM analysis (**figure 4.9 a**) and is compatible with the corresponding so-called 5 nm diameter dodecyl-terminated sample (**figure 4.9 b**) and others previously reported samples of alkyl-terminated SiNCs prepared by the same methodology.[106,216,217]

The **Si-PEG** TEM characterization is also showing the presence of nanocrystals embedded in an amorphous matrix, which is consistent with the presence of the polymeric ligand. SiNCs diameter is (4.9 ± 1.2) nm, as displayed by the lognormal fitting of the size distribution displayed in **figure 4.9 a**. In addition, the EDS

spectrum clearly shows an increasing amount of oxygen with respect to SiNCs passivated with simple dodecyl chains, sample available from previous work.[216]
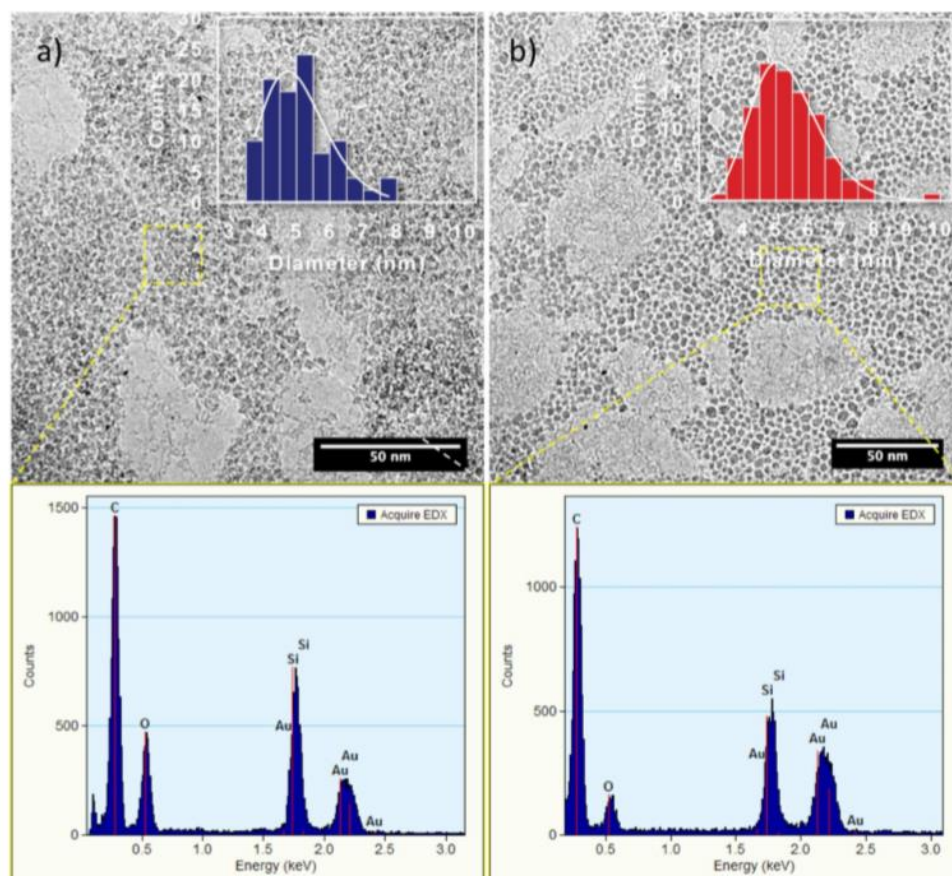
Figure 4.9- TEM micrograph (top) of **Si-PEG** (a) and SiNCs passivated with dodecyl chains (b), and corresponding EDS spectra (bottom) acquired on an area of the sample covered by SiNCs, as highlighted in the micrograph. Size distribution for both samples is displayed in the insets. The estimated nanocrystal diameter is: (4.9 ± 1.2) nm (a) and (5.1 ± 1.1) nm (b).

Photophysical properties

The absorption spectra of **Si-PEG** exhibit an unstructured absorption profile that is characteristic of SiNCs (solid lines in **figure 4.10 a**).[47,164] The photophysical data reported in **table 4.1** for **Si-allyl** and **Si-PEG** in toluene demonstrate that the radiative transition is characterized by the same energy, similar photoluminescence

intensity decays (τ) and a decrease of the photoluminescence quantum yield (PLQY) in the case of 4 nm SiNCs. This decrease of PLQY with no effect on the lifetime might be indicative of the complete quenching of part of the nanocrystal ensemble (corresponding to lifetimes shorter than 5 μs). This effect can be ascribed to partial surface oxidation during the click reaction of the fraction of nanocrystals with incomplete surface functionalization in step a (**figure 4.1 a**), as previously reported by some of us in a different post-functionalisation reaction of SiNCs.[167] The photophysical properties of **Si-PEG** in distilled water are reported in **figure 4.10** and in **table 4.1**: bright red to NIR emission (λ_{max}=735 and 945 nm) are observed for average core diameter of 4 and 5 nm, respectively.

Figure 4.10- (a) Absorption (solid lines) and normalized photoluminescence spectra (dashed lines) of **Si-PEG** nanocrystals in water with an average diameter of the silicon core of 4 nm (black-line) and 5 nm (red-line); (b) Picture of **Si-PEG** with a silicon core diameter of 4 nm dispersed in water under visible light, on the left, and under 365 nm UV light excitation, on the right.
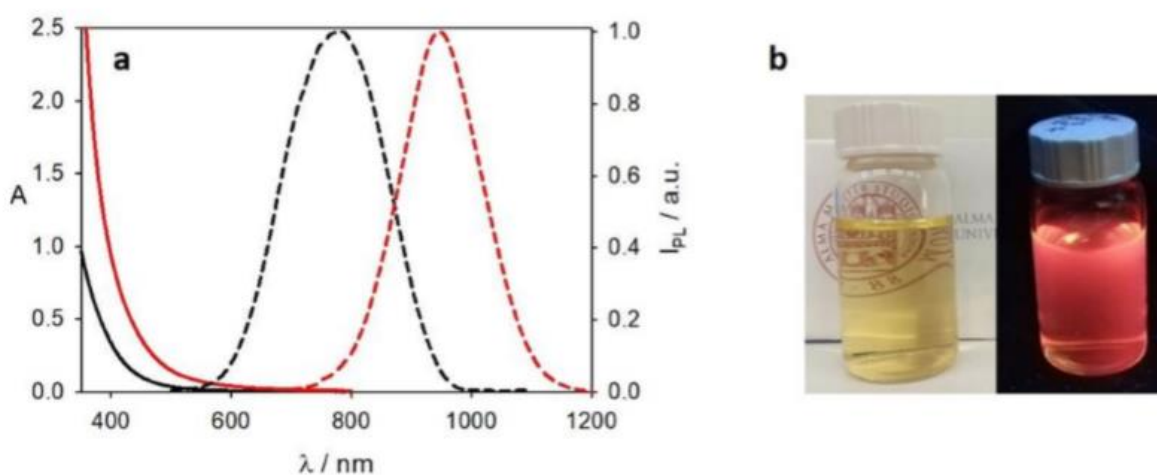
SiNC	solvent	diameter = 4 nm			diameter = 5 nm		
		λ_{max} (nm)	PLQY	τ (μs)	λ_{max} (nm)	PLQY	τ (μs)
Si-allyl	toluene	770	0.41	74	955	0.30	135
Si-PEG	toluene	770	0.20	68	950	0.29	130
Si-PEG	water	735	0.16	60	945	0.18	120

Table 4.1- Photoluminescence band maximum (λ_{max}), quantum yield (PLQY) and lifetime (τ) of **Si-PEG** and **Si-allyl** in toluene or distilled water. The reported diameters are referred to the silicon core.

Stability and pH-sensitivity

Dynamic light scattering analysis (DLS) was used to evaluate hydrodynamic volumes of **Si-PEG** samples in water and their stability as a function of time. The results indicate diameters of around (30 ± 10) nm for both 4 and 5 nm **Si-PEG** nanoparticles (**figure 4.11**). No significant change was observed over a one-week time interval, demonstrating no aggregation. Even the optical properties do not change with time: the samples remained transparent for several months when stored at room temperature. Moreover, photoluminescence lifetime of an **Si-PEG** sample in distilled water shows no change (**figure 4.12**) in a 1-day range and a little decrease in blood serum at 37°C (**figure 4.13**), suggesting that the PEG surface functionalization was able to prevent interaction with serum proteins. The pH dependence on the optical properties is also a fundamental issue for luminescent probes: at basic pH (>8) a significant decrease of lifetime was observed and lifetime changes were not fully reversible upon acidification to the initial pH value (**figure 4.14**). On the contrary, at acidic pH, we observed a significant and fully reversible increase of lifetime (**figure 4.15**), suggesting the possibility of implementing a pH sensor based on the luminescent lifetime of **Si-PEG**. It is worth noting that the lifetimes reported in **figure 4.15** are lower than the value reported in distilled water

(**table 4.1**) and is due to the effect of ionic strength in aqueous solution. In addition, the photoluminescence lifetime was proven not to be affected by the oxygen concentration (**figure 4.16**), whose presence may affect the signal detected and reduce the reliability of the sensor.
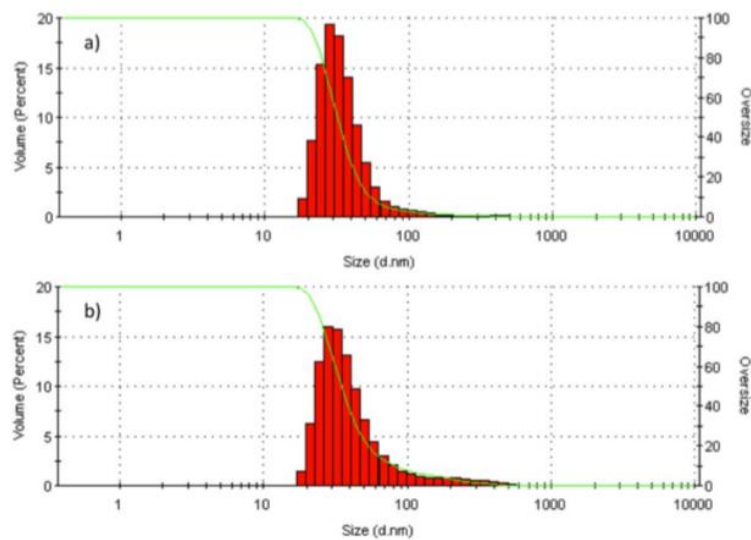
Figure 4.11- Dynamic light scattering analysis of a) 3 nm and b) 5 nm **Si-PEG** in water
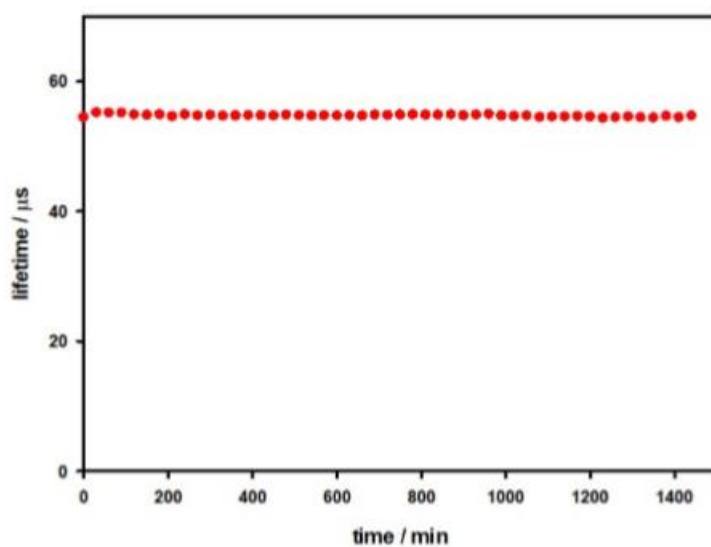
Figure 4.12- Stability test of 4 nm **Si-PEG** in distilled water at room temperature
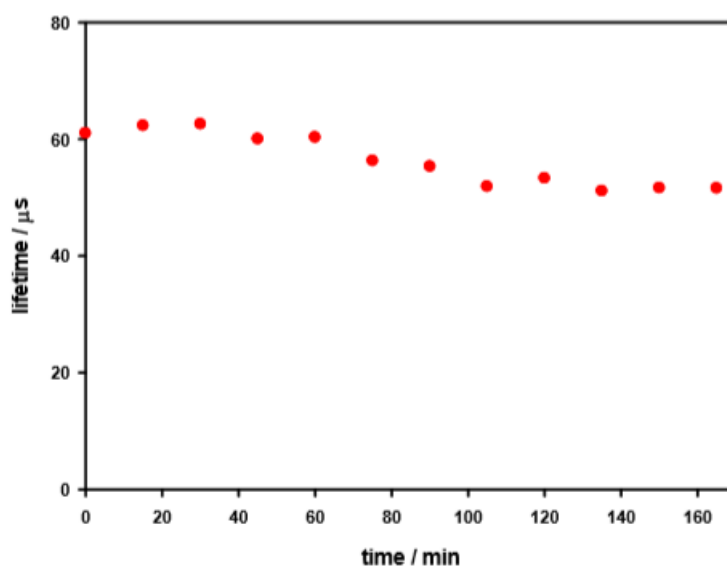
Figure 4.13- Stability test of 4 nm **Si-PEG** in blood serum. Lifetime values were recorded with a regular schedule while heating the sample at 37°C for 4 hours
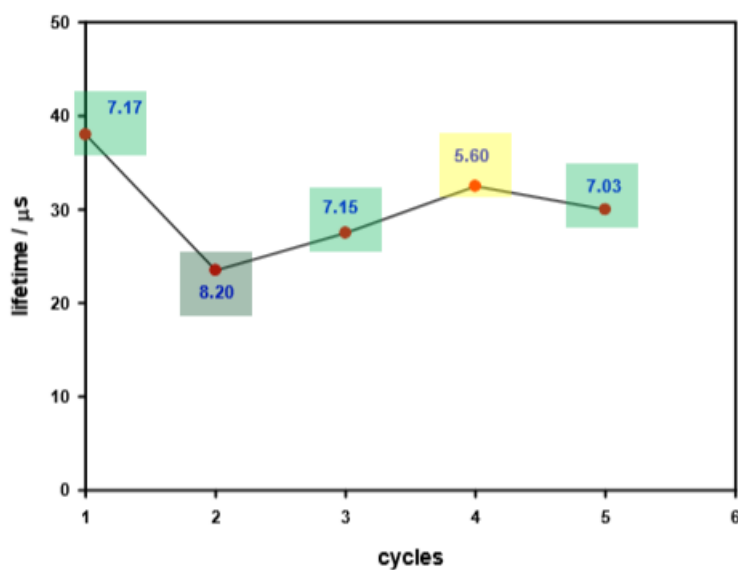
Figure 4.14- Luminescence lifetimes as a function of pH (values reported in blue) in successive additions of KOH and HCl to a 7.5 x 10⁻⁷ M solution of 4 nm **Si-PEG** in water. λ_{ex}=365nm; λ_{em} > 550 nm
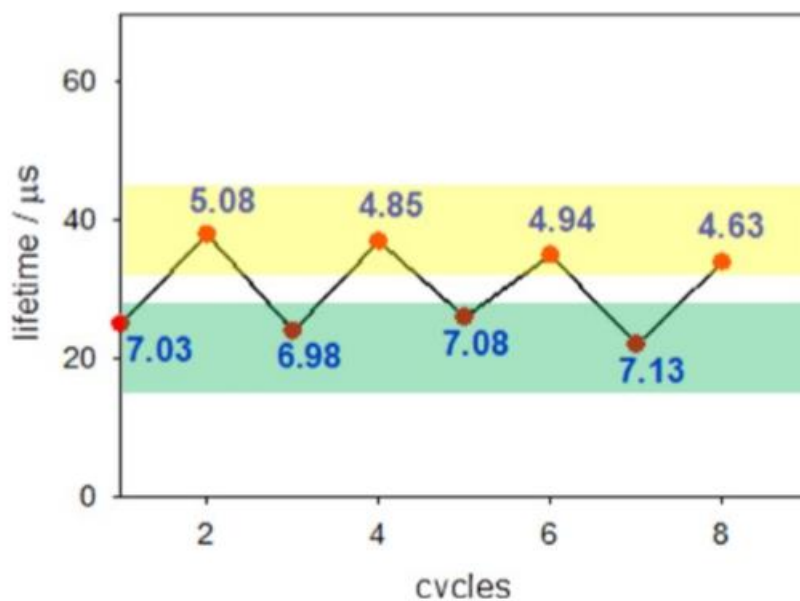
Figure 4.15- Luminescence lifetimes as a function of pH (values reported in blue) in successive additions of HCl and KOH to a 7.5 x 10⁻⁷ M solution of 4 nm **Si-PEG** in water. λ_{ex}=365nm; λ_{em} > 550 nm
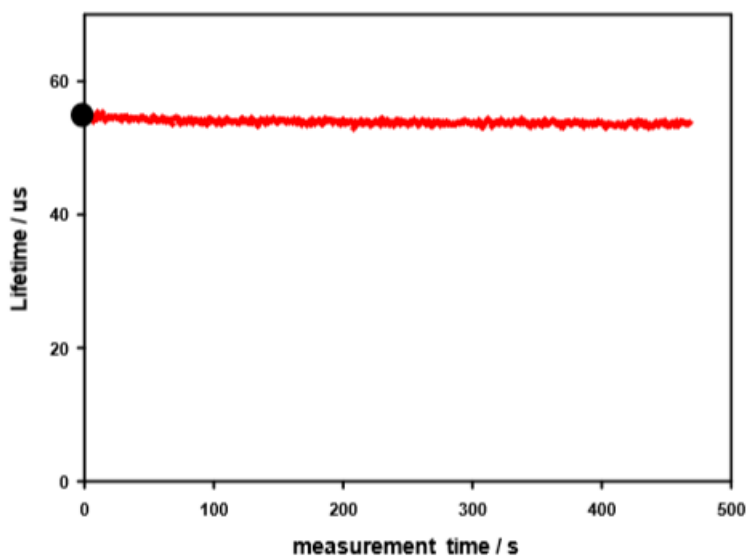
Figure 4.16- Luminescence lifetimes before (black dot) and after (red line) the addition of glucose oxidase and catalase

Dioxygen was removed from aqueous solutions of 4 nm **Si-PEG** using two enzymes, glucose oxydase and catalase14. These two enzymes in the presence of glucose and oxygen catalyze a reaction in which in the first step 1 eq of oxygen is consumed to produce hydrogen peroxide, and in the second step the peroxide regenerates 0.5 eq of oxygen and 0.5 eq of water. The net effect is that 0.5 eq. of oxygen is removed per catalytic cycle.

The dependence of luminescence lifetime from temperature in a biologically relevant interval was further investigated. The PL lifetimes decrease by increasing the temperature, with a linear trend. The variation is reversible upon increasing or decreasing the temperature, even if a slight variation of the slope was observed. The same behaviour is observed for both 4 nm and 5 nm nanocrystals, but the slope is higher for 5 nm nanocrystals, as reported in the picture inset (**figure 4.17**).[218]
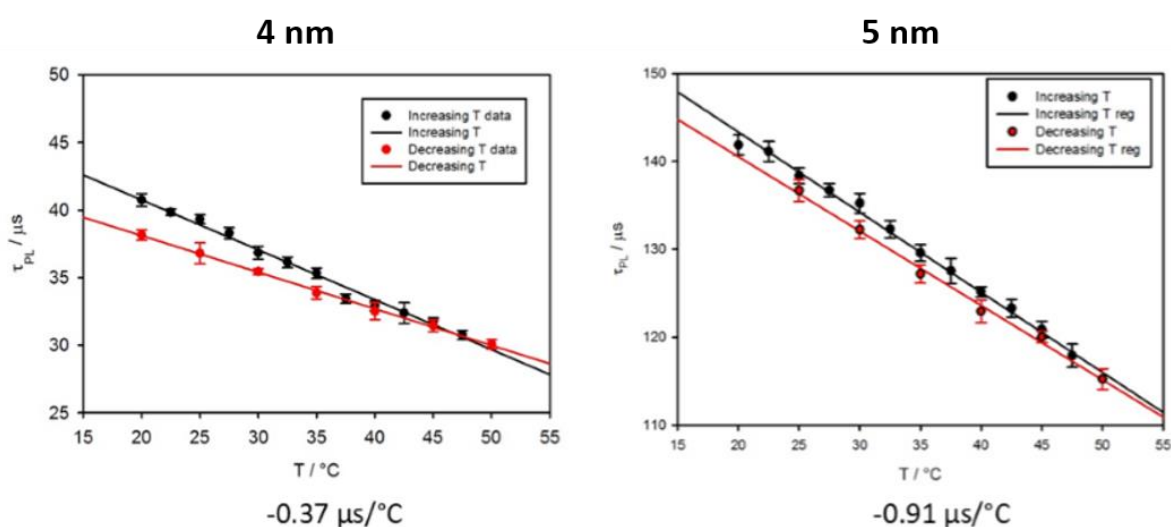
Figure 4.17- temperature dependence of the PL lifetime of 4 nm (left) and 5 nm (right) SiNCs functionalised with PEG in DW. The black dots are the luminescence lifetimes obtained rising the temperature from 20 to 50°C, while the red ones are obtained following the reverse path. Below the pictures the slope of the linear regression fit of the black dots is reported.

Biodistribution and luminescence bioimaging

For the evaluation of biodistribution and potential of **Si-PEG** to be utilized for luminescence guided surgery, we selected an **Si-PEG** sample with average diameter of 4 nm because of the higher sensitivity of detectors in this spectral range as compared to the NIR-II spectral region. We found that in vivo (IV) injected **Si-PEG** were primarily excreted through the liver in athymic nude mice (**figure 4.18**), with maximum excretion occurring at 24 h, as determined via ex vivo imaging (see appendix A for more details about in vivo animal studies). In addition, a time study of accumulation of IV injected **Si-PEG** in mice with MDA-MB-231 flank tumors was conducted. **Si-PEG** were found to accumulate in these tumors over time, with maximum localization at 24 h. These SiNCs were found to remain in these tumors for 48 h (**figure 4.19**). Therefore, SiNCs accumulate in the liver as well as in MDA-MB-231 tumors. The efficiency of targeting the tumor in comparison to accumulation in the liver was estimated by the emission intensity ratio as a function of time: an intensity ratio of 0.9 (tumor to liver) was observed at 2 h post injection (**figure 4.20**). A comparison of steady-state versus time-gated luminescence imaging was undertaken. **Si-PEG** (1.5 μM) were subcutaneously injected in athymic nude mice and the luminescence measured via both steady-state and time-gated detection. We found that the signal to background ratio is enhanced by a factor of 3 when utilizing time-gated luminescence imaging compared to steady-state luminescence imaging (**figure 4.21**).
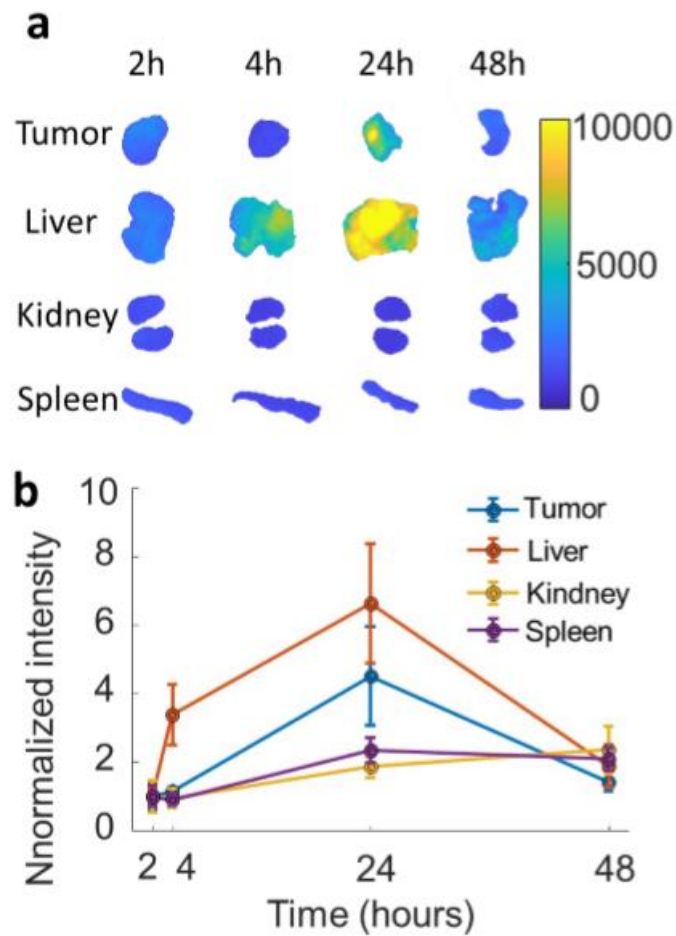
Figure 4.18- (a) Biodistribution of **Si-PEG** measured ex-vivo after in vivo injection. (b) Luminescence images of tumor, liver, kidney and spleen at different time points. Normalised luminescence intensities as a function of time. The intensity value and error bar for each organ are the average and standard deviation of luminescence intensities of all pixels in the organ area
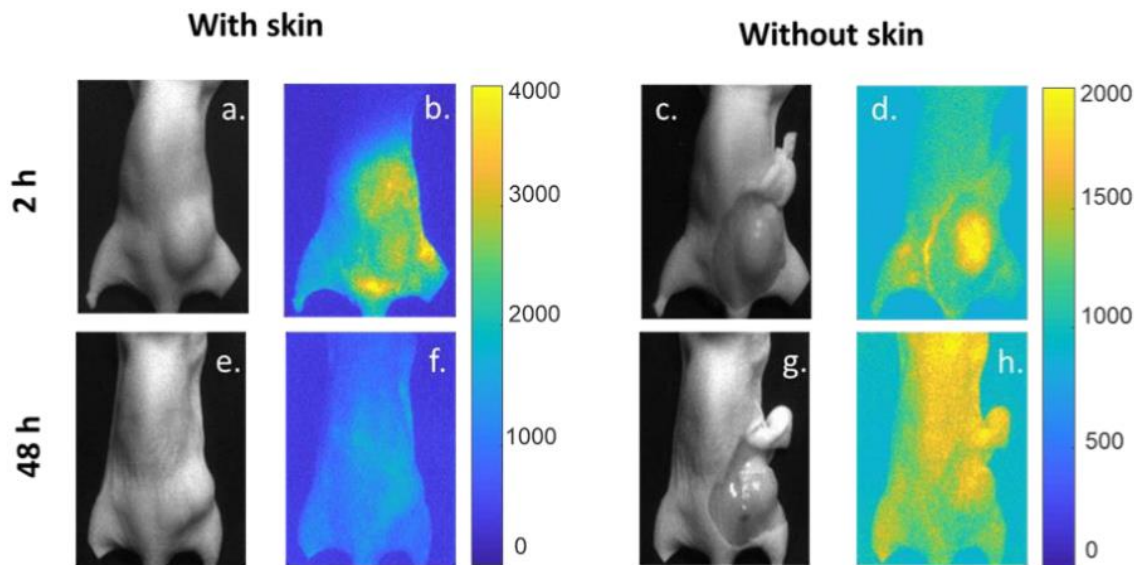
Figure 4.19- SiNCs localized in MDA-MB-231 tumors. **Si-PEG** (1.5 μM) were IV injected and the luminescence in MDA-MB-231 tumors was imaged. (a and c) White light images with skin intact and with skin removed, respectively, 2 h post injection; (b and d) luminescence images 2 h post injection with skin intact and skin removed, respectively; (e and g) white light images with skin intact and skin removed, respectively, 48 h after injection; (f and h) luminescence images 48 h post injection.
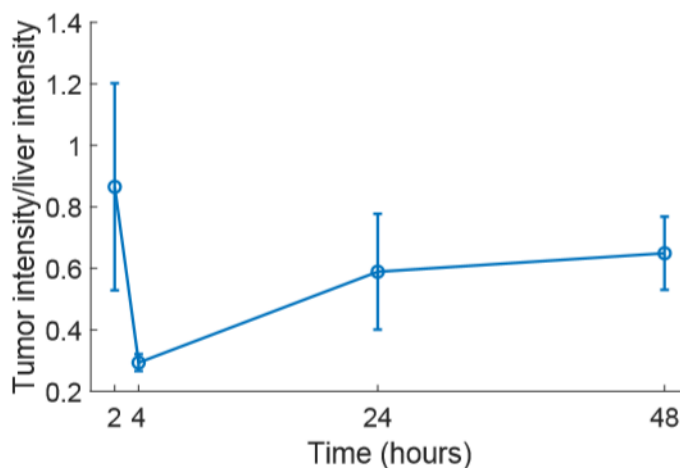
Figure 4.20- Ratio of the luminescence intensities of **Si-PEG** localized in tumours and liver measured ex-vivo as a function of time after in vivo injection. The intensity values and error bars are the average and standard deviation of luminescence intensities of all pixels in the tumor and liver area.
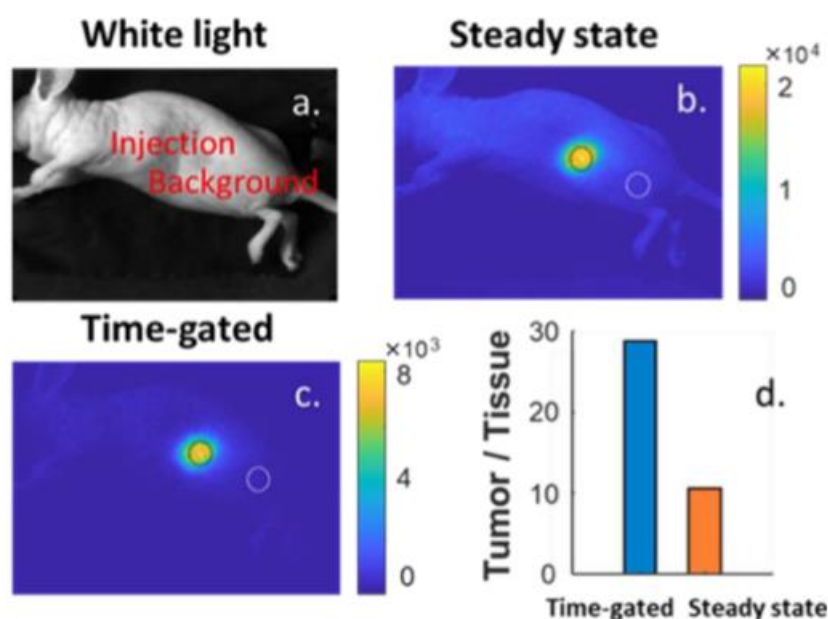
Figure 4.21- Advantages of time-gated imaging. **Si-PEG** (1.5 μM) were subcutaneously injected into athymic nude mice (a) white light image indicating location of injection and location of quantitation of background luminescence; (b) steady state fluorescence imaging of SiNCs; (c) time-gated luminescence imaging; (d) difference in signal to background ratio afforded by time-gated imaging (delay 10 μs).

4.3.2 PEG-Passivated SiNCs by Direct Hydrosilylation

Photophysical properties

Si-PEG$_{550}$ absorption and emission spectra in water show the general SiNCs photophysical features (**figure 4.22**), thus these SiNCs are well functionalized and the polar environment does not affect their properties. The luminescence quantum yield was measured to be equal to 7% in water and the luminescence lifetime 50 μs. These values are typical for 4 nm diameter SiNCs in water.
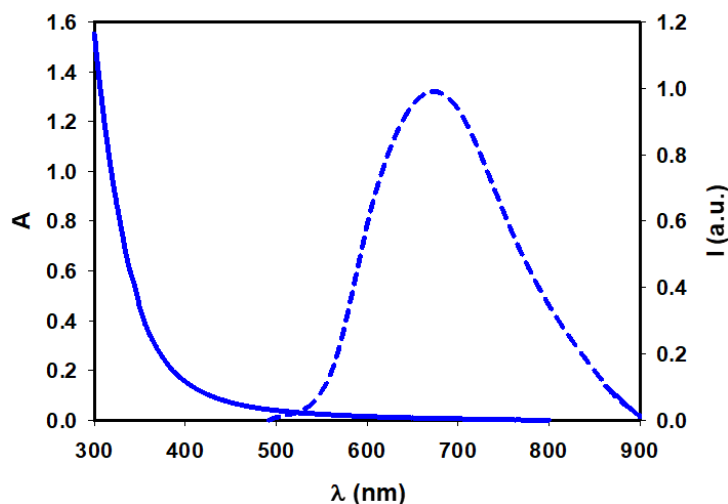
Figure 4.22- absorption (continuous line) and emission (dashed line, λ_{exc}= 460 nm) spectra of **Si-PEG$_{500}$** in water

Si-(10%)PEG$_{2000}$, **Si-(15%)PEG$_{2000}$** and **Si-(20%)PEG$_{2000}$** samples were characterized by acquiring their emission spectra (**figure 4.23** a, b and c respectively), their luminescene quantum yield (PLQY) and their luminescence lifetimes (τ) in three different solvents, CHCl$_3$ (before the reaction with TFA), EtOH and distilled water (DW), in order to determine eventual photophysical properties variations caused by the three different environment polarities.
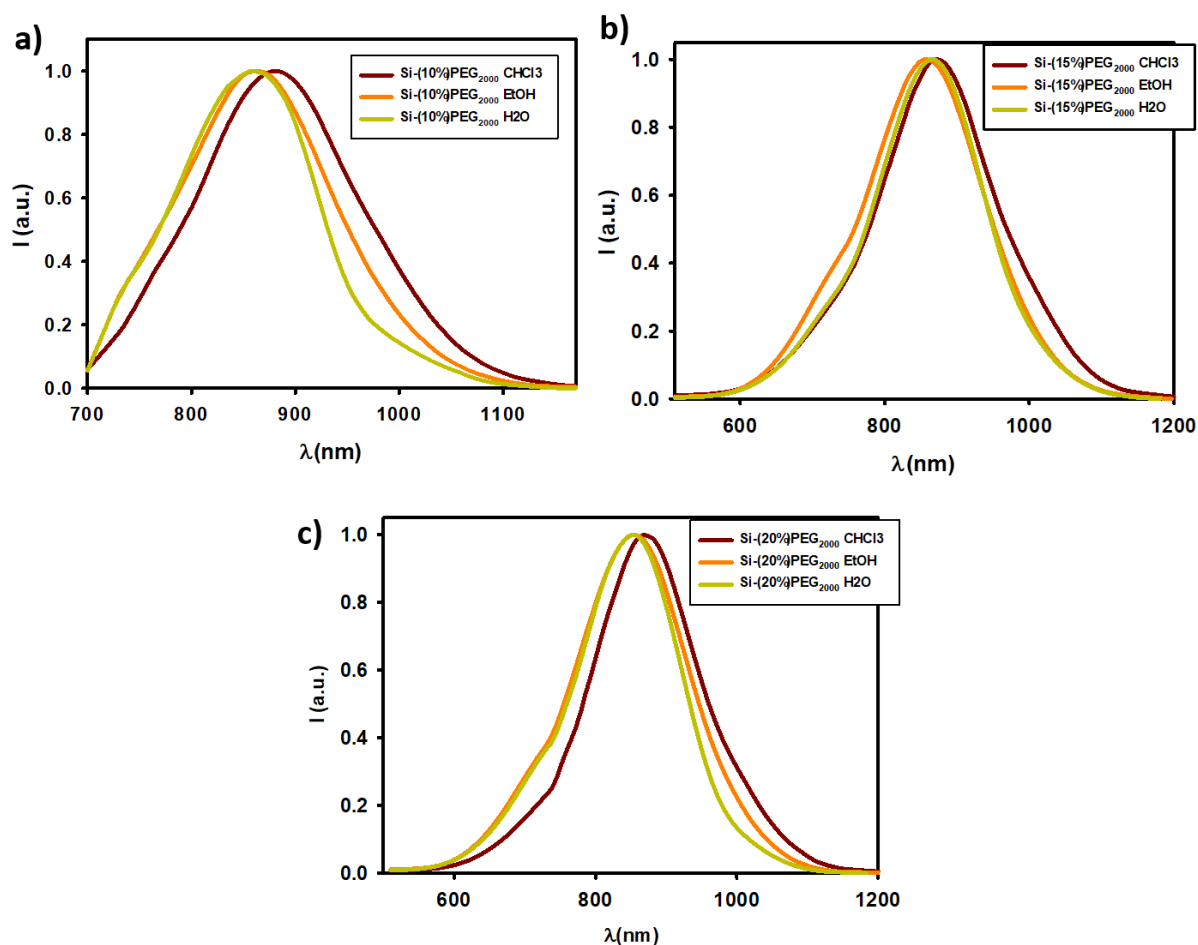
Figure 4.23- emission spectra in chloroform (dark red line), ethanol (orange line) and distilled water (green line) for **Si-(10%)PEG$_{2000}$** (a), **Si-(15%)PEG$_{2000}$** (b) and **Si-(20%)PEG$_{2000}$**, λ_{exc}= 460 nm

The $\lambda_{em, max}$ of the three samples is about 900 nm, does not matter the ratio between the two ligands used to passivate the SiNCs surface. A little blue-shift of few nm is observed going from chloroform to ethanol, otherwise, no $\lambda_{em, max}$ shift is observed from ethanol to DW. The PLQY and the τ values increase after the reaction with TFA, the registered values in EtOH are higher respect to those registered in CHCl$_3$, even though a little decrease is observed going from EtOH to DW, which is always expected (**table 4.2**). We can estimate a good surface functionalization since the different solvent polarity does not really affect the SiNCs photophysical properties.

	Solvent	PLQY (%)	τ (µs)
Si-(10%)PEG$_{2000}$	CHCl$_3$	20	120
	EtOH	25	150
	DW	15	100
Si-(15%)PEG$_{2000}$	CHCl$_3$	15	100
	EtOH	20	150
	DW	22	100
Si-(20%)PEG$_{2000}$	CHCl$_3$	13	100
	EtOH	23	140
	DW	15	110

Table 4.2- Photoluminescence quantum yield (PLQY) and lifetime (τ) of **Si-(10%)PEG$_{2000}$**, **Si-(15%)PEG$_{2000}$** and **Si-(20%)PEG$_{2000}$** in chloroform (before TFA reaction), ethanol or distilled water.
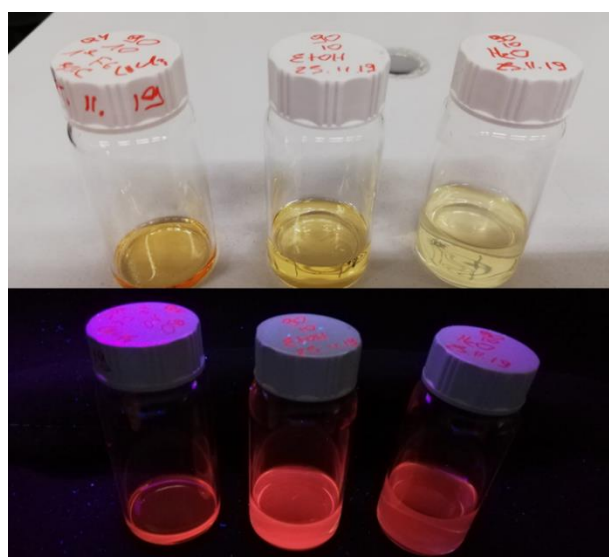
Figure 4.24- photos of **Si-(10%)PEG$_{2000}$** in chloroform, ethanol and distilled water (from left to right) under sun-light (on the top) and under UV irradiation (on the bottom)

The photophysical properties of the samples **Si-(10%)PEG₂₀₀₀**, **Si-(15%)PEG₂₀₀₀** and **Si-(20%)PEG₂₀₀₀** in DW were acquired again after two weeks in order to estimate the samples stability over time. No significant change was observed (**figure 4.25**), the samples showed a good stability and they are still well disperse in water even after two weeks.
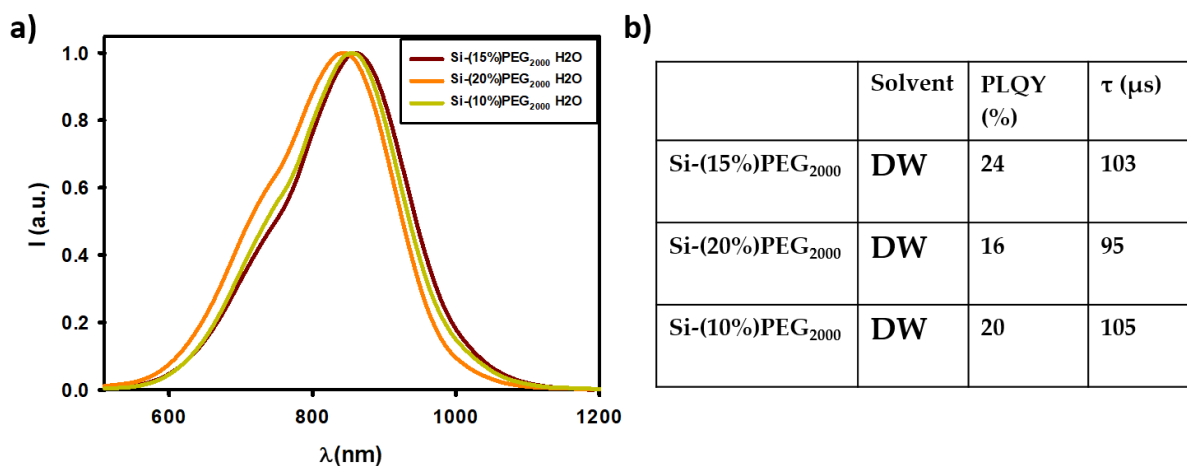
Figure 4.25- photophysical properties acquired after two weeks. (a) Emission spectra in distilled water for **Si-(10%)PEG₂₀₀₀** (green line), **Si-(15%)PEG₂₀₀₀** (dark red line) and **Si-(20%)PEG₂₀₀₀** (orange line), λ_{exc}= 460 nm; (b) photoluminescence quantum yield (PLQY) and lifetime (τ) of **Si-(10%)PEG₂₀₀₀** , **Si-(15%)PEG₂₀₀₀** and **Si-(20%)PEG₂₀₀₀** in distilled water.

The sample **Si-(15%)PEG₂₀₀₀** was also analysed in terms of PLQY and τ in a PBS solution. We estimated a PLQY equal to 5% and a τ equal to 60 µs for a fresh solution and a PLQY of 2.5% and a τ of 70 µs for the same solution, a week later.

Stability tests and pH-sensitivity

The sample **Si-PEG₅₅₀** was diluted to reach a volume equal to 5 mL by adding a phosphate buffer (PBS) solution (0.05 M, pH= 7.2), commonly used in the biological

research to mimic the human body environment since the osmolarity and the ion concentrations of this solution match those of the human body. The sample revealed to be a well stable colloidal solution even after 4 days of stirring, with no sign of SiNCs aggregation and precipitation.

The sample **Si-(15%)PEG$_{2000}$** (we used the one functionalized with 85% of tert-butyl 10-undecenoate and 15% of **PEG$_{2000}$DB**, since it revealed to be the best one in terms of luminescence quantum yield and stability) was diluted to reach a volume equal to 5 mL by adding a phosphate buffer (PBS) solution (0.05 M, pH= 7.2), as in the previous case. Even this sample was stirred for 4 days and, afterwards, it was heated to 37°C for 4 hours. It showed no sign of aggregation or deterioration with this treatment and this was confirmed by acquiring absorption and emission spectra (**figure 4.26**) and luminescence lifetimes over time (**figure 4.27**).
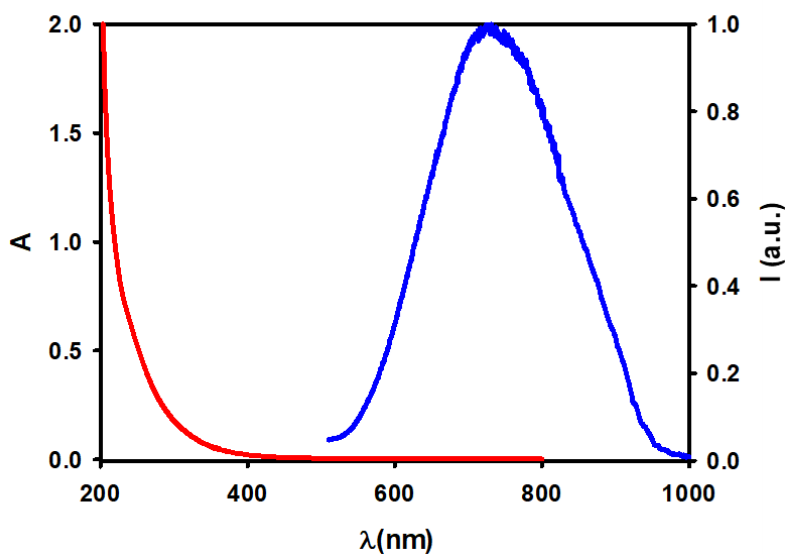
Figure 4.26- absorption (red line) and emission (blue line, λ_{exc}= 365 nm) spectra of the sample **Si-(15%)PEG$_{2000}$** in PBS solution after 4 days of stirring and heating to 37°C for 4 hours

In **figure 4.26** we can observe the classic un-featured SiNCs absorption spectrum and the classic Gaussian-shaped red-emitting SiNCs emission band. The **Si-**

(15%)PEG₂₀₀₀ photophysical properties are not changed because of the buffer presence, the stirring and the heating procedure.

As soon as the sample is diluted with the PBS solution, the luminescence lifetime decrease from 100 µs to 50 µs, however, it remain very stable during the 4 days of stirring in PBS and, moreover, the acquired measurements show a lifetime value which slowly increase along time, reaching 85 µs at the fourth day of measurements (**figure 4.27 b**). Emission intensity and the emission color do not change during the experiment (**figure 4.27 a**).
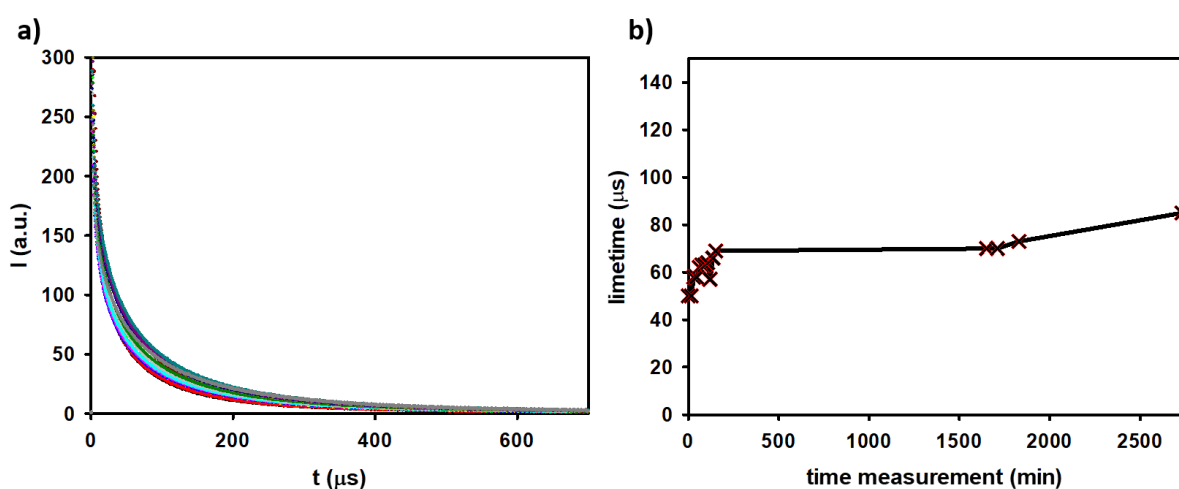
Figure 4.27- Si-(15%)PEG₂₀₀₀ luminescence lifetime measurements along 4 days of stirring at room temperature in PBS solution. (a) luminescence intensity decay, which remain almost the same during the experiment; (b) lifetime values registered during the 4 days

Subsequently, the same sample was heated to 37°C. The luminescence lifetime rapidly drops down from 80 µs to 65 µs during the first half hour of measurement. Then the sample acquires a stable lifetime value of 65 µs (**figure 4.28 b**) with no further emission intensity or emission color changes for one day of measurements (**figure 4.28 a**). The sample was then cooled down to room temperature and, as a consequence, the luminescence lifetime was restored from 65 µs to 75 µs (**figure 4.28 b**). **Si-(15%)PEG₂₀₀₀** in PBS still appear as a stable, clear, red-emitting colloidal

solution, for all of these reasons it could be a good candidate for biological imaging experiments.
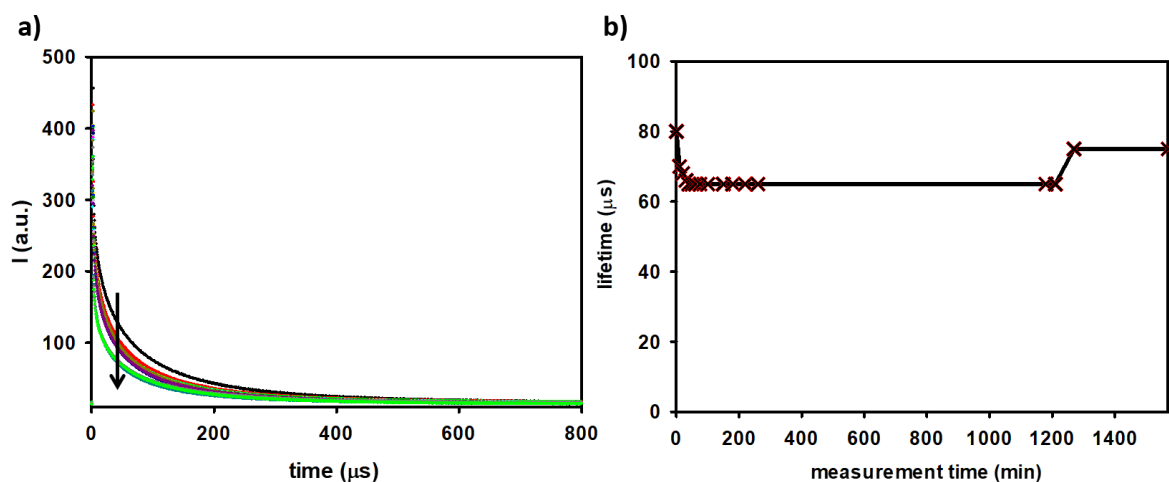
Figure 4.28- Si-(15%)PEG$_{2000}$ luminescence lifetime measurements along 1 day of stirring at 37°C in PBS solution. (a) luminescence intensity decay, which slowly decrease during the experiment; (b) lifetime values registered during the 24 hours of experiment

Dynamic light scattering analysis (DLS) was used to evaluate hydrodynamic volumes of **Si-(10%)PEG$_{2000}$**, **Si-(15%)PEG$_{2000}$** and **Si-(20%)PEG$_{2000}$** samples in water and their stability as a function of time. The results indicate diameters of around (30 ± 5) nm for the three samples and no significant change was observed over a two-week time interval, demonstrating no aggregation. **Figure 4.29** reports the DLS measurement of **Si-(15%)PEG$_{2000}$**, where we can observe two different populations. The population with the bigger average diameter, which is negligible in terms of weight percentage, could be due to some SiNCs aggregation that we can not remove by all the purification steps applied to the sample.
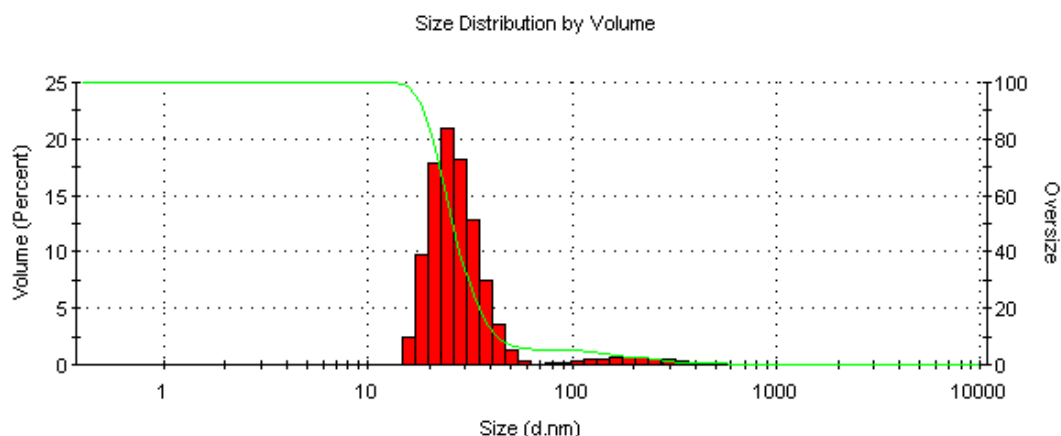
Figure 4.29- Dynamic light scattering analysis of **Si-(15%)PEG$_{2000}$** in water (equal to the measurements done for the other samples)

The optical properties pH dependence were then studied for the sample **Si-(15%)PEG$_{2000}$** in PBS solution (0.05 M, pH= 7.2). At basic pH ($\geq$ 8) a significant decrease of lifetime was observed and lifetime changes were not fully reversible upon acidification to the initial pH value (pH around 7 units) (**figure 4.30**). On the contrary, at acidic pH (a pH around 3 units was reached in this experiment), we observed a significant and fully reversible increase of lifetime (**figure 4.30**), suggesting the possibility of implementing a pH sensor based on the luminescent lifetime of **Si-(15%)PEG$_{2000}$**. It is worth noting that the lifetimes reported in **figure 4.28** are lower than the values reported in distilled water (**table 4.2** and **figure 4.25 b**) and is due to the effect of ionic strength in the PBS solution.

113
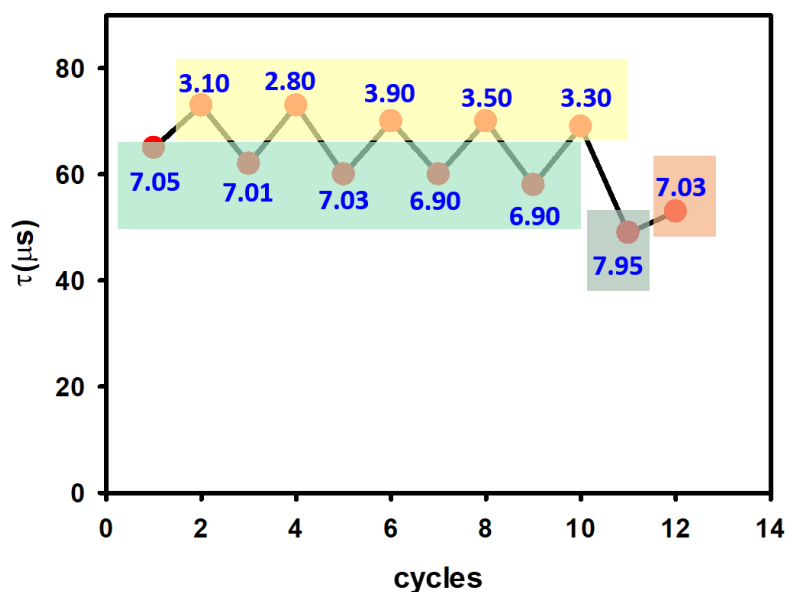
Figure 4.30- Luminescence lifetimes as a function of pH (values reported in blue) in successive additions of KOH and HCl to a 7.5 x 10^{-7} M solution of **Si-(15%)PEG$_{2000}$** in PBS solution. λ_{ex}=365nm; λ_{em} > 550 nm

It is worth noting that the fresh **Si-(15%)PEG$_{2000}$** sample has a pH value equal to 2 units. This acidic pH could be explained by considering the reaction step involving the TFA during the synthetic procedure to obtain the final sample itself. In order to bring the sample to a neutral pH value, a dialysis was done (RC dialysis tube, Millipore, MW cut off=14000) and a pH equal to 6.5 units was reached. The photophysical properties of this sample revealed to be not enormously affected by this purification step since we measured a PLQY of 15%, a τ of 75 μs and a $\lambda_{em,max}$ equal to 800 nm. Even the hydrodynamic volume, (25 ± 5) nm is the registered value, is not really affected. The dialysed sample appeared to be stable in terms of τ (75 μs over the time), acquiring these values by stirring the sample at RT for one day. Therefore, the same sample was heated to 37°C for 8 hours. As we have previously seen, a rapid decrease in τ values was recorded, until reaching a stable value of 60

µs. Interesting is that, cooling the sample to room temperature, a full lifetime recovery to its initial value was seen (**figure 4.31**).
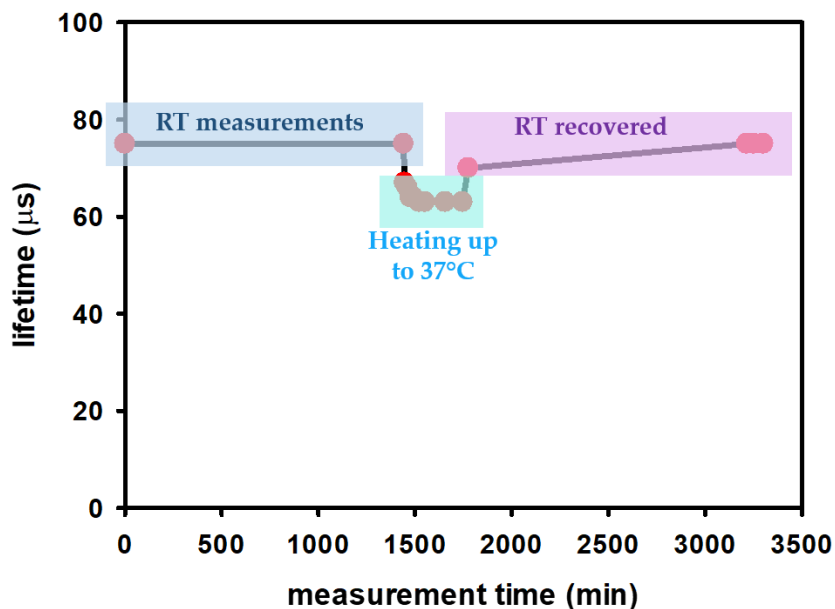
Figure 4.31- Stability test of **Si-(15%)PEG$_{2000}$** in DW after dialysis. Lifetime values were recorded for one day at room temperature, then heating the sample to 37°C for 8 hours and finally for another day after the RT recovering. λ_{ex}=365nm; λ_{em} > 550 nm

4.3.3 PEG-Passivated SiNCs by Amide Bond Formation

Photophysical properties

SiNCs passivated with dodecene and 10-undecenoic acid

The sample **Si-COOH** (DDE 70%, 10-undecenoic acid 30%) has been photophysically characterized both in EtOH and in PBS solution (pH=0.07; 0.05 M). In **figure 4.32** we can observe that the functionalization does not change the classical 4 nm diameter SiNCs absorption end emission properties, with an unfeatured absorption spectrum and an emission band cantered around λ = 800 nm. Even the

solvent does not affect these properties, revealing a good surface functionalization of the product.
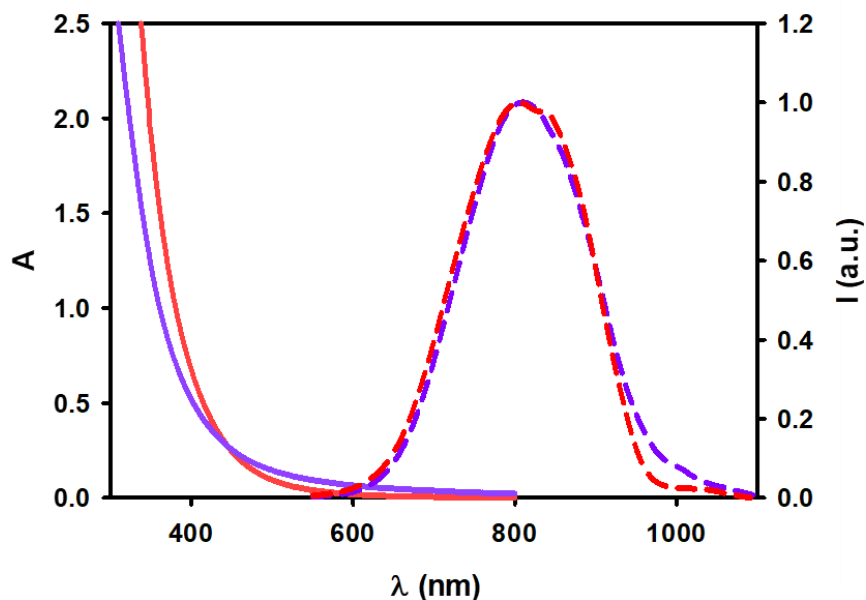
Figure 4.32- absorption (continuous line) and normalized emission spectra (dashed line) of the sample **Si-COOH** (DDE 70%, 10-undecenoic acid 30%) in EtOH (red lines) and in PBS solution (purple line). λ_{exc} = 460 nm

The measured PLQYs are equal to 10% in EtOH and to 5% in PBS solution, the measured τ are equal to 100 μs in EtOH and 76 μs in PBS solution.

SiNCs functionalized with poly(ethylene glycol) methyl ether amine

The sample **Si-NH-PEG$_{750}$** has been photophysically characterized both in EtOH and in distilled water (**figure 4.33**). Even in this case, the absorption spectra appear to be equal to the 4 nm diameter SiNCs classic absorption spectrum. The emission spectra are centered at $\lambda_{em,max}$ = 770 nm in EtOH and at $\lambda_{em,max}$ = 790 nm in distilled water.
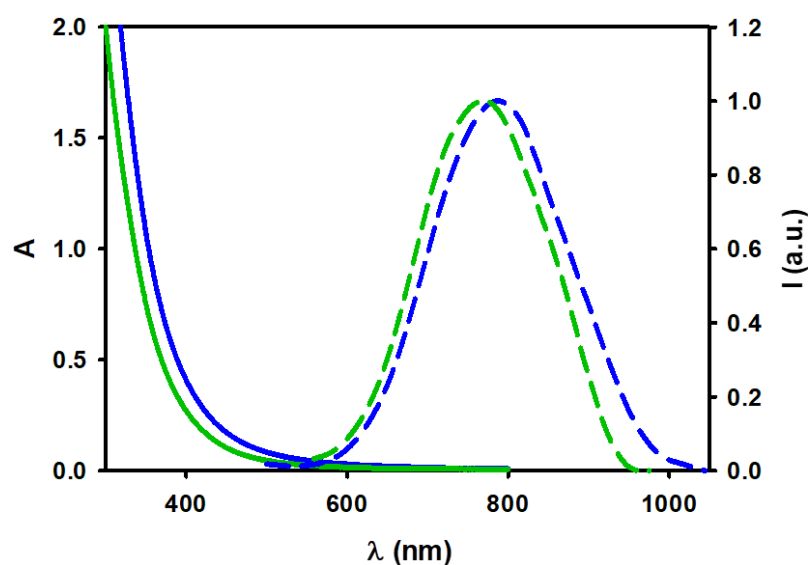
Figure 4.33- absorption (continuous line) and normalized emission spectra (dashed line) of the sample **Si-NH-PEG₇₅₀** in EtOH (green lines) and in distilled water (blue line). λ_{exc} = 460 nm

The measured PLQYs are equal to 8% in EtOH and to 7% in DW, the measured τ are equal to 94 μs in EtOH and 82 μs in DW.

Stability tests

A little amount of the **Si-NH-PEG₇₅₀** sample has been diluted to a volume of 5 mL, by adding a PBS solution (pH = 7; 0.05 M), in order to determine the sample stability in this environment which mimics the one inside the human body. The sample revealed to be not stable enough, since it started to aggregate and to precipitate an hour later the solution was done.

The current studies demonstrate new synthesis of polyethylene glycol functionalized silicon nanocrystals (average core diameter of 4 and 5 nm) with advantageous optical properties of NIR emission. All the registered values acquired in DW are reported in **table 4.3,** to make a comparison between the synthesized samples. The best two synthesized samples are **Si-PEG** and **Si-(15%)PEG$_{2000}$** in terms of all the photophysical measurements, the sample stability in different aqueous solutions and the reaction chemical yields. This is the reason why the pH sensitivity has been studied only for these two samples, leading to the same results and suggesting the possibility to realize a pH-sensitive device based on these silicon nanocrystals solutions.

It has also been shown that the **Si-PEG** sample, obtained by the thiol-ene click reaction, have the potential to be utilized for luminescence guided surgery, since they accumulate in the tumor and are excreted within 48 hours, as demonstrated in mice with MDA-MB-231 tumors. In addition, due to the long emission lifetime of these SiNCs (60 μs), the signal to background ratio and background ambient light suppression can be enhanced via time-gated luminescence imaging.

Future studies are aimed at increasing the molar absorption coefficient of SiNCs in the red and NIR spectral region by a light-harvesting approach. This approach was already demonstrated in organic solvents:[129,163,164,167] upon excitation of dye molecules appended at the nanocrystal surface, sensitized emission of the Si core is observed. This will enable red excitation of SiNCs coupled to time-gated NIR luminescence for deeper tissue penetration. Furthermore, conjugation of the terminal OH group of the PEG shell to a tumor targeting agent will be investigated for active targeting of the tumor.

	$\lambda_{max,em}$ (nm)	PLQY (%)	PL τ (μs)	DLS (nm)	Stability	pH sensitivity
Si-PEG	735	16	60	30 ± 10	- Stable in DW at RT - Stable in blood serum at 37°C for 4h under stirring	- Not stable at basic pH - Stable at acid pH
Si-PEG$_{550}$	690	7	50		- Stable in PBS solution for 4 days under stirring	
Si-(10%)PEG$_{2000}$	860	15	100	30 ± 5		
Si-(15%)PEG$_{2000}$	860	22	100	30 ± 5	- Stable in PBS solution for 4 days under stirring - Stable if heated to 37°C for 4h	- Not stable at basic pH - Stable at acid pH
Si-(20%)PEG$_{2000}$	860	15	110	30 ± 5		
Si-NH-PEG$_{750}$	790	7	82		- Not stable in PBS solution under stirring	

Table 4.3- comparison between $\lambda_{max,em}$, PLQY, PL τ, DLS measurements, stability over time in DW or PBS solution or blood serum and pH sensitivity of the following samples: **Si-PEG**; **SiPEG$_{550}$**, **Si-(10%)PEG$_{2000}$**, **Si-(15%)PEG$_{2000}$**, **Si-(20%)PEG$_{2000}$** and **Si-NH-PEG$_{750}$**.

5 Silicon Nanocrystals and Fluorescent Dyes Encapsulated in Water-Soluble Polymer Nanoparticles for Fluorescent Bioimaging

5.1 Introduction

Fluorescent Polymer Nanoparticles (**PNPs**), which are many fold brighter than organic dyes, can improve many relevant features in the fluorescent bioimaging field, such as *speed*, *resolution* and *sensitivity*. The field is currently dominated by inorganic nanoparticles, QDs for example; nevertheless, dye-loaded **PNPs** have recently shown better properties as the ability to combine superior brightness with biodegradability and low toxicity. The resulting **PNPs** now surpass the brightness of QDs by ≈ 10-fold for a comparable size, and have started reaching the level of the brightest conjugated polymer NPs. A large number of dyes needs to be confined in a very small volume, the **PNP** itself, in order to achieve a very high brightness value (**figure 5.1**), by increasing the molar absorption coefficient.[219]
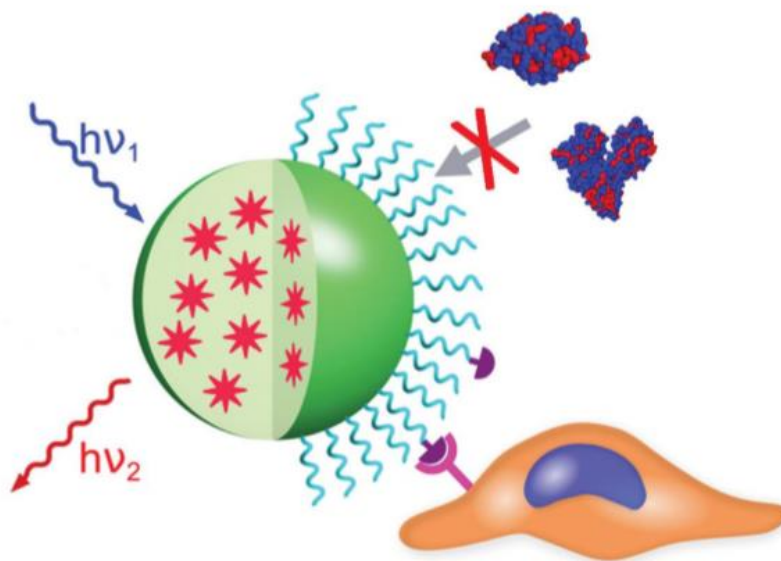
Figure 5.1- Schematic view of a dye-loaded **PNP** and its principal characteristics: brightness (proportional to number of encapsulated dyes, their extinction coefficient and quantum yield), control of nonspecific interactions, and implementation of selectivity. Reprinted with permission from the ref.[219]

However, at such high dyes-loadings confined in such small volumes, the typically flat aromatic structure of fluorophores favours aggregation caused quenching (ACQ), which is further enhanced through the fast excitation energy transfer (EET) due to the small inter-fluorophore distances.[220] Together these two effects strongly decrease the PLQY and limit the brightness of dye-loaded polymer NPs. Recently, several approaches were introduced allowing a strong ACQ reduction, such as dye modification with bulky side groups[221,222] and bulky counterions.[168] These new possibilities and the increasing need for ultra-bright fluorescent probes lead to a rapid growth of the field of bright dye-loaded **PNPs**.[219]

In this work, SiNCs and high concentrations of organic dyes are together encapsulated within **PNPs** to obtain an ultra-bright fluorescent probe. Exciting the organic dyes, in absence of ACQ, they usually give an ultra-fast EET, which ensures

collective behaviour of multiple fluorophores, allowing their simultaneous quenching in the presence of a radical dark species (if any) (**figure 3.4**, chapter 3.2), useful for signal amplification in chemo and biosensor.[223,224] This collective behaviour is exemplified by on/off switching (blinking), a process normally observed for single emitters such as a single fluorophore[225] or QDs.[226] In this work, a large number of fluorophores is collectively quenched by **PNPs** trapped SiNCs, resulting in their photoluminescence sensitization. This is the non-covalent approach to obtain the efficient light-harvesting antennae that we previously discussed in chapter 3.2. Particularly helpful for in-vivo applications is the use of NIR-emitting SiNCs (5 nm diameter) as acceptor units.

Synthesis of Dye-Loaded and SiNCs-Loaded Polymer Nanoparticles

PNPs can be synthesized starting either from preformed polymers that are assembled into NPs, or from the corresponding monomers that are polymerized in emulsions to yield NPs. The polymerization of monomers is conducted in different kinds of emulsions depending on the system composition and the used conditions. We can usually distinguish between *(conventional-)emulsion*, *mini-emulsion*, and *micro-emulsion* polymerization.[227] When NPs are realized after the polymer synthesis, a wide range of polymers can be used, including some biodegradable polymers, such as poly(lactic- co glycolic acid) (PLGA), polycaprolactone (PCL) and some specially designed block-copolymers. The three main approaches used to prepare dye-loaded NPs from preformed polymers are: *emulsification solvent evaporation*, *nanoprecipitation*, and *self-assembly*.

Nanoprecipitation, also called solvent displacement, is the chosen method in this work. The polymer is dissolved in a water-miscible solvent, e.g. tetrahydrofuran (THF), together with the organic dyes and the alkyl-terminated SiNCs in pre-established concentration values. Upon the addition of this solution to an aqueous

phase, the rapid diffusion of the solvent into the aqueous phase (and vice versa) and the a-polarity of dyes and SiNCs, lead to the supersaturation status of the polymer and the formation of dyes-and-SiNCs-loaded NPs.[228] In this system, dyes and SiNCs are physically trapped inside the polymer NPs (**figure 5.2**).
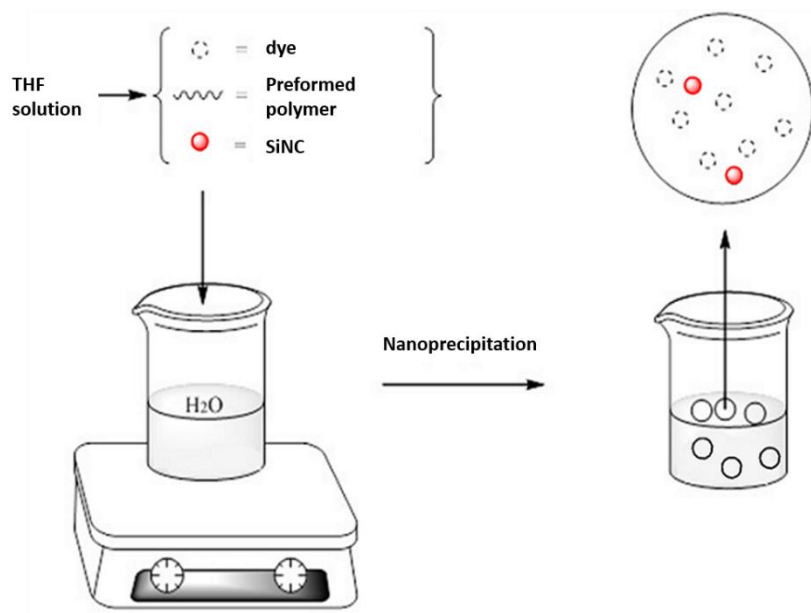
Figure 5.2- Schematic representation of Nanoprecipitation technique used for the preparation of dyes and SiNCs loaded NPs from preformed polymers.

Nanoprecipitation is a kinetically controlled process,[229,230] in which the particles' size is influenced by the polymer concentration, the relative amounts of organic and aqueous phase, the presence of stabilizers and the mixing procedure.[228,231] The use of a stabilizer is not essential for the formation of small polymer NPs. In its absence, polar groups or charged groups on the polymer chains play an important role in the NPs formation.[232] NPs from ca. 10 nm to several hundreds of nm can be obtained through this technique. The kinetically controlled formation mechanism favours the entrapment of desired units.[233–235] However, strong differences in the solubility of these units and the polymer in the organic and/or aqueous phase can, at high unit loadings, influence particle formation and thus lead to inhomogeneous distribution of the units within NPs.[236] In dye-loaded **PNPs** high and efficient loading are

important. The release of dyes and SiNCs from fluorescent **PNPs** is undesired and detrimental to their use in bioimaging applications.

Polymer Nanoparticles Properties

Different parameters need to be controlled in order to prepare a stable colloidal solution of **PNPs** with high brightness and employable in bioimaging applications.

Brightness

The brightness of a fluorescent dye, $B = \varepsilon \times QY$, determines the signal that can be obtained from a single molecule and thus defines sensitivity and resolution. For dye-loaded polymer NPs, ε depends directly on the number of encapsulated fluorescent dyes. Therefore, in order to increase the brightness, one can increase the dye concentration in the polymer matrix and/or particle size. For biological applications, it is useful to increase the particle brightness and to reduce its size in the same time.

In this work, **PNPs** are loaded both with dyes and SiNCs so we can see the SiNCs sensitized luminescence thanks to the EET process which takes place. The SiNCs sensitization is higher by encapsulating a higher number of organic dyes inside the **PNPs**.

Size

In order to use polymer NPs for biological applications, the control of their size is a very important point. The size defines the NPs destiny after their injection inside the human body. In general, the smaller their diameter, the easier their expulsion and their passive targeting via Enhanced Permeation and Retention effect (EPR). Using the different methods listed above, it is possible to prepare NPs with sizes ranging between 15 and 500 nm. **PNPs** with appropriate size for the scope could be

prepared because the quantum yield of encapsulated dyes does not directly depend on NPs size, but mostly on dye concentration and the possible ACQ.[219]

A wide variety of dye-loaded polymer NPs has been synthesized through nanoprecipitation procedure. In the case of the most common polymers for biomedical applications such as PLGA, PCL and PMMA, the standard protocols based on nanoprecipitation give relatively large NPs of 50-300 nm.[237–239] In order to obtain smaller NPs, it is possible to use an alternative self-assembly approach, which is based on charge-controlled nanoprecipitation. In this case, a single-charged group on the polymer, such as PLGA, PCL and PMMA could decrease the size of the obtained particle to less than 15 nm.[168]

Photostability

The photostability of encapsulated organic dyes is influenced by several factors. On one hand, the rigid polymer matrix confers significantly improved photostability to some dyes, due to the protection from oxygen or other chemical species that could take part in photo-degradation reactions.[240,241] On the other hand, at high concentrations organic dyes may form ground and excited state aggregates, which may change the photochemistry of dyes and determine a decrease in the photostability.[222]

Surface Chemistry and Colloidal Stability

Surface chemistry allows us to enhance the properties of fluorescent polymer NPs for bioimaging applications, by introducing hydrophilic groups that can ensure their colloidal stability, minimize non-specific interactions with biological molecules and improve specific-interactions with molecules or cells of interest. The surface chemistry of NPs clearly depends on the preparation method used and on the type of encapsulated dyes.[168]

Bioimaging Applications

Fluorescent NPs can be used either for detection of analytes, cellular or animal imaging. Different applications need ultra-bright NPs with different requirements. For example, cellular imaging generally needs the smallest possible NPs because them can easily penetrate into the cells and provide less interference with the molecular processes studied. In contrast, in vivo studies prefer particles in a size between 30 and 200 nm. NPs should not be too large in order to prevent accumulation in the liver or in the lungs, neither too small in order to avoid rapid clearance through the kydneys.[242,243] Furthermore, cellular imaging requires dyes with an emission in the range from blue to red (400-650 nm). In contrast, in vivo applications require NIR (≥ 700 nm) or at least far red (600-700 nm) emitting dyes, because of the partial transparency of biological tissues in these spectral regions.[244,245] Currently, dye-loaded **PNPs** are becoming an interesting alternative to dyes and QDs in bioimaging applications, offering new possibilities beyond bioimaging.[168]

Dye-loaded **PNPs** could be prepared by using biocompatible and biodegradable polymers such as PLGA and PCL, and studies show that they typically have no significant toxicity because of the encapsulation of the dyes.[246] Currently, they can be safely used for cellular imaging applications. However, in vivo studies are not enough to demonstrate their non-toxicity on the whole body. Therefore, dye-loaded **PNPs** are currently one of the major candidates for applications of fluorescent NPs directly in a biomedical context, such as development of theranostic devices.[247–250]

In chapter 4, it has been already demonstrated that NIR-emitting SiNCs could be efficiently used in time-gated luminescence bioimaging

The work presented on this chapter is focused on the synthesis of dye-loaded and SiNCs-loaded polymer nanoparticles (NPs) obtained via the nanoprecipitation technique. For this purpose, 5 nm diameter SiNCs stabilized with appropriate

chains were synthesized and characterized. Tetrahydrofuran (THF) has been chosen as the solvent for the nanoprecipitation synthesis because of its water miscibility. Nanoprecipitation was performed in order to physically encapsulate the organic dyes and the SiNCs inside the **PNPs** made of preformed polymers. The aim is to obtain non-toxic fluorescent NPs brighter than the organic dyes and the QDs alone, capable to improve the speed, the resolution, the sensitivity of today's fluorescence bioimaging.[219] With the confinement of a large number of organic dyes in a restricted space, it is possible to increase the percentage of absorbed light and to have an ultra-fast EET due to the small inter-chromophores distances.[220] The EET ensure the collective behaviour of the fluorophores, which could be collectively quenched by the SiNCs, if their distance allows it. In this way, the SiNCs emission can be sensitized. The 5 nm diameter SiNCs are particularly interesting as ultra-bright luminescent probes, because of their emission in the NIR regions, where the human tissues are semi-transparent, and, most importantly, because of their long-lived emission (hundreds of μs).

5.2 Synthesis of Dye-Loaded and SiNCs-Loaded PNPs

Synthesis of 5 nm diameter SiNCs functionalized with dodecyl chains

The synthetic procedure to obtain SiNCs functionalized with dodecyl chains have been already reported in chapter 3, considering in this case a 5 nm diameter (**SiDDE5**). **SiDDE5** absorption spectrum shows the classic featureless tail (**figure 5.3**), because of the indirect band gap of Si. 4 and 5 nm diameter SiNCs show the same spectrum shape; on the contrary, the molar absorption coefficient is significantly influenced by the SiNCs size and: at $\lambda = 400$ nm it assumes the value of $\varepsilon = 3*10^5$ M^{-1} cm^{-1} and $5*10^5$ M^{-1} cm^{-1} respectively. 5 nm diameter SiNCs have been chosen because of the higher ε value and because of the NIR emission, in order to have an EET from the excited dyes, which emit at higher energies, to **SiDDE5**. The

emission spectrum shows a Gaussian shaped band and the maximum emission wavelength, $\lambda_{em,max}$, changes with the SiNCs size. In particular, as we can see in **figure 5.3**, **SiDDE5** has $\lambda_{em,max}$ = 960 nm.
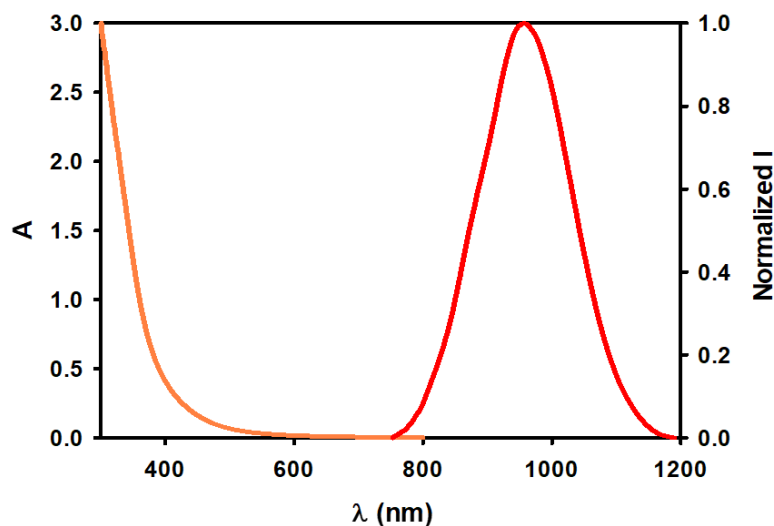
Figure 5.3- absorption (orange line) and emission spectra (red line) of **SiDDE5** in THF. λ_{ex} = 380 nm

The measured PLQY in THF solution is equal to 35 % and the photoluminescence lifetime 250 μs.

Synthesis of Dye-Loaded and Silicon Nanocrystals-Loaded Polymer Nanoparticles

Dye-loaded and SiNCs-loaded polymer NPs (**PNPs**) were obtained with the nanoprecipitation technique previously described, which is a kinetically controlled process,[229,230] so the particles size is influenced by the polymer concentration, the relative amounts of organic and aqueous phase, the presence of stabilizers and the mixing procedure,[228,231] as we have already reported.

A copolymer of poly(methyl methacrylate) (PMMA, frequently used in biomedical applications) with methacrylic acid modified with sulfonate groups with a modification degree of about 85% and with the charged groups randomly occurring along the PMMA chain (**PMMA-SO₃H, figure 5.4**), is the nanoprecipitated polymer (PMMA, average Mw ~ 34000 by GPC, average Mn ~ 15000 by GPC). It has been demonstrated by Reisch[232] et al. that the size of the resulting **PNPs** made from uncharged chains (just PMMA for instance) was largest, being typically above 100 nm and the TEM images of these **PNPs**, reported in their work, revealed a strong tendency of aggregate formation which makes the analysis of the particle sizes difficult. Sulfonate bearing polymers gave smaller nanoparticles with sizes typically below 25 nm. The influence of one to two charged groups per chain thus largely influence the resulting nanoparticle size. The use of this kind of polymer allows us not to use a stabilizer during the procedure, since the sulfonate group undergoes deprotonation in distilled water, bringing to an already charged **PNP** surface, which avoids aggregation by itself. **PMMA-SO₃H** has also been chosen since it allowed us to work at a neutral pH value, avoiding basic pH buffer solutions, which are well known to be detrimental to the SiNCs photophysical properties.
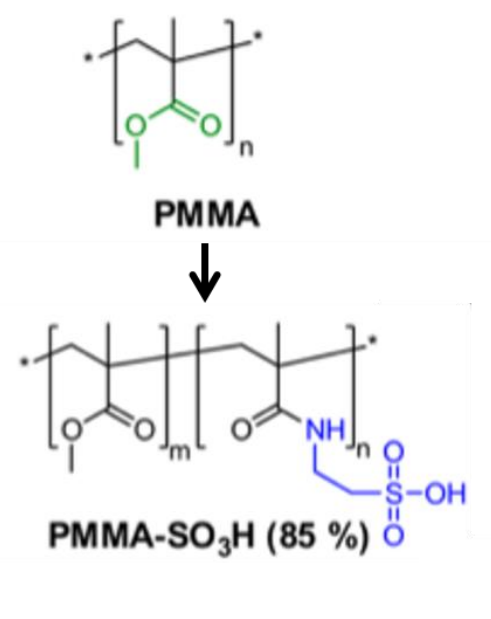
Figure 5.4- schematic view of the chemically modified PMMA to its copolymer with methacrylic acid modified with sulfonate groups with 85% of modification degree. Adapted from the ref.[232]

In this non-covalent approach to obtain a light-harvesting antenna, 9,10-diphenylanthracene (**DPA)** or N,N'-Bis-(2,6-diisopropylphenyl)1,6,7,12-tetraphenoxy-3,4,9,10-perylenebis(dicarboximide) (the so-called Lumogen Red, **LR)**[222] have been the chosen dyes to be physically entrapped inside the **PNPs**, alone or together with **SiDDE5**, during the nanoprecipitation technique. They have been chosen since their emission is more energetic in respect to the **SiDDE5** emission, so an energy transfer from the firsts to the seconds is photophysically allowed. Furthermore, they are ACQ-free since their three-dimensional structure avoid the π-stacking aggregates formation (**figure 5.5 a,b**). Furthermore, our group has already demonstrated the excellent **DPA** energy transfer to the SiNCs,[129] which also occurs without any kind of SiNCs emission quenching. On the contrary, the possible energy transfer from **LR** to **SiDDE5** has never been studied before, but **LR** is with no doubts a better dye for bioimaging applications. Cellular studies of **LR** dyes inside **PNPs** composed of the biodegradable polymer PLGA, showed low toxicity and strong potential for bioimaging applications.[222]
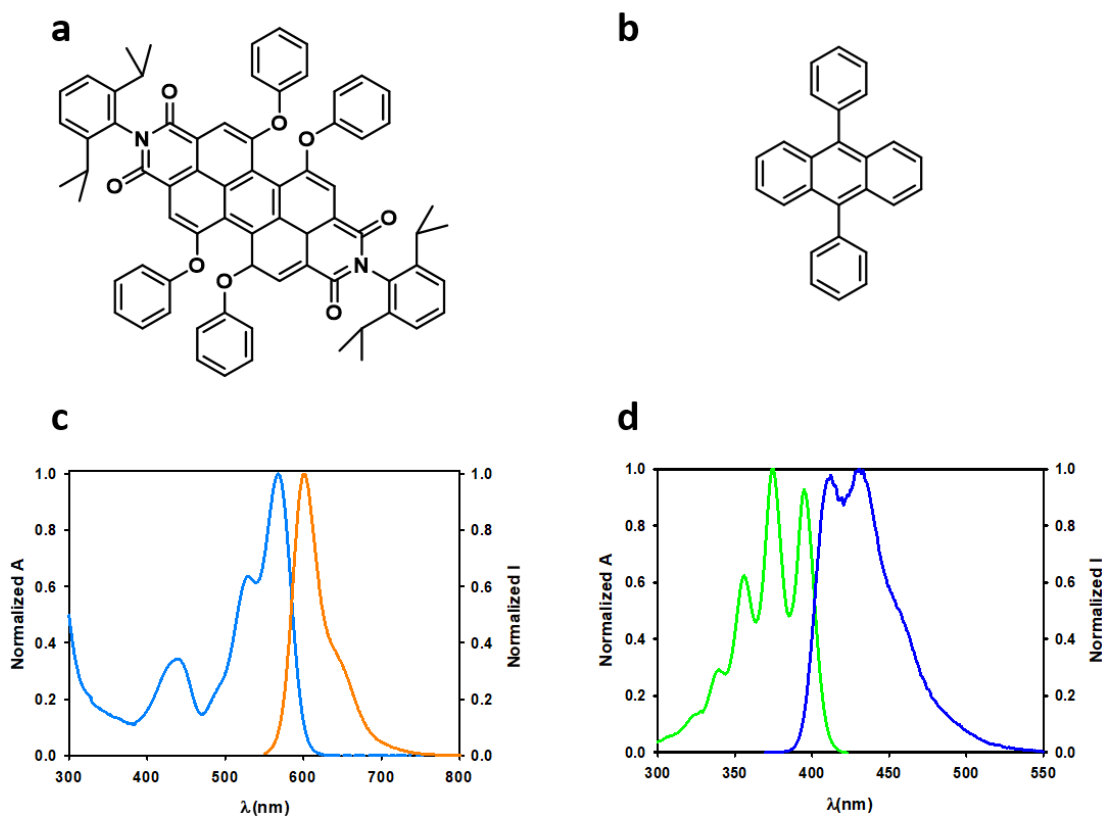
Figure 5.5- (a) **LR** structure; (b) **DPA** structure; (c) **LR** absorption (light blue line) and emission spectra (orange line), λ_{ex}=500 nm; (d) **DPA** absorption (green line) and emission spectra (blue line),), λ_{ex}=375 nm.

LR (absorption and emission spectra reported in **figure 5.5 c**), before being nanoprecipitated together with **SiDDE5**, has been studied with a Stern-Volmer (SV) experiment in order to understand its ability to quench the SiNCs luminescence in a THF solution with the experiment-required concentrations of the two components.

A stock solution of **LR** 3.1×10^{-4} M was prepared and 10 aliquots of this solution were added to a **SiDDE5** solution 7.7×10^{-7} M in THF, so that the **LR** concentration changes in the range from 5×10^{-6} M to 5×10^{-5} M. Absorption (**figure 5.6**) and emission spectra (not reported since it never changes), as well as the decay of **SiDDE5** luminescence

131

(reported in **figure 5.7** even if it is almost always the same) were acquired after every addition of **LR**.
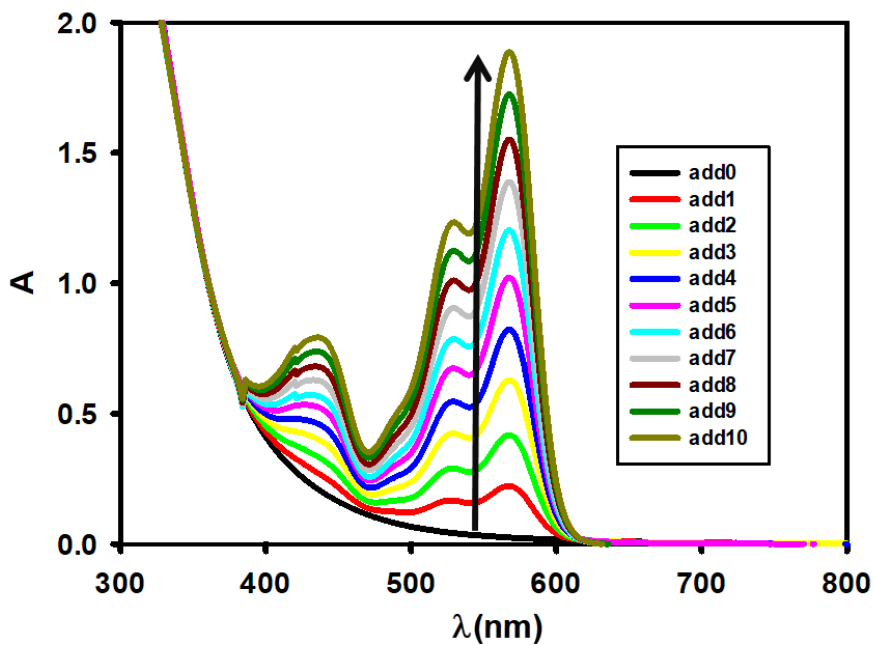
Figure 5.6- absorption spectra of **SiDDE5** upon every addition of **LR** in THF solution
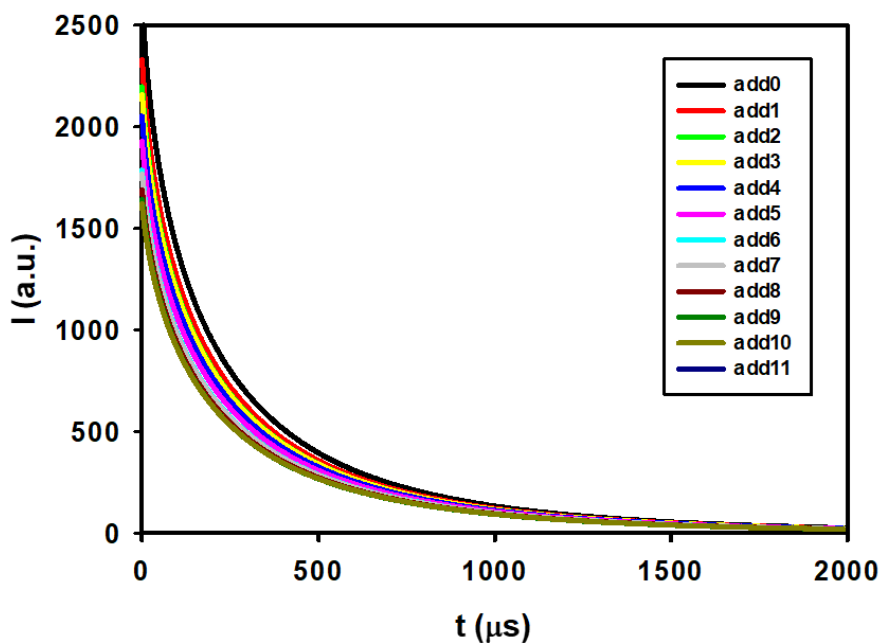
Figure 5.7- decay of **SiDDE5** luminescence upon every addition of **LR** in THF. λex= 380 nm, cut-off filter at 715nm.

Figure 5.8 shows how the **SiDDE5** luminescence lifetime changes upon every **LR** addition. The τ value does not change over the time, thus **LR** does not quench **SiDDE5** luminescence, also at the higher concentrations, meaning that it is a good candidate for nanoprecipitation experiments.
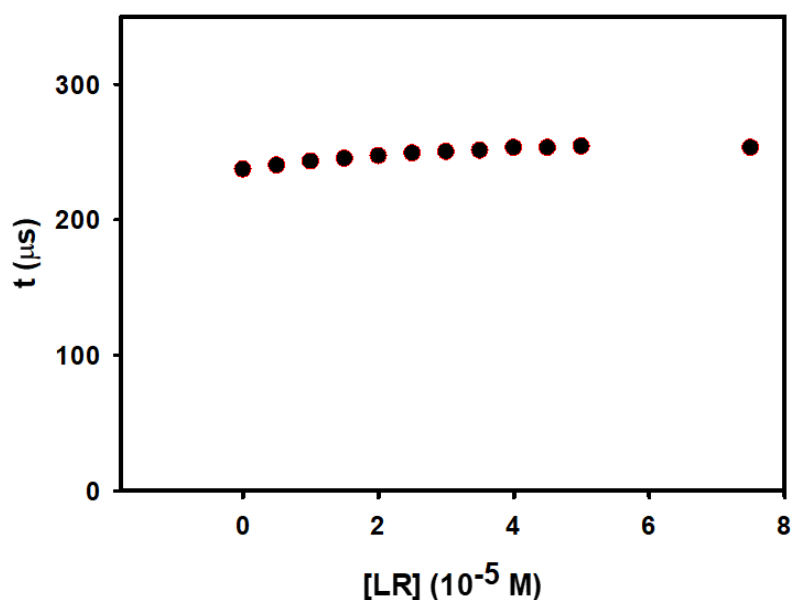
Figure 5.8- luminescence lifetimes of **SiDDE5** upon every addition of **LR** in THF. λex= 380 nm, cut-off filter at 715 nm

The synthesis of the dyes-loaded and -or- SiNCs-loaded **PNPs** followed an adaptation of a literature procedure.[168,219,222,232] A 10 g/L THF solution of the polymer **PMMA-SO₃H** was prepared by weighing 20 mg of the pre-formed polymer and dissolving them in 2 mL of THF. The solution was stirred overnight and then stored in a fridge. The nanoprecipitation optimized procedure uses 2 g/L **PMMA-SO₃H** THF solution, **LR** 0.5 wt% in THF respect to **PMMA-SO₃H**, **SiDDE5** 1.5 μM in THF solution. Four different samples were made, the **empty PNPs**, the **PNPs+LR+SiDDE5**, the **PNPs+SiDDE5** and the **PNPs+LR**. For the synthesis of the **empty PNPs** sample the 10 g/L **PMMA-SO₃H** THF solution was diluted fivefold in THF in order to obtain the 2 g/L solution. This solution was added quickly and under stirring (shaking at 1000 rpm) using a micropipette to a tenfold volume excess

133

of Milli-Q water. The particle solution was then filtered with a 0.2 μm hydrophilic filter. The sample **PNPs+LR+SiDDE5** was then prepared. This time, the 10 g/L solution of **PMMA-SO₃H** was diluted fivefold in THF containing **LR** 0.5 wt% respect to **PMMA-SO₃H** and **SiDDE5** 1.5 μM in order to obtain the 2 g/L solution of **PMMA-SO₃H**. This solution was added quickly and under stirring (shaking at 1000 rpm) using a micropipette to a tenfold volume excess of Milli-Q water. The particle solution was then filtered with a 0.2 μm hydrophilic filter. For the sample **PNPs + SiDDE5,** the 10 g/L solution of **PMMA-SO₃H** was diluted fivefold in THF containing **SiDDE5** 1.5 μM in order to obtain the 2 g/L solution of **PMMA-SO₃H**. This solution was added quickly and under stirring (shaking at 1000 rpm) using a micropipette to a tenfold volume excess of Milli-Q water. The particle solution was then filtered with a 0.2 μm hydrophilic filter. In the end, the **PNPs+LR** sample was prepared. The 10 g/L solution of **PMMA-SO₃H** was diluted fivefold in THF containing **LR** 0.5 wt% respect to **PMMA-SO₃H** in order to obtain the 2 g/L solution of **PMMA-SO₃H**. This solution was added quickly and under stirring (shaking at 1000 rpm) using a micropipette to a tenfold volume excess of Milli-Q water. The particle solution was then filtered with a 0.2 μm hydrophilic filter. The four nanoprecipitated samples were stored in a fridge.

Four more samples were then synthesised, **empty PNPs**, the **PNPs+DPA+SiDDE5**, the **PNPs+SiDDE5** and the **PNPs+DPA.** The synthetic procedure is the same used for all the **LR** containing samples but with a different chromophore concentration (**DPA** absorption and emission spectra are reported in **figure 5.5 d**). The optimized procedure in this case uses 2 g/L **PMMA-SO₃H** THF solution, **DPA** 10 wt% in THF respect to **PMMA-SO₃H** and **SiDDE5** 1.5 μM in THF solution. Even this time the four nanoprecipitated samples were stored in a fridge.

5.3 Results and Discussions

Photophysical Properties of LR-Loaded and Silicon Nanocrystals-Loaded Polymer Nanoparticles

In **figure 5.9 empty PNPs, PNPs+LR+SiDDE5, PNPs+SiDDE5** and **PNPs+LR** absorption spectra are reported. **PNPs+LR+SiDDE5** shows the sum of the featureless SiNCs absorption spectrum and the **LR** spectrum with its characteristic peak with the maximum absorption wavelength at λ = 560 nm, indicating that no ground interaction are occurring. Furthermore, SiNCs are not precipitating or aggregating during the nanoprecipitation in MilliQ water.
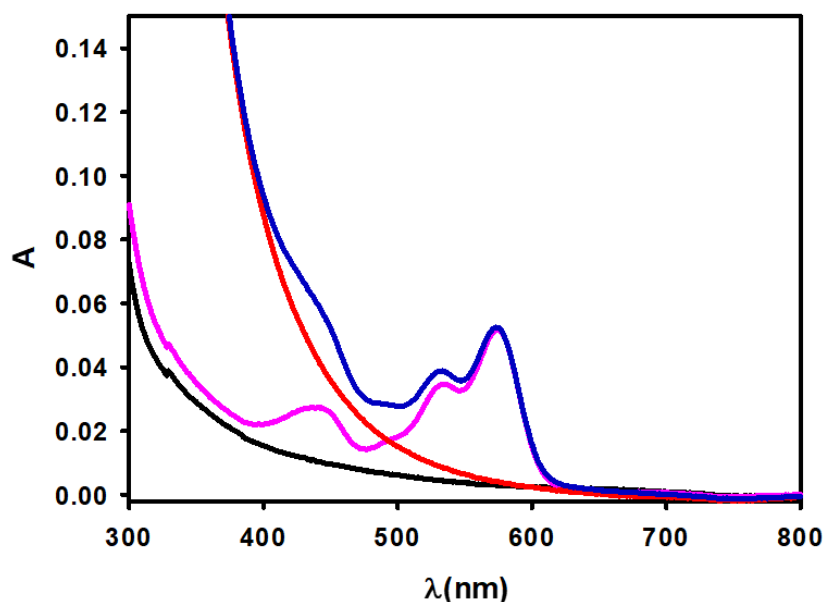
Figure 5.9- empty PNPs (black line), **PNPs+LR+SiDDE5** (blue line), **PNPs+SiDDE5** (red line) and **PNPs+LR** (pink line) absorption spectra

In **figure 5.10 LR** emission spectra of **PNPs+LR+SiDDE5** and **PNPs+LR** nanoprecipitated samples are reported, exciting at λ_{exc} = 560 nm, where the two samples show exactly the same absorption value. The **LR** emission quenching in the sample containing both the SiNCs and the dyes is evident, indicating a possible EET

from the chromophores (donors) to the encapsulated SiNCs (acceptors). The quenching efficiency was then calculated (see appendix A for more details) to be equal to 30%.
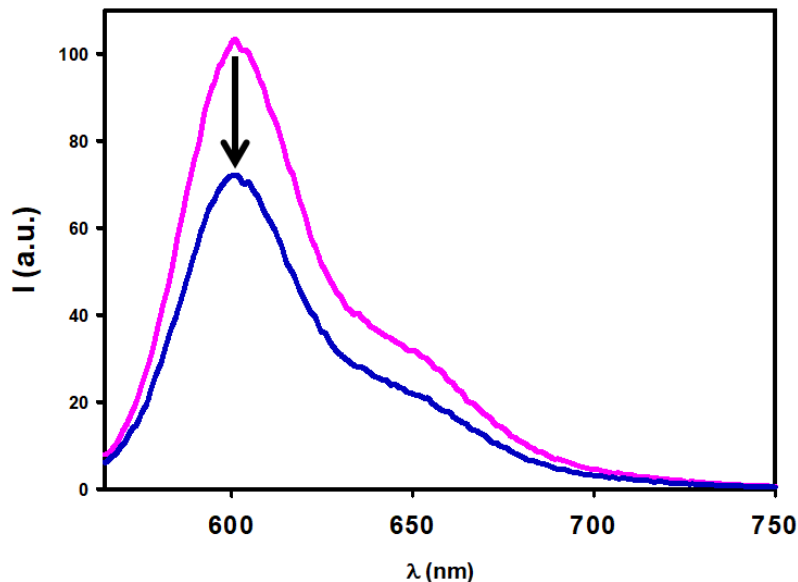
Figure 5.10- LR emission spectra of **PNPs+LR+SiDDE5** (blue line) and **PNPs+LR** (pink line) samples, in MilliQ water. λ_{exc}= 560 nm, where the two samples have the same absorption
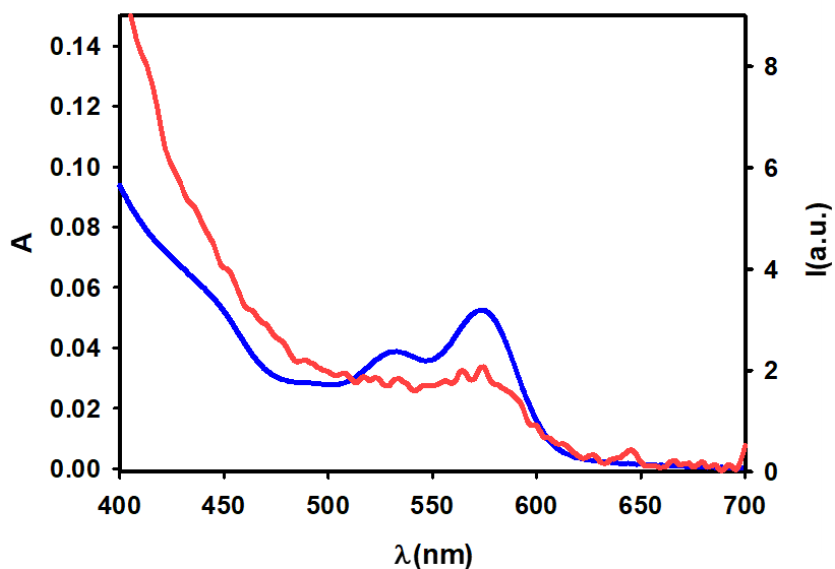
Figure 5.11- Absorption (blue line) and excitation spectra (red line) of **PNPs+SiDDE5+LR** obtained setting λ_{em} = 850 nm and a 0.05 ms detection delay

The excitation spectrum is a powerful mean to verify the existence of the energy transfer between the chromophores and the acceptors, the excitation spectrum need to be similar and superimposable with the absorption one (**figure 5.11**). Excitation spectra (**figure 5.12**) were acquired by setting the emission wavelength at $\lambda_{em} = 850$ nm, where only the SiNCs emits, and by scanning the spectral region from $\lambda = 300$ nm to $\lambda = 700$ nm, where the sample absorb the light. An increasing detection delay was set for the sample **PNPs+SiDDE5+LR** (starting from no delay and reaching 0.05 ms of delay); while a 0.05 ms detection delay was set for the sample **PNPs+SiDDE5.** **PNPs+SiDDE5+LR** spectra shows the **LR** contribution, which unlikely decreases by incrementing the detection delay, nevertheless, even setting a 0.05 ms delay, is still possible to observe the **LR** characteristic peak from 500 to 600 nm, indicating the existence of a (weak) energy transfer.
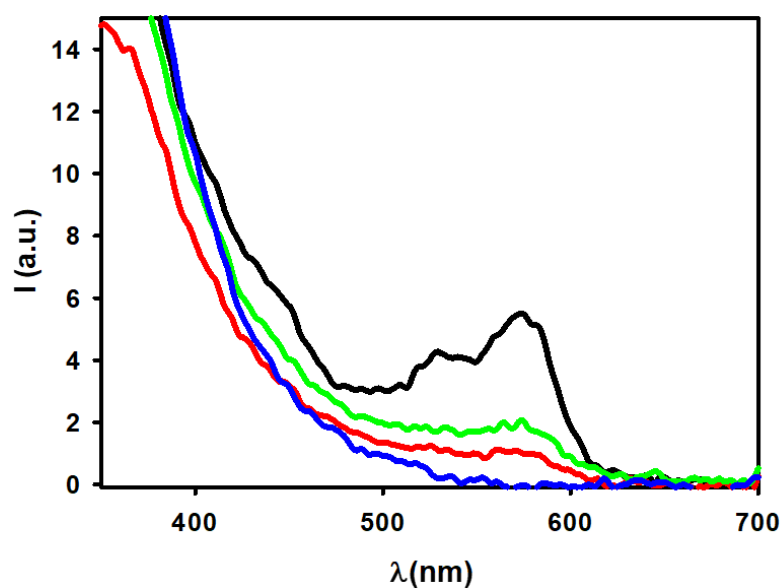
Figure 5.12- PNPs+SiDDE5+LR excitation spectra in Milli-Q water, obtained setting $\lambda_{em} = 850$ nm and an increasing detection delay: no delay (black line), 0.03 ms delay (green line), 0.05 ms delay (red line) and **PNPs+SiDDE5** excitation spectra in Milli-Q water, obtained setting $\lambda_{em} = 850$ nm and a detection delay of 0.05 ms (blue line).

The SiNCs emission quenching, which did not happen during the SV experiment, is unlikely seen, due to the presence of the **SiDDE5** and **LR** molecules confined in a very little space (inside the **PNPs**). This quenching is confirmed by a comparison between the photoluminescence lifetime of the SiNCs encapsulated together with the dyes and the photoluminescence lifetime of the SiNCs encapsulated by themselves (which is equal to **SiDDE5** lifetime in a THF solution) (**table 5.1**). For this reason, it was impossible to acquire the Silicon emission spectrum, which was very low and partially superimposed with the intense **LR** emission spectrum.

Sample	τ (μs)
SiDDE5 in THF solution	252
PNPs+SiDDE5	250
PNPs+SiDDE5+LR	90

Table 5.1- Silicon photoluminescence lifetimes recorded from the nanoprecipitated samples **PNPs+SiDDE5+LR, PNPs+SiDDE5** and from **SiDDE5** in a THF solution

Sample	τ (ns)
LR in THF solution	7.5
PNPs+LR	7.2
PNPs+SiDDE5+LR	7.9 and 1.8

Table 5.2- LR photoluminescence lifetimes recorded from the nanoprecipitated samples **PNPs+SiDDE5+LR, PNPs+LR** and from **LR** free in a THF solution

Looking at the **LR** photoluminescence lifetimes in the **PNPs+SiDDE5+LR** sample (**table 5.2**), one can assume the presence of an energy transfer: the higher value

138

should be addressed to the **LR** molecules not quenched by the SiNCs, similar to the lifetime registered for both the **LR** free in solution and the **LR** encapsulated by itself, while the lower one to the **LR** molecules quenched by the SiNCs as a consequence of the EET process.

Photophysical Properties of DPA-Loaded and Silicon Nanocrystals-Loaded Polymer Nanoparticles

In **figure 5.13 empty PNPs, PNPs+DPA+SiDDE5, PNPs+SiDDE5** and **PNPs+DPA** absorption spectra are reported. **PNPs+DPA+SiDDE5** shows the sum of the featureless SiNCs absorption spectrum and the **DPA** spectrum with its characteristic peak with the maximum absorption wavelength at λ = 375 nm, indicating that no ground interaction are occurring. Furthermore, SiNCs are not precipitating or aggregating during the nanoprecipitation in MilliQ water.
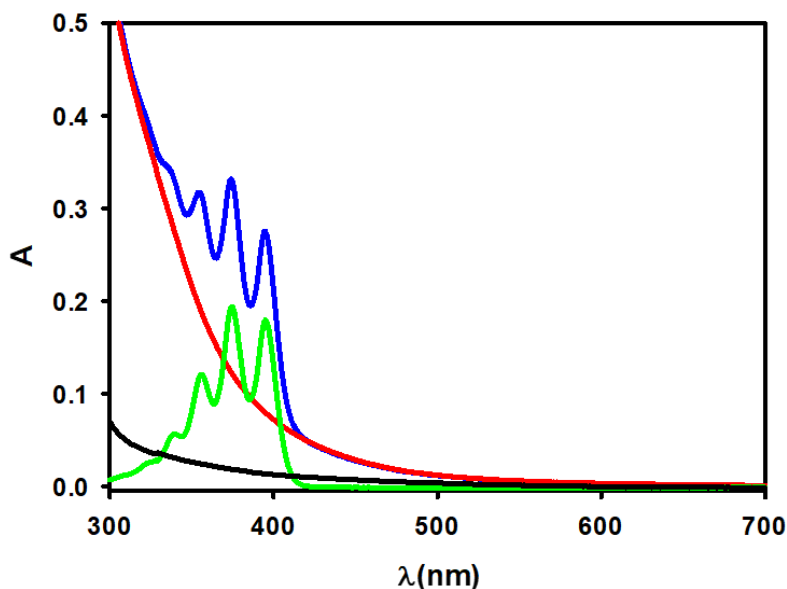
Figure 5.13- empty PNPs (black line), **PNPs+DPA+SiDDE5** (blue line), **PNPs+SiDDE5** (red line) and **PNPs+DPA** (green line) absorption spectra

In **figure 5.14 DPA** emission spectra of **PNPs+DPA+SiDDE5** and **PNPs+DPA** nanoprecipitated samples are reported, exciting at λ_{exc} = 355 nm (**DPA** concentration is the same in the two samples). The **DPA** emission quenching in the sample containing both the SiNCs and the dyes is evident, indicating a possible EET from the chromophores (donors) to the encapsulated SiNCs (acceptors). The quenching efficiency was then calculated (see appendix A for more details) to be equal to 60%.
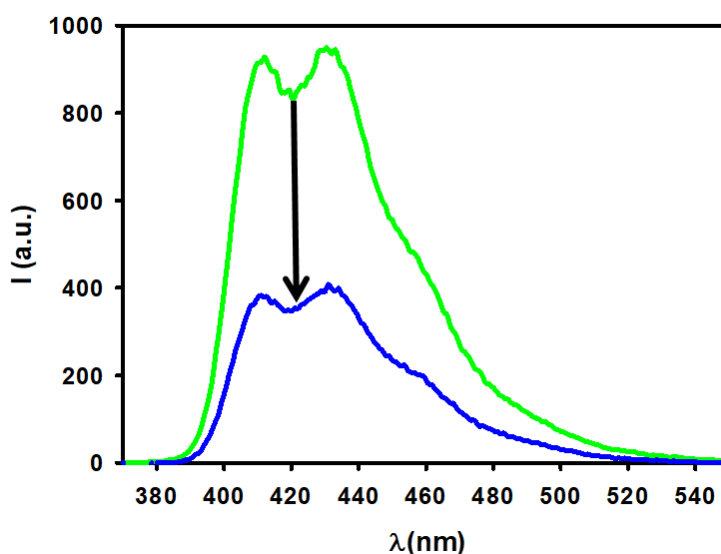
Figure 5.14- **DPA** emission spectra of **PNPs+DPA+SiDDE5** (blue line) and **PNPs+DPA** (green line) samples, in MilliQ water. λ_{exc} = 355 nm (the **DPA** concentration is the same)

SiNCs emission spectra were acquired exciting the **PNPs+DPA+SiDDE5** and **PNPs+SiDDE5** nanoprecipitated samples at λ_{exc} = 375 nm, where SiNCs absorption is the same. The SiNCs sensitized emission in **PNPs+DPA+SiDDE5** respect to **PNPs+SiDDE5** is evident and could be interpreted as another EET sign.
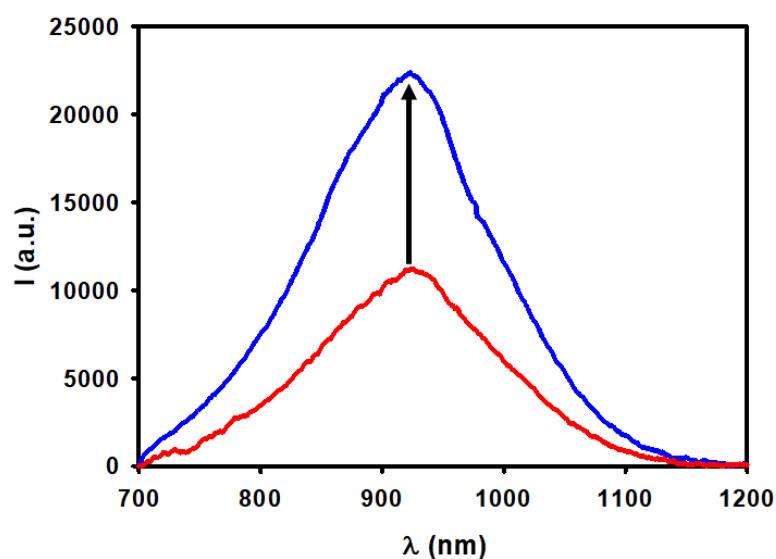
Figure 5.15- **PNPs+SiDDE5+DPA** (blue line) and **PNPs+SiDDE5** (red line) emission spectra in MilliQ water, exciting at λ_{exc} = 375 nm, where the **SiDDE5** concentration is the same.

The **PNPs+SiDDE5+DPA** excitation spectrum, recorded setting λ_{em} = 850 nm and a 0.05 ms detection delay, shows the classic **DPA** peak, proving the EET existence (**figure 5.16**).
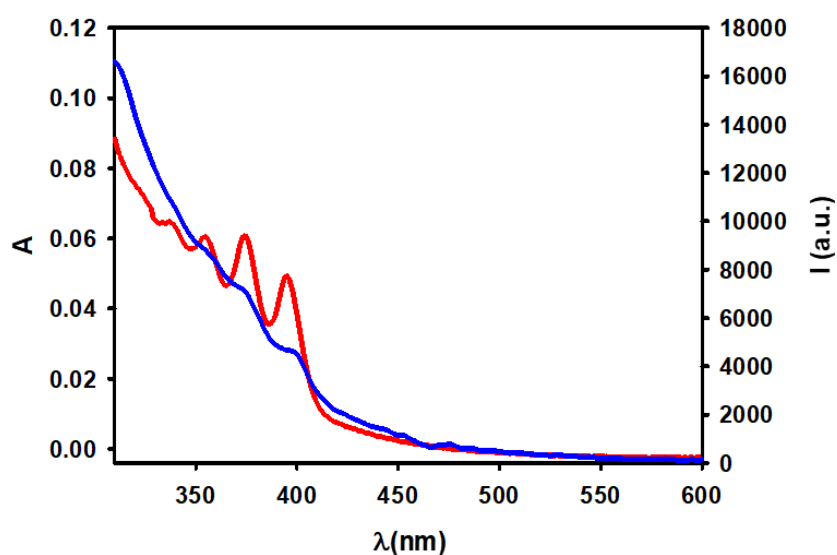
Figure 5.16- Absorption (red line) and excitation spectra (blue line) of **PNPs+SiDDE5+DPA** obtained setting λ_{em} = 850 nm and a 0.05 ms detection delay

The SiNCs emission is not quenched because of the confinement of both **SiDDE5** and **DPA** molecules inside the **PNPs**. This was also confirmed by acquiring the SiNCs photoluminescence lifetime from the **SiDDE5 in THF**, **PNPs+SiDDE5** and **PNPs+SiDDE5+DPA** samples, which did not change neither after the nanoprecipitation of SiNCs by themselves neither after the nanoprecipitation of SiNCs together with the dye molecules (**table 5.3**).

Sample	τ (μs)
SiDDE5 in THF solution	220
PNPs+SiDDE5	200
PNPs+SiDDE5+DPA	200

Table 5.3- Silicon photoluminescence lifetimes recorded from the nanoprecipitated samples **PNPs+SiDDE5+DPA, PNPs+SiDDE5** and from **SiDDE5** in a THF solution

5.4 Conclusions

With the non-covalent method, we have demonstrated that 5 nm diameter SiNCs, previously synthesized and stabilized with dodecyl chains, can be physically encapsulated, together with **LR** or **DPA** units, inside polymer nanoparticles made of **PMMA-SO₃H**, via nanoprecipitation technique. The use of **LR** or **DPA** as the chromophores and as the donors in such light harvesting molecular antenna, avoids the self-quenching caused by π-stacking, which takes place with flat molecules. The fundamental phenomenon observed in this system, at high chromophore concentration, is excitation energy transfer (EET). EET shuttles the excitation energy between the encapsulated dye units until the interaction with an encapsulated SiNC: if it happens, the closest excited dye to the SiNC works as the donor, while the SiNC works as the acceptor. In this way, it is possible to sensitize the SiNCs emission. Through the photophysical characterization, we have showed the EET

presence in both **PNPs+SiDDE5+LR** and **PNPs+SiDDE5+DPA** samples. The EET was lower for the first prepared sample and more intense for the second one. **DPA** quenching measurement showed a good value, equal to 60%.

6 Silicon Nanocrystals Functionalized with Photochromic Azobenzene Units

6.1 Introduction

Photochromic units are widely used as optical switchers since they impart photoresponsive properties to (supra)molecular architectures and materials.[251–254] They are molecules that experience a large and reversible structural change after their optical excitation. Azobenzene belongs to this family of molecules, which has already demonstrated to be a valid candidate for optical storage devices. Azobenzene photochromic properties have already been utilized as a light triggered switch in a variety of polymers,[255,256] surface-modified materials,[257–259] protein probes,[260–263] molecular machines,[264–266] holographic recording devices[267–269] and metal ion chelators.[270–273] Azobenzene shows two isomers, the trans-form, which is thermally stable and characterized by a planar geometry, and the metastable non-planar cis-form, where the two benzene rings are clapped together. An external stimulus is needed for the trans form to be converted into the cis form. Differently, the cis-form relaxes back thermally to the trans-form within several hours. Anyway, the two isomers can be easily interchanged by optical excitations, bringing to not only a change in colour, but also a large structural rearrangement (the *para* carbon atoms distance decreases from 9.0 to 5.5 Å) and an evident increase in the dipole moment from zero to 3.0 Debye by converting the trans to the cis isomer (**figure 6.1**).[274,275] The azobenzene absorption spectrum shows two distinct bands: a strong $\pi\pi^*$ absorption band peaking at ca. 290 nm (cis-form) and 320 nm (trans-form) and a much weaker $n\pi^*$ band with a peak around 440 nm (cis and trans-form). The reported wavelengths slightly depend on the used solvent and on the possible

connected chains to the original azobenzene structure, which is also valid for the photoisomerization quantum yields.[275] Azobenzene also exhibits remarkable photostability as negligible decomposition occurs even after prolonged irradiation.[251]
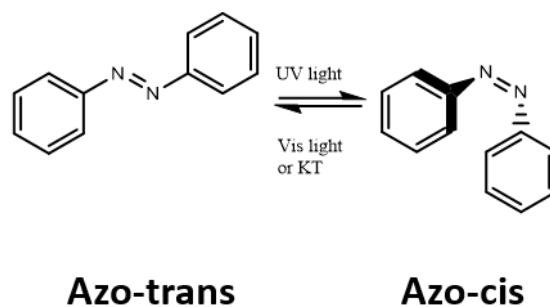
Figure 6.1- Azobenzene isomerization reaction

In recent years, several photo-switchable Quantum Dots (QDs) have been designed. Most of them operate on the same principle: photo-responsive molecules are bound to the surface of QDs and they change their configuration if excited by light with different wavelengths. These configurations have different absorption spectra, with one capable of quenching QD fluorescence efficiently through Förster resonance energy transfer (FRET) or electron transfer and the other having a low quenching efficiency.[276] In the literature there are many cases of photochromic units functionalized QDs such as CdS,[277–280] CdSe,[281] CdTe,[282] CuO,[283] ZnSe,[284] core-shell CdSe/ZnS,[285286] core–shell–shell CdSe/CdS/ZnS,[287]. Herein, we report for the first time Silicon Nanocrystals (SiNCs) functionalized with photochromic units. Two different azobenzene derivatives have been attached onto the SiNCs surface, both synthesized in our laboratory, in order to study the effects on the SiNCs' photophysical and photochemical properties. The reasons why SiNCs are attractive materials[47] have already been shown in the previous chapters of this dissertation.[129,164,218] The azobenzene derivatives have been attached on the SiNCs surface thanks to a three step procedure, first involving the synthesis of a

145

chlorosilane-terminated SiNCs sample, second its reaction with the azobenzene derivative and third a capping step of the eventual non-reacted sites to prevent SiNCs oxidation, degradation and precipitation. We report the photophysical and photochemical properties of the two samples, using the two different azobenzene derivatives, making a comparison between their trans and cis isomers in terms of PLQY, PL lifetime, maximum emission wavelength, number of attached photochromic units, photoisomerization QY, dispersibility in different solvents, chemical stability and photostability.

6.2 Synthesis of Azobenzene Derivatives-Functionalized SiNCs

A cloudy solution of free-standing hydride terminated Silicon Nanocrystals (H-SiNCs) in toluene was prepared thanks to the disproportionation reaction of hydrogen silsesquioxane (HSQ, $[HSiO_{3/2}]_n$) (see chapter 2 for more details), previously synthesized in our laboratory, setting up the furnace at 1100 °C to obtain SiNCs with 3.5 nm average diameter embedded in SiO_2, followed by the etching procedure using a mixture of EtOH:H_2O:HF=1:1:1.[47,129,218] H-SiNCs surface was then functionalized with a three-step reaction path: (i) a room temperature diazonium salt (4-decylbenzene diazonium tetrafluoroborate, 4-DDB) activated hydrosilylation, in the presence of chloro(dimethyl)vinylsilane, yields chlorosilane-passivated SiNCs (**Si-DMVSiCl**, **figure 6.2.a**); (ii) a second room temperature reaction-step mediated by a primary alcohol such as (E)-3-(4-(phenyldiazenyl)phenoxy)propan-1-ol (**AzoC₃OH**) to yield **Si-O-C₃Azo** (**figure 6.2.a.2**), or 2-(2-(2-(4-(phenyldiazenyl)phenoxy)ethoxy)ethoxy)ethan-1-ol (**AzoPeg**) to yield **Si-O-PegAzo** (**figure 6.2.a.3**), in the presence of imidazole; (iii) a third "capping" step by simply adding butanol to the reaction mixture in order to cap the previously unreacted chlorosilane functional groups on the SiNCs surface. The

three steps above were carried out in a nitrogen-filled glove box. A control sample was also synthesized, **SiBuOH** (**figure 6.2.a.1**), obtained by following the previously reported three-step reaction choosing butanol as the primary alcohol.
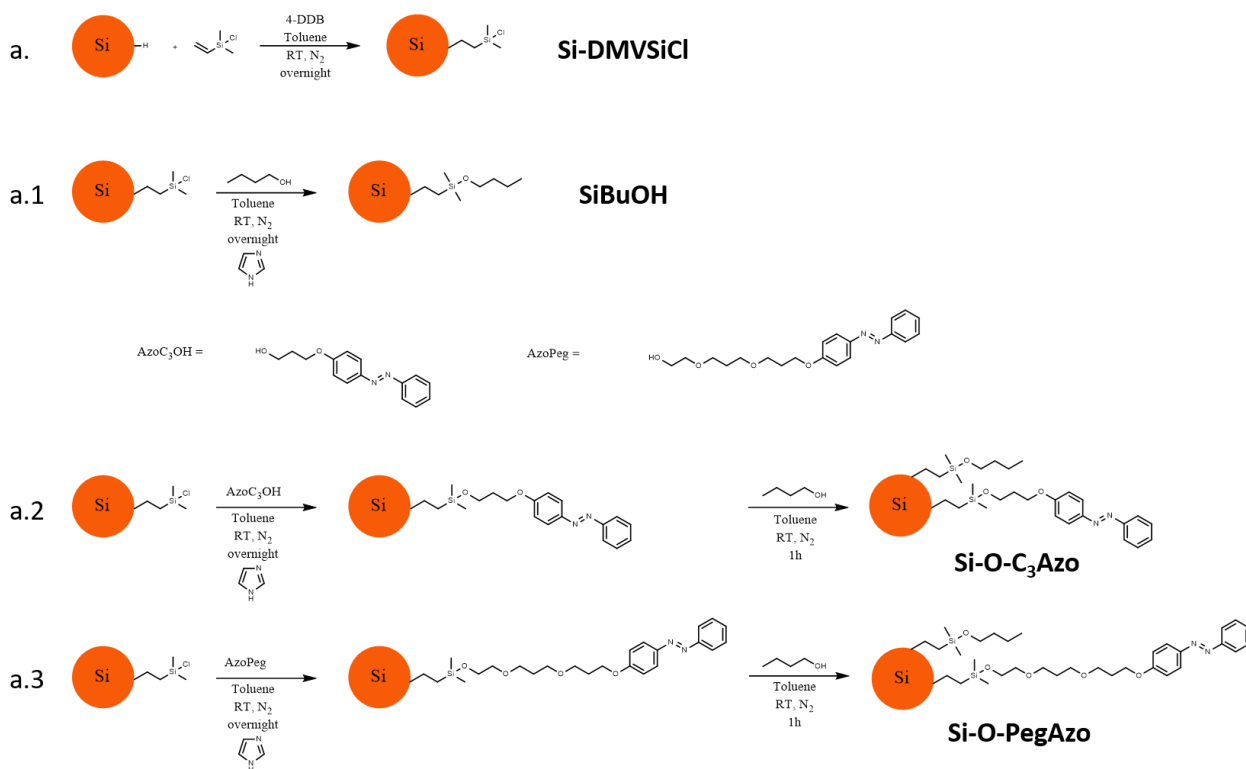
Figure 6.2- Synthetic procedure for the functionalization of hydride-terminated SiNCs by chloro(dimethyl)vinylsilane (**a.**, **Si-DMVSiCl**) followed by three different post-functionalization paths with butanol (**a.1**, **SiBuOH**), (E)-3-(4-(phenyldiazenyl)phenoxy)propan-1-ol (**a.2**, **Si-O-C₃Azo**) and 2-(2-(2-(4-(phenyldiazenyl)phenoxy)ethoxy)ethoxy)ethan-1-ol (**a.3**, **Si-O-PegAzo**).

6.2.1 SiNCs Passivated with Chlorodimethylvinylsilane

Hydride-terminated SiNCs, obtained after the etching procedure of 300 mg oxide-embedded SiNCs powder (see chapter 2 for more details), were dispersed in 1.5 mL of dry toluene and two milligrams of 4-DDB (about 6 μmol) were added together with 400 μL of chlorodimethylvinylsilane (DMVSiCl, 3 mmol) to obtain the sample

Si-DMVSiCl (**figure 6.2.a**). The mixture was stirred overnight inside a nitrogen-filled glovebox at RT. The mixture of chlorosilane-passivated SiNCs was then filtered, concentrated under vacuum to remove the DMVSiCl in excess, then refilled with 3 mL of fresh anhydrous toluene and kept under inert atmosphere.

6.2.2 Synthesis of (E)-3-(4-(phenyldiazenyl) phenoxy) propan-1-ol

(E)-3-(4-(phenyldiazenyl)phenoxy)propan-1-ol (**AzoC₃OH**, **figure 6.2**) is one of the two employed azobenzene derivatives to functionalize the SiNCs surface. It was synthesised in our laboratory, following a literature reported procedure (**figure 6.3**).[288]
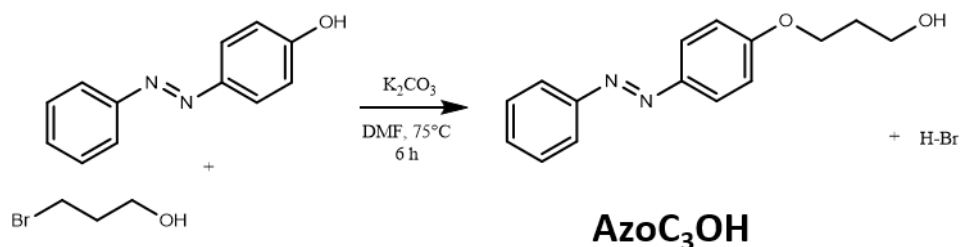
Figure 6.3- Reaction scheme for the (E)-3-(4-(phenyldiazenyl)phenoxy)propan-1-ol (**AzoC₃OH**) synthesis.

To a suspension of degassed dimethylformamide (DMF, 10 mL) and previously anhydrified K_2CO_3 (525 mg, 3.8 mmol), under nitrogen atmosphere, 4-phenylazophenol (507 mg, 2.56 mmol), was added at room temperature. The resulting mixture was stirred until the complete dissolution of the solid compounds. Thus, 3-bromo-1-propanol (0.3 mL, 3.3 mmol) was added. The resulting reaction mixture was heated 6 hours at 75°C and then cooled to room temperature. The formation of an orange precipitate was observed. 80 mL of distilled water were added to the reaction mixture, the organic phase was separated from the aqueous

one and the latter was extracted 4 times using 20 mL of DCM each time. All the organic phases were unified, washed with a brine solution, anhydrified over Na$_2$SO$_4$, filtered and concentrated in vacuum. The crude orange oil was purified via flash chromatography using DCM/EtOAc 8:1 as the eluent. The product was recovered as an orange solid after evaporation of solvents, with a yield of 88% (577 mg, 2.25 mmol).
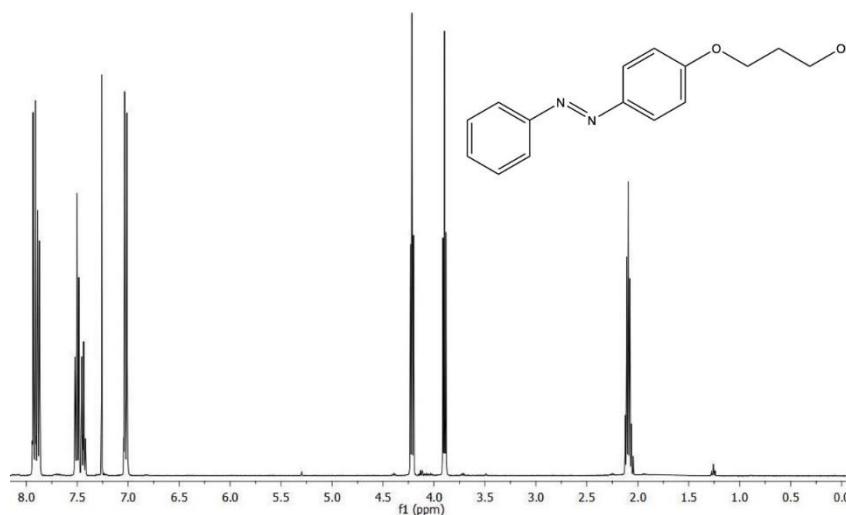
Figure 6.4- (E)-3-(4-(phenyldiazenyl)phenoxy)propan-1-ol ^{1}H-NMR spectrum in CDCl$_3$.

^{1}H-NMR (400 MHz, CDCl$_3$), δ 7.92 ppm (d, J = 9.0 Hz, 2H), 7.88 ppm (d, J = 7.1 Hz, 2H), 7.55 – 7.41 ppm (m, 3H), 7.02 ppm (dt, J = 9.0 Hz, 2.6 Hz, 2H), 4.22 ppm (t, J = 6.0 Hz, 2H), 3.90 ppm (t, J = 5.9 Hz, 2H), 2.09 ppm (p, J = 6.0 Hz, 2H); 7.26 ppm (s, CDCl$_3$), 5.30 ppm (s, DCM), 4.12 ppm (q, EtOAc), 2.05 ppm (s, EtOAc), 1.26 ppm (t, EtOAc) (**figure 6.4**).

6.2.3 Synthesis of 2-(2-(2-(4- (phenyldiazenyl) phenoxy) ethoxy) ethoxy) ethan-1-ol

2-(2-(2-(4- (phenyldiazenyl) phenoxy) ethoxy) ethoxy) ethan-1-ol (**AzoPeg**, **figure 6.2**) is the other employed azobenzene derivative to functionalize the SiNCs surface. It was synthesised in our laboratory, following a literature reported procedure (**figure 6.5**).[274]
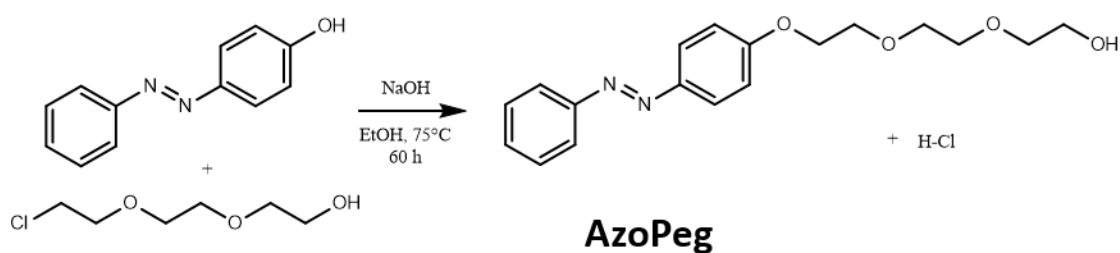
Figure 6.5- Reaction scheme for the (E)-3-(4-(phenyldiazenyl)phenoxy)propan-1-ol (**AzoPeg**) synthesis.

To a solution of absolute EtOH (30 mL) and NaOH (410 mg, 10 mmol), under nitrogen atmosphere, 4-phenylazophenol (2 g, 10 mmol), was added. The resulting mixture was stirred until the complete dissolution of the solid compounds. Thus, a solution of 2-[2-(2- chloroethoxy)ethoxy]ethanol (4.3 g, 25 mmol,) in EtOH (5mL) was added dropwise. The resulting reaction mixture was heated under stirring for 60 hours at 75°C and then cooled to room temperature. Ethanol was removed from the reaction mixture and the raw red oil was purified by filtration through a pad of silica gel with n-hexane/ethyl acetate 7:2 as an eluent to remove the unreacted 4-phenylazophenol and then with ethyl acetate to recover the desired product. The solvent was evaporated under reduced pressure and the obtained red oil was purified by distillation in a Kugelrohr apparatus (Buchi) at 125°C and 0.5 mmHg. The product was obtained as a red-orange crystalline solid (2.5 g, 7.7 mmol, yield 76%).

^{1}HNMR (400 MHz, CDCl$_3$): δ 7.91 ppm (d, J = 9.0, 2H), 7.87 ppm (d, J = 7.0 Hz, 2H), 7.49 ppm (t, J = 7.0 Hz 2H), 7.42 ppm (t, 7.0 Hz 1H), 7.02 ppm (d, J = 9.0 2H), 4.19 ppm (m, 2H), 3.87 ppm (m, 2H), 3.70 ppm (m, 6H), 3.60 ppm (m, 2H).

6.2.4 Passivation of SiNCs with Butanol to obtain the SiBuOH Sample

The **SiBuOH** control sample (**figure 6.2.a.1**) was synthesised by adding butanol (0.14 mL, 1.5 mmol) to a 1 mL of the previously prepared **Si-DMVSiCl** solution, together with a catalytic amount of imidazole. The reaction was stirred for 12 h inside a nitrogen-filled glove box. Thus the sample was washed by adding 5 mL of dry ACN to the reaction mixture, the precipitated SiNCs were collected on a PTFE filter, washed other 3 times with 5 mL of dry ACN and then dispersed in 1 mL of distilled toluene.

6.2.5 Passivation of SiNCs with (E)-3-(4- (phenyldiazenyl) phenoxy) propan-1-ol to obtain the Si-O-C$_3$Azo Sample

The **Si-O-C$_3$Azo** sample (**figure 6.2.a.2**) was synthesised by adding (E)-3-(4-(phenyldiazenyl) phenoxy) propan-1-ol (33 mg, 0.13 mmol) to a 1 mL of the previously prepared **Si-DMVSiCl** solution, together with a catalytic amount of imidazole. The reaction was stirred for 12 h inside a nitrogen-filled glove box and then 0.1 mL of butanol were added in order to cap the non-reacted Si-Cl groups on the Si surface. The reaction mixture was stirred for another hour. Thus the sample was washed by adding 5 mL of dry ACN to the reaction mixture, the precipitated SiNCs were collected on a PTFE filter, washed other 3 times with 5 mL of dry ACN and then dispersed in 1 mL of distilled toluene or cyclohexane.

6.2.6 Passivation of SiNCs with 2-(2-(2-(4-(phenyldiazenyl) phenoxy) ethoxy) ethoxy) ethan-1-ol to obtain the **Si-O-PegAzo** Sample

The **Si-O-PegAzo** sample (**figure 6.2.a.3**) was synthesised by adding 2-(2-(2-(4-(phenyldiazenyl) phenoxy) ethoxy) ethoxy) ethan-1-ol (43 mg, 0.13 mmol) to a 1 mL of the previously prepared **Si-DMVSiCl** solution, together with a catalytic amount of imidazole. The reaction was stirred for 12 h inside a nitrogen-filled glove box and then 0.1 mL of butanol were added in order to cap the eventual non-reacted Si-Cl groups on the Si surface. The reaction mixture was stirred for another hour. Thus the sample was washed by adding 5 mL of dry ACN to the reaction mixture, the precipitated SiNCs were collected on a PTFE filter, washed other 3 times with 5 mL of dry ACN and then dispersed in 1 mL of distilled toluene or cyclohexane.

6.3 Results and Discussions

Photophysical Characterization in Solution

Figure 6.6 reports absorption and photoluminescence spectra for **Si-O-C₃Azo-trans**, **Si-O-C₃Azo-cis**, **Si-O-PegAzo-trans** and **Si-O-PegAzo-cis**; while **figure 6.7** reports absorption and photoluminescence spectra for **SiBuOH**. The **Si-O-C₃Azo** absorption spectrum perfectly matches the one of **SiBuOH,** the control sample, plus **AzoC₃OH,** suggesting that no ground state interaction is affecting their optical properties (**figure 6.8**). This is also true for **Si-O-PegAzo**.
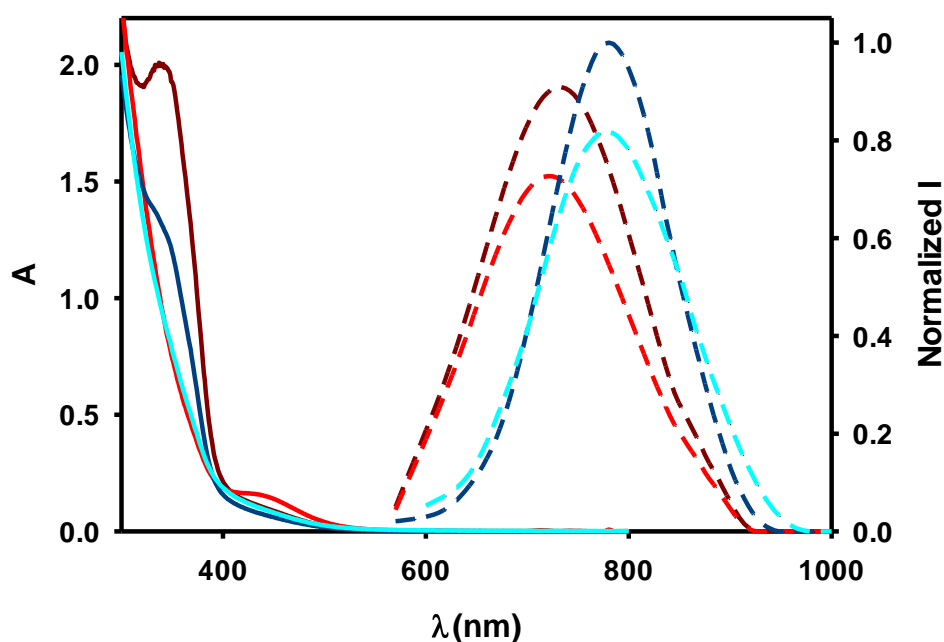
Figure 6.6- Absorption (solid lines) and photoluminescence spectra (dashed lines) of **Si-O-C₃Azo-trans** (dark red lines), **Si-O-C₃Azo-cis** (light red lines), **Si-O-PegAzo-trans** (dark blue lines) and **Si-O-PegAzo-cis** (light blue lines) in toluene, exciting at λ=540 nm. Photoluminescence spectra intensities are corrected for the different samples' PLQY.
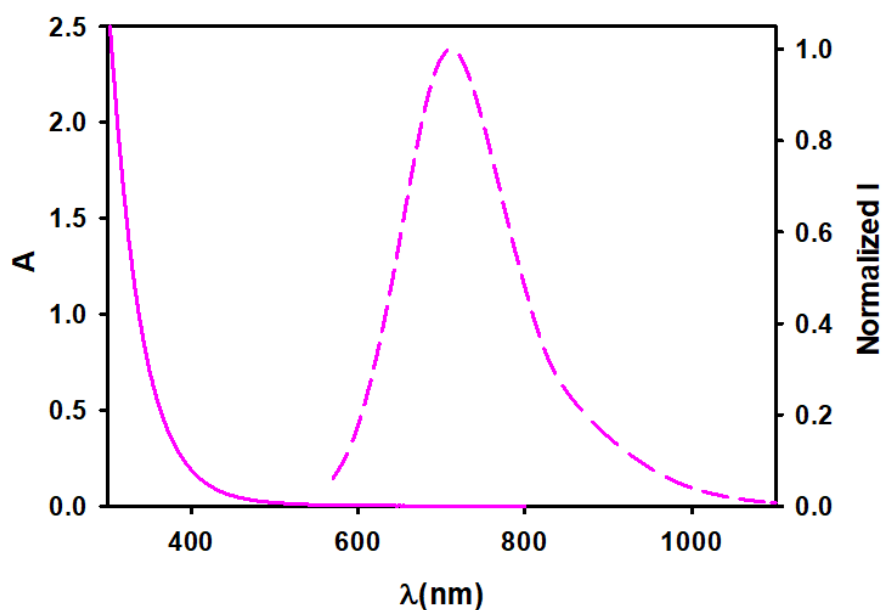
Figure 6.7- Absorption (solid line) and normalized photoluminescence spectra (dashed line) of **SiBuOH** in toluene, exciting at λ=540nm.
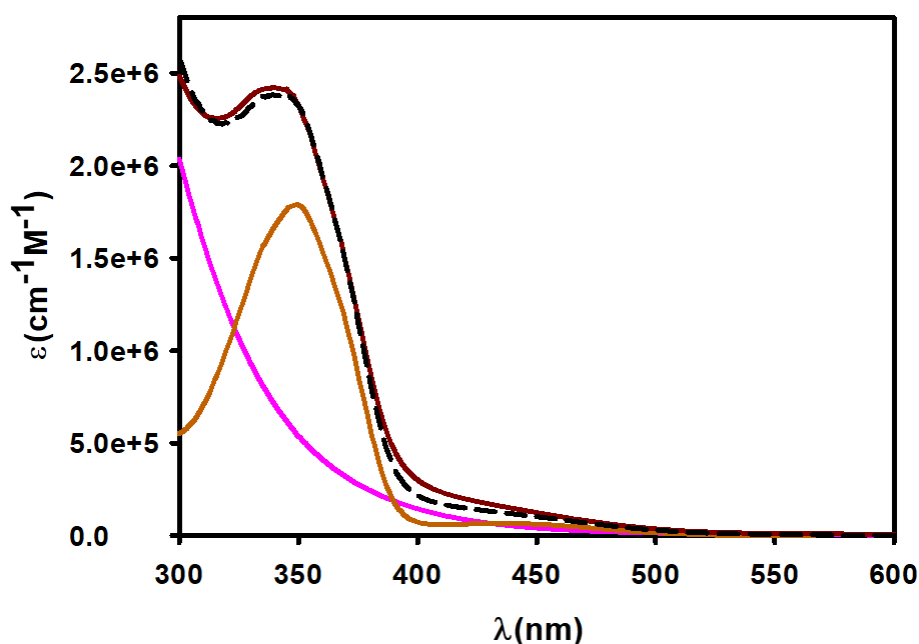
Figure 6.8- Molar absorption coefficient versus wavelength of **SiBuOH** (pink line), **AzoC₃OH** (dark orange line), **Si-O-C₃Azo** (dark red line) and physical mixture of **SiBuOH** + **AzoC₃OH** (dashed black line), in toluene.

Considering the molar absorption coefficient of SiNCs we measured in recent works,[101,129] (ε_{430} nm = 1 × 10⁵ M⁻¹ cm⁻¹ for 3.5 nm diameter) and the calculated molar absorption coefficients of the trans isomer of the two azobenzene derivatives (**AzoC₃OH** $\varepsilon_{350(Trans)}$ nm = 2.8 × 10⁴ M⁻¹ cm⁻¹; **PegAzo** $\varepsilon_{350(Trans)}$ nm = 2.5 × 10⁴ M⁻¹ cm⁻¹) we estimated an average number of about 80 and 65 photochromic units per SiNC, covalently attached as shown in **figure 6.2**. We hypothesized that the worst outcome of the **PegAzo** involving reaction is due to the presence of a residual amount of water in the sample, which causes the hydrolysis of the new forming bonds.

Si-O-C₃Azo and **Si-O-PegAzo** show a photoluminescence band with a maximum emission wavelength at about 750 nm and 790 nm respectively (**figure 6.6**), similar to the control sample **SiBuOH** (**figure 6.7**). **Si-O-PegAzo** emission band is slightly red shifted with respect to the one of **Si-O-C₃Azo**, probably due to the higher

polarity of the peg chains. We can also evidence no particular changes in the photoluminescence band of **Si-O-C₃Azo-trans** and **Si-O-C₃Azo-cis**. The same is also valid for **Si-O-PegAzo-trans** and **Si-O-PegAzo-cis**. The PL quantum yields (PLQY) of the SiNCs in all the prepared samples were measured upon selective excitation of the Si core at 540 nm, where only the SiNCs can absorb the light, avoiding the azobenzene derivatives absorption. The resulting values, together with the measured luminescence lifetimes (τ) and the photoluminescence band maximum (λ_{max}) are reported in **table 6.1**.

	λ_{max} **(nm)**	**PLQY (%)**	**τ (μs)**
SiBuOH	750	35	80
Si-O-C₃Azo-trans	750	10	45
Si-O-C₃Azo-cis	750	8	40
Si-O-PegAzo-trans	790	11	43
Si-O-PegAzo-cis	790	9	40

Table 6.1- Photoluminescence band maximum (λmax), quantum yield (PLQY) and lifetime (τ) of **SiBuOH**, **Si-O-C₃Azo-trans**, **Si-O-C₃Azo-cis**, **Si-O-PegAzo-trans** and **Si-O-PegAzo-cis** in toluene.

Considering the reported values in **table 6.1,** we can evidence a PLQY and a τ decrease in all the azobenzene derivatives-functionalized samples with respect to the control sample **SiBuOH**. The partial deterioration of the SiNCs' photophysical properties could be due to an electron or energy transfer process from the Si core to

the azobenzene derivatives covalently linked to its surface. To better study the possible energy transfer process, which is theoretically allowed considering the SiNCs band gap and the azobenzene triplet state energies,[289] we decided to excite the SiNCs of a **Si-O-C₃Azo-trans** degassed solution with a 590 nm emitting LED. Since the triplet state is involved in the azobenzene photoisomerization reaction,[290] the **Si-O-C₃Azo-trans** absorption variation is a demonstration of the energy transfer process to occur (**figure 6.9**).
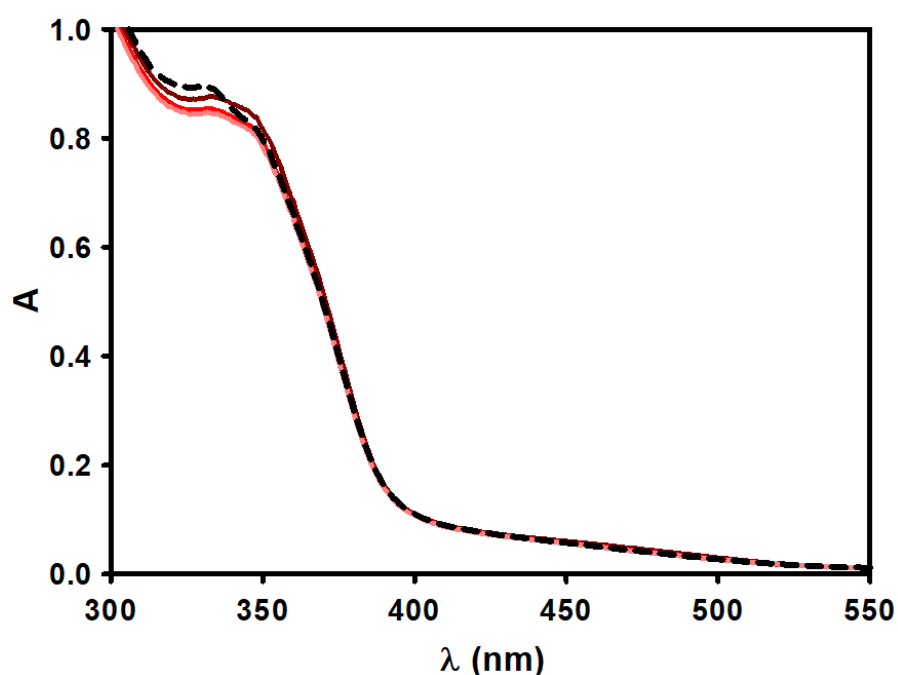
Figure 6.9- Si-O-C₃Azo-trans absorption variation under 590 nm LED irradiation, in toluene. The dark red spectrum was acquired before the irradiation (all trans), the red and pink spectra after 1 and 2 hours of irradiation respectively and the black dashed spectrum after the thermal return.

Figure 6.9 also shows the thermal return of the azobenzene derivatives onto the Si surface, which is a further demonstration of the presence of an energy transfer process. Therefore, this process possibly quenches the Si core photoluminescence.

Moreover, we can observe that the cis isomer functionalized SiNCs photophysical properties are always slightly worse than the trans isomer functionalized SiNCs photophysical properties and this statement is valid for both the samples, indicating that the Si core is more quenched by the cis configuration of both the azobenzene derivatives.

Therefore, we prepared a physical mixture of SiNCs (**Si** sample, see chapter 3 for more details) plus **AzoC₃OH-trans** at a very high concentration (8×10^{-4} M) in order to compare the PL lifetime of this solution with the one of a simple SiNCs solution (**Si** sample in chapter 3) to evidence the eventual presence of a bimolecular quenching. We acquired the PL lifetime of both the solution and a third value after having irradiated the physical mixture at λ = 365 nm to convert the azobenzene derivatives into its **AzoC₃OH-cis** isomer (**table 6.2**).

	τ (μs)
SiNCs (**Si** sample in chapter 3)	66
SiNCs + AzoC₃OH-trans	66
SiNCs + AzoC₃OH-cis	61

Table 6.2- Comparison of the photoluminescence lifetime of a SiNCs solution and of a physical mixture of SiNCs plus **AzoC₃OH** before and after its irradiation at λ = 365 nm.

As we can observe from the **table 6.2**, the photochromic unit do not quench the Si core luminescence in its trans isomer, differently it was possible to detect a lower PL lifetime of the Si core after the mixture irradiation. This experiment allowed us

to underline that the Si core photoluminescence properties are differently influenced by the two different isomers of **AzoC₃OH**, suggesting the possibility to increment systems based on the SiNCs' photocontrollable emission. Both the static and the dynamic process quench the Si luminescence; in the first scenario Si PL is quenched by both the azobenzene isomers with an higher effect of the cis form compared to the trans one, in the second case only the cis isomer is capable to quench the Si PL.

We also evaluated the possibility of an energy transfer process from the azobenzene derivatives to the Si core by acquiring the **Si-O-C₃Azo-trans** and **Si-O-C₃Azo-cis** excitation spectra, performed at the SiNC emission (λ_{em}=750 nm), and comparing them to the respective absorption spectra. No match of the excitation spectrum and the absorption spectrum was observed for both the samples, revealing the absence of an energy transfer process from the molecules to the Si core (**figure 6.10**). Therefore, the Si PL is not sensitized by their functionalization with the azobenzene derivatives.
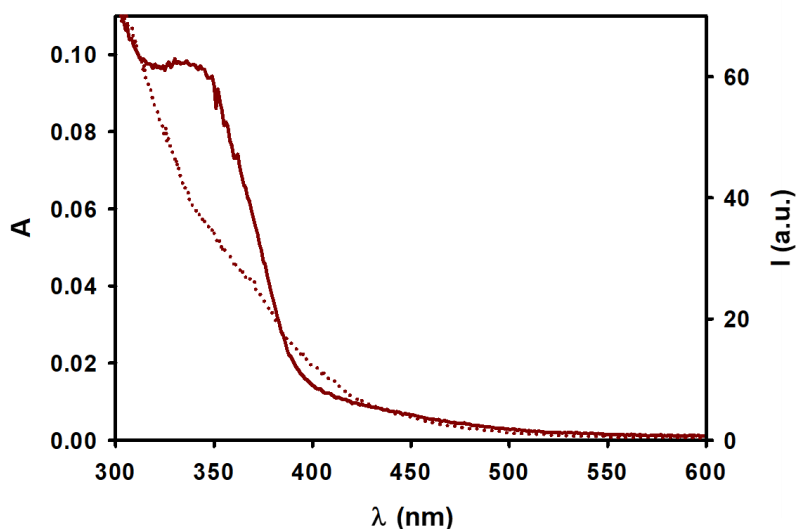
Figure 6.10- Absorption (dark red continuous line) and excitation (λ_{em}=750 nm, dark red dotted line) spectra of **Si-O-C₃Azo-trans** in toluene.

Free-azobenzene derivatives units photoisomerization Quantum Yields

Photoisomerization QY is a fundamental physico-chemical characteristic of azobenzenes and azobenzenes derivatives and their dependence on the wavelength and on the environment is a key for their function in many photo-switching applications.[291] The QYs of azobenzene derivatives photoisomerization in toluene solutions (**figure 6.11**) were determined on the basis of the following molar absorption coefficients, **AzoC₃OH** $\varepsilon_{365(Trans)}$ nm = 2.2 × 10^4 M^{-1} cm^{-1}, $\varepsilon_{365(Cis)}$ nm = 8 × 10^1 M^{-1} cm^{-1} and **PegAzo** $\varepsilon_{365(Trans)}$ nm = 1.8 × 10^4 M^{-1} cm^{-1}, $\varepsilon_{365(Cis)}$ nm = 3 × 10^2 M^{-1} cm^{-1}, focusing our attention on two irradiating wavelength, 365 nm and 436 nm and using known solutions volumes. In this way, we were able to calculate the photoisomerization QY values reported in **table 6.3**.

	$\Phi_{T\to C}$ (%)	$\Phi_{C\to T}$ (%)
AzoC₃OH	15	34
PegAzo	17	36
Si-O-C₃Azo	15	35
Si-O-PegAzo	18	38

Table 6.3- **AzoC₃OH**, **PegAzo**, **Si-O-C₃Azo** and **Si-O-PegAzo** photoisomerization QY percentages, irradiating all the toluene solutions at λ=365 nm and λ=436 nm to get the cis and the trans isomers respectively.
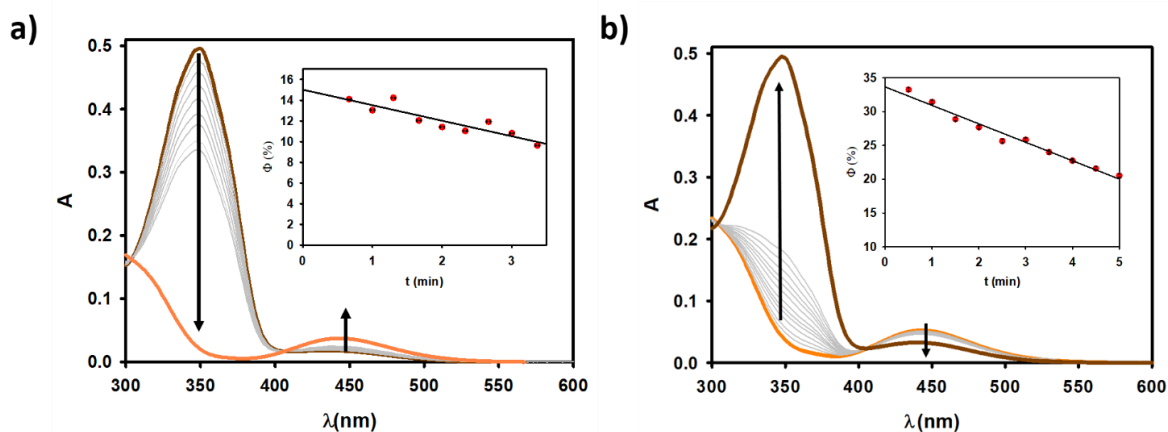
Figure 6.11- Absorption spectra of an **AzoC₃OH** solution in toluene a) before (dark orange spectrum), during (grey spectra) and after (light orange spectrum) irradiation at 365 nm, b) before (light orange spectrum), during (grey spectra) and after (dark orange spectrum) irradiation at 436 nm. Insets: photoisomerization QY fitting respect to the irradiation time.

We also calculated the photostationary states for both **AzoC₃OH** and **PegAzo** samples, using NMR spectroscopy (**figure 6.12**) for the first measurement and then a faster photochemical method for all the others, which was considered to be reliable by comparing its result with the one obtained from the NMR spectra. Two NMR spectra were acquired for an **AzoC₃OH** solution in DMSO-d6, one before the irradiation at λ=365 nm and the other one after. The photochemical method consists of mathematically reproducing the sample spectrum combining the respective 100% trans and 100% cis spectra (verified by NMR) through a percentage-weighted sum to reproduced it. The obtained percentages indicate the amount of the trans and the cis forms in the obtained photostationary state.

Irradiating the two solutions at λ=365 nm we obtained a ratio of 1 to 99 of trans isomer with respect to the cis isomer for both the samples. Irradiating the two solutions at λ=436 nm we obtained a ratio of 72 to 28 of trans isomer with respect to

the cis isomer for **AzoC₃OH** and a ratio of 67 to 33 of trans isomer with respect to the cis isomer for **PegAzo**.
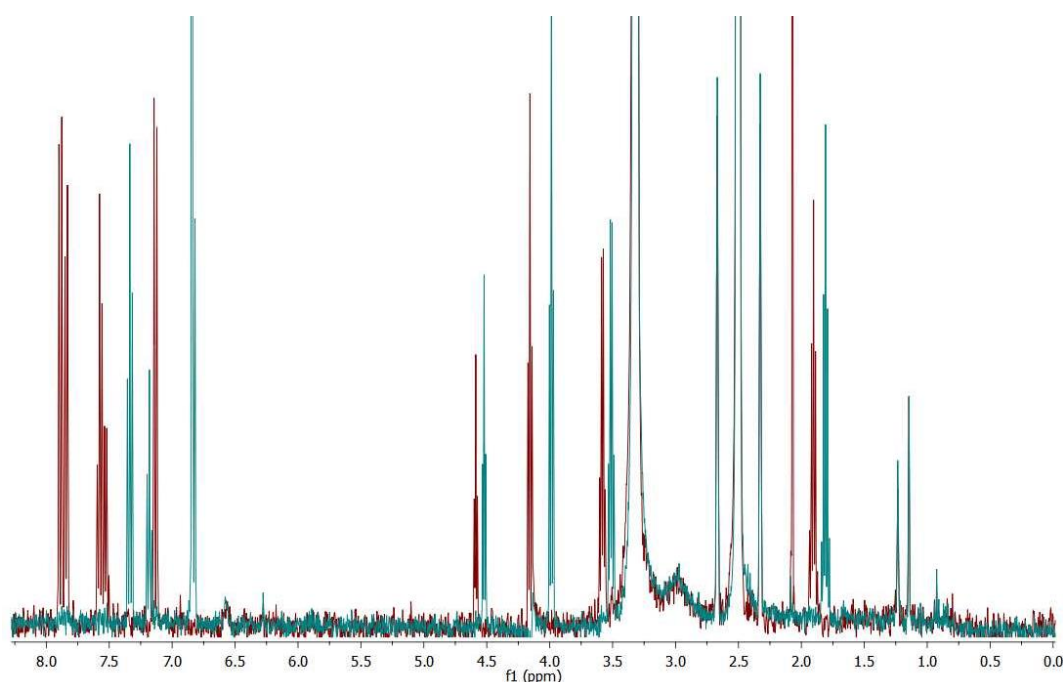
Figure 6.12- AzoC₃OH-trans ^{1}H NMR (red spectrum) compared to **AzoC₃OH-cis** ^{1}H NMR (green spectrum)

AzoC₃OH-trans ^{1}H NMR (400 MHz, DMSO-d6) δ 7.89 ppm (d, J = 8.9 Hz, 2H), 7.84 ppm (d, J = 7.6 Hz, 2H), 7.58 ppm (t, J = 7.4 Hz, 2H), 7.53 ppm (d, J = 6.9 Hz, 1H), 7.13 ppm (d, J = 8.9 Hz, 2H), 4.59 ppm (t, J = 5.2 Hz, 1H), 4.16 ppm (t, J = 6.4 Hz, 2H), 3.58 ppm (q, J = 5.9 Hz, 2H), 1.90 ppm (p, J = 6.4 Hz, 2H); 3.33 ppm (bs, H_2O), 2.67 ppm (s, DMSO), 2.50 ppm (s, DMSO), 2.33 ppm (s, DMSO), 2.09 ppm (s, Acetone), 1.24 ppm (bs, grease), 0.88-0.82 ppm (m, grease).

AzoC₃OH-cis ^{1}H NMR (401 MHz, DMSO-d6) δ 7.34 ppm (t, J = 7.8 Hz, 2H), 7.18 ppm (t, J = 7.4 Hz, 1H), 6.84 ppm (s, 5H), 6.82 ppm (s, 1H), 4.52 ppm (t, J = 5.2 Hz, 1H), 3.99 ppm (t, J = 6.3 Hz, 2H), 3.51 ppm (q, J = 6.0 Hz, 2H), 1.81 ppm (p, J = 6.2 Hz, 2H); 3.33 ppm (bs, H_2O), 2.67 ppm (s, DMSO), 2.50 ppm (s, DMSO), 2.33 ppm (s, DMSO), 2.09 ppm (s, Acetone), 1.24 ppm (bs, grease), 0.88-0.82 ppm (m, grease).

Azobenzene derivatives units-functionalized SiNCs photoisomerization Quantum Yield

We then measured in the same way the photoisomerization QYs of **Si-O-C₃Azo** (**figure 6.13**) and **Si-O-PegAzo**, values reported in **table 6.2**.
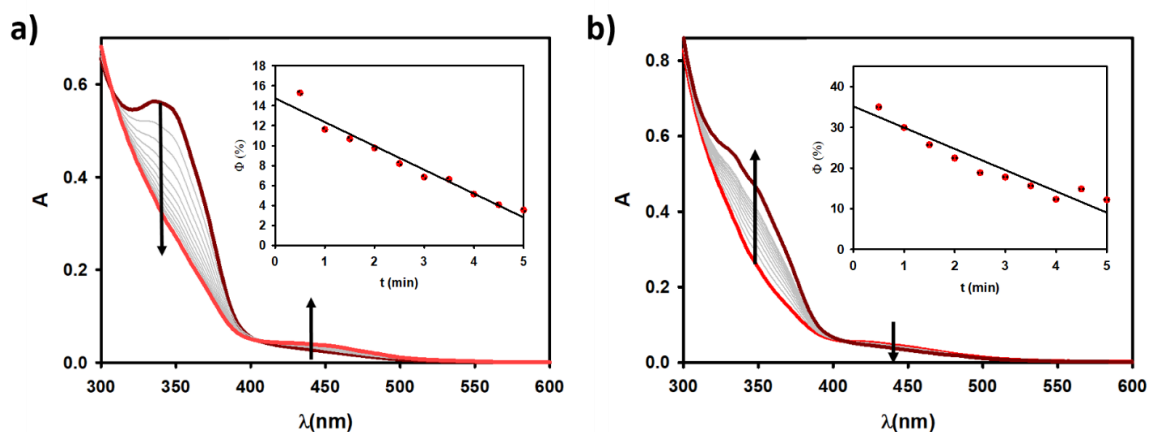
Figure 6.13- Absorption spectra of a **Si-O-C₃Azo** solution in toluene a) before (dark red spectrum), during (grey spectra) and after (light red spectrum) irradiation at 365 nm; b) before (light red spectrum), during (grey spectra) and after (dark red spectrum) irradiation at 436 nm. Insets: photoisomerization QY fitting respect to the irradiation time.

Considering the fraction of the light absorbed by the SiNCs in **Si-O-C₃Azo** and **Si-O-PegAzo** samples and correcting the total absorbed photons moles for this value, we can obtain the real amount of light absorbed by the azobenzene derivatives. Therefore, the covalent samples measured photoisomerization QY values are really close to the respective free azobenzene derivatives measured photoisomerization QY values, indicating that SiNCs are not deteriorating the azobenzene derivatives properties neither are negatively influencing the environment around them. We also calculated the photostationary states of **Si-O-C₃Azo**. Irradiating the solution at λ=365 nm we obtained a ratio of 1 to 99 of trans isomer with respect to the cis isomer.

Irradiating at λ=436 nm we obtained a ratio of 70 to 30 of trans isomer with respect to the cis isomer.

Aerated-samples stability study by time

A **Si-O-C₃Azo** solution was air-equilibrated, in order to study the sample stability by time and the atmospheric oxygen and water effect on the new covalent realized bond (**figure 6.2**), which links the azobenzene derivatives to the SiNCs surface. Indeed, this chemical bond is very sensitive to water since it can hydrolyse and if this happens the azobenzene derivatives are released, thus SiNCs firstly improve their PLQY and then, in some cases, aggregate and precipitate. **Figure 6.14** reports the absorption and normalized photoluminescence spectra acquired for the solution, in three different times: immediately after the solution preparation (called day 1), 6 days later (called day 6) and 15 days later (called day 15). The aerated sample is stable enough for the first week, then the PLQY and lifetime values (reported in **table 6.4**) start to increase, indicating the disjunction of the photochromic molecules from the SiNCs surface caused by the hydrolysis of their connecting bond. **Si-O-PegAzo** sample was treated in the same way. **Figure 6.14** also illustrates the absorption and normalized photoluminescence spectra acquired for this sample in two different times: immediately after the solution preparation (called day 1) and 6 days later (called day 6). Differently from **Si-O-C₃Azo** sample, this time we can immediately (day 1) notice a visible degradation of the aerated sample since the photoluminesce intensity at the day 6 is much lower than the day 1 and the PLQY and PL lifetime values either (**table 6.4**). After 6 days, this aerated sample was not only hydrolysed but also precipitated and the maximum emission wavelength blue-shifted. Therefore, it was not possible to acquire its photophysical properties such as the PL lifetime (**table 6.4**). The **Si-O-PegAzo** experiment ended on the day 6.
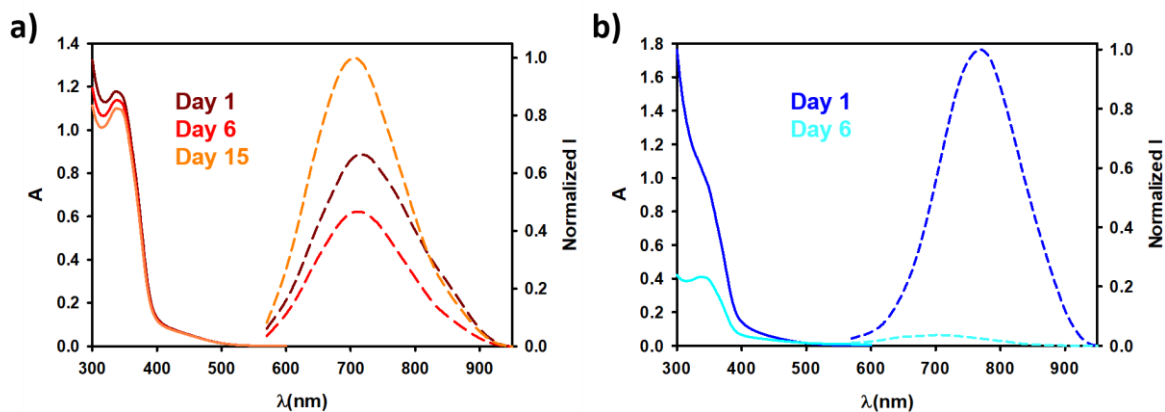
Figure 6.14- Absorption (solid lines) and normalized photoluminescence spectra corrected for the relative QY values (dashed lines) of **a)** aerated **Si-O-C₃Azo** and **b)** aerated **Si-O-PegAzo**, to study their stability by time, in toluene, exciting at λ=540 nm (where only SiNCs absorb the incident light).

	Si-O-C₃Azo-areated		Si-O-PegAzo-areated	
	PLQY (%)	τ (μs)	PLQY (%)	τ (μs)
Day 1	10	45	11	41
Day 6	7	45	0.4	x
Day 15	15	48	x	x

Table 6.4- PLQY and lifetime measurements for **Si-O-C₃Azo** and **Si-O-PegAzo** aerated toluene solutions, acquired immediately after the solutions preparation, after 6 days and after 15 days.

The different **Si-O-PegAzo** behaviour respect to the one of **Si-O-C₃Azo** could be justify considering two different aspects: i) thinking about its higher polarity which

could bring the sample residual water molecules closer to the Si core, making its surface bond hydrolysis easier or ii) considering that this sample has a lower number of azobenzene units attached onto the surface, thus the water or oxygen molecules can easier reach the inner part (the core) of this nanoparticles.

Samples stability study under light irradiation

In order to evaluate the samples stability under light irradiation, two toluene solutions of **Si-O-C₃Azo** and **Si-O-PegAzo** under inert atmosphere were prepared. Each solution was irradiated many times at λ=365 nm and λ=436 nm, varying the irradiation wavelength each time, allowing the azobenzene derivatives onto the SiNCs surface to convert from the trans isomer to the cis isomer, thus from the cis isomer to the trans isomer for a total of three cycles. PLQY, PL lifetime and the maximum emission wavelength were measured each time and all the values are illustrated in **figure 6.15** and **6.16**. The first value reported in all the graphs is relative to the samples containing the azobenzene derivatives in their 100% trans form, obtained by a thermic route, which is the reason why it is always different form the other values.
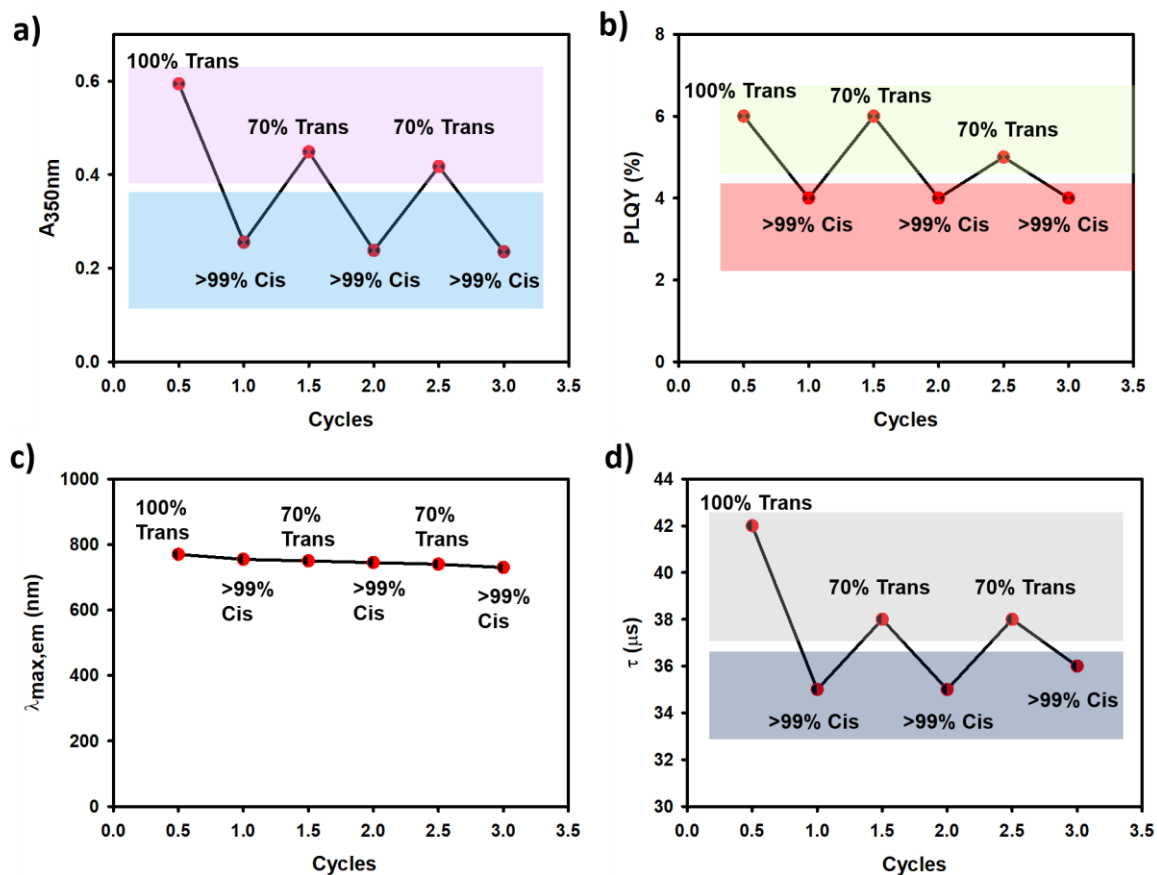
Figure 6.15- a) absorption values at λ = 350 nm **b)** photoluminescence QYs **c)** maximum emission wavelengths and **d)** photoluminescence lifetimes as a function of irradiation cycles (λexc = 540 nm) of **Si-O-C₃Azo** in toluene.
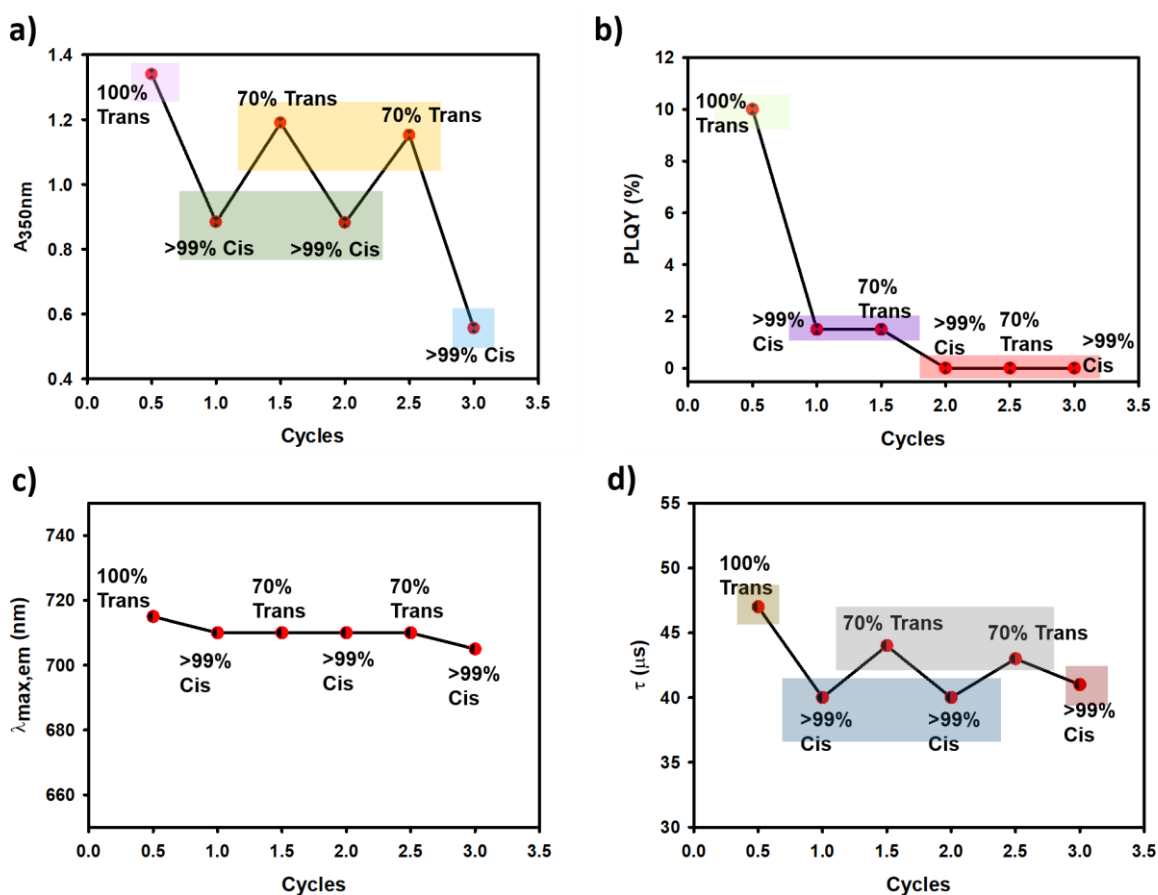
Figure 6.16- a) absorption values at λ = 350 nm **b)** photoluminescence QYs **c)** maximum emission wavelengths and **d)** photoluminescence lifetimes as a function of irradiation cycles (λexc = 540 nm) of **Si-O-PegAzo** in toluene.

The values illustrated in **figure 6.15** show the ability of **Si-O-C₃Azo** to almost totally recover its photophysical properties. We can observe a constant trend for the absorption value at λ = 350 nm, the PLQY and the PL lifetime, by going from the trans isomer to the cis isomer and thus on the other way, for a total of three cycles (or at least very small variations which lay under the experimental error). The maximum emission wavelength is the only value to do not show this constant trend, which slightly and continuously decreases. This could be due to the start of the sample degradation. Differently, the values reported in **figure 6.16** demonstrate that **Si-O-PegAzo** is not able to recover its photophysical properties at all, since its

degradation and precipitation start already at the first irradiation, bringing to a PL quenching with a final PLQY value close to the zero.

Yang et al.[292] demonstrated that dodecyl-functionalized SiNCs, under nitrogen atmosphere, constantly UV-irradiated for 4 hours, retain only a half of the PLQY initial value, with no shift in the maximum emission wavelength, indicating that the irradiation is not modifying the SiNCs dimensions neither is making them precipitate. The photobleaching was attributed to the possibility of structural distortion or dangling bond formation due to the cleavage of some residual Si-H surface bond, thus to the introduction of new trap states. They also studied the effect of simultaneous exposure to air and UV irradiation. In that case, a PLQY decrease to 16% of the initial value was seen. In that case, the more intense photobleaching is not due to a dynamic quenching caused by the molecular oxygen in the solution, but it is due to the surface photo-oxidation reactions, which are happening.[39,47,167,293–296]

Considering these previous studies, we can assume that the Si surface is better functionalized in **Si-O-C₃Azo** respect to **Si-O-PegAzo** (the oxygen presence is not an option in our case since we have always worked under nitrogen atmosphere), reducing the possibility of trap states formation under light irradiation for the first sample and enhancing the chance of their formation for the second one, bringing to its degradation and precipitation more rapidly. This is evident in **figure 6.16**.

Solvent affinity variation upon light irradiation

Considering the high azobenzene and azobenzene derivatives solubility in polar solvents such as MeOH, we decided to test the dispersibility of **Si-O-C₃Azo** and **Si-O-PegAzo** in this solvent, also comparing the trans and the cis isomers behaviour for both the samples. Alkyl-functionalized SiNCs are extremely dispersible in non-polar solvents and obtaining SiNCs dispersible in polar solvents is usually a big

challenge. First, we found two immiscible solvents, cyclohexane and MeOH in this case, thus we acquired the samples' absportion spectra in cyclohexane and then we added a volume of MeOH equal to the one of cyclohexane (8 mL). After complete separation of the two phases, we extracted the cyclohexane phase, which was analysed by absorption spectroscopy again. In **figure 6.17,** the **Si-O-C₃Azo** results are reported. We found out that the sample goes in MeOH with a percentage of 35% in the trans form and of 80% in the cis form. Unfortunately, we could not reproduce the experiment for the **Si-O-PegAzo** sample since it was totally precipitated due to the high a-polarity of cyclohexane, the solvent of the sample conservation, but we expect a **Si-O-PegAzo** even higher affinity for MeOH.
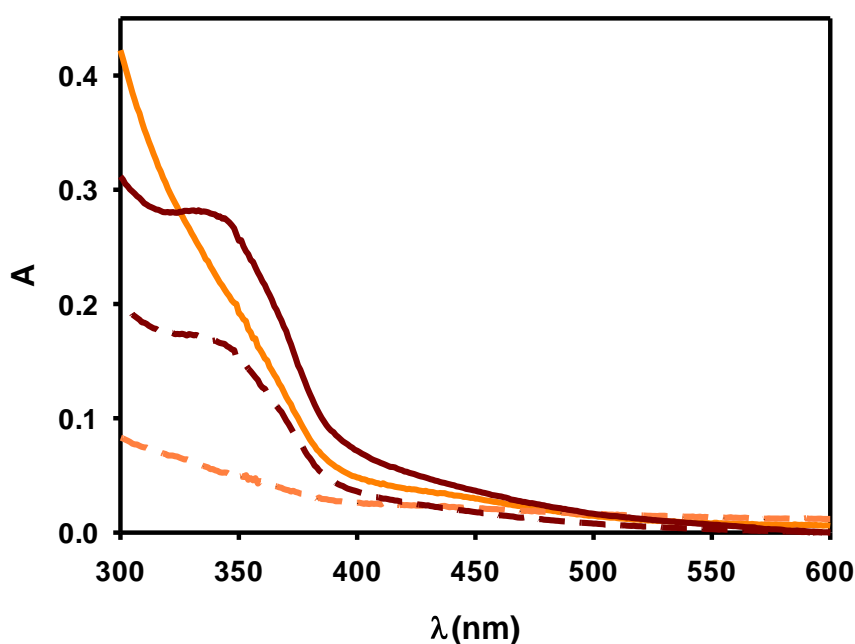
Figure 6.17- Absorption of **Si-O-C₃Azo-trans** (dark red lines) and **Si-O-C₃Azo-cis** (orange lines) in cyclohexane, exciting at λ=540 nm, before (solid lines) and after (dashed lines) repartition with methanol.

Interesting is the different polarity of the sample **Si-O-C₃Azo** by varying the azobezene derivative isomer configuration, which reproduce the azobenzene

performances by itself. Indeed, the azobenzene structural rearrangement brings to a different molecular geometry, thus a variation in its polarity. The trans isomer has a null dipole moment ($\mu \approx 0D$), on the other way the cis isomer shows a higher value, equal to 3 ($\mu \approx 3D$).[274,297] The higher dipole moment of the cis isomer gives an higher polarity to the **Si-O-C₃Azo-cis** sample respect to the **Si-O-C₃Azo-trans** sample, making it more dispersible in MeOH.

6.4 Conclusions

Azobenzene derivatives-functionalized Silicon Nanocrystals were synthesized for the first time by following a three steps reaction starting from the synthesis of a chlorosilane-terminated SiNCs sample, following with its reaction with the azobenzene of choice, functionalized with an alcoholic group, in the presence of imidazole and ending with the final capping step to literally cap the eventual un-reacted sites to improve SiNCs colloidal stability. Two different azobenzene derivatives have been used, the so-called **AzoC₃OH** and **AzoPeg**. We obtained a better functionalization using the first one, since 80 and 65 azobenzene units on the SiNCs surface have been respectively calculated, bringing to a better stability of **Si-O-C₃Azo** respect to **Si-O-PegAzo** in terms of sample degradation by time or under irradiation. A better surface functionalization means having a better and more solid protective shell around the Si core, avoiding the oxygen and water penetration and thus the Si oxidation and degradation. PLQY and PL lifetime have been measured for both the samples and for the **SiBuOH** control sample as well, resulting in lower values for the first two with respect to the control. A Si dynamic and static PL quenching in solution caused by the linked or the free azobenzene derivatives (covalent and physical mixtures respectively) was detected, so we can tell that these molecules quench the Si core luminescence and this effect is bigger considering the cis isomer with respect to the trans isomer, suggesting the possibility of incrementing a SiNCs-based device with photo-switchable optical behaviours. On

the other side, the photoisomerization QY measured for both the azobenzene derivatives has the same value no matter if the photochromic unit is free in solution or attached on the SiNCs surface, meaning that they are not influenced by the presence of SiNCs. Interesting is also the change in the **Si-O-C₃Azo** sample polarity by irradiating it at λ = 365 nm. **Si-O-C₃Azo-cis** showed a better dispersibility in MeOH with respect to **Si-O-C₃Azo-trans**, suggesting the possibility of incrementing a light-driven motion.

7 A Comparative Study of Thermal Hydrosilylation vs Radical Initiated Hydrosilylation of Silicon Nanocrystals

7.1 Introduction

Silicon Nanocrystals (SiNCs) are characterized by a bright size-tunable PL colour over much of the visible to the near-infrared spectrum that we can control by setting different furnace temperatures during the disproportion reaction of HSQ to obtain the silica matrix embedded with SiNCs, as we have already demonstrated in the previous chapters of this dissertation. Since SiNCs are extremely susceptible to surface oxidation, the surface functionalization with organic molecules, by the realization of strong and covalent Si-C bonds, is a step of enormous importance to prevent their degradation and aggregation. Hydride-terminated SiNCs, obtained after the etching procedure, have been functionalized trough the so-called hydrosilylation reaction, which can provide the Si-C covalent bond mentioned above.[116,205] This reaction can be promoted in different ways (see chapter 2 for more details).

The aim of this chapter is comparing two of them, the thermal hydrosilylation and the room temperature radical initiator (4-DDB) promoted hydrosilylation in the presence of 1-dodecene, in terms of (i) the optical properties of the obtained SiNCs solutions and (ii) the kind of surface functionalization, as a function of the Si core diameter, through the spectroscopic characterization, the thermal gravimetric

analysis and the X-ray Photoelectron Spectroscopy. For the hydrosilylation reaction mechanism, see chapter 2.

7.2 Synthesis of Dodecyl Chains-Terminated SiNCs

1-Dodecene was chosen as the SiNCs surface functionalization ligand, since its behaviour in the hydrosilylation reaction is well understood,[89] providing a reliable comparison between the thermal and the radical initiated reactions (**figure 7.1**).
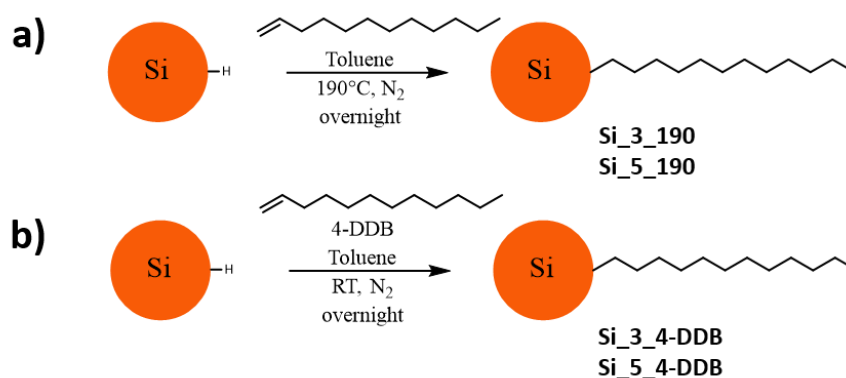
Figure 7.1- reaction schemes of the 3 and 5 nm diameter SiNCs surface functionalization with 1-dodecene by a) thermal hydrosilylation and b) room temperature radical initiator promoted hydrosilylation.

7.2.1 The SiNCs Thermal Hydrosilylation

SiNCs were obtained via thermal decomposition of HSQ, followed by the etching procedure with HF and the hydrosilylation reaction. FOx-16 (a commercial HSQ solution, purchased from Dow Corning) was loaded into a round bottom flask, and the solvent was evaporated on a Schlenk line for 4 h to generate glassy hydrogen silsesquioxane (HSQ), which was subsequently heated to 1100 or 1200 °C for 1 h under hydrogen/nitrogen (7%/93%) forming gas flow. Higher temperature produces larger nanocrystals, thus we can easily and efficiently control the Si-core diameter. The product, containing Si nanocrystals (10% in weight) embedded in

SiO$_2$ matrix (90% in weight), was ground with an agate mortar and pestle for 10 min and shaken in a wrist-action shaker for 9 h with 3 mm borosilicate glass beads. One gram of the ground powder was etched in 3 mL of 37.5% HCl and 30 mL of 48% HF in the dark for 3.30 or 4.30 h to yield 3 and 5 nm diameter hydride-terminated SiNCs respectively. These nanocrystals were isolated by centrifugation at 8000 rpm for 5 min and rinsed once with distilled water, twice with ethanol, and once with chloroform, and finally dispersed in 1-dodecene and heated to 190 °C for 12 h after 3 freeze–pump–thaw cycles to achieve the surface passivation. Functionalized SiNCs were thus cleaned thrice by centrifugation at 8000 rpm for 5 min to precipitate poorly capped nanocrystals, using ethanol as the anti-solvent and toluene to redisperse them.[160]

Two different samples were synthesized: **Si_3_190** and **Si_5_190** using the SiO$_2$/SiNCs powders obtained by heating the HSQ to 1100 and 1200°C respectively (**figure 7.1**).

7.2.2 The SiNCs Radical Initiated Hydrosilylation

H-terminated SiNCs were obtained as discussed above (chapter 7.2.1). After the etching procedure, the obtained precipitate was rinsed with anhydrous toluene inside a nitrogen filled glove box. 1-dodecene, the ligand, and 4-DDB, the radical initiator, were added to the mixture. The solution was then stirred, at room temperature, overnight, to achieve the surface passivation (see chapter 2 for more details). Functionalized SiNCs were thus cleaned thrice by centrifugation at 8000 rpm for 5 min to precipitate poorly capped nanocrystals, using ethanol as the anti-solvent and toluene to redisperse them.[116]

Two different samples were synthesized: **Si_3_4-DDB**, **Si_5_4-DDB** using the SiO$_2$/SiNCs powders obtained by heating the HSQ to 1100 and 1200°C respectively (**figure 7.1**).

7.3 Results and Discussions

Photophysical Characterization in Solution

Figure 7.2 shows absorption and emission spectra acquired for the samples **Si_3_190**, **Si_5_190**, **Si_3_4-DDB** and **Si_5_4-DDB**. **Figure 7.2 a)** compares 3 nm diameter SiNCs functionalized with the two different hydrosilylation reactions. In particular, we can observe the classic unstructured absorption profile of SiNCs for both the samples and the typical emission band with a maximum emission wavelength centred at ca. 640 nm for the sample obtained with the thermal reaction and at ca. 615 nm for the one obtained with the radical initiated hydrosilylation. The two emission bands are corrected per the relative samples PLQY, the values are reported in **table 7.1** together with the different luminescence lifetimes. **Figure 7.2 b)** compares 5 nm diameter SiNCs functionalized with the two different hydrosilylation reactions. We can still observe the classic unstructured absorption profile of SiNCs for both the samples and the typical emission band with a maximum emission wavelength centred at ca. 910 nm for the sample obtained with the thermal reaction and at ca. 880 nm for the one obtained with the radical initiated hydrosilylation. Like in the previous case, the two emission bands are corrected per the relative samples PLQY and the values are reported in **table 7.1,** together with the different luminescence lifetimes.
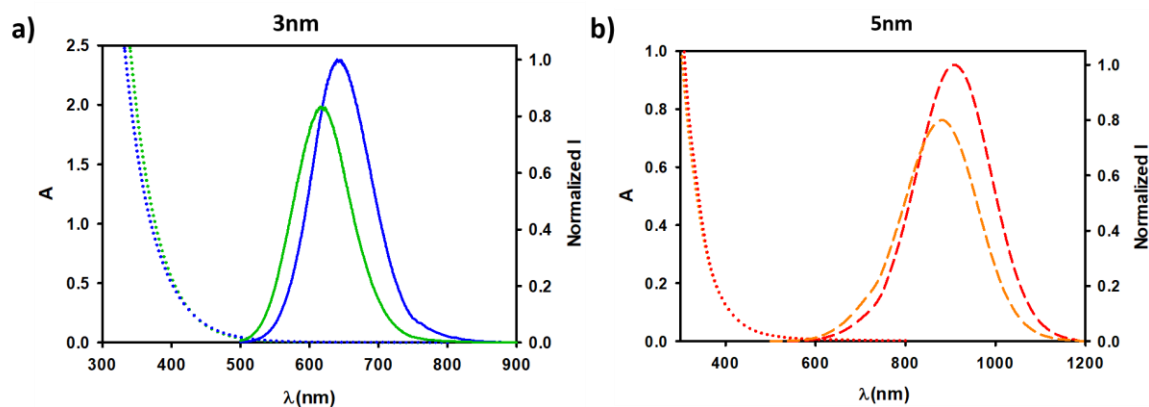
Figure 7.2- absorption (dotted lines) and emission (continuous and dashed lines) spectra of a) 3 nm diameter SiNCs functionalized with 1-dodecene by thermal (blue lines) and 4-DDB initiated (green lines) hydrosilylation reaction and b) 5 nm diameter SiNCs functionalized with 1-dodecene by thermal (red lines) and 4-DDB initiated (orange lines) hydrosilylation reaction, in toluene, exciting the samples at λ = 440 nm.

	PLQY (%)	PL Lifetime (µs)
Si_3_190	30	50
Si_3_4-DDB	25	35
Si_5_190	50	180
Si_5_4-DDB	40	150

Table 7.1- PLQY and PL lifetime measurements for **Si_3_190, Si_3_4-DDB, Si_5_190, Si_5_4-DDB**, in toluene, exciting the samples at λ = 440 nm for the PLQY and at λ = 365 nm for the PL lifetime**.**

Table 7.1 shows better results for the two thermal hydrosilylated samples with respect to the two 4-DDB hydrosilylated samples, in terms of both the PLQY and the PL lifetime, for SiNCs of the same size. These results suggest a better surface

176

functionalization achieved by the thermal hydrosilylation, allowing the realization of a better protective shell around the Si core, thus all the Si optical properties are better preserved. 4-DDB hydrosilylated samples present a little more trap states or dangling bonds on their surface, which is also more exposed to the environmental oxygen, resulting in its oxidation and thus in the luminescence quench. Worth noting is considering that the thermal hydrosilylation gives better photoluminescence properties, but it needs very high temperatures to be promoted and many ligands could undergo degradation or oligomerization[102] caused by the heating. Moreover, the reaction cannot be carried out using a solvent, thus it needs an excess of the ligand, which works also as the solvent. Therefore, this limit the use of pricy molecules in this kind of functionalization. We also notice that the smaller SiNCs usually have lower PLQYs with respect to the bigger SiNCs and this is possibly due to the higher probability of their excitons to interact with the trap states on the Si surface.[217]

Thermal gravimetric analysis

Thermogravimetric analysis (TGA) was performed on a Mettler Toledo model TGA/DSC 1 with alumina crucibles (Mettler Toledo). The 70μL crucibles were cleaned by sonication for 15 min in concentrated nitric acid and rinsed with deionized water before being baked at 800 °C in air for 45 min. A 70μL aliquot of SiNCs dispersed in chloroform was added to the crucible and the solvent was allowed to evaporate, providing roughly 5/10 mg of dry SiNCs in the crucible. The sample was heated from 25 to 800 at 10 °C/min under air flowing at 5 mL/min. Therefore, the sample was kept at 800 °C for 30 min allowing its complete oxidation. TGA/DSC simultaneously recorded the heat flow and crucible mass versus time and temperature.[46]
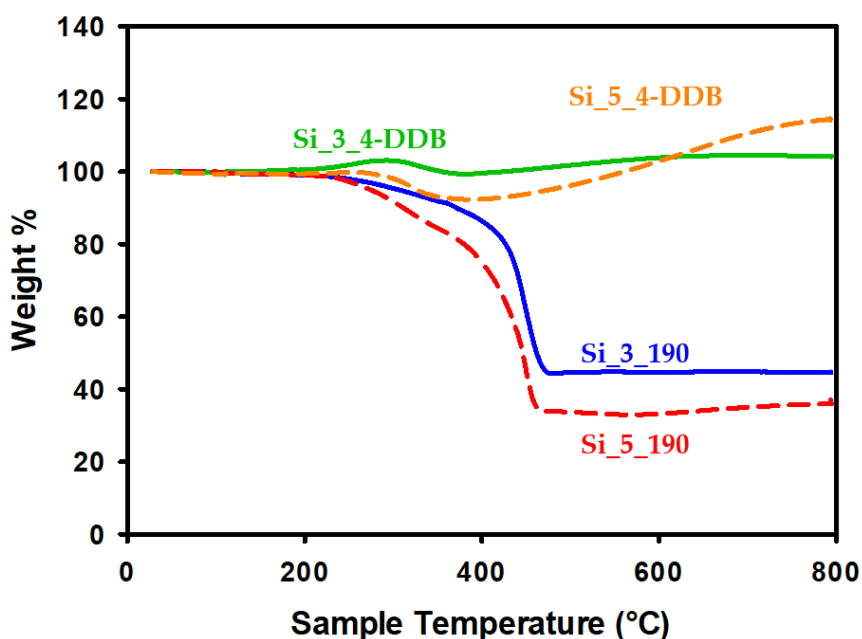
Table 7.3- Thermogravimetric heating curves for **Si_3_190** (continuous blue line)**, Si_3_4-DDB** (continuous green line), **Si_5_190** (dashed red line) and **Si_5_4-DDB** (dashed orange line). Experiments were performed under oxygen atmosphere, which led to oxidation of the nanocrystals and a weight gain at temperatures above about 500°C.

In literature the ligand desorption usually leads to a net weight loss, while Si oxidation produces an increase in mass.[46,205] **Figure 7.3** shows TGA data of SiNCs passivated with 1-dodecene and the following thermal events are observed: (i) oxidation of the non-functionalized sites on the Si surface in the temperature range around 210 °C only for the two samples synthesized trough the RT, 4-DDB promoted, hydrosilylation; (ii) loss of the bonded ligand around 300 °C, for all the samples; (iii) degradation of the formed oligomers onto the thermally hydrosilylated samples around 410 °C; (iv) oxidation of remaining Si to fully oxidized particles (SiO$_2$) at temperatures above 450 °C for the two thermal samples and above 400 °C for the two RT, 4-DDB promoted, samples.

Analysing the spectra we can notice that there is no free-ligand residual in all the solutions since 1-dodecene evaporates at 213 °C and the weight% drop was not detected around that temperature. In addition, the loss of the bonded ligand was detected in all the samples around 300 °C and no significant weight% difference was seen comparing the samples synthesized with the two different hydrosilylation reactions. The second big weight% drop in the two thermally hydrosilylated samples may be due to the degradation and evaporation of the probably formed oligomers onto the SiNCs surface. TGA spectra suggest us that the oligomers formation is only verified handling the samples at very high temperatures and is avoided through the RT, 4-DDB promoted, hydrosilylation. Nevertheless, the two RT hydrosilylated samples TGA curves show a weight% increase around 210 °C, relative to the Si surface oxidation, indicating a worse surface passivation for these samples compared to the high temperature hydrosilylated ones: they have more dangling bonds on their surface and thus less bonded ligands.

X-ray photoelectron spectroscopy

SiNCs surface was characterized by X-ray photoelectron spectroscopy (XPS) after the hydrosilylation reaction and after the washing procedure of the functionalized SiNCs from the non-reacted ligands and from the non-functionalized and precipitated SiNCs. The four air-equilibrated solution have been stored for one month and then the samples were drop-casted on the conductive face of FTO glasses and the solvent was air-evaporated.
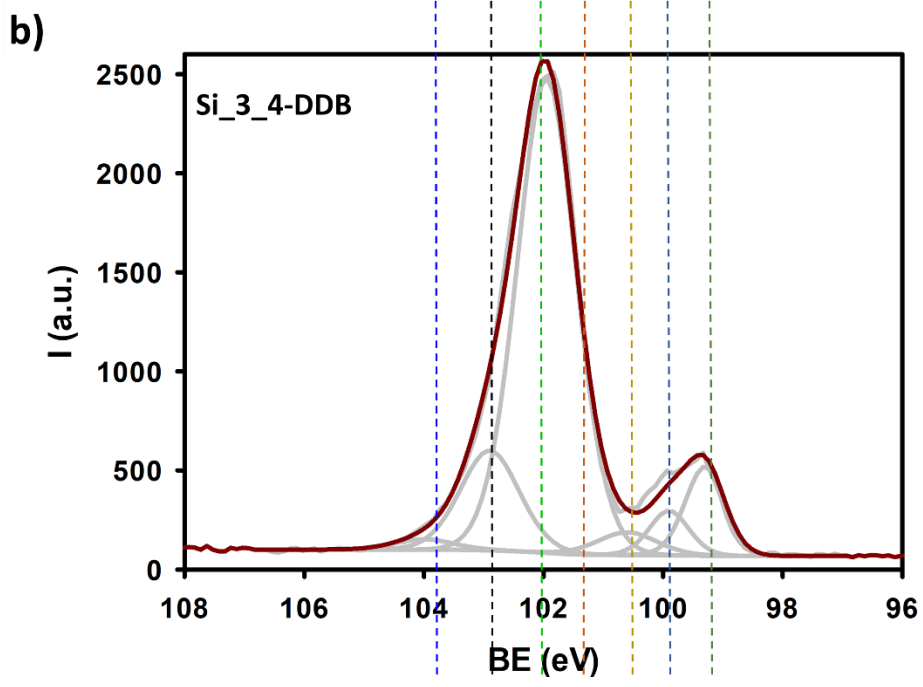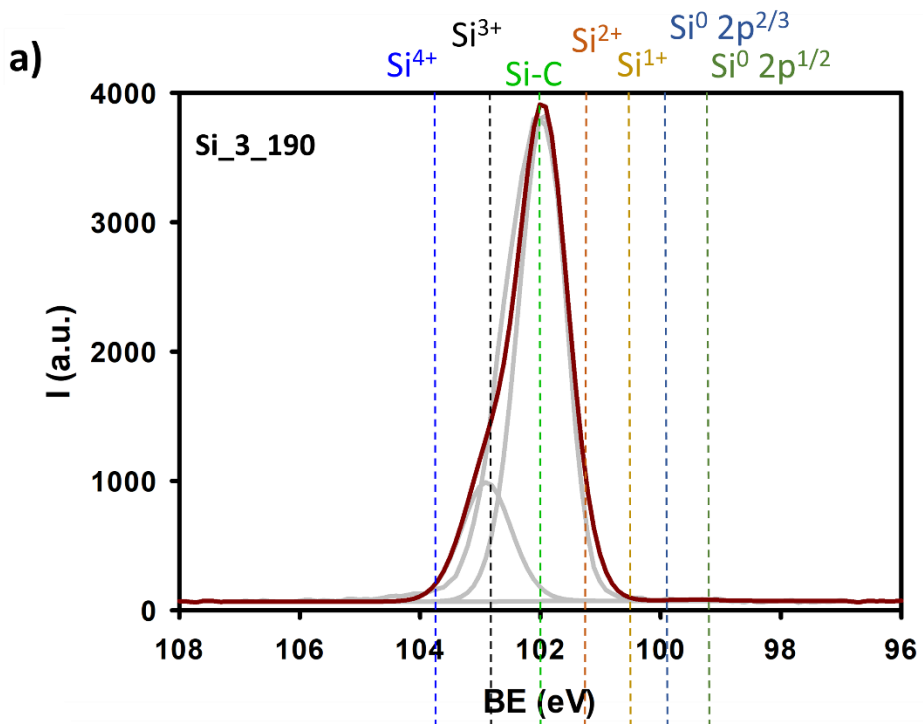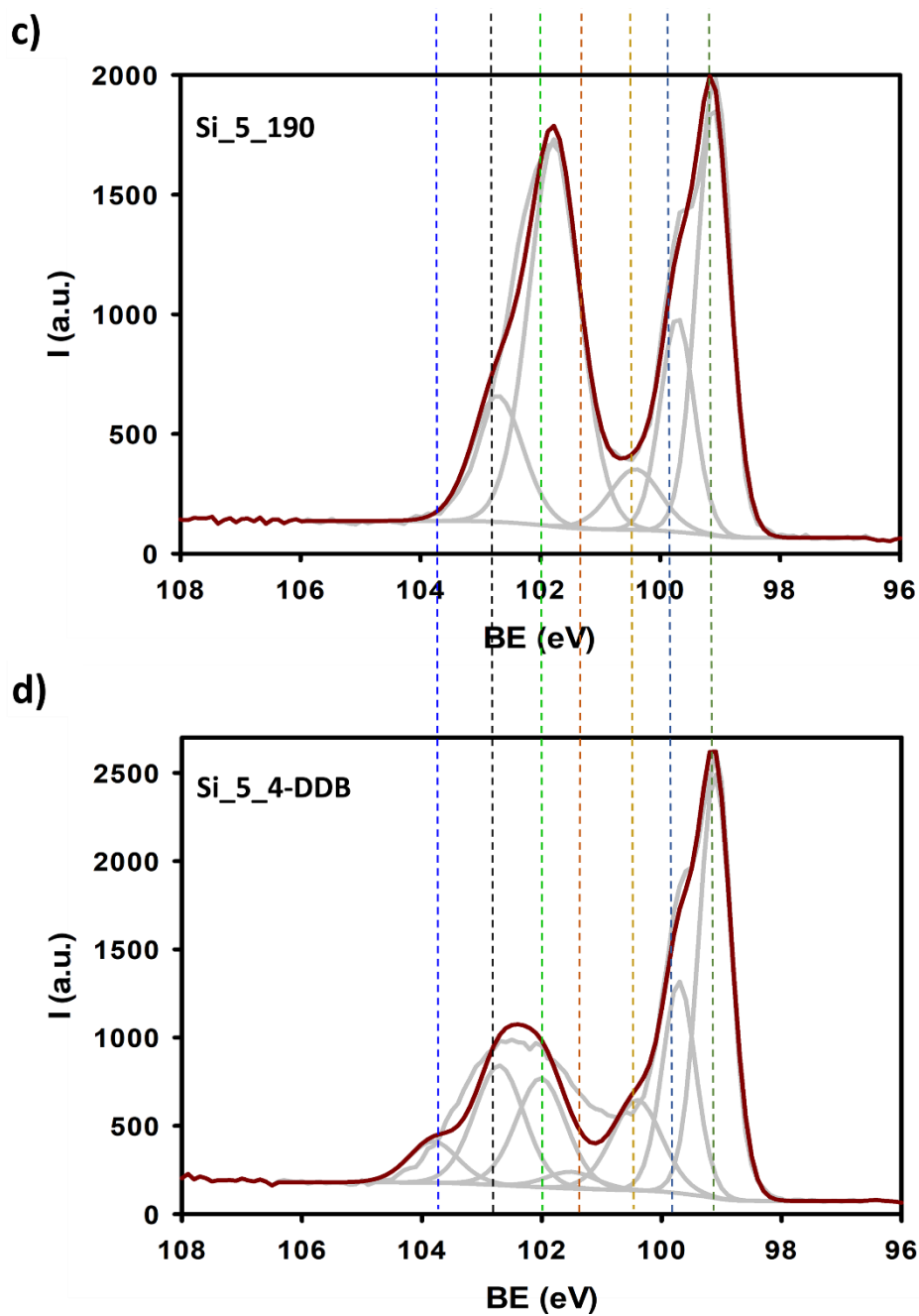
Figure 7.4- XPS measurements of 1-dodecene-passivated SiNCs synthesized at 1100°C (top) and 1200°C (bottom), functionalized with the thermal hydrosilylation reaction (a and c) and with the 4-DDB promoted hydrosilylation reaction (b and d). The dark red line is the fitting of the different peak contributions: Si^0 $2p^{3/2}$, Si^0 $2p^{1/2}$, Si^{1+}, Si^{2+}, Si^{3+}, Si^{4+}, and Si-C signals (dashed coloured lines).

We know from the literature that oxide-embedded nanocrystals exhibit prominent peaks characteristic of elemental Si and SiO_2 at ~ 99.5 eV (zero valent Si shows two distinct peaks: Si^0 $2p^{3/2}$ at 99.8 eV and Si^0 $2p^{1/2}$ at 99.3 eV) and ~ 103.5 eV respectively.[46,57,298] After the etching and the hydrosilylation reaction, the peaks in the XPS spectra are centred at ~ 99.5 and ~102.0 eV, with a small shoulder at 103.5 eV. The new raised peak at 102.0 eV is attributed to the Si-C bond at the SiNCs surface, the small shoulder at 103.5 eV corresponds to sub-oxide species that form during the handling and clean-up steps. The doublet peak centred at 99.5 (Si^0 $2p^{3/2}$ at 99.8 eV and Si^0 $2p^{1/2}$ at 99.3 eV) represents the Si-Si bond, whose intensity increases with respect to the intensity of the same doublet peak found in the oxide-embedded SiNCs sample.[46,299]

Figure 7.4 shows XPS spectra acquired for **Si_3_190, Si_3_4-DDB, Si_5_190** and **Si_5_4-DDB**. We can observe that the peak centred at 102 eV was detected for all the synthesized samples, corresponding to the Si-C surface functionalization as we expected. **Si_3_190** seems to show the best surface functionalization by comparing the intensities of these peaks (at 102 eV) in all the different samples. The doublet peak centred at 99.5 eV, corresponding to the characteristic peaks of elemental Si was not detected for **Si_3_190**, probably due to an error occurred during the measurement acquisition, we think that the sample charging was not accurately accounted for, thus the peaks are shifted at higher energies and maybe overlapped with the observable peaks. All the samples present the shoulder at around 103.5 eV, corresponding to the sub-oxide species produced during the samples washing procedure. By analysing these data, we can probably conclude that the best surface functionalization of 5 nm diameter SiNCs is achieved for the sample obtained with the thermal hydrosilylation **Si_5_190** (considering the intensity of the Si-C peak), which could also explain the better photophysical properties obtained, even though the **Si_5_4-DDB** has the least oxidation. Differently, it is difficult to conclude anything regarding the 3 nm diameter SiNCs samples, since their XPS spectra are

of difficult interpretation. We can only say that these samples showed the higher oxidation value, as we expected.

7.4 Conclusions

Two different hydrosilylation reactions to functionalize hydride-terminated SiNCs have been investigated and compared, in terms of the photophysical properties, such as PLQY and PL lifetime, the thermal gravimetric analysis and the X-Ray Photoelectron Spectroscopy of the obtained colloidal solutions. We also focused our attention on two different SiNCs diameters, 3 and 5 nm, obtained by heating the HSQ powder to 1100 and 1200°C respectively, during the disproportionation reaction. By analysing all the acquired data, we can conclude that, in general, all the samples functionalized by the thermal hydrosilylation reaction have better photophysical properties, with respect to the samples functionalized by the 4-DDB promoted hydrosilylation. Moreover, 3nm diameter SiNCs showed worse photophysical properties with respect to 5nm diameter SiNCs, maybe due to the higher probability of their excitons to interact with the possible trap states on the Si surface.[217] TGA and XPS data confirmed the results obtained through the photophysical measurements, indicating a better surface passivation achieved by the thermally induce hydrosilylation with respect to the RT, 4-DDB promoted, one. Nevertheless, it is worth noting considering that the thermal hydrosilylation needs very high temperatures to be promoted and many ligands could undergo degradation or oligomerization caused by the heating, as mentioned above. Moreover, the reaction cannot be carried out using a solvent, thus it needs an excess of the ligand, which works also as the solvent. Therefore, this limit the use of pricy molecules in this kind of functionalization.

8 Conclusions

During my PhD, I had the chance to thoroughly examine the world of SiNCs in terms of both the synthetic and the characterization point of views. SiNCs, opportunely functionalized with strong Si-C covalent bonds, revealed to be extremely interesting materials for biomedical imaging and energy conversion applications mainly, thanks to their remarkable properties. Hybrid organic-inorganic systems based on SiNCs were synthesized and studied, through many different techniques and some of their applications, on the already mentioned fields, are even shown.

Specifically, the first example of LSC based on a light-harvesting antenna made of DPA-functionalized SiNCs is shown. The PL and photovoltaic properties were compared for LSCs based on only the organic chromophore (**DPA**), only SiNCs (**Si**), a physical mixture of the two components (**Si+DPA**) and the covalent system (**Si-DPA**). The best optical and photovoltaic performances were obtained for **Si+DPA** sample, demonstrating that coupling organic dyes and inorganic SiNCs is a promising route to enhance LSC performances. Its performances are even superior with respect to the ones of the covalent system **Si-DPA** because of the decreased PLQY of the Si core upon covalent functionalization. In the **Si+DPA** LSC, a trivial energy transfer mechanism, enhanced by the long optical path typically encountered in LSC devices, minimizes the loss due to self-reabsorption of DPA luminescence. Optical efficiency as high as 4.25% was achieved with this device architecture.

SiNCs have also been functionalized, in three different ways, with PEG chains, achieving water dispersibility. The two best synthesized samples have been **Si-PEG** and **Si-(15%)PEG$_{2000}$** in terms of all the photophysical properties, the sample stability in different aqueous solutions and the reaction chemical yields. The pH

sensitivity has been also studied for these two samples, suggesting the possibility to realize a pH-sensitive device based on these SiNCs solutions. Moreover, it has been shown that the **Si-PEG** sample, obtained by the thiol-ene click reaction, has the potential to be utilized for luminescence-guided surgery, since it accumulate in the tumor and is excreted within 48 hours, as demonstrated in mice with MDA-MB-231 tumors. In addition, due to the long emission lifetime of these SiNCs (60 μs), the signal to background ratio and the background ambient light suppression can be enhanced via time-gated luminescence imaging. Future studies are aimed at increasing the molar absorption coefficient of SiNCs in the red and NIR spectral region by a light-harvesting approach. This will enable red excitation of SiNCs coupled to time-gated NIR luminescence for deeper tissue penetration. Furthermore, conjugation of the terminal OH group of the PEG shell to a tumor targeting agent will be investigated for active targeting of the tumor.

A different approach, the so-called non-covalent method, to disperse SiNCs in water was also examined. We have demonstrated that 5 nm diameter SiNCs, previously synthesized and stabilized with dodecyl chains, can be physically encapsulated, together with **LR** or **DPA** units, inside polymer nanoparticles made of **PMMA-SO₃H**, via nanoprecipitation technique. The fundamental phenomenon observed in these system, at high chromophore concentration, is the excitation energy transfer (EET). EET shuttles the excitation energy between the encapsulated dye units until the interaction with an encapsulated SiNC: if it happens, the closest excited dye to the SiNC works as the donor, while the SiNC works as the acceptor. In this way, it is possible to sensitize the SiNCs emission. Through the photophysical characterization, we have showed the EET presence in both **PNPs+SiDDE5+LR** and **PNPs+SiDDE5+DPA** samples. The EET was lower for the first prepared sample and more intense for the second one.

Azobenzene derivatives-functionalized SiNCs were also synthesized for the first time. Two different azobenzene derivatives have been used, the so-called **AzoC₃OH**

and **AzoPeg**. We obtained a better functionalization using the first one, bringing to a better stability of **Si-O-C₃Azo** respect to **Si-O-PegAzo** in terms of sample degradation by time or under irradiation. PLQY and PL lifetime have been measured for both the samples and for the **SiBuOH** control sample as well, resulting in lower values for the first two with respect to the control. A Si dynamic and static PL quenching in solution caused by the linked or the free azobenzene derivatives (covalent and physical mixtures respectively) was detected, so we can tell that these molecules quench the Si core luminescence and this effect is bigger considering the cis isomer with respect to the trans isomer, suggesting the possibility of incrementing a SiNCs-based device with photo-switchable optical behaviours. Interesting is also the change in the **Si-O-C₃Azo** sample polarity by irradiating it at $\lambda = 365$ nm. **Si-O-C₃Azo-cis** showed a better dispersibility in MeOH with respect to **Si-O-C₃Azo-trans**, suggesting the possibility of incrementing a light-driven motion.

In the end, during my stay at the University of Texas at Austin I had the chance to study and compare two different hydrosilylation reactions to functionalize hydride-terminated SiNCs, in terms of the photophysical properties, the thermal gravimetric analysis and the X-Ray Photoelectron Spectroscopy of the obtained colloidal solutions, focusing my attention on two different SiNCs diameters, 3 and 5 nm. In general, all the samples functionalized by the thermal hydrosilylation reaction showed better photophysical properties, with respect to the samples functionalized by the 4-DDB promoted hydrosilylation. Moreover, 3 nm diameter SiNCs showed worse photophysical properties with respect to 5 nm diameter SiNCs, maybe due to the higher probability of their excitons to interact with the possible trap states on the Si surface. TGA and XPS data confirmed the results obtained through the photophysical measurements, indicating a better surface passivation achieved by the thermally induce hydrosilylation with respect to the RT, 4-DDB promoted, one. Nevertheless, it is worth noting considering that the thermal hydrosilylation needs

very high temperatures to be promoted and many ligands could undergo degradation or oligomerization caused by the heating, as mentioned above. Moreover, the reaction cannot be carried out using a solvent, thus it needs an excess of the ligand, which works also as the solvent. Therefore, this limit the use of pricy molecules in this kind of functionalization.

Appendix A - Photophysical Methods

SiNCs were characterized by the acquisition of absorption, emission and excitation spectra, luminescence lifetimes, anisotropy measurements, the number of the attached molecules onto the SiNCs surface, the Si luminescence quantum yield, the surface-attached chromophore quenching efficiency and the SiNCs sensitization efficiency. All solution phase experiments were run in 1 cm optical path quartz cuvettes; high purity or distilled solvents were used. Experiments in de-oxygenated atmosphere were performed in a modified 1 cm optical path quartz cuvette provided with vacuum manifold, compatible stopcock and PTFE valve.

A.1 Electronic absorption spectra

UV-Visible absorption spectra are the result of electronic transitions taking place when photons are absorbed by a ground-state species, producing excited states. Each chemical species has its own sequence of excited states and then its own characteristic absorption spectrum. Absorption spectra were acquired with the double beam UV-Vis spectrophotometer, Perkin-Elmer Lambda 650, which is shown in **figure A.1**.
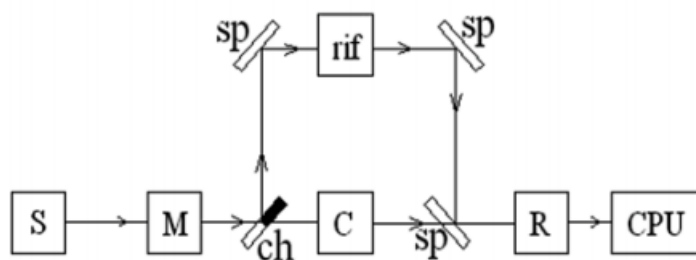
Figure A.1- double-beam UV-Vis spectrophotometer scheme where S=light source (a tungsten lamp operates between 900 and 320 nm, while an Hydrogen one works between 320 and 190 nm); M=monochromator (diffraction grating); C= Sample; rif= reference; R= detector (photo-multiplier tube) ch=chopper; Sp= mirrors; CPU= computer.

The chopper splits the analyzing light beam in two parts, so the reference absorbance and the sample absorbance are measured at the same time and the first one is subtracted from the second one. Using the Lambert-Beer law, it is possible to calculate the value of the molar absorption coefficient ε (expressed in $M^{-1}\,cm^{-1}$) from the spectra acquired:

$$A = \varepsilon * b * c$$

Where A is the sample absorbance, b is the cuvette optical path (1cm in our case) and c is the sample molar concentration.

A.2 Number of chromophore units on the SiNCs surface

In order to calculate the number of chromophore units, two solutions are needed: one containing the chromophore-functionalized SiNCs and another one containing only SiNCs at the same concentration of SiNCs in the first solution. The equation used to calculate the number of chromophores for each SiNC is:

$$n° \frac{\text{chromophores}}{\text{SiNC}} = \frac{C_{ch.}}{C_{SiNCs}}$$

where $C_{ch.}$ is the chromophore concentration and C_{SiNCs} is the SiNCs concentration; both of them can be calculated using the Lambert-Beer law (see above), knowing their molar absorption coefficients at their maximum absorption wavelength λ_{abs_max}.

SiNCs concentration calculation: $C_{SiNCs} = \frac{A_{max\_SiNCs}}{\varepsilon_{max\_SiNCs} \, x \, b}$

where A_{max_SiNCs} is the SiNCs absorbance at their λ_{abs_max}, ε_{max_SiNCs} is the SiNCs molar absorption coefficient at their λ_{abs_max} and b is the light path of the used cuvette (1 cm).

Chromophore concentration calculation: $C_{ch.} = \frac{A_{max\_ch.}}{\varepsilon_{max\_ch.} x \, b}$

where A_{max_ch} is the chromophore absorbance at his λ_{abs_max}, ε_{max_ch} is the chromophore molar absorption coefficient at his λ_{abs_max} and b is the light path of the used cuvette (1 cm). A_{max_ch} can be calculated subtracting the SiNCs absorbance at λ_{abs_max} of the chromophore (A_{SiNCs_ch}) from the total absorbance at the same λ_{abs_max} (A_{TOT}):

$$A_{max\_ch} = A_{TOT} - A_{SiNCs\_ch}$$

A.3 Emission and excitation spectra

The sample luminescence can give precious information on the nature of the emitting excited state and can be exploited for qualitative and quantitative analyses. Emission spectra in the visible range (3nm diameter SiNCs) were acquired with the fluorimeter Perkin-Elmer LS55 and emission spectra in the NIR (near-infrared) range (5nm diameter SiNCs) were acquired using the Edimburgh F900, a fluorimeter equipped with a high sensitivity germanium detector together with a

liquid nitrogen cooling system, where the signal acquisition is performed by a lock-in amplifier connected to a chopper in order to maximize the signal to noise ratio. In **figure A.2** a general spectrofluorimeter diagram is shown.
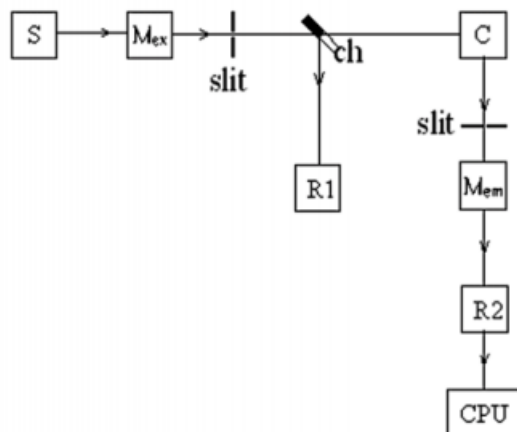
Figure A.2- Spectrofluorimeter scheme. S=light source (Xe, 2µs pulsed lamp); M=monochromators (diffraction grating); C= Sample; R1= reference detector to correct lamp emission; R2 = detector (photo-multiplier tube) ch=chopper; CPU= computer.

This instrument is used to study the molecular radiative transitions from the excited state (in general S1 or T1) to the ground state (S0). In addition, setting a delay between the lamp pulse and the light detection it is possible to divide the fluorescence from the phosphorescence. Emission spectra are characterized by a fixed excitation wavelength, while emission monochromator scans emission wavelengths; excitation spectra, on the opposite, are taken fixing an emission wavelength but tuning excitation ones. Furthermore, a correct excitation spectrum must be registered on the so-called linearity interval, which means that the sample solution must show absorbance under 0.1 in the whole absorption spectrum since, only for little values of absorbance, the dependence of the emission intensity can be approximated as linear. Excitation spectra are a powerful tool to evidence the

energy transfer processes, which take place inside the studied sample. In general, the higher excited states populated by excitation are converted with unitary efficiency into the lowest emitting excited state (Kasha rule). For this reason, the shape of the excitation spectrum is a replica of the absorption spectrum of the sample.

A.4 Luminescence lifetime

Most lifetime measuring techniques are based on the recording of the excited state concentration as a function of time. They consider a direct proportionality at any time between the number of emitted photons and the number of excited states present. Luminescence lifetime of an excited species (τ) is defined as the time in which its concentration become 1/e than the initial value. In order to acquire this value, two different methods were used: time-gated fluorescence detection, which is generally used for longer lifetimes (SiNCs have a luminescence lifetime in the μs-range), and time-correlated single-photon counting, which is generally used for smaller lifetime (chromophores have a luminescence lifetime in the ns-range). Emission intensity decays in the μs-range were performed on a homemade time-resolved phosphorimeter equipped with an Avalanche PhotoDiode C12703 with a peak sensitivity wavelength of 800 nm of the emitted light and a pulsed LED as the excitation source. The second method used is the time-correlated single-photon counting (TCSPC), which is based on the probability that one single photon emitted by the fluorescent sample is captured by a high sensitivity detector. This probability is directly dependent on the excited states concentration variation during time. For this purpose, the time correlated single-photon counter is the instrument used, which is able to detect the shortest lifetimes (from 0.5 ns to 20 μs). In **figure A.3** the schematic diagram of a single-photon counter is shown.
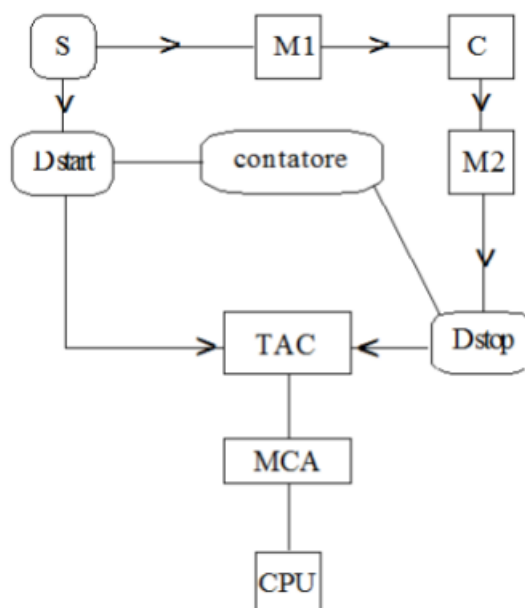
Figure A.3- schematic diagram of a single-photon counter, where S is the light source, M1 and M2 are the excitation and emission diffraction grating monochromators, D start and D stop are the source and the sample photomultipliers, C is the sample, TAC is a time to amplitude converter, MCA is the multichannel analyser and CPU is the computer.

The analysis of the acquired lifetimes start by examining the intensity decay data on a logarithmic scale. The following two possibilities represent the most common cases:

1. The decay appears linear. In this case, a simple first-order decay model is usually correct. Data are analysed by a mono-exponential fit.

2. The decay does not look linear, or the mono-exponential fit was not satisfactory. In this case, a more complex model should be considered, taking into account the peculiarities of the investigated system. Most commonly, the decay of the total emission intensity is fitted as a sum of two exponential terms, which means that the system contains two different and independent luminescent compounds with two

different lifetimes τ1 and τ2. In such a case, the pre-exponential factors A1 and A2 are determined by the emission quantum yield of them, by their emission intensity and by their concentration.

$$I(t) = A_1 \exp\left(-\frac{t}{\tau_1}\right) + A_2 \exp\left(-\frac{t}{\tau_2}\right)$$

A.5 Luminescence quantum yield

The luminescence quantum yield Φ is an important parameter for the characterization of luminescent excited state and it is defined as:

$$\Phi = \frac{\text{n° of emitted photons}}{\text{n° of absorbed photons}}$$

It can be calculated by the relative method, which consists in the use of a reference compound with a known Φ and in the comparison between its emission spectrum and the sample emission spectrum. The two emission spectra, corrected by the detector response, must be acquired in the same spectral range. Subsequently, the Φ is calculated by the equation:

$$\Phi_S = \Phi_R \frac{S_S}{S_R} \frac{A_R}{A_S} \frac{n_S^2}{n_R^2}$$

Where Φ_S and Φ_R are the sample and the reference luminescence quantum yield respectively, S_S and S_R are the areas underneath the emission spectra of the sample and of the reference respectively, A_S and A_R are the sample and reference absorbance at the excitation wavelength respectively, n_S and n_R are the refraction indexes of the sample and of the reference solvent respectively. Exciting the two samples at the same wavelength, in which the two solutions have the same absorption, the equation could be simplified in:

$$\Phi_S = \Phi_R \frac{S_S}{S_R} \frac{n_S^2}{n_R^2}$$

The reference is chosen considering the excitation wavelength, the emission spectral range and the attended Φ value. A water solution of $[Ru(bpy)_3]^{2+}$ $2Cl^-$ is commonly used as the reference for 3 nm diameter SiNCs, while an EtOH solution of 1,1′,3,3,3′,3′-hexamethyl-indotricarbocyanine iodide (HITCI) is commonly used as the reference for 5 nm diameter SiNCs.

Even when performed with great care, the measurement of luminescent quantum yields remains prone to errors; data obtained in different laboratories can easily differ by 10% or more.

A.6 Chromophore quenching efficiency

The quenching efficiency of the chromophores can be calculated using the equation:

$$Ratio = \frac{Int._S}{Int._{0\%}}$$

and subtracting this value from the unity:

$$\eta q = 1 - Ratio$$

where η_q is the quenching efficiency, $Int._S$ is the integral of the sample emission and $Int._{0\%}$ is the integral of the emission of a solution with 0% of energy transfer. The two emission spectra must be acquired exciting at an isosbestic point.

The 0% energy transfer solution is a solution made of the same chromophore concentration and the same SiNCs concentration of the real sample, but herein the two compounds are not linked together and the energy transfer is not observed.

A.6 SiNCs sensitization efficiency

The SiNCs sensitization efficiency ( ) can be calculated with the equation:

$$\eta_s = \frac{I_s - I_{0\%}}{I_{100\%} - I_{0\%}}$$

where I_s is the integral of the sample emission (the sum of the SiNCs emission caused by the SiNCs direct absorption at the excitation wavelength and the SiNCs sensitization due to the energy transfer from the chromophores), $I_{0\%}$ is the integral of the SiNCs emission with the 0% of energy transfer (see above) and $I_{100\%}$ is the integral of the SiNCs emission with the 100% of energy transfer (mathematically reproduced). The solutions must be excited at the same wavelength (maximum absorbance wavelength of the involved chromophore) and the same spectral region must be investigated for the emissions.

A.7 Luminescence anisotropy

Luminescence anisotropy can be exploited to study any kind of process that causes a change in the orientation of the dipole moment associated with the electronic distribution of a luminescent excited state. The most commonly studied processes are molecular rotation and energy migration. Luminescence anisotropy measurements are based on the fact that excitation with linearly polarized light of a randomly orientated sample may produce a polarized emission. Considering an isotropic solution (with randomly orientated molecules) immobilized by freezing the solvent and with a very low concentration (in order to avoid electronic interactions), if a linearly polarized radiation is sent to the sample, the absorption probability will be greatest for the molecules with the transition moment parallel to the polarization direction. Thus, the population of the formed excited states will possess a preferential orientation with respect to the direction of polarization of the

excitation light. Because of solution rigidity, the emitting dipole of the excited states will also be oriented preferentially in a given direction and the emitted light will be polarized. With this measurement is also possible to obtain information on the angular displacement (β) of the transition moment vector between absorption (TM$_{abs}$) and emission (TM$_{em}$) (**figure A.4**).
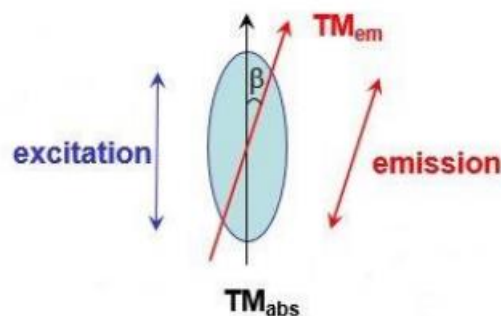
Figure A.4: Representation of the angular displacement (β) of the transition moment vector between absorption (TM$_{abs}$) and emission (TM$_{em}$).

In general, luminescence anisotropy is measured with conventional spectrofluorimeters by adding two polarizers in the excitation and emission beams, respectively. The sample is excited with vertically polarized light, and the fluorescence is analyzed with the emission polarizer. Two intensity values are measured: I$_{//}$, with the emission polarizer in the vertical position (parallel to the excitation one) and I$_\perp$, with the emission polarizer in the horizontal position (perpendicular to the excitation one). The polarization of the sample emission is quantified by the anisotropy value r, defined by the equation:

$$r = \frac{I_{//} - I_\perp}{I_{//} + 2I_\perp}$$

For randomly oriented molecules in diluted rigid solution, the limiting values for r are -0.2 and +0.4, corresponding to parallel and perpendicular orientations, respectively, of the absorption and emission transition moments. If the solution is

not rigid and dilute, several depolarization processes can come into play. These can cause a reduction of the population of the selectively oriented excited states initially created, leading to lower r values. Such depolarization processes are energy migration, rotational diffusion and trivial processes. Energy migration can occur at sufficiently high concentration. If the donor and the acceptor have a random relative orientation, the preferential orientation of the initially formed excited state is lost. The rotational diffusion is the most important depolarization process in fluid solutions. The rate of rotational diffusion of small molecule in low-viscosity media is typically faster than the rate of excited state decay, leading to randomly oriented excited states, with complete depolarization of the emission.

A.8 Dynamic Light Scattering (DLS)

DLS is a useful technique for the particles size determination. With the measurement of the intensity fluctuations of the scattered light during time, it is possible to obtain the value of the translational diffusion coefficient (D) of a particle in a liquid solution. D defines the Brownian motion of the particle (the random movement of the particles in a liquid solution due to the collisions with the solvent molecules around) and so it is directly proportional to the particle size. In order to acquire the value of D, many experimental conditions are needed: (i) Temperature and dispersant viscosity must be accurately known; (ii) Particles number in the investigated volume must be constant; (iii) Temperature must be constant (absence of convection currents in the sample is required). The diffusion coefficient D is correlated to the hydrodynamic diameter d(H) thanks to the Stock-Einstein equation:

$$d(H) = \frac{KT}{3\pi\eta(T)D}$$

Where K is the Boltzmann's constant, T the absolute temperature, η(T) the dispersant viscosity at the given temperature and d(H) is the diameter of a sphere with the same diffusion coefficient as the particles, this value refers to how a particle moves within a liquid. The intensity distribution can be converted into a volume distribution if the optical properties (n) of the particles are known. The volume distribution could provide more realistic results for non-perfectly monodisperse samples. The intensity fluctuations of the scattered light depend on the speed of the particle diffusion due to the Brownian motion, thus they also depend on the particles size (smaller particles are faster than bigger particles). In addition, constructive or destructive interference on scattered light may occur because of the motion. The algorithm used to study the intensity fluctuation during time is the correlation function G(τ):

$$G(\tau) = \int_0^\infty I(t) * I(t + \tau)d\tau$$

which measures the degree of similarity between two signals, or one signal with itself at varying time intervals. The sample time of the correlator is τ. The equation gives the signal correlation as a function of time. For large particles, the correlation persists for a long time due to their slow motion; in contrast, for small particles, the correlation disappears more rapidly because of their fast motion. The particle mean size and the distribution width are obtained with the cumulant analysis: assuming a one particle size or a narrow distribution and fitting the correlation curve with a mono-exponential equation:

$$(\tau) = [1 + B\,(-2Dq^{\,2}\,\tau)]$$

Where A is the baseline of the correlation function, B is the intercept of the correlation function, D is the translational diffusion coefficient and q:

$$q = \frac{4\pi n}{\lambda_0}\,sen\frac{\theta}{2}$$

where n is the refractive index of the solution, λ_0 is the wavelength of the laser and θ is the scattering angle.

A.9 Photophysical measurements on LSC (see chapter 3)

UV-Vis transmittance spectra of the prepared LSCs were collected on an Agilent Cary 5000 UV-Vis-NIR spectrophotometer equipped with solid state holder. Color Rendering Index (CRI) and Colour Coordinates were calculated by multiplying the transmittance spectrum to the incident AM 1.5G spectrum, in order to simulate the spectrum of the light transmitted through the LSC:

$$T = \frac{I_T}{I_0} \rightarrow I_T = I_0 \times T$$

The resulting spectra were processed with CIE 13.3 CRI (1994) software© (Péter Sylvester, University of Veszprém) and the obtained coordinates plotted in the CIE 1931 color space chromaticity diagram. The fraction of photons absorbed in the visible region of the solar spectrum (λ_{abs} = 400-700 nm) was calculated as follows:

$$\eta_{abs}^{400-700nm} = \frac{\int_{\lambda=400nm}^{\lambda=700nm} I_0 - I_T}{\int_{\lambda=400nm}^{\lambda=700nm} I_0}$$

PL spectra were registered with the same equipment described for the solution-phase characterization, but sample holder and excitation source were adapted depending on the specific measurement. PLQY of the LSCs was calculated with the integrating sphere using the method described by De Mello.[300] A reference polymer slab with the same composition was used as blank sample. The optical efficiency of the LSC was measured adapting a method previously described by Coropceanu et al.[171] based on the integrating sphere determination. Black tape was used to cover the edges of the LSC and the PLQY was measured in this condition and compared with the one measured on the same LSC with free edges.

Inner filter correction

In order to take into account of the inner filter effect and to compare the PL spectra of the **Si-DPA** and **Si+DPA** samples with the one with pristine SiNCs, **Si**, the following correction has to be applied to the latter:

$$I_{1,inner\ filter} = I_{1,no\ inner\ filter} \frac{A_1}{A_{tot}} (1 - 10^{-(A_{tot})})$$

Where $I_{1,\ inner\ filter}$ is the intensity measured in the sample with an absorbance equal to A_{tot}, $I_{1,\ no\ inner\ filter}$ is the calculated value in absence of inner filter effect and A_1 is the absorbance of the investigated specie (SINCs) in the reference mixture (either **Si-DPA** or **Si+DPA**) having overall absorption A_{tot}. **Figure 3.14** reports the calculated **Si** spectrum following this approach, in comparison with pristine **Si+DPA** and **Si-DPA** samples, both exhibiting higher PL intensity with respect to corrected **Si**.

Photovoltaic characteristics determination

For the photovoltaic characterization of the LSC devices, a-Si PV cell was masked, exposing an area of 1.08 cm² in order to fully cover the LSC short edge in all samples. The cell was fixed to the side of a homemade black cell and connected to a source picoammeter (Keithley 2401) equipped with a solar simulator. The solar simulator consists in a Xe lamp with an AM 1.5 - Global filter, which can generate vis-UV light with the power intensity of 1 Sun (100 mW cm⁻²). The light intensity of the solar simulator was controlled through a calibrated silicon solar cell. The optical contact between the cell and the LSC was optimized by adding a clear tape layer between them, in order to reduce the roughness of the slab and increase the quality of the optical interface. Photovoltaic characteristics in direct illumination configuration of the a-Si cell was performed, obtaining PCE equal to 18.1%, J$_{SC}$ = 44.1 mA and V$_{OC}$ = 592 mV. The G-factor was calculated as follows, by using the size of each LSC reported in **table A.1**:

$$G = \frac{A_{top}}{2A_{edge,long} + 2A_{edge,short}}$$

Where A_{top}= Lxl, $A_{edge,long}$= Lxt and $A_{edge,short}$= lxt.

	G	L	I	t	q_re-shaping	η_opt,q
Blank	2.86	6.40	2.35	0.30	-	
DPA	2.69	6.10	2.20	0.30	0.75	4.81
Si	2.64	5.70	2.20	0.30	1.07	3.30
Si+DPA	2.56	5.40	2.05	0.29	0.85	3.34
Si-DPA	2.98	5.60	2.15	0.26	0.93	4.98

Table A.1- G factor and lateral size of the prepared LSCs, expressed in cm. Re-shaping factor (q_re-shaping), is defined as the ratio between the c-Si PV cell EQE over the emission spectrum of the luminophore $\langle QPL \rangle$ and the EQE over the full solar spectrum $\langle Qs \rangle$. Optical efficiency corrected for the re-shaping factor (η_opt,q).

The JSC values were normalized for the area mismatch between LSC/PV cell contact area and the exposed area of the cell employed for the direct illumination configuration (i.e. 1.08 cm²). The values were calculated as follows:[148]

$$\eta_{opt,q} = \frac{\eta_{opt}}{q_{re-shaping}}$$

Appendix B - Supplementary Techniques and Characterizations

B.1 Trasmission Electron Microscope (TEM)

HR-TEM and STEM-HAADF micrographs were recorded on a FEI Tecnai F20T TEM equipped with a Schottky emitter and operated at 120kV to minimize beam-induced damage in low atomic weight materials. The TEM is provided with a Gatan MSC794 CCD camera, 127 Fischione High Angle Annular Dark Field STEM detector and double tilt specimen holder. Compositional analysis of the samples is possible thanks to an attached EDAX EDS X-ray spectrometer PV9761 with Super Ultra thin window. The information limit provided by this instrumental setup is equal to 0.14 nm, while the point resolution in TEM mode (Scherzer defocus) is equal to 0.24 nm and the one in STEM mode is 0.19 nm. **Figure B.1** displays the different optical setups employed to obtain a) selected area diffraction (SAD or SAED), b) high resolution micrographs (HR-TEM or HREM) and scanning transmission micrographs (STEM). Further details on the theory of the TEM working modes can be found in literature.[301] The samples are usually prepared by drop casting of few drops of the sample solution on carbon coated copper TEM grids. The shape of the carbon film is chosen depending on the expected size and shape factor of the material of interest. The solvent is then removed by vacuum pumping the grid or, when the material is not heat sensitive, by rapid heating over the solvent boiling point.
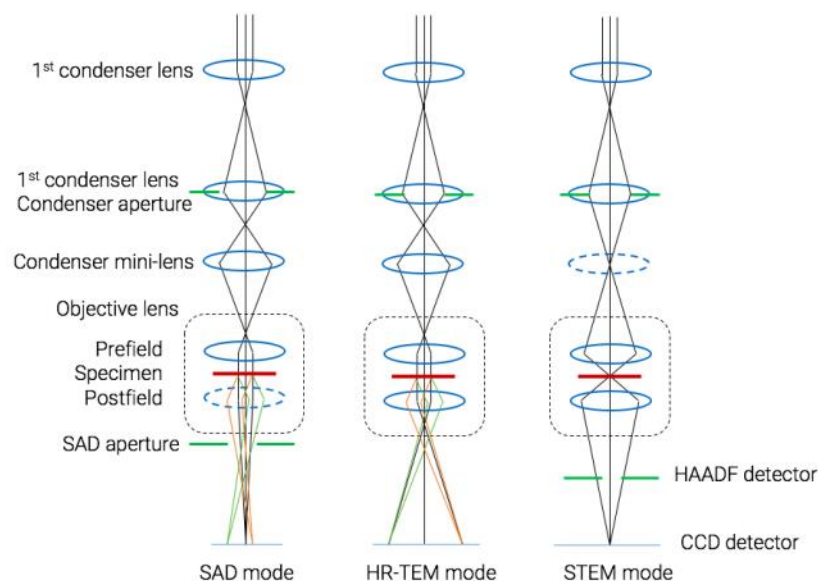
Figure B.1- Schematic representation of a TEM column in different working modes.

B.2 X-ray Photoelectron Spectroscopy (XPS)

X-ray photoelectron spectroscopy (XPS) was performed using a commercial X-ray photoelectron spectrometer (Kratos Axis Ultra), utilizing a monochromatic Al Kα X-ray source (hv=1486.5 eV), hybrid optics (employing a magnetic and electrostatic lens simultaneously) and a multi-channel plate detector coupled to a hemispherical analyzer. Si nanocrystal films were drop-cast onto indium tin oxide coated glass slides and were secured on the experimental tray using double-sided Cu tape. The photoelectron take-off angle was normal to the surface of the sample and 45° with respect to the X-ray beam. All spectra were recorded using a single sweep and an aperture slot of 300 μm by 700 μm. High-resolution spectra were collected with 20 eV pass energy. Spectra were collected at 0.1 eV intervals and 1500 ms integration time through a tungsten coil set at 4.8 V bias with respect to the sample. The pressure in the analysis chamber was typically 3×10^{-9} Torr during data acquisition. Sample charging was corrected by shifting the Si^0 2p$^{3/2}$ to a binding energy of 99.3 eV. Background subtraction was done using a Shirley background model. The Si^0

2p$^{3/2}$ and Si^0 2p$^{1/2}$ peaks were fit with Voigt profiles (30% Gaussian character) centered at 99.3 and 99.8 eV, respectively, maintaining the appropriate intensity ratio of 2:1 corresponding to the spin-orbit splitting ratio for p-orbitals. Peak contributions from Si^{1+}, Si^{2+}, Si^{3+}, Si^{4+}, and Si-C were fit using Voigt profiles centered at 100.4 eV, 101.5 eV, 102.6 eV, and 103.7 eV, and 102.0 eV, respectively.[215]

B.3 Proton Nuclear Magnetic Resonance (^{1}H-NMR)

^{1}H-NMR spectra were acquired with the Varian Mercury 400 MHz, which uses a pulse system with a Fourier transform. In **figure B.2** an NMR spectrometer is shown. Chemical shifts are reported in ppm using tetramethylsilane as the internal reference standard. Data are reported as follows: chemical shift, multiplicity (s = singlet, d = doublet, t = triplet, q = quartet, br = broad, m = multiplet), coupling constants (Hz).
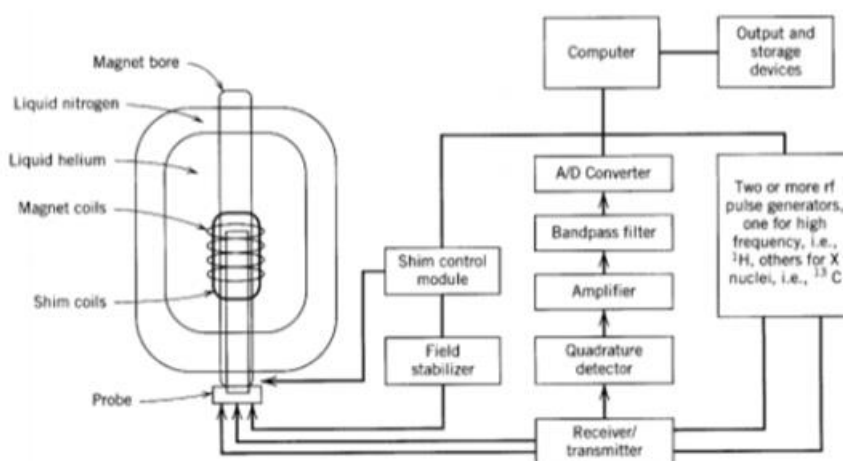
Figure B.2- schematic representation of an NMR spectrometer.

The instrument uses a superconductor magnet, which is immersed in liquid helium (4.2 kelvin) and inserted inside a nitrogen-filled Dewar container (77.4 kelvin). This set-up allows us to work at very low temperature, near the absolute zero, and to

avoid helium rapid evaporation. The sample is introduced inside the probe, which contains magnet coils and shim coils used to create the radiofrequency and to keep the magnetic field constant. Proton Larmor frequency, which is the resonance frequency for the spin inversion of an isolated proton, can be calculated with the equation:

$$\nu = \frac{\gamma}{2\pi} B_0$$

where γ is the proton gyromagnetic ratio and B_0 is the applied magnetic field. Thanks to the magnet coils, a radiofrequency pulse can be sent to the sample, causing the inversion of the spin of protons with the precession axes aligned to the magnetic field direction. The analysis of the protons relaxation process allows us to obtain the transversal magnetization free induction decays, subsequently analysed through the Fourier transform in order to obtain the frequency-dependent NMR spectra. The resonance frequency of the protons varies with the local chemical environment, observing the law:

$$\nu_{eff} = \frac{\gamma}{2\pi} B_0 \, (1{-}\sigma)$$

where σ is the shield constant, which depends on the local chemical environment; for this reason it is possible to distinguish the different protons in the sample. The frequency could be converted in the chemical shift (δ), expressed in ppm, with the formula:

$$[ppm] = \frac{\nu_{protone}[Hz] - \nu_{TMS}[Hz]}{\nu_{app}[Hz]} \times 10^6 ppm$$

Where tetramethylsilane (TMS) is the reference compound. The expression of the frequency in ppm is advantageous in order to have smaller numbers and to be independent from the frequency applied to the instrument. In this way, it is also possible to compare directly spectra acquired with different resolutions.

Appendix C – Details on In Vivo Animal Studies

C.1 In vivo animal studies[101] (see chapter 4)

All animal procedures were approved by the Institutional Animal Care and Use Committee, and the studies here were carried out in compliance with these approved procedures. Briefly, 10^5 MDA-MB-231 cells were injected under the skin on the flank of a nude mouse (Charles River Laboratories, Wilmington, MA). Once tumors of approximately 100 mm^3 developed, these mice were then In Vivo (IV) injected with 200 µL of 4 nm **Si-PEG** (1.5 µM) and were allowed to rest for 2, 4, 24, and 48 h prior to imaging. The animals were imaged both in vivo under anesthesia and then after sacrifice the organs were extracted for ex vivo imaging. The imaging was performed based on a custom fluorescence imaging system, which used a 457 nm Diode-pumped solid-state laser (DPSS laser, Laserglow Tech, Toronto ON Canada) for excitation and imaging with an ICCD camera (PI-MAX 4 1024i, Princeton Instruments, Acton MA USA) for optical signal collection. **Figure C.1** shows the profile of the laser intensity as a function of time. A 10 µs delay after a complete shutdown of the excitation source was chosen for time-gated imaging. A function generator (Agilent 33120A, Agilent Technologies, Inc., Santa Clara, CA 95051, United States) was used to synchronize the ICCD camera and DPSS laser for time gating detection. A 1 kHz square wave with duty cycle of 20% was used to modulate the DPSS laser for time-gating mode, and 200 µs was accumulated on the ICCD camera with 100 µs delay after the falling edge. To increase the exposure time, 1000 frames were accumulated on the chip of the ICCD camera before each readout, so the total exposure time was 0.2 s. The gain was set to the maximum value for the ICCD camera to improve the detection sensitivity. A Sigma 70 mm f/2.8 DG ART

macro lens was coupled with the ICCD camera, with a final field of view (FOV) of 10 cm x 10 cm. An 800 nm bandpass filter with full width at half maximum (FWHM) of 40 nm (Tharlab Inc. Newton, New Jersey, United States) was coupled between the lens and the ICCD camera to filter out the 457 nm laser when collecting the emission of SiNCs. For comparison between time-gated and continuous wave (CW) imaging, the latter was tested using the same laser and camera working with the same exposure time and accumulated number of frames, but in CW mode.
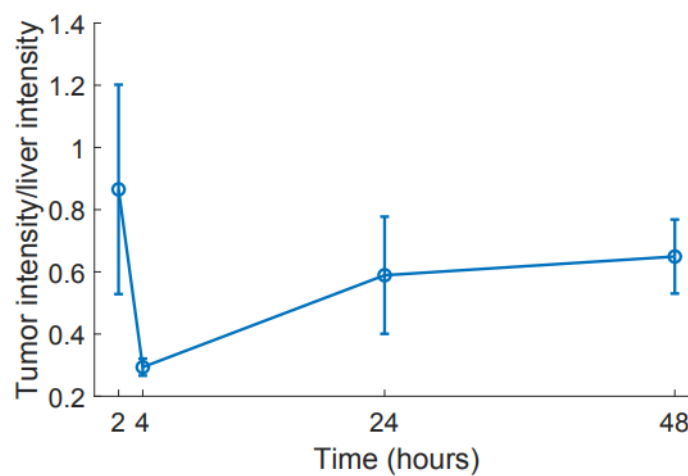
Figure C.1- Intensity decay profile of the diode-pumped solid state laser.

REFERENCES

1. Taniguchi, N. (1974). On the basic concept of "Nano-Technology", Proceedings of the International Conference on Production Engineering Tokyo, Part II. In Japan Society of Precision Engineering, Tokyo, pp. 5–10.

2. Armaroli, N., and Balzani, V. (2007). The future of energy supply: Challenges and opportunities. Angew. Chemie - Int. Ed. *46*, 52–66.

3. Maxwell, J.C. (1873). A Treatise on Electricity And Magnetism (Press, Oxford: Clarendon).

4. Einstein, A. (1905). Über einen die Erzeugung und Verwandlung des Lichtes betreffenden heuristischen Gesichtspunkt. Ann. Phys. *17*, 132–148.

5. Lewis, G. (1926). The Conservation of Photons. Nature *118*, 874–875.

6. De Broglie, L. (1924). Tentative theory of light quanta. Philos. Mag. *47*, 446–458.

7. Balzani, V., Ceroni, P., and Juris, A. (2014). Photochemistry and Photophysics: concepts, research, applications (WILEY-VCH Verlag).

8. Bonazzi, M. (2010). Communicating Nanotechnology — why, to whom, saying what and how? E. Commission, ed.

9. Hull, M.S. (2019). Multidimensional Impacts of Nanotechnology on Public Health (Elsevier Inc.).

10. Nunes, D., Pimentel, A., Santos, L., Barquinha, P., Pereira, L., Fortunato, E., and Martins, R. (2019). Metal Oxide Nanostructures: Synthesis, Properties and Applications (Elsevier).

11. Richard Zsigmondy (1966). Properties of colloids. In Nobel Lectures in Chemistry 1922-1941 (Elsevier Publishing Company).

12. Langmuir, I. (1966). Surface chemistry. In Nobel Lectures in Chemistry 1922-1941 (Elsevier Publishing Company).

13. Feynman, R.P. (1960). There's plenty of room at the bottom. Eng. Sci., 22–36.

14. Editorial: "Plenty of room" revisited (2009). Nat. Nanotechnol. *4*, 781.

15. Cappy, A., Stievenard, D., and Vuillaume, D. (2002). Nanotechnology: The next industrial revolution? In Gallium Arsenide applications symposium.

16. Binnig, G., and Rohrer, H. (1993). Scanning Tunneling Microscopy, from birth to adolescence. In Nobel Lectures in Physics 1981-1990, W. S. P. Co., ed.

17. Binnig, G., Quate, C.F., and Gerber, C. (1986). Atomic force microscope. Phys.

Rev. Lett *56*, 930.

18. Sahoo, S.K., Parveen, S., and Panda, J.J. (2007). The present and future of nanotechnology in human health care. Nanomedicine Nanotechnology, Biol. Med. *3*, 20–31.

19. Mino, L., Agostini, G., Borfecchia, E., Gianolio, D., Piovano, A., Gallo, E., and Lamberti, C. (2013). Low-dimensional systems investigated by x-ray absorption spectroscopy: A selection of 2D, 1D and 0D cases. J. Phys. D. Appl. Phys. *46*.

20. Chryssolouris, G., Stavropoulos, P., Tsoukantas, G., Salonitis, K., and Stournaras, A. (2004). Nanomanufacturing processes: a critical review. Int. J. Mater. Prod. Technol. *21*, 331–348.

21. Alivisatos, A.P. (1996). Semiconductor clusters, nanocrystals, and quantum dots. Science (80-.). *271*, 933–937.

22. Mansur, H.S. (2010). Quantum dots and nanocomposites. WIREs Nanomedicine and Nanobiotechnology *2*, 113–129.

23. Brus, L.E. (1983). A simple model for the ionization potential, electron affinity, and aqueous redox potentials of small semiconductor crystallites. J. Chem. Phys. *79*, 5566–5571.

24. Efros, A., and Efros, A. (1982). Interband Light Absorption in Semiconductor Spheres. Sov. Phys. Semicond. *16*, 772–775.

25. Resch-Genger, U., Grabolle, M., Cavaliere-Jaricot, S., Nitschke, R., and Nann, T. (2008). Quantum dots versus organic dyes as fluorescent labels. Nat. Methods *5*, 763–775.

26. Hötzer, B., Medintz, I.L., and Hildebrandt, N. (2012). Fluorescence in nanobiotechnology: Sophisticated fluorophores for novel applications. Small *8*, 2297–2326.

27. Silvi, S., and Credi, A. (2015). Luminescent sensors based on quantum dot-molecule conjugates. Chem. Soc. Rev. *44*, 4275–4289.

28. Yong, K.T., Law, W.C., Hu, R., Ye, L., Liu, L., Swihart, M.T., and Prasad, P.N. (2013). Nanotoxicity assessment of quantum dots: From cellular to primate studies. Chem. Soc. Rev. *42*, 1236–1250.

29. Dasog, M., Kehrle, J., Rieger, B., and Veinot, J.G.C. (2016). Silicon Nanocrystals and Silicon-Polymer Hybrids: Synthesis, Surface Engineering, and Applications. Angew. Chemie Int. Ed. *55*, 2322–2339.

30. Cullis, A.G., and Canham, L.T. (1991). Visible-light emission due to quantum size effects in porous crystalline silicon. Nature *353*, 335–338.

31. Proot, J.P., Delerue, C., and Allan, G. (1992). Electronic structure and optical properties of silicon crystallites: Application to porous silicon. Appl. Phys. Lett. *61*, 1948–1950.

32. Park, J.H., Gu, L., Von Maltzahn, G., Ruoslahti, E., Bhatia, S.N., and Sailor, M.J. (2009). Biodegradable luminescent porous silicon nanoparticles for in vivo applications. Nat. Mater. *8*, 331–336.

33. Cunin, F., Schmedake, T.A., Link, J.R., Li, Y.Y., Kom, J., Bhatia, S.N., and Sailor, M.J. (2002). Biomolecular screening with encoded porous-silicon photonic crystals. Nat. Mater. *1*, 39–41.

34. Priolo, F., Pavesi, L., Negro, L.D., Mazzoleni, C., and Franzo, G. (2000). Optical gain in silicon nanocrystals. Nature *408*, 440–444.

35. Sirleto, L., Ferrara, M.A., Nikitin, T., Novikov, S., and Khriachtchev, L. (2012). Giant Raman gain in silicon nanocrystals. Nat. Commun. *3*, 1181–1186.

36. Paper, P.H., Chandra, S., Masuda, Y., and Shirahata, N. (2017). Transition-Metal-Doped NIR-Emitting Silicon Nanocrystals. Angew. Chem. Int. Ed. *56*, 1–5.

37. Sugimoto, H., Yamamura, M., Fujii, R., and Fujii, M. (2018). Donor-Acceptor Pair Recombination in Size- Purified Silicon Quantum Dots. Nano Lett. *18*, 7282–7288.

38. Sun, W., Qian, C., Chen, K.K., and Ozin, G.A. (2016). Silicon nanocrystals: It's simply a matter of size. ChemNanoMat *2*, 847–855.

39. Dohnalová, K., Gregorkiewicz, T., and Kůsová, K. (2014). Silicon quantum dots: Surface matters. J. Phys. Condens. Matter *26*, 173201.

40. Dohnalová, K., Poddubny, A.N., Prokofiev, A.A., De Boer, W.D., Umesh, C.P., Paulusse, J.M., Zuilhof, H., and Gregorkiewicz, T. (2013). Surface brightens up Si quantum dots: Direct bandgap-like size-tunable emission. Light Sci. Appl. *2*.

41. Hapala, P. (2013). Theoretical analysis of electronic band structure of 2- to 3-nm Si nanocrystals. Phys. Rev. B *87*, 195420.

42. Sychugov, I., Pevere, F., Luo, J.W., Zunger, A., and Linnros, J. (2016). Single-dot absorption spectroscopy and theory of silicon nanocrystals. Phys. Rev. B *93*, 2–6.

43. Lee, B.G., Luo, J.W., Neale, N.R., Beard, M.C., Hiller, D., Zacharias, M., Stradins, P., and Zunger, A. (2016). Quasi-Direct Optical Transitions in Silicon Nanocrystals with Intensity Exceeding the Bulk. Nano Lett. *16*, 1583–1589.

44. Pavesi, L., and Turan, R. (2010). Silicon Nanocrystals (Wiley-VCH Verlag

GmbH & Co. KGaA).

45. Dasog, M., De Los Reyes, G.B., Titova, L. V., Hegmann, F.A., and Veinot, J.G.C. (2014). Size vs Surface: Tuning the Photoluminescence of Freestanding Silicon Nanocrystals Across the Visible Spectrum via Surface Groups. ACS Nano *8*, 9636–9648.

46. Hessel, C. M.; Reid, D.; Panthani, M. G.; Rasch, M.R.., and Goodfellow, B. W.; Wei, J.; Fujii, H.; Akhavan, V.; Korgel, B.A. (2012). Synthesis of Ligand-Stabilized Silicon Nanocrystals with Size-Dependent Photoluminescence Spanning Visible to Near-Infrared Wavelengths. Chem. Mater *24*, 393–401.

47. Mazzaro, R., Romano, F., and Ceroni, P. (2017). Long-lived luminescence of silicon nanocrystals: from principles to applications. Phys. Chem. Chem. Phys. *19*, 26507–26526.

48. Purkait, T.K., Iqbal, M., Islam, M.A., Mobarok, M.H., Gonzalez, C.M., Hadidi, L., and Veinot, J.G.C. (2016). Alkoxy-Terminated Si Surfaces: A New Reactive Platform for the Functionalization and Derivatization of Silicon Quantum Dots. J. Am. Chem. Soc. *138*, 7114–7120.

49. Mastronardi, M.L., Maier-Flaig, F., Faulkner, D., Henderson, E.J., Kübel, C., Lemmer, U., and Ozin, G.A. (2012). Size-dependent absolute quantum yields for size-separated colloidally-stable silicon nanocrystals. Nano Lett. *12*, 337–342.

50. Sangghaleh, F., Sychugov, I., Yang, Z., Veinot, J.G.C., and Linnros, J. (2015). Near-Unity Internal Quantum Efficiency of Luminescent Silicon Nanocrystals with Ligand Passivation. ACS Nano *9*, 7097–7104.

51. Pevere, F., Sychugov, I., Sangghaleh, F., Fucikova, A., and Linnros, J. (2015). Biexciton emission as a probe of auger recombination in individual silicon nanocrystals. J. Phys. Chem. C *119*, 7499–7505.

52. Dasog, M., Yang, Z., Regli, S., Atkins, T.M., Faramus, A., Singh, M.P., Muthuswamy, E., Kauzlarich, S.M., Tilley, R.D., and Veinot, J.G.C. (2013). Chemical insight into the origin of red and blue photoluminescence arising from freestanding silicon nanocrystals. ACS Nano *7*, 2676–2685.

53. Shiohara, A., Hanada, S., Prabakar, S., Fujioka, K., Lim, T.H., Yamamoto, K., Northcote, P.T., and Tilley, R.D. (2010). Chemical reactions on surface molecules attached to silicon quantum dots. J. Am. Chem. Soc. *132*, 248–253.

54. Chandra, S., Ghosh, B., Beaune, G., Nagarajan, U., Yasui, T., Nakamura, J., Tsuruoka, T., Baba, Y., Shirahata, N., and Winnik, F.M. (2016). Functional Double-Shelled Silicon Nanocrystals for Two-Photon Fluorescence Cell Imaging: Spectral Evolution and Tuning. Nanoscale *8*, 9009–9019.

55. Wen, X., Zhang, P., Smith, T.A., Anthony, R.J., Kortshagen, U.R., Yu, P., Feng, Y., Shrestha, S., and Coniber, G. (2015). Tunability Limit of Photoluminescence in Colloidal Silicon Nanocrystals. Sci. Rep. *5*, 12469.

56. English, D.S., Pell, L.E., Yu, Z., Barbara, P.F., and Korgel, B.A. (2002). Size Tunable Visible Luminescence from Individual Organic Monolayer Stabilized Silicon Nanocrystal Quantum Dots. Nano Lett. *2*, 681–685.

57. Hessel, C.M., Henderson, E.J., and Veinot, J.G.C. (2006). Hydrogen Silsesquioxane: A Molecular Precursor for Nanocrystalline Si–SiO2 Composites and Freestanding Hydride-Surface-Terminated Silicon Nanoparticles. Chem. Mater. *18*, 6139–6146.

58. Prokofiev, A.A., Moskalenko, A.S., Yassievich, I.N., Boer, W.D.A.M. De, Timmerman, D., Zhang, H., Buma, W.J., and Gregorkiewicz, T. (2010). Direct Bandgap Optical Transitions in Si Nanocrystals. JETP lett. *90*, 758–762.

59. Shirahata, N., Nakamura, J., Inoue, J.I., Ghosh, B., Nemoto, K., Nemoto, Y., Takeguchi, M., Masuda, Y., Tanaka, M., and Ozin, G.A. (2020). Emerging Atomic Energy Levels in Zero-Dimensional Silicon Quantum Dots. Nano Lett. *20*, 1491–1498.

60. Kortshagen, U.R., Sankaran, R.M., Pereira, R.N., Girshick, S.L., Wu, J.J., and Aydil, E.S. (2016). Nonthermal Plasma Synthesis of Nanocrystals : Fundamental Principles , Materials , and Applications. Chem Rev *116*, 11061–11127.

61. Ghosh, B., Hamaoka, T., Nemoto, Y., Takeguchi, M., and Shirahata, N. (2018). Impact of Anchoring Monolayers on the Enhancement of Radiative Recombination in Light-Emitting Diodes Based on Silicon Nanocrystals Impact of Anchoring Monolayers on the Enhancement of Radiative Recombination in Light-Emitting Diodes based on Silicon Nano. J. Phys. Chem. *122*, 6422–6430.

62. Canham, L.T. (1990). Silicon quantum wire array fabrication by electrochemical and chemical dissolution of wafers. *57*, 1046–1048.

63. Uhlir, B.A. (1956). Electrolytic Shaping of Germanium and Silicon. Bell Syst. Tech. J. *35*, 333–348.

64. Shimizuiwayama, T., Fujita, K., Nakao, S., Saitoh, K., Fujita, T., Shimizu-lwayama, T., and Fujita, K. (1994). Visible photoluminescence in Si + implanted silica glass. J. Appl. Phys. *75*, 7779–83.

65. Zhu, J.G., White, C.W., Budai, J.D., Withrow, S.P., Chen, Y., Zhu, J.G., White, C.W., Budai, J.D., Withrow, S.P., and Chenb, Y. (1995). Growth of Ge , Si , and SiGe nanocrystals in SiO2 matrices. J. Appl. Phys. *78*, 4386–9.

66. Kenyon, A.J., Trwoga, P.F., Pitt, C.W., Rehm, G., Kenyon, A.J., Trwoga, P.F., and Pitt, C.W. (1996). The origin of photoluminescence from thin films of siliconrich silica. J. Appl. Phys. *79*, 9291–9300.

67. Inokuma, T., Wakayama, Y., Muramoto, T., Aoki, R., Kurata, Y., Hasegawa, S., Inokuma, T., Wakayama, Y., Muramoto, T., Aoki, R., et al. (1998). Optical properties of Si clusters and Si nanocrystallites in high-temperature annealed SiO x films. J. Appl. Phys. *83*, 2228–2234.

68. Iacona, F., Franzò, G., Spinella, C., and Spinella, C. (2000). Correlation between luminescence and structural properties of Si nanocrystals. J. Appl. Phys. *87*, 1295–1303.

69. Iacona, F., Bongiorno, C., Spinella, C., Catania, S., Primosole, S., Boninelli, S., and Priolo, F. (2004). Formation and evolution of luminescent Si nanoclusters produced by thermal annealing of SiOx films. J. Appl. Phys. *95*, 3723–3732.

70. Charvet, S., Madelon, R., Gourbilleau, F., and Rizk, R. (1999). Spectroscopic ellipsometry analyses of sputtered Si / SiO2 nanostructures. J. Appl. Phys. *85*, 4032–4039.

71. Takeoka, S. (2000). Size-dependent photoluminescence from surface-oxidized Si nanocrystals in a weak confinement regime. J. Appl. Phys. *62*, 16820–16825.

72. Gourbilleau, F., Portier, X., Ternon, C., Voivenel, P., Madelon, R., and Rizk, R. (2001). Si-rich/SiO2 nanostructured multilayers by reactive magnetron sputtering. J. Appl. Phys. *78*, 3058–3060.

73. Khriachtchev, L., Novikov, S., Lahtinen, J., and Novikov, S. (2002). Thermal annealing of Si / SiO2 materials : Modification of structural and photoluminescence emission properties. J. Appl. Phys. *92*, 5856–5862.

74. Švrček, V., Rehspringer, J.-L., Gaffet, E., Slaoui, A., and Muller, J.-C. (2005). Unaggregated silicon nanocrystals obtained by ball milling. J. Cryst. Growth *275*, 589–597.

75. Lehmann, V., and Gösele, U. (1991). Porous silicon formation : A quantum wire effect. Appl. Phys. Lett. *58*, 856.

76. Heinrich, J.L., Curns, C.L., Credo, G.M., Kavanagh, K.L., and Sailor, M.J. (1992). Luminescent Colloidal Silicon Suspensions from Porous Silicon. Science (80-.). *255*, 66–68.

77. Mansour, N., Momeni, A., Karimzadeh, R., and Amini, M. (2013). Surface effects on the luminescence properties of colloidal silicon nanocrystals in water. Phys. Scr. *87*, 035701.

78. Cannon, W.R., Haggerty, J.S., and Marra, R.A. (1981). Sinterable Ceramic Powders from Laser-Driven Reactions : I , Process Description and Modeling.

J. Am. Ceram. Soc. *65*, 324–330.

79. Cannon, W.R., Danforth, S.C., Haggerty, J.S., and Marra, R.A. (1981). Sinterable Ceramic Powders from Laser-Driven Reactions : II , Powder Characteristics and Process Variables. J. Am. Ceram. Soc., 330–335.

80. Littau, K.A., Szajowski, P.J., Muller, A.J., Kortan, A.R., and Brus, L.E. (1993). A Luminescent Silicon Nanocrystal Colloid via a High-Temperature Aerosol Reaction. J. Phys. Chem. *97*, 1224–1230.

81. Kortshagen, U. (2009). Nonthermal plasma synthesis of semiconductor nanocrystals. J. Phys. D. Appl. Phys. *42*, 113001.

82. Jariwala, B.N., Kramer, N.J., Petcu, M.C., Bobela, D.C., Sanden, M.C.M. Van De, Stradins, P., Ciobanu, C. V, and Agarwal, S. (2011). Surface Hydride Composition of Plasma-Synthesized Si Nanoparticles. J. Phys. Chem. C *115*, 20375–20379.

83. Jurbergs, D., Rogojina, E., Mangoli, L., and Kortshagen, U. (2006). Silicon nanocrystals with ensemble quantum yields exceeding 60%. Appl. Phys. Lett. *88*, 233116–8.

84. Doğan, İ., Kramer, N.J., Westermann, R.H.J., Dohnalová, K., and Smets, A.H.M. (2013). Ultrahigh throughput plasma processing of free standing silicon nanocrystals with lognormal size distribution. J. Appl. Phys. *113*, 134306.

85. Heath, J.R. (1992). A Liquid-Solution-Phase Synthesis of Crystalline Silicon. Science (80-.). *258*, 1131–1133.

86. Pettigrew, K.A., Liu, Q., Power, P.P., and Kauzlarich, S.M. (2003). Solution Synthesis of Alkyl- and Alkyl / Alkoxy-Capped Silicon Nanoparticles via Oxidation of Mg2Si. Chem Mater *15*, 4005–4011.

87. Cho, E., Park, S., Hao, X., Song, D., Conibeer, G., Park, S., and Green, M.A. (2008). Silicon quantum dot / crystalline silicon solar cells. Nanotechnology *19*, 245201.

88. Antonova, I. V, and Gulyaev, M. (2008). Charge storage , photoluminescence , and cluster statistics in ensembles of Si quantum dots. Phys. Rev. B *77*, 125318.

89. Clark, R.J., Aghajamali, M., Gonzalez, C.M., Hadidi, L., Islam, M.A., Javadi, M., Mobarok, H., Purkait, T.K., Robidillo, C.J.T., Sinelnikov, R., et al. (2017). From Hydrogen Silsesquioxane to Functionalized Silicon Nanocrystals. Chem Mater *29*, 80–89.

90. Kelly, J.A., Henderson, E.J., Veinot, J.G.C., Kelly, J.A., and Henderson, E.J. (2010). Sol – gel precursors for group 14 nanocrystals. Chem Commun *46*,

8704.

91.   Draeger, E.W., Grossman, J.C., Williamson, A.J., Galli, G., Draeger, E.W., Grossman, J.C., Williamson, A.J., and Galli, G. (2004). Optical properties of passivated silicon nanoclusters : The role of synthesis. J. Chem. Phys. *120*.

92.   Kovalev, D., and Fujii, M. (2005). Silicon Nanocrystals : Photosensitizers for Oxygen Molecules. Adv. Mater. *17*, 2531–2544.

93.   Wolkin, M. V, Jorne, J., and Fauchet, P.M. (1999). Electronic States and Luminescence in Porous Silicon Quantum Dots : The Role of Oxygen. Phys. Rev. Lett *82*, 197–200.

94.   Dohnalová, K., Kůsová, K., Pelant, I., Dohnalová, K., K, K., and Pelant, I. (2009). Time-resolved photoluminescence spectroscopy of the initial oxidation stage of small silicon nanocrystals. Appl. Phys. Lett. *94*, 211903.

95.   Prendergast, D., Grossman, J.C., Williamson, A.J., Fattebert, J., and Galli, G. (2004). Optical Properties of Silicon Clusters in the Presence of Water : A First Principles Theoretical Analysis. J. Am. Chem. Soc. *126*, 13827–13837.

96.   Sato, S., and Swihart, M.T. (2006). Propionic-Acid-Terminated Silicon Nanoparticles : Synthesis and Optical Characterization. Chem Mater, 4083–4088.

97.   Warner, J.H., Hoshino, A., Yamamoto, K., and Tilley, R.D. (2005). Water-Soluble Photoluminescent Silicon Quantum Dots. Angew. Chem. Int. Ed. *44*, 4550–4554.

98.   Li, Z.F., and Ruckenstein, E. (2004). Water-Soluble Poly (acrylic acid) Grafted Luminescent Silicon Nanoparticles and Their Use as Fluorescent Biological Staining Labels. Nano Lett. *4*, 1463–1467.

99.   Islam, M.A., Sinelnikov, R., Howlader, M.A., Faramus, A., and Veinot, J.G.C. (2018). Mixed Surface Chemistry: An Approach to Highly Luminescent Biocompatible Amphiphilic Silicon Nanocrystals. Chem. Mater. *30*, 8925–8931.

100.   Zhai, Y., Dasog, M., Snitynsky, R.B., Purkait, T.K., Aghajamali, M., Hahn, A.H., Sturdy, C.B., Lowary, L., and Veinot, J.G.C. (2014). Water-soluble photoluminescent D-mannose and L-alanine functionalized silicon nanocrystals and their application to cancer cell imaging. J. Mater. Chem. B *2*, 8427–8433.

101.   Romano, F., Angeloni, S., Morselli, G., Morandi, V., Shell, J.R., Cao, X., Pogue, W., and Ceroni, P. (2020). Water-soluble silicon nanocrystals as NIR luminescent probes for time-gated biomedical imaging. Nanoscale.

102.   Yang, Z., Iqbal, M., Dobbie, A.R., and Veinot, J.G.C. (2013). Surface-Induced

Alkene Oligomerization : Does Thermal Hydrosilylation Really Lead to Monolayer Protected Silicon Nanocrystals ? J. Am. Chem. Soc. *135*, 17595–17601.

103. Weeks, S.L., Macco, B., and Agarwal, S. (2012). Gas-Phase Hydrosilylation of Plasma-Synthesized Silicon Nanocrystals with Short- and Long-Chain Alkynes. Langmuir *28*, 17295–17301.

104. Cicero, R.L., Linford, M.R., and Chidsey, C.E.D. (2000). Photoreactivity of unsaturated compounds with hydrogen-terminated silicon(111). Langmuir *16*, 5688–5695.

105. Stewart, M.P., and Buriak, J.M. (1998). Photopatterned hydrosilylation on porous silicon. Angew. Chemie - Int. Ed. *37*, 3257–3260.

106. Kelly, J.A., and Veinot, J.G.C. (2010). An Investigation into Near-UV Hydrosilylation of Freestanding Silicon Nanocrystals. ACS Nano *4*, 4645–4656.

107. Wang, X., Ruther, R.E., Streifer, J.A., and Hamers, R.J. (2010). UV-Induced Grafting of Alkenes to Silicon Surfaces : Photoemission versus Excitons. J. Am. Chem. Soc. *132*, 4048–4049.

108. Buriak, J.M. (2014). Illuminating silicon surface hydrosilylation: An unexpected plurality of mechanisms. Chem. Mater. *26*, 763–772.

109. Clark, R.J., Dang, M.K.M., and Veinot, J.G.C. (2010). Exploration of organic acid chain length on water-soluble silicon quantum dot surfaces. Langmuir *26*, 15657–15664.

110. Wheeler, O.H., and Mateos, J.L. (1956). The ultraviolet absorption of isolated double bonds. J. Org. Chem. *21*, 1110–1112.

111. Sun, Q.Y., De Smet, L.C.P.M., Van Lagen, B., Giesbers, M., Thüne, P.C., Van Engelenburg, J., De Wolf, F.A., Zuilhof, H., and Sudhölter, E.J.R. (2005). Covalently attached monolayers on crystalline hydrogen-terminated silicon: Extremely mild attachment by visible light. J. Am. Chem. Soc. *127*, 2514–2523.

112. De Smet, L.C.P.M., Pukin, A. V., Sun, Q.Y., Eves, B.J., Lopinski, G.P., Visser, G.M., Zuilhof, H., and Sudhölter, E.J.R. (2005). Visible-light attachment of SiC linked functionalized organic monolayers on silicon surfaces. Appl. Surf. Sci. *252*, 24–30.

113. Purkait, T.K., Iqbal, M., Wahl, M.H., Gottschling, K., Gonzalez, C.M., Islam, M.A., and Veinot, J.G.C. (2014). Borane-catalyzed room-temperature hydrosilylation of alkenes/alkynes on silicon nanocrystal surfaces. J. Am. Chem. Soc. *136*, 17914–17917.

114. Paulusse, J.M.J., Nielen, M.W.F., and Zuilhof, H. (2012). Preparation,

Characterization, and Surface Modification of Trifluoroethyl Ester-Terminated Silicon Nanoparticles. Chem Mater *24*, 4311–4318.

115. Buriak, J.M. (2002). Organometallic Chemistry on Silicon and Germanium Surfaces. *102*, 1271–1308.

116. Höhlein, I.M.D., Kehrle, J., Helbich, T., Yang, Z., Veinot, J.G.C., and Rieger, B. (2014). Diazonium salts as grafting agents and efficient radical-hydrosilylation initiators for freestanding photoluminescent silicon nanocrystals. Chem. - A Eur. J. *20*, 4212–4216.

117. Höhlein, I.M.D., Kehrle, J., Purkait, T.K., Veinot, J.G.C., and Rieger, B. (2014). Photoluminescent silicon nanocrystals with chlorosilane surfaces-synthesis and reactivity. Nanoscale *7*, 914–918.

118. Dasog, M., and Veinot, J.G.C. (2014). Tuning silicon quantum dot luminescence via surface groups. Phys. Status Solidi B *251*, 2216–2220.

119. Fuzell, J., Thibert, A., Atkins, T.M., Dasog, M., Busby, E., Veinot, J.G.C., Kauzlarich, S.M., and Larsen, D.S. (2013). Red States versus Blue States in Colloidal Silicon Nanocrystals: Exciton Sequestration into Low-Density Traps. J. Phys. Chem. Lett. *4*, 3806–3812.

120. Wolf, O., Dasog, M., Yang, Z., Balberg, I., Veinot, J.G.C., and Millo, O. (2013). Doping and Quantum Confinement Effects in Single Si Nanocrystals Observed by Scanning Tunneling Spectroscopy. Nano Lett. *13*, 2516–2521.

121. Hçhlein, I.M.D., Angı, A., Sinelnikov, R., Veinot, J.G.C., and Rieger, B. (2015). Functionalization of Hydride-Terminated Photoluminescent Silicon Nanocrystals with Organolithium Reagents. Chem. Eur. J. *21*, 2755–2758.

122. Veinot, J.G.C. (2006). Synthesis, surface functionalization, and properties of freestanding silicon nanocrystals. Chem. Commun., 4160–4168.

123. Cheng, X., Lowe, S.B., Reece, P.J., and Gooding, J.J. (2014). Colloidal silicon quantum dots: From preparation to the modification of self-assembled monolayers (SAMs) for bio-applications. Chem. Soc. Rev. *43*, 2680–2700.

124. Dasog, M., and Veinot, J.G.C. (2012). Size independent blue luminescence in nitrogen passivated silicon nanocrystals. Phys. Status Solidi *209*, 1844–1846.

125. Dasog, M., Bader, K., and Veinot, J.G.C. (2015). Influence of halides on the optical properties of silicon quantum dots. Chem. Mater. *27*, 1153–1156.

126. Christmann, J., Ley, C., Allonas, X., Ibrahim, A., and Croutxé-Barghorn, C. (2019). Experimental and theoretical investigations of free radical photopolymerization: Inhibition and termination reactions. Polymer (Guildf). *160*, 254–264.

127. Christmann, J., Allonas, X., Ley, C., and Croutxé-Barghorn, C. (2019). The role of ketyl radicals in free radical photopolymerization: New experimental and theoretical insights. Polym. Chem. *10*, 1099–1109.

128. Höhlein, I.M.D., Kehrle, J., Purkait, T.K., Veinot, J.G.C., and Rieger, B. (2015). Photoluminescent silicon nanocrystals with chlorosilane surfaces – synthesis and reactivity. Nanoscale *7*, 914–918.

129. Mazzaro, R., Gradone, A., Angeloni, S., Morselli, G., Cozzi, P.G., Romano, F., Vomiero, A., and Ceroni, P. (2019). Hybrid Silicon Nanocrystals for Color-Neutral and Transparent Luminescent Solar Concentrators. ACS Photonics *6*.

130. Mirkhalaf, F., Paprotny, J., and Schiffrin, D.J. (2006). Synthesis of metal nanoparticles stabilized by metal-carbon bonds. J. Am. Chem. Soc. *128*, 7400–7401.

131. Batchelder, J.S., Zewail, A.H., and Cole, T. (1979). Luminescent solar concentrators. 1: Theory of operation and techniques for performance evaluation. Appl. Opt. *18*, 3090–3110.

132. Debije, M.G., and Verbunt, P.P.C. (2012). Thirty years of luminescent solar concentrator research: Solar energy for the built environment. Adv. Energy Mater. *2*, 12–35.

133. Currie, M.J., Mapel, J.K., Heidel, T.D., Goffri, S., and Baldo, M.A. (2008). High-efficiency organic solar concentrators for photovoltaics. Science (80-.). *321*, 226–228.

134. Chemisana, D. (2011). Building integrated concentrating photovoltaics: A review. Renew. Sustain. Energy Rev. *15*, 603–611.

135. Jelle, B., Breivik, C., and Rokenes, D. (2012). Building Integrated Photovoltaics Products: A State-of-the-Art Review and Future Research Opportunities. Sol. Energy Mater. Sol. Cells *100*, 69–96.

136. Meinardi, F., Bruni, F., and Brovelli, S. (2017). Luminescent solar concentrators for building-integrated photovoltaics. Nat. Rev. Mater. *2*, 1–9.

137. Goetzberger, A. (1978). Applied Physics Fluorescent Solar Energy Collectors : Operating Conditions with Diffuse Light. Appl. Phys. *16*, 399–404.

138. Carrascosa, M., Unamuno, S., and Agullo-Lopez, F. (1983). Monte Carlo simulation of the performance of PMMA luminescent solar collectors. Appl. Opt. *22*, 3236.

139. Liu, G., Mazzaro, R., Wang, Y., Zhao, H., and Vomiero, A. (2019). High efficiency sandwich structure luminescent solar concentrators based on colloidal quantum dots. Nano Energy *60*, 119–126.

140. Slooff, L.H., Bende, E.E., Burgers, A.R., Budel, T., Pravettoni, M., Kenny, R.P., Dunlop, E.D., and Büchtemann, A. (2008). A Luminescent Solar Concentrator with 7.1% power conversion efficiency. Phys. Status Solidi - Rapid Res. Lett. *2*, 257–259.

141. Yang, C., and Lunt, R.R. (2017). Limits of Visibly Transparent Luminescent Solar Concentrators. Adv. Opt. Mater. *5*, 1–10.

142. Zhao, Y., and Lunt, R.R. (2013). Transparent luminescent solar concentrators for large-area solar windows enabled by massive stokes-shift nanocluster phosphors. Adv. Energy Mater. *3*, 1143–1148.

143. Correia, S.F.H., De Zea Bermudez, V., Ribeiro, S.J.L., André, P.S., Ferreira, R.A.S., and Carlos, L.D. (2014). Luminescent solar concentrators: Challenges for lanthanide-based organic-inorganic hybrid materials. J. Mater. Chem. A *2*, 5580–5596.

144. Gutierrez, G.D., Coropceanu, I., Bawendi, M.G., and Swager, T.M. (2016). A Low Reabsorbing Luminescent Solar Concentrator Employing π-Conjugated Polymers. Adv. Mater. *28*, 497–501.

145. Lee, S.M., Dhar, P., Chen, H., Montenegro, A., Liaw, L., Kang, D., Gai, B., Benderskii, A. V., and Yoon, J. (2017). Synergistically Enhanced Performance of Ultrathin Nanostructured Silicon Solar Cells Embedded in Plasmonically Assisted, Multispectral Luminescent Waveguides. ACS Nano *11*, 4077–4085.

146. Mazzaro, R., and Vomiero, A. (2018). The Renaissance of Luminescent Solar Concentrators: The Role of Inorganic Nanomaterials. Adv. Energy Mater. *8*, 1801903.

147. Bronstein, N.D., Yao, Y., Xu, L., O'Brien, E., Powers, A.S., Ferry, V.E., Alivisatos, A.P., and Nuzzo, R.G. (2015). Quantum Dot Luminescent Concentrator Cavity Exhibiting 30-fold Concentration. ACS Photonics *2*, 1576–1583.

148. Li, H., Wu, K., Lim, J., Song, H.J., and Klimov, V.I. (2016). Doctor-blade deposition of quantum dots onto standard window glass for low-loss large-area luminescent solar concentrators. Nat. Energy *1*, 16157.

149. Meinardi, F., Colombo, A., Velizhanin, K.A., Simonutti, R., Lorenzon, M., Beverina, L., Viswanatha, R., Klimov, V.I., and Brovelli, S. (2014). Large-area luminescent solar concentrators based on Stokes-shift-engineered nanocrystals in a mass-polymerized PMMA matrix. Nat. Photonics *8*, 392–399.

150. Zhao, H., Benetti, D., Jin, L., Zhou, Y., Rosei, F., and Vomiero, A. (2016). Solar Concentrators: Absorption Enhancement in "Giant" Core/Alloyed-Shell Quantum Dots for Luminescent Solar Concentrator. Small *12*, 5368–5368.

151. Zhou, Y., Benetti, D., Fan, Z., Zhao, H., Ma, D., Govorov, A.O., Vomiero, A., and Rosei, F. (2016). Near Infrared, Highly Efficient Luminescent Solar Concentrators. Adv. Energy Mater. *6*, 1501913.

152. Shcherbatyuk, G. V., Inman, R.H., Wang, C., Winston, R., and Ghosh, S. (2010). Viability of using near infrared PbS quantum dots as active materials in luminescent solar concentrators. Appl. Phys. Lett. *96*, 1–4.

153. Wei, M., de Arquer, F.P.G., Walters, G., Yang, Z., Quan, L.N., Kim, Y., Sabatini, R., Quintero-Bermudez, R., Gao, L., Fan, J.Z., et al. (2019). Ultrafast narrowband exciton routing within layered perovskite nanoplatelets enables low-loss luminescent solar concentrators. Nat. Energy *4*, 197–205.

154. Meinardi, F., Akkerman, Q.A., Bruni, F., Park, S., Mauri, M., Dang, Z., Manna, L., and Brovelli, S. (2017). Doped Halide Perovskite Nanocrystals for Reabsorption-Free Luminescent Solar Concentrators. ACS Energy Lett. *2*, 2368–2377.

155. Zhao, H., Zhou, Y., Benetti, D., Ma, D., and Rosei, F. (2017). Perovskite quantum dots integrated in large-area luminescent solar concentrators. Nano Energy *37*, 214–223.

156. Erickson, C.S., Bradshaw, L.R., McDowall, S., Gilbertson, J.D., Gamelin, D.R., and Patrick, D.L. (2014). Zero-Reabsorption Doped-Nanocrystal Luminescent Solar Concentrators. ACS Nano, 3461–3467.

157. Meinardi, F., McDaniel, H., Carulli, F., Colombo, A., Velizhanin, K.A., Makarov, N.S., Simonutti, R., Klimov, V.I., and Brovelli, S. (2015). Highly efficient large-area colourless luminescent solar concentrators using heavy-metal-free colloidal quantum dots. Nat. Nanotechnol. *10*, 878–885.

158. Li, Y., Miao, P., Zhou, W., Gong, X., and Zhao, X. (2017). N-doped carbon-dots for luminescent solar concentrators. J. Mater. Chem. A *5*, 21452–21459.

159. Zhou, Y., Benetti, D., Tong, X., Jin, L., Wang, Z.M., Ma, D., Zhao, H., and Rosei, F. (2018). Colloidal carbon dots based highly stable luminescent solar concentrators. Nano Energy *44*, 378–387.

160. Yu, Y., Fan, G., Fermi, A., Mazzaro, R., Morandi, V., Ceroni, P., Smilgies, D.M., and Korgel, B.A. (2017). Size-Dependent Photoluminescence Efficiency of Silicon Nanocrystal Quantum Dots. J. Phys. Chem. C *121*, 23240–23248.

161. Meinardi, F., Ehrenberg, S., Dhamo, L., Carulli, F., Mauri, M., Bruni, F., Simonutti, R., Kortshagen, U., and Brovelli, S. (2017). Highly efficient luminescent solar concentrators based on earth-Abundant indirect-bandgap silicon quantum dots. Nat. Photonics *11*, 177–185.

162. Wu, K., Li, H., and Klimov, V.I. (2018). Tandem luminescent solar

concentrators based on engineered quantum dots. Nat. Photonics *12*, 105–110.

163. Romano, F., Yu, Y., Korgel, B.A., Bergamini, G., and Ceroni, P. (2016). Light-Harvesting Antennae Based on Silicon Nanocrystals. Top. Curr. Chem. *374*, 89–106.

164. Locritani, M., Yu, Y., Bergamini, G., Baroncini, M., Molloy, J.K., Korgel, B.A., and Ceroni, P. (2014). Silicon nanocrystals functionalized with pyrene units: Efficient light-harvesting antennae with bright near-infrared emission. J. Phys. Chem. Lett. *5*, 3325–3329.

165. Mazzaro, R., Locritani, M., Molloy, J.K., Montalti, M., Yu, Y., Korgel, B.A., Bergamini, G., Morandi, V., and Ceroni, P. (2015). Photoinduced Processes between Pyrene-Functionalized Silicon Nanocrystals and Carbon Allotropes. Chem. Mater. *27*, 4390–4397.

166. Fermi, A., Locritani, M., Di Carlo, G., Pizzotti, M., Caramori, S., Yu, Y., Korgel, B.A., Bergamini, G., and Ceroni, P. (2015). Light-harvesting antennae based on photoactive silicon nanocrystals functionalized with porphyrin chromophores. Faraday Discuss. *185*, 481–495.

167. Ravotto, L., Chen, Q., Ma, Y., Vinogradov, S.A., Locritani, M., Bergamini, G., Negri, F., Yu, Y., Korgel, B.A., and Ceroni, P. (2017). Bright Long-Lived Luminescence of Silicon Nanocrystals Sensitized by Two-Photon Absorbing Antenna. Chem *2*, 550–560.

168. Reisch, A., Didier, P., Richert, L., Oncul, S., Arntz, Y., Mély, Y., and Klymchenko, A.S. (2014). Collective fluorescence switching of counterion-assembled dyes in polymer nanoparticles. Nat. Commun. *5*, 4089.

169. Ravotto, L., Chen, Q., Ma, Y., Vinogradov, S.A., Locritani, M., Bergamini, G., Negri, F., Yu, Y., Korgel, B.A., and Ceroni, P. (2017). Bright Long-Lived Luminescence of Silicon Nanocrystals Sensitized by Two-Photon Absorbing Antenna. Chem *2*, 550–560.

170. Montalti, M., Credi, A., Prodi, L., and Gandolfi, M.T. (2006). Handbook of photochemistry 3rd ed. (CRC Press.).

171. Coropceanu, I., and Bawendi, M.G. (2014). Core/shell quantum dot based luminescent solar concentrators with reduced reabsorption and enhanced efficiency. Nano Lett. *14*, 4097–4101.

172. Klimov, V.I., Baker, T.A., Lim, J., Velizhanin, K.A., and McDaniel, H. (2016). Quality Factor of Luminescent Solar Concentrators and Practical Concentration Limits Attainable with Semiconductor Quantum Dots. ACS Photonics *3*, 1138–1148.

173. Weissleder, R. (2001). A clearer vision for in vivo imaging. Nat. Biotechnol.,

316–317.

174. Li, C., and Wang, Q. (2018). Challenges and Opportunities for Intravital Near-Infrared Fluorescence Imaging Technology in the Second Transparency Window. ACS Nano *12*, 9654–9659.

175. Berezin, M.Y., and Achilefu, S. (2010). Fluorescence Lifetime Measurements and Biological Imaging. Chem Rev *110*, 2641–2684.

176. Nguyen, Q.T., Olson, E.S., Aguilera, T.A., Jiang, T., Scadeng, M., Ellies, L.G., and Tsien, R.Y. (2010). Surgery with molecular fluorescence imaging using activatable cell-penetrating peptides decreases residual cancer and improves survival. Proc. Natl. Acad. Sci. *107*, 4317–4322.

177. Nguyen, Q.T., and Tsien, R.Y. (2013). Fluorescence-guided surgery with live molecular navigation-a new cutting edge. Nat. Rev. Cancer *13*, 653–662.

178. Gioux, S., Choi, H.S., and Frangioni, J. V. (2010). Image-guided surgery using invisible near-infrared light: Fundamentals of clinical translation. Mol. Imaging *9*, 237–255.

179. Choi, H.S., and Frangioni, J. V (2010). Nanoparticles for Biomedical Imaging : Fundamentals of Clinical Translation. Mol. Imaging *9*, 291–310.

180. Dsouza, A. V, Henderson, E.R., Samkoe, K.S., Pogue, B.W., Dsouza, A. V, Lin, H., Henderson, E.R., Samkoe, K.S., and Pogue, B.W. (2016). Review of fluorescence guided surgery systems : identification of key performance capabilities beyond indocyanine green imaging Review of fluorescence guided surgery systems : identification of key performance capabilities. J. Biomed. Opt. *21*, 080901-1–15.

181. Liu, P., Mu, X., Zhang, X.D., and Ming, D. (2020). The Near-Infrared-II Fluorophores and Advanced Microscopy Technologies Development and Application in Bioimaging. Bioconjug. Chem. *31*, 260–275.

182. Guosong, H., Alexander, L.A., and Hongjie, D. (2017). Near-infrared fluorophores for biomedical imaging. Nat. Biomed. Eng.

183. Fan, Y., Wang, P., Lu, Y., Wang, R., Zhou, L., Zheng, X., Li, X., Piper, J.A., and Zhang, F. (2018). Lifetime-engineered NIR-II nanoparticles unlock multiplexed in vivo imaging. Nat. Nanotechnol. *13*, 941–946.

184. Zhang, H., Fan, Y., Pei, P., Sun, C., Lu, L., and Zhang, F. (2019). Tm3+-Sensitized NIR-II Fluorescent Nanocrystals for In Vivo Information Storage and Decoding. Angew. Chemie - Int. Ed. *58*, 10153–10157.

185. New, E.J., Parker, D., Smith, D.G., and Walton, J.W. (2010). Development of responsive lanthanide probes for cellular applications. Curr. Opin. Chem. Biol. *14*, 238–246.

186. Sun, L., Wei, R., Feng, J., and Zhang, H. (2018). Tailored lanthanide-doped upconversion nanoparticles and their promising bioapplication prospects. Coord. Chem. Rev. *364*, 10–32.

187. Amoroso, A.J., and Pope, S.J.A. (2015). Using lanthanide ions in molecular bioimaging. Chem Soc Rev *44*, 4723–4742.

188. Baggaley, E., Weinstein, J.A., and William, J.A.G. (2014). Luminescent and Photoactive Transition Metal Complexes as Biomolecular Probes and Cellular Reagents (Springer, Berlin, Heidelberg).

189. Zhang, K.Y., Yu, Q., Wei, H., Liu, S., Zhao, Q., and Huang, W. (2018). Long-Lived Emissive Probes for Time-Resolved Photoluminescence Bioimaging and Biosensing. Chem Rev *118*, 1770–1839.

190. Esipova, T., Barrett, M., Erlebach, E., Masunov, A., Weber, B., and Vinogradov, S. (2019). Oxyphor 2P: A High-Performance Probe for Deep-Tissue Longitudinal Oxygen Imaging. Cell Metab *29*, 736–744.

191. Erogbogbo, F., Yong, K.-T., Roy, I., Hu, R., Law, W.-C., Zhao, W., Ding, H., Wu, F., Kumar, R., Swihart, M.T., et al. (2011). In Vivo Targeted Cancer Imaging, Sentinel Lymph Node Mapping and Multi-Channel Imaging with Biocompatible Silicon Nanocrystals. ACS Nano *5*, 413–423.

192. Joo, J., Liu, X., Kotamraju, V.R., Ruoslahti, E., Nam, Y., and Sailor, M.J. (2015). Gated Luminescence Imaging of Silicon Nanoparticles. ACS Nano *9*, 6233–6241.

193. Yang, W., Srivastava, P.K., Han, S., Jing, L., Tu, C., and Chen, S. (2019). Optomechanical Time-Gated Fluorescence Imaging Using Long-Lived Silicon Quantum Dot Nanoparticles. Anal. Chem. *91*, 5499–5503.

194. Ohta, N., and Li, Y. (2017). Time-Gated Imaging on Live Cancer Cells Using Silicon Quantum Dot Nanoparticles with Long-Lived Fluorescence. ACS Photonics *4*, 1306–1315.

195. Hessel, C.M., Rasch, M.R., Hueso, J.L., Goodfellow, B.W., Akhavan, V.A., Puvanakrishnan, P., Tunnel, J.W., and Korgel, B.A. (2010). Alkyl Passivation and Amphiphilic Polymer Coating of Silicon Nanocrystals for Diagnostic Imaging. Small *6*, 2026–2034.

196. Henderson, E.J., Shuhendler, A.J., Prasad, P., Baumann, V., Maier-Flaig, F., Faulkner, D.O., Lemmer, U., Wu, X.Y., and Ozin, G.A. (2011). Colloidally stable silicon nanocrystals with near-infrared photoluminescence for biological fluorescence imaging. Small *7*, 2507–16.

197. Pi, X., Yu, T., and Yang, D. (2014). Silicon Quantum Dots: Water-Dispersible Silicon-Quantum-Dot-Containing Micelles Self-Assembled from an

Amphiphilic Polymer. Part. Part. Syst. Charact. *31*, 751–756.

198. Silbaugh, D.A., Ferrer-Tasies, L., Faraudo, J., Veciana, J., Ventosa, N., and Korgel, B.A. (2017). Highly Fluorescent Silicon Nanocrystals Stabilized in Water Using Quatsomes. Langmuir *33*, 14366–14377.

199. Erogbogbo, F., Yong, K., Roy, I., Xu, G., Prasad, P.N., and Swihart, M.T. (2008). Biocompatible luminescent silicon quantum dots for imaging of cancer cells. ACS Nano *2*, 873–878.

200. Furey, B.J., Silbaugh, D.A., Yu, Y., Guillaussier, A.C., Estrada, A.D., Stevens, C., Maynard, J.A., Korgel, B.A., and Downer, M.C. (2018). Measurement of Two-Photon Absorption of Silicon Nanocrystals in Colloidal Suspension for Bio-Imaging Applications. Phys. Status Solidi Basic Res. *255*, 1–7.

201. Maurice, V., Slostowski, C., Herlin-Boime, N., and Carrot, G. (2012). Polymer-Grafted Silicon Nanoparticles Obtained Either via Peptide Bonding or Click Chemistry. Macromol. Chem. Phys. *213*, 2498–2503.

202. Ruizendaal, L., Pujari, S.P., Gevaerts, V., Paulusse, J.M.J., and Zuilhof, H. (2011). Biofunctional silicon nanoparticles by means of thiol-ene click chemistry. Chem. - An Asian J. *6*, 2776–2786.

203. He, Y., Kang, Z.-H.H., Li, Q.-S.S., Tsang, C.H.A., Fan, C.-H.H., and Lee, S.-T.T. (2009). Ultrastable, highly fluorescent, and water-dispersed silicon-based nanospheres as cellular probes. Angew. Chemie - Int. Ed. *48*, 128–132.

204. He, Y., Zhong, Y., Peng, F., Wei, X., Su, Y., Lu, Y., Su, S., Gu, W., Liao, L., and Lee, S.-T. (2011). One-Pot Microwave Synthesis of Water-Dispersible, Ultraphoto- and pH-Stable, and Highly Fluorescent Silicon Quantum Dots. J. Am. Chem. Soc. *133*, 14192–14195.

205. Yu, Y., Hessel, C.M., Bogart, T.D., Panthani, M.G., Rasch, M.R., and Korgel, B.A. (2013). Room temperature hydrosilylation of silicon nanocrystals with bifunctional terminal alkenes. Langmuir *29*, 1533–1540.

206. Chen, K.K., Liao, K., Casillas, G., Li, Y., and Ozin, G.A. (2016). Cationic Silicon Nanocrystals with Colloidal Stability, pH-Independent Positive Surface Charge and Size Tunable Photoluminescence in the Near-Infrared to Red Spectral Range. Adv. Sci. *3*, 1500263.

207. Erogbogbo, F., Chang, C.-W., Yong, K.-T., Swihart, M.T., and Prasad, P.N. (2011). Bioconjugation of Luminescent Silicon Quantum Dots for Selective Uptake by Cancer Cells. Bioconjugate Chem *22*, 1081–1088.

208. Tu, C.C., Chen, K.P., Yang, T.A., Chou, M.Y., Lin, L.Y., and Li, Y.K. (2016). Silicon Quantum Dot Nanoparticles with Antifouling Coatings for Immunostaining on Live Cancer Cells. ACS Appl. Mater. Interfaces *8*, 13714–

13723.

209. Cheng, X., Gondosiswanto, R., Ciampi, S., Reece, P.J., and Gooding, J.J. (2012). One-pot synthesis of colloidal silicon quantum dots and surface functionalization via thiol–ene click chemistry. Chem Commun *48*, 11874–11876.

210. Robidillo, C.J.T., Aghajamali, M., Faramus, A., Sinelnikov, R., and Veinot, J.G.C. (2018). Interfacing enzymes with silicon nanocrystals through the thiol–ene reaction. Nanoscale *10*, 18706–18719.

211. Hessel, C.M., Reid, D., Panthani, M.G., Rasch, M.R., Goodfellow, B.W., Wei, J., Fujii, H., Akhavan, V., and Korgel, B.A. (2012). Synthesis of ligand-stabilized silicon nanocrystals with size-dependent photoluminescence spanning visible to near-infrared wavelengths. Chem. Mater. *24*, 393–401.

212. Du, Y.J., and Brash, J.L. (2003). Synthesis and characterization of thiol-terminated poly(ethylene oxide) for chemisorption to gold surface. J. Appl. Polym. Sci. *90*, 594–607.

213. Riccardi, L., Gabrielli, L., Sun, X., De Biasi, F., Rastrelli, F., Mancin, F., and De Vivo, M. (2017). Nanoparticle-Based Receptors Mimic Protein-Ligand Recognition. Chem *3*, 92–109.

214. Sudeep, P.K., Page, Z., and Emrick, T. (2008). PEGylated silicon nanoparticles: Synthesis and characterization. Chem. Commun., 6126–6127.

215. Yu, Y., Hessel, C.M., Bogart, T.D., Panthani, M.G., Rasch, M.R., and Korgel, B.A. (2013). Room temperature hydrosilylation of silicon nanocrystals with bifunctional terminal alkenes. Langmuir *29*, 1533–1540.

216. Arrigo, A., Mazzaro, R., Romano, F., Bergamini, G., and Ceroni, P. (2016). Photoinduced electron-transfer quenching of luminescent silicon nanocrystals as a way to estimate the position of the conduction and valence bands by Marcus theory. Chem. Mater. *28*, 6664–6671.

217. Yu, Y., Fan, G., Fermi, A., Mazzaro, R., Morandi, V., Ceroni, P., Smilgies, D.-M., and Korgel, B.A. (2017). Size-Dependent Photoluminescence E ffi ciency of Silicon Nanocrystal Quantum Dots. J. Phys. Chem. *121*, 23240–23248.

218. Romano, F., Angeloni, S., Morselli, G., Mazzaro, R., and Ceroni, P. (2019). Colloidally stable silicon quantum dots as temperature biosensors. In European Conferences on Biomedical Optics.

219. Reisch, A., and Klymchenko, A.S. (2016). Fluorescent Polymer Nanoparticles Based on Dyes: Seeking Brighter Tools for Bioimaging. Small *12*, 1968–1992.

220. Genovese, D., Rampazzo, E., Bonacchi, S., Montalti, M., Zaccheroni, N., and Prodi, L. (2014). Energy transfer processes in dye-doped nanostructures yield

cooperative and versatile fluorescent probes. Nanoscale *6*, 3022–3036.

221. Tian, Z., Shaller, A.D., and Li, A.D.Q. (2009). Twisted perylene dyes enable highly fluorescent and photostable nanoparticles. Chem. Commun., 180–182.

222. Trofymchuk, K., Reisch, A., Shulov, I., Mély, Y., and Klymchenko, A.S. (2014). Tuning the color and photostability of perylene diimides inside polymer nanoparticles: Towards biodegradable substitutes of quantum dots. Nanoscale *6*, 12934–12942.

223. Achyuthan, K.E., Bergstedt, T.S., Chen, L., Jones, R.M., Kumaraswamy, S., Kushon, S.A., Ley, K.D., Lu, L., McBranch, D., Mukundan, H., et al. (2005). Fluorescence superquenching of conjugated polyelectrolytes: Applications for biosensing and drug discovery. J. Mater. Chem. *15*, 2648–2656.

224. Thomas, S.W., Joly, G.D., and Swager, T.M. (2007). Chemical sensors based on amplifying fluorescent conjugated polymers. Chem. Rev. *107*, 1339–1386.

225. Dickson, R.M., Cubittt, A.B., Tsient, R.Y., and Moerner, W.E. (1997). On/off blinking and switching behaviour of single molecules of green fluorescent protein. Nature *388*, 355–358.

226. Nirmal, M., Dabbousi, B. 0., Bawendi, M.G., Macklint, J.J., Trautmant, J.K., Harrist:J, T.D., and Brust, L.E. (1996). Fluorescence intermittency in single cadmium selenide nanocrystals. Nat. Protoc. *383*, 802–804.

227. Odian, G. (2004). Principles of Polymerization 4th ed. (Wiley-Interscience).

228. Mora-Huertas, C.E., Fessi, H., and Elaissari, A. (2011). Influence of process and formulation parameters on the formation of submicron particles by solvent displacement and emulsification-diffusion methods: Critical comparison. Adv. Colloid Interface Sci. *163*, 90–122.

229. Ganachaud, F., and Katz, J.L. (2005). Nanoparticles and nanocapsules created using the ouzo effect: Spontaneous emulsification as an alternative to ultrasonic and high-shear devices. ChemPhysChem *6*, 209–216.

230. D'Addio, S.M., and Prud'homme, R.K. (2011). Controlling drug nanoparticle formation by rapid precipitation. Adv. Drug Deliv. Rev. *63*, 417–426.

231. Lince, F., Marchisio, D.L., and Barresi, A.A. (2008). Strategies to control the particle size distribution of poly-ε-caprolactone nanoparticles for pharmaceutical applications. J. Colloid Interface Sci. *322*, 505–515.

232. Reisch, A., Runser, A., Arntz, Y., Mély, Y., and Klymchenko, A.S. (2015). Charge-controlled nanoprecipitation as a modular approach to ultrasmall polymer nanocarriers: Making bright and stable nanoparticles. ACS Nano *9*, 5104–5116.

233. Lepeltier, E., Bourgaux, C., and Couvreur, P. (2014). Nanoprecipitation and the "Ouzo effect": Application to drug delivery devices. Adv. Drug Deliv. Rev. *71*, 86–97.

234. Barichello, J.M., Morishita, M., Takayama, K., and Nagai, T. (1999). Encapsulation of Hydrophilic and Lipophilic Drugs in PLGA Nanoparticles by the Nanoprecipitation Method. Drug Dev. Ind. Pharm. *25*, 471–476.

235. Danhier, F., Lecouturier, N., Vroman, B., Jérôme, C., Marchand-Brynaert, J., Feron, O., and Préat, V. (2009). Paclitaxel-loaded PEGylated PLGA-based nanoparticles: In vitro and in vivo evaluation. J. Control. Release *133*, 11–17.

236. Beck-Broichsitter, M., Rytting, E., Lebhardt, T., Wang, X., and Kissel, T. (2010). Preparation of nanoparticles by solvent displacement for drug delivery: A shift in the " ouzo region" upon drug loading. Eur. J. Pharm. Sci. *41*, 244–253.

237. Rao, J.P., and Geckeler, K.E. (2011). Polymer nanoparticles: Preparation techniques and size-control parameters. Prog. Polym. Sci. *36*, 887–913.

238. Schubert, S., Delaney, J.T., and Schubert, U.S. (2011). Nanoprecipitation and nanoformulation of polymers: From history to powerful possibilities beyond poly(lactic acid). Soft Matter *7*, 1581–1588.

239. Govender, T., Stolnik, S., Garnett, M.C., Illum, L., and Davis, S.S. (1999). PLGA nanoparticles prepared by nanoprecipitation: Drug loading and release studies of a water soluble drug. J. Control. Release *57*, 171–185.

240. Zheng, C., Zheng, M., Gong, P., Jia, D., Zhang, P., Shi, B., Sheng, Z., Ma, Y., and Cai, L. (2012). Indocyanine green-loaded biodegradable tumor targeting nanoprobes for in vitro and in vivo imaging. Biomaterials *33*, 5603–5609.

241. Saxena, V., Sadoqi, M., and Shao, J. (2004). Enhanced photo-stability, thermal-stability and aqueous-stability of indocyanine green in polymeric nanoparticulate systems. J. Photochem. Photobiol. B Biol. *74*, 29–38.

242. Kulkarni, S.A., and Feng, S.S. (2013). Effects of particle size and surface modification on cellular uptake and biodistribution of polymeric nanoparticles for drug delivery. Pharm. Res. *30*, 2512–2522.

243. Soo Choi, H., Liu, W., Misra, P., Tanaka, E., Zimmer, J.P., Itty Ipe, B., Bawendi, M.G., and Frangioni, J. V. (2007). Renal clearance of quantum dots. Nat. Biotechnol. *25*, 1165–1170.

244. Frangioni, J. V. (2003). In vivo near-infrared fluorescence imaging. Curr. Opin. Chem. Biol. *7*, 626–634.

245. Weissleder, R. (2001). A clearer vision for in vivo imaging. Nat. Biotechnol. *19*, 316–317.

246. Wang, D., Qian, J., He, S., Park, J.S., Lee, K.S., Han, S., and Mu, Y. (2011). Aggregation-enhanced fluorescence in PEGylated phospholipid nanomicelles for in vivo imaging. Biomaterials *32*, 5880–5888.

247. Panyam, J., and Labhasetwar, V. (2003). Biodegradable nanoparticles for drug and gene delivery to cells and tissue. Adv. Drug Deliv. Rev. *55*, 329–347.

248. Kumari, A., Yadav, S.K., and Yadav, S.C. (2010). Biodegradable polymeric nanoparticles based drug delivery systems. Colloids Surfaces B Biointerfaces *75*, 1–18.

249. Krasia-Christoforou, T., and Georgiou, T.K. (2013). Polymeric theranostics: Using polymer-based systems for simultaneous imaging and therapy. J. Mater. Chem. B *1*, 3002–3025.

250. Nicolas, J., Mura, S., Brambilla, D., MacKiewicz, N., and Couvreur, P. (2013). Design, functionalization strategies and biomedical applications of targeted biodegradable/biocompatible polymer-based nanocarriers for drug delivery. Chem. Soc. Rev. *42*, 1147–1235.

251. Mukhopadhyay, R.D., Praveen, V.K., and Ajayaghosh, A. (2014). Photoresponsive metal-organic materials: Exploiting the azobenzene switch. Mater. Horizons *1*, 572–576.

252. Bandara, H.M.D., and Burdette, S.C. (2012). Photoisomerization in different classes of azobenzene. Chem. Soc. Rev. *41*, 1809–1825.

253. Baroncini, M., and Bergamini, G. (2017). Azobenzene: A Photoactive Building Block for Supramolecular Architectures. Chem. Rec. *17*, 700–712.

254. Tamai, N., and Miyasaka, H. (2000). Ultrafast Dynamics of Photochromic Systems. Chem. Rev. *100*, 1875–1890.

255. Puntoriero, F., Ceroni, P., Balzani, V., Bergamini, G., and Vögtle, F. (2007). Photoswitchable dendritic hosts: A dendrimer with peripheral azobenzene groups. J. Am. Chem. Soc. *129*, 10714–10719.

256. Parker, R.M., Gates, J.C., Rogers, H.L., Smith, P.G.R., and Grossel, M.C. (2010). Using the photoinduced reversible refractive-index change of an azobenzene co-polymer to reconfigure an optical Bragg grating. J. Mater. Chem. *20*, 9118–9125.

257. Ferri, V., Elbing, M., Pace, G., Dickey, M.D., Zharnikov, M., Samor, P., Mayor, M., and Rampi, M.A. (2008). Light-powered electrical switch based on cargo-lifting azobenzene monolayers. Angew. Chemie - Int. Ed. *47*, 3407–3409.

258. McElhinny, K.M., Park, J., Ahn, Y., Huang, P., Joo, Y., Lakkham, A., Pateras, A., Wen, H., Gopalan, P., and Evans, P.G. (2018). Photoisomerization Dynamics in a Densely Packed Optically Transformable Azobenzene

Monolayer. Langmuir *34*, 10828–10836.

259. Kakiage, K., Yamamura, M., Ido, E., Kyomen, T., Unno, M., and Hanaya, M. (2011). Reactivity of alkoxysilyl compounds: Chemical surface modification of nano-porous alumina membrane using alkoxysilylazobenzenes. Appl. Organomet. Chem. *25*, 98–104.

260. Banghart, M.R., Mourot, A., Fortin, D.L., Yao, J.Z., Kramer, R.H., and Trauner, D. (2009). Photochromic blockers of voltage-gated potassium channels. Angew. Chemie - Int. Ed. *48*, 9097–9101.

261. Kim, Y., Phillips, J.A., Liu, H., Kang, H., and Tan, W. (2009). Using photons to manipulate enzyme inhibition by an azobenzene-modified nucleic acid probe. Proc. Natl. Acad. Sci. U. S. A. *106*, 6489–6494.

262. Wang, J., Liu, H.B., and Ha, C.S. (2009). Zinc-supported azobenzene derivative-based colorimetric fluorescent "turn-on" sensing of bovine serum albumin. Tetrahedron *65*, 9686–9689.

263. Banghart, M., Borges, K., Isacoff, E., Trauner, D., and Kramer, R.H. (2004). Light-activated ion channels for remote control of neuronal firing. Nat. Neurosci. *7*, 1381–1386.

264. Norikane, Y., and Tamaoki, N. (2004). Light-driven molecular hinge: A new molecular machine showing a light-intensity-dependent photoresponse that utilizes the trans-cis isomerization of azobenzene. Org. Lett. *6*, 2595–2598.

265. Murakami, H., Kawabuchi, A., Kotoo, K., Kunitake, M., and Nakashima, N. (1997). A light-driven molecular shuttle based on a rotaxane. J. Am. Chem. Soc. *119*, 7605–7606.

266. Muraoka, T., Kinbara, K., and Aida, T. (2006). Mechanical twisting of a guest by a photoresponsive host. Nature *440*, 512–515.

267. Sobolewska, A., Miniewicz, A., Grabiec, E., and Sek, D. (2006). Holographic grating recording in azobenzene functionalized polymers. Cent. Eur. J. Chem. *4*, 266–284.

268. Koppa, P. (2007). Phase-to-amplitude data page conversion for holographic storage and optical encryption. Appl. Opt. *46*, 3561–3571.

269. Yadavalli, N.S., Saphiannikova, M., and Santer, S. (2014). Photosensitive response of azobenzene containing films towards pure intensity or polarization interference patterns. Appl. Phys. Lett. *105*.

270. Evangelio, E., Saiz-Poseu, J., Maspoch, D., Wurst, K., Busque, F., and Ruiz-Molina, D. (2008). Synthesis, X-ray structure and reactivity of a sterically protected azobisphenol ligand: On the quest for new multifunctional active ligands. Eur. J. Inorg. Chem., 2278–2285.

271. Shinkai, S., Nakaji, T., Nishida, Y., Ogawa, T., and Manabe, O. (1980). Photoresponsive Crown Ethers. 1. Cis-Trans Isomerism of Azobenzene as a Tool to Enforce Conformational Changes of Crown Ethers and Polymers. J. Am. Chem. Soc. *102*, 5860–5865.

272. Luboch, E., Wagner-Wysiecka, E., and Rzymowski, T. (2009). 4-Hexylresorcinol-derived hydroxyazobenzocrown ethers as chromoionophores. Tetrahedron *65*, 10671–10678.

273. Luboch, E., Wagner-Wysiecka, E., Poleska-Muchlado, Z., and Kravtsov, V.C. (2005). Synthesis and properties of azobenzocrown ethers with π-electron donor, or π-electron donor and π-electron acceptor group(s) on benzene ring(s). Tetrahedron *61*, 10738–10747.

274. Villa, M., Bergamini, G., Ceroni, P., and Baroncini, M. (2019). Photocontrolled self-assembly of azobenzene nanocontainers in water: Light-triggered uptake and release of lipophilic molecules. Chem. Commun. *55*, 11860–11863.

275. Satzger, H., Root, C., and Braun, M. (2004). Excited-state dynamics of trans- and cis-azobenzene after UV excitation in the $\pi\pi^*$ band. J. Phys. Chem. A *108*, 6265–6271.

276. Fan, Q., Nabar, G., Miller, C., Castro, C., and Winter, J. (2014). Photo-switchable quantum dots based on reversible FRET. Nanoscale Imaging, Sensing, Actuation Biomed. Appl. XI *8954*, 89540D.

277. Hierrezuelo, J., Rico, R., Valpuesta, M., Díaz, A., López-Romero, J.M., Rutkis, M., Kreigberga, J., Kampars, V., and Algarra, M. (2013). Synthesis of azobenzene substituted tripod-shaped bi(p-phenylene)s. Adsorption on gold and CdS quantum-dots surfaces. Tetrahedron *69*, 3465–3474.

278. Javed, H., Fatima, K., Akhter, Z., Nadeem, M.A., Siddiq, M., and Iqbal, A. (2016). Fluorescence modulation of cadmium sulfide quantum dots by azobenzene photochromic switches. Proc. R. Soc. A Math. Phys. Eng. Sci. *472*.

279. Fang, D., Chen, R., Liu, H., Zhang, Z., and Ding, Z. (2010). Temperature dependent luminescence of azobenzene capped CdS quantum dots. J. Nanosci. Nanotechnol. *10*, 7600–7602.

280. Farah, A.A., Dares, C., and Pietro, W.J. (2010). Using a push - Pull azobenzene haptan to probe surface - Core electronic communication in surface-functionalized CdS quantum dots. J. Phys. Chem. C *114*, 20410–20416.

281. Chu, I.H., Trinastic, J., Wang, L.W., and Cheng, H.P. (2014). Using light-switching molecules to modulate charge mobility in a quantum dot array. Phys. Rev. B - Condens. Matter Mater. Phys. *89*, 1–8.

282. Saeed, S., Yin, J., Khalid, M.A., Channar, P.A., Shabir, G., Saeed, A., Arif

Nadeem, M., Soci, C., and Iqbal, A. (2019). Photoresponsive azobenzene ligand as an efficient electron acceptor for luminous CdTe quantum dots. J. Photochem. Photobiol. A Chem. *375*, 48–53.

283. Saeed, S., Channar, P.A., Larik, F.A., Saeed, A., Nadeem, M.A., and Iqbal, A. (2019). Charge/energy transfer dynamics in CuO quantum dots attached to photoresponsive azobenzene ligand. J. Photochem. Photobiol. A Chem. *371*, 44–49.

284. Irvine, S.E., Staudt, T., Rittweger, E., Engelhardt, J., and Hell, S.W. (2008). Direct light-driven modulation of luminescence from Mn-doped ZnSe quantum dots. Angew. Chemie - Int. Ed. *47*, 2685–2688.

285. Díaz, S.A., Menéndez, G.O., Etchehon, M.H., Giordano, L., Jovin, T.M., and Jares-Erijman, E.A. (2011). Photoswitchable water-soluble quantum dots: PcFRET based on amphiphilic photochromic polymer coating. ACS Nano *5*, 2795–2805.

286. Impellizzeri, S., McCaughan, B., Callan, J.F., and Raymo, F.M. (2012). Photoinduced enhancement in the luminescence of hydrophilic quantum dots coated with photocleavable ligands. J. Am. Chem. Soc. *134*, 2276–2283.

287. Díaz, S.A., Giordano, L., Jovin, T.M., and Jares-Erijman, E.A. (2012). Modulation of a photoswitchable dual-color quantum dot containing a photochromic FRET acceptor and an internal standard. Nano Lett. *12*, 3537–3544.

288. Liu, Y., Yu, C., Jin, H., Jiang, B., Zhu, X., Zhou, Y., Lu, Z., and Yan, D. (2013). A supramolecular Janus hyperbranched polymer and its photoresponsive self-assembly of vesicles with narrow size distribution. J. Am. Chem. Soc. *135*, 4765–4770.

289. Dubecký, M., Derian, R., Horváthová, L., Allan, M., and Štich, I. (2011). Disentanglement of triplet and singlet states of azobenzene: Direct EELS detection and QMC modeling. Phys. Chem. Chem. Phys. *13*, 20939–20945.

290. Cembran, A., Bernardi, F., Garavelli, M., Gagliardi, L., and Orlandi, G. (2004). On the Mechanism of the cis-trans Isomerization in the Lowest Electronic States of Azobenzene: S0, S1, and T1. J. Am. Chem. Soc. *126*, 3234–3243.

291. Ladányi, V., Dvořák, P., Al Anshori, J., Vetráková, Ľ., Wirz, J., and Heger, D. (2017). Azobenzene photoisomerization quantum yields in methanol redetermined. Photochem. Photobiol. Sci. *16*, 1757–1761.

292. Yang, J., Liptak, R., Rowe, D., Wu, J., Casey, J., Witker, D., Campbell, S.A., and Kortshagen, U. (2014). UV and air stability of high-efficiency photoluminescent silicon nanocrystals. Appl. Surf. Sci. *323*, 54–58.

293. Carroll, G.M., Limpens, R., and Neale, N.R. (2018). Tuning Confinement in Colloidal Silicon Nanocrystals with Saturated Surface Ligands. Nano Lett. *18*, 3118–3124.

294. Balagurov, L.A., Leiferov, B.M., Petrova, E.A., Orlov, A.F., and Panasenko, E.M. (1996). Influence of water and alcohols on photoluminescence of porous silicon. J. Appl. Phys. *79*, 7143–7147.

295. Yang, Z., De Los Reyes, G.B., Titova, L. V., Sychugov, I., Dasog, M., Linnros, J., Hegmann, F.A., and Veinot, J.G.C. (2015). Evolution of the ultrafast photoluminescence of colloidal silicon nanocrystals with changing surface chemistry. ACS Photonics *2*, 595–605.

296. Mastronardi, M.L., Chen, K.K., Liao, K., Casillas, G., and Ozin, G.A. (2015). Size-dependent chemical reactivity of silicon nanocrystals with water and oxygen. J. Phys. Chem. C *119*, 826–834.

297. Klajn, R., Wesson, P.J., Bishop, K.J.M., and Grzybowski, B.A. (2009). Writing self-erasing images using metastable nanoparticle "inks." Angew. Chemie - Int. Ed. *48*, 7035–7039.

298. Hessel, C.M., Henderson, E.J., and Veinot, J.G.C. (2007). An investigation of the formation and growth of oxide-embedded silicon nanocrystals in hydrogen silsesquioxane-derived nanocomposites. J. Phys. Chem. C *111*, 6956–6961.

299. Hessel, C.M., Rasch, M.R., Hueso, J.L., Goodfellow, B.W., Akhavan, V.A., Puvanakrishnan, P., Tunnel, J.W., and Korgel, B.A. (2010). Alkyl passivation and amphiphilic polymer coating of silicon nanocrystals for diagnostic imaging. Small *6*, 2026–2034.

300. de Mello, J. C.; Wittmann, H. F.; Friend, R.H. (1997). An Improved Experimental Determination of External Photoluminescence Quantum Efficiency. Adv. Mater. *9*, 230–232.

301. Williams, D.B., and Carter, C.B. Trasmission Electron Microscopy Springer, ed.